UNIVERSITÀ DEGLI STUDI DI TRIESTE

XXVIII CICLO DEL DOTTORATO DI RICERCA IN

INGEGNERIA E ARCHITETTURA - INDIRIZZO INGEGNERIA MECCANICA, NAVALE, DELL'ENERGIA E DELLA PRODUZIONE

Large Workspace Robots

Settore scientifico-disciplinare: **ING-IND/13 MECCANICA APPLICATA ALLE MACCHINE**

DOTTORANDO	**Stefano Seriani**
COORDINATORE	**Prof. Guido Micheli**
SUPERVISORE DI TESI	**Prof. Paolo Gallina**

ANNO ACCADEMICO 2014 / 2015

UNIVERSITÀ DEGLI STUDI DI TRIESTE

XXVIII CICLO DEL DOTTORATO DI RICERCA IN

INGEGNERIA E ARCHITETTURA - INDIRIZZO INGEGNERIA MECCANICA, NAVALE, DELL'ENERGIA E DELLA PRODUZIONE

Large Workspace Robots

Settore scientifico-disciplinare: **ING-IND/13 MECCANICA APPLICATA ALLE MACCHINE**

DOTTORANDO
Stefano Seriani

COORDINATORE
Prof. Guido Micheli

SUPERVISORE DI TESI
Prof. Paolo Gallina

ANNO ACCADEMICO 2014 / 2015

Sommario

In questo lavoro, una nuova classe di robot viene presentata con la denominazione di Large Workspace Robots (LWR), robots a grande spazio di lavoro. Al fine di permettere una classificazione coerente di sistemi esistenti o di nuova concezione, viene data una definizione basata sull'estensione del workspace e la massa del robot.

Lo scopo di questo studio è di produrre un framework o struttura coerente e organica, che permetta la progettazione e l'analisi di questa neodefinita classe di sistemi robotizzati. Molti aspetti sono stati esplorati, e la ricerca è stata suddivisa in tre parti, la prima delle quali è relativa a metodi topologicamente efficienti per Repetitive Workspace Robots (RWR), ovvero robot a spazio di lavoro ripetitivo. Questi sono sistemi dove un robot arbitrariamente piccolo viene utilizzato per coprire una grande superficie muovendosi seguendo una griglia. Sono stati definiti tre algoritmi per il calcolo di un indice I_{RWR} specialmente definito: il Genetic Covering Algorithm (GCA), lUniform Expansion Covering Algorithm (UECA) e infine il Corrected Inertial Ellipsoid Covering Algorithm (CIECA).

La seconda parte riguarda l'argomento del controllo di robot che sono destinati a lavorare su superfici molto grandi; a questo proposito è stata definita una metodologia per la pianificazione della traiettoria e del profilo di velocit. Il maggior campo applicativo è quello della pitturazione robotizzata di immagini foto-realistiche su grandi superfici, come ad esempio la facciata di un palazzo. Indagini sperimentali sono state effettuate sul cono di spruzzo.

La terza parte è relativa all'hardware e agli aspetti del progetto di LWR. Sono stati studiati vari tipi di attuatori che potrebbero portare dei vantaggi in questo campo. In particolare, viene descritto un attuatore basato sugli

Storable Tubular Extendible Members (STEMs). La progettazione e valutazione di un prototipo ha mostrato notevoli doti strutturali, una grande estensione e ingombri limitati. È stato presentato e analizzato in profondità, un robot parallelo planare sovra-attuato che valorizza questo tipo di attuatori. I risultati mostrano che la sovra-attuazione aiuta a limitare l'estensione delle singolarità del meccanismo e il sistema concepito risulta classificabile come LWR viste le sue doti di leggerezza e il grande spazio di lavoro.

Allo stesso modo, sono stati presentati attuatori lineari d'impiego nella progettazione di un carroponte; questi sono basati sul meccanismo conosciuto come Variable Radius Drum Mechanism (VRDM). E' stata descritta una metodologia di sintesi analitica per la progettazione delle VRD. Queste sono costituite da un tamburo con raggio variabile in modo continuo; questo permette un accoppiamento non lineare tra l'avvolgimento (e lo svolgimento) del cavo e la rotazione del tamburo stesso.

Successivamente, è stato descritto un Cable Driven Parallel Robot (CDPR) per applicazioni spaziali: ispezione e manipolazione leggera sulla Luna, Marte e su altri corpi celesti. Il sistema si compone di un rover con manipolatore seriale, tre moduli e un end-effector. Questi ultimi componenti vengono assemblati insieme dal rover, costituendo infine il CDPR. In questo studio il robot viene analizzato particolarmente per quanto riguarda l'influenza della stabilità dei suoi moduli sulla morfologia del workspace. Infine sono descritte diverse applicazioni specifiche.

In ultimo, sono presentate alcune possibili applicazioni che spaziano attraverso più di uno tra gli aspetti propri degli LWR; del CDPR per applicazioni spaziali vengono discussi anche potenziali ulteriori sviluppi e miglioramenti tecnologici, specialmente riguardo l'attuazione e la stabilizzazione.

Le conclusioni affermano lo scopo della definizione della classe dei LWR e come i vari aspetti influenzino la progettazione e l'analisi di questi tipi di robot.

Abstract

A new class of robots is presented in this research, with the denomination of Large Workspace Robots (LWR). A definition based on the workspace extension and the mass of the robot is provided, to allow a proper classification of existing and new systems.

The aim of the present study is to produce a coherent and organic framework to allow the design and analysis of this newly defined class of robotic systems. Several aspects were explored, and the research was partitioned in three parts, the first being topological efficiency methods for Repetitive Workspace Robots (RWR), which are systems where an arbitrarily small conventional robot is used to cover a large surface by moving it in a grid-like fashion. Three algorithms are defined to compute an especially defined I_{RWR} index: the Genetic Covering Algorithm (GCA), the Uniform Expansion Covering Algorithm (UECA) and finally the Corrected Inertial Ellipsoid Covering Algorithm (CIECA).

The second part regards the topic of controlling robots that are intended to work upon very large surfaces; to this end, a trajectory- and speed profile-planning methodology is defined. The main field of application is robotized painting of photo-realistic images on large surfaces like the façade of buildings. Experimental investigations were performed on the spray-cone of paint.

The third part is related to hardware and design aspects of LWRs. Different types of actuators are studied that could carry advantages in this context. In particular, an actuator based on Storable Tubular Extendible Members (STEMs) is presented. The design and evaluation of a prototype shows remarkable structural characteristics, very large stroke and a limited bulk. Exploiting this actuator, a planar, parallel, over-actuated robot is presented

and analysed in detail. Results show that the over-actuation helps with limiting the singularities of the mechanism and the design proves to be classifiable as a LWR, in light of its extremely large workspace and lightness of the structure.

Along the same lines, linear actuators applied to the design of an overhead crane are presented that exploit the mechanisms known as Variable Radius Drum Mechanisms (VRDM). An analytical synthesis methodology is presented to allow these VRD to be designed. The VRD is a drum with a continuously variable radius; this feature allows non-linear coupling between the winding (or unwinding) of the cable and the rotation of the drum itself. Moreover, a modular Cable Driven Parallel Robot (CDPR) is presented for space applications: inspection and light manipulation of the Moon and Mars and other celestial bodies. The system comprises a serial manipulator-equipped rover, three modules and an end-effector. These last components are assembled together by the rover and ultimately constitute the CDPR. In this study, the robot is analysed, particularly for what concerns the influence of the stability of the modules to the morphology of the workspace of the robot. Several applications are described.

Finally, several possible applications are presented that encompass multiple of the discussed aspects belonging to LWRs; technological improvement on the CDPR for space applications are discussed as well, particularly regarding actuation and stabilization.

The conclusions state the purpose of the definition of the class of LWRs and how the various discussed aspect influence the design and analysis process of this kind of robots.

Contents

1

Introduction

There is, in the robotics-related industry, an ever-increasing need for automated machines capable of operating on large scale workspaces. However, there is no specific classification that takes into account the size of the workspace by itself.

Traditionally, robots are defined — and selected — based on their kinematics, structure or other functional characteristics [1]; the way large workspaces are often treated is simply by the use of a scale factor on the size of the robot. Hence, in general, if a very large volume needs to be addressed, a suitably large robot will be selected and employed.

The drawback of this way of thinking is that it makes it hard to find more efficient solutions; scaling-up is, in fact, a generally very poor and inefficient way to solve a "larger" problem.

In this work another point of view is proposed on the matter, one which focuses precisely on robots with large scale workspaces and how to address them, the first step being the concept of Large Workspace Robots (LWR). This is a *class* that defines robots conceived explicitly to act upon large volumes of space, regardless of their kinematic configuration or hardware.

The second step is the development of a design and analysis paradigm for these systems: the main parameters are discussed against several examples of applications. Unconventional solutions are presented, both from a geometrical and mathematical point of view as for what regards the practical implementation of these systems.

1.1 Definition of Large Workspace Robots

The LWRs classification criterion is not an immediate concept. One could wonder: "How large should the workspace be to be classified as *large*?". Indeed, since a simple scale factor could be employed to every conceivable robot to reach the desired workspace size, it seems apparent that a more rigorous definition should be employed. With this in mind, a robot can be classified as a Large Workspace Robot if the following is valid,

$$\frac{W}{m} \geq 0.2, \tag{1.1}$$

where m stands for the mass (in Kg) of the robot, and W is a value that describes the size of the workspace. It corresponds to a volumetric quantity (in m^3) for 3D robots, an area (in m^2) for 2D robots and a linear quantity (in m) for 1D robots.

In Fig. 1.1 a state-of-the-art serial manipulator for industrial tasks is illustrated. The robot depicted represents a class of robotics systems which do not fall in the classification we have just seen. This is to say that the vast majority of robots which exist at the moment in the industry cannot be classified as a LWR; in fact, this robot attains a W/m value of approximately just 0.08.

Figure 1.1: A small industrial serial manipulator by KUKA AG.

1.2 State of the Art

The Large Workspace Robot concept covers a very broad set of subjects. It is an expression that includes many different aspects and covers a very wide set of technologies. Being it an entirely novel classification, the state-of-the-art lacks proper explicit research in this specific direction. Despite this, many examples can nevertheless be found with ease in current industrial applications. In the following sections, an analysis of the main definitions, applications, as well as practical examples is presented.

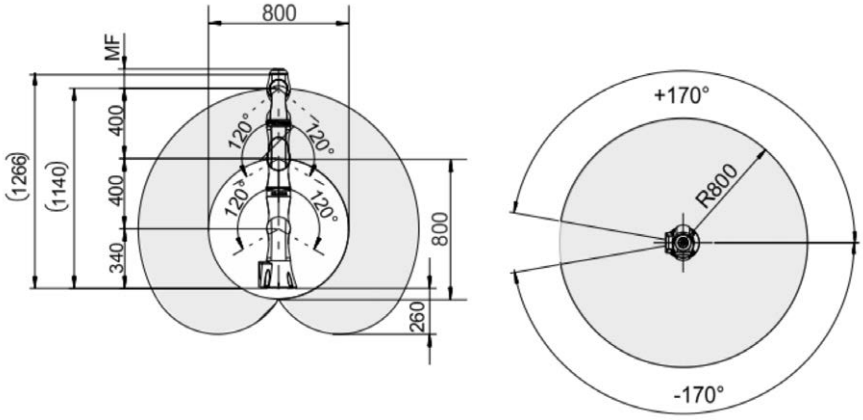

Figure 1.2: The workspace specifications for the KUKA AG LBR iiwa 7 R800, a robot similar to the one depicted in Fig. 1.1. On the left, a vertical section of the workspace is shown, whereas on the right the workspace is seen from the top. Measures are in mm.

1.2.1 Workspace

The concept of workspace itself is well defined in robotics; as a concept, it is the space the robot is able to work upon. An example is given in Fig. 1.2, where the longitudinal and horizontal workspace sections are visible in detail. This definition is though very limited in scope, since the end-effector – the device that is placed at the end of the robot and interacts with the environment – is never point-like and can work in every orientation. An example would be a drill. It is clear that the workspace defined by the simple reach of the point of the drill-bit will be very different compared to the one that takes into account also the orientation of the drill-bit, which is paramount to the system operating correctly.

Fortunately, several much more precise definitions exist. The workspace (or *reachable* workspace) is defined as the volume of space within which every point can be reached by the end-effector in at least one orientation. The dexterous workspace is the volume of space within which every point can be reached by the end-effector in all possible orientations, as reported for example in [1]. A controllable workspace is defined as a set of postures where forces and torques at the end-effector can be controlled [2, 3]. Sometimes the workspace is analyzed in terms of manipulability [4–6] and dexterity [7]. Following a geometrical approach, Gosselin [8] defined a dynamic workspace in which the shape of the workspace depends on the accelerations of the end-effector. A survey of the basic workspace terminologies for cable-driven robots can be found in [9].

1.2.2 LWRs in the industry

Perhaps the most appropriate representative of the LWRs class is the Cable Direct Driven Robot (CDDR), or Cable Driven Parallel Robot (CDPR) [3, 4, 7, 8, 10–13]. In 1989, the first appearance of a CDPR was the NIST Robocrane [14, 15], a system for large-scale load handling. In 1995, a ultra-fast FALCON robot [16] was described for pick-and-place operations. In recent years the IPAnema family of cable robots was presented [17–20].

A widely known example is Skycam [21], visible in Fig. 1.3 and its successor Spidercam[1]. These are probably amongst the few commercially viable CDPRs consistently used in the industry.

Pott et al. [20] describe a CDPR designed for industrial applications. Another, rather interesting application is described by Izard et al. [22] related to the use of a CDPR for inspection and manipulation in future fusion reactors of current design.

Another type of robots which can be classified as LWR are systems where the robot is free to roam by employing a wheeled system, a legged one, or yet some other means of locomotion. This covers the broad field of rovers, examples of which can be seen in [23–28]. However, these systems do not generally have great accuracy and can move only in the space defined by the ground. An exception is represented by rovers that have some type of additional manipulation capability, e.g. a robotic arm. An example is for example NASA's Mars Science Laboratory [26], or the robotized excavating machines presented in [29, 30]. In the year 2000 a truck-mounted robot for the maintenance and

[1] http://www.spidercam.tv/

Figure 1.3: The CDPR based Skycam. On the top the electronics is visible, and on the bottom are the pan-tilt motor, stabilization sensors and the camera.

inspection of bridges was developed by Lorenc et al. [31]. Lastly, a novel type of robot designed for painting façades was presented by Kim et al. in 2007 [32].

1.3 Industrial Requirements and Applications

As mentioned in the opening of this manuscript, there is an ever-increasing need, in the industrial and – more broadly – technological world, of the robots we can classify as Large Workspace Robots. Tasks which are traditionally carried out using the omnipresent serial or parallel manipulators[1], could be taken care of perhaps using CDPRs or hybrid systems based on rovers or wheeled platforms in general.

A collection of possible applications that will be covered in the following several chapters, is summarized in the following list:

- Visual inspection of large volumes of space,
- Sensor-based inspection of large volumes of spaces,

[1] A very comprehensive first glance on the matter of serial (and parallel) manipulators can be had from [1].

- Cleaning of large surfaces or bodies,
- Painting of large surfaces.

As an example, an illustration of the exploitation of a CDPR for the visual or sensor-based inspection of large volumes is shown in Fig. 1.4. This precise concept will be covered in-depth in 4.3 on page 128.

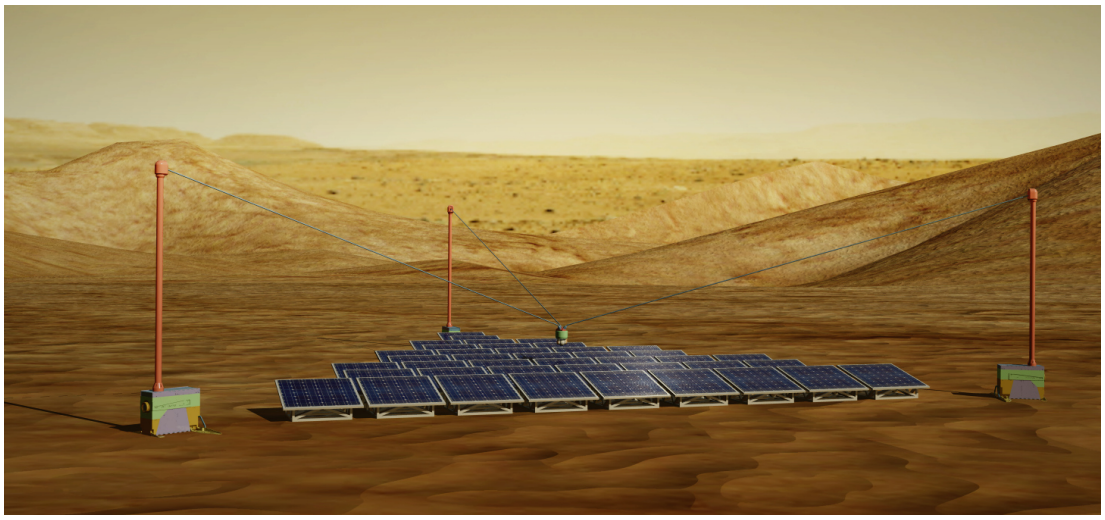

Figure 1.4: The inspection of a large solar panel array deployed on Mars is shown as an example of application of CDPRs as a LWR.

1.4 Methodology Outline

Facing the task of developing specific tools for the management of the design and analysis process of an entirely novel class of robotic system is not straightforward. For instance, many aspects that are not normally considered in robotics' state-of-the-art are paramount for exploiting LWRs, and are indeed main design parameters in some cases.

Given these considerations, and taking into account the inherent width and multi-facet nature of the subject, the work has been split in three main research branches:

- **The topology of large workspaces.** In the usual practice of robotics the workspace is considered as a simple envelope in which all the operations that need

to be addressed should be contained. Rarely the entire workspace is used or is important at all. In this case, instead, a special kind of LWR is considered, named Repetitive Workspace Robot (RWR). This is a robot that covers indefinitely large areas by splitting it into subsets which are then addressed sequentially by moving the robot's base.

- **The control of LWRs.** In particular, a path-planning methodology and algorithm was developed for spray-painting robots that are designed to operate on extremely large surfaces, like the façade of a building or the side of a ship. Robots of this type include for example Cable Direct Driven Robots (CDDRs) but the method can be extended to include also more traditional robots or even RWRs.

- **The design and actuation of LWRs.** A parallel robot was designed and analysed, with links based on an actuator which takes advantage of Storable Tubular Extendible Members (STEMs). Furthermore, a modular CDDR for space application that is deployed by a rover was conceived in collaboration with the Robotics and Mechatronics Center of the DLR[1], the German Space Agency.

The methodologies and tools presented in these areas are subsequently used to describe and analyse a series of practical applications. In the end, this partitioning covers very well the most important and novel aspects of LWRs research, from design to analysis, and provide a quality, specialized paradigm to this field of robotics.

[1]Deutsches Zentrum für Luft- und Raumfahrt

2

Topological Methods

As mentioned in the opening of this manuscript, when large spaces need to be covered by a robotic system, the most common solution is to design or employ a robot with a comparably large workspace. This is the most straightforward solution, but is one that carries along several important disadvantages, namely large dimensions, mass, high power requirements, and ultimately high costs. It is one of the reason why most of the relevant applications are usually addressed by manual labour or semi-automatic technologies of low impact. An example that stands tall is the painting of buildings or of large structures of whatever type.

Since manual painting is a task that requires time and can rarely avoid exploiting some sort of elevation techniques like Aerial Work Platforms (AWP) – an example of which is visible in Fig. 2.1 – the costs, both fixed and running, associated with this kind of endeavour are typically consistent.

An expert painter with an AWP at his disposal, faced with the task of addressing a very large surface like the façade of a building (e.g. a warehouse or industrial depot) would start by positioning the AWP in a suitable place at either end of the complex and start painting the area that it can reach while on the locked platform. Once this is completed, and he cannot reach beyond, he will unlock the AWP and move it to paint the next portion of the untreated surface. This sequence will need to be repeated until a complete covering of the surface is carried out.

The outlined procedure can be replicated by using autonomous systems well within reach of current technology and state-of-the-art hardware. Locomotion-enabled, fully- or semi-automated AWP can be used as mobile base for industrial serial robots. The

Figure 2.1: An example of an Aerial Work Platform with an integrated locomotion system. The wheeled base can be driven around and has, attached, a telescopic or otherwise articulated arm which, at the end, holds the cabin for the operator.

two sub-systems can be coordinated so as to act collaboratively, constituting, in the end, a LWR.

A human operator is able, through experience and eyesight, to efficiently cover a large surface, by moving the AWP in the best way possible. Robotic systems need some sort of algorithm or procedure to act similarly. Exceptions are for very simple local workspaces like rectangles, for examples, where the movement of the base can be calculated by using simple geometry notions.

In this section a new methodology [33] is described consisting in an efficient *partitioning* of space, in order to use robotic systems with a workspace of arbitrarily smaller size. These robots are thus called Repetitive Workspace Robots (RWR). An illustration of the concept in a practical application is shown in Fig. 2.2.

In order to simplify the research in this stage, only 2D planar robots are considered.

2.1 State of the Art

A complete and rigorous dissertation on a topological partition of space to allow the exploitation of a RWR has not yet surfaced in scientific literature up to this point.

Despite this, several attempts at covering space through repetition of an arbitrarily sized workspace have been reported in literature. For example Lorenc et al. [31], developed a robotic system to carry out maintenance operations on bridges that can be translated with the aid of a truck and peeper crane. As was mentioned previously, an interesting application is the painting tasks of large surfaces, like the façades of buildings or structures of other kind. Kim et al. approached this problem in [32].

Systems which feature wheeled bases or hybrid rover systems have been described in [29, 30], in the form of robotized excavators or bulldozers. These are, in fact, systems in which the machine operates in a set of predetermined positions, one at a time, to dig an area that is much bigger than the local workspace. This type of asynchronous motion can be referred to as *indexed*.

All of the authors of these examples of research have not attempted to address the problem of precisely deciding the overall pattern of the mobile platform in order

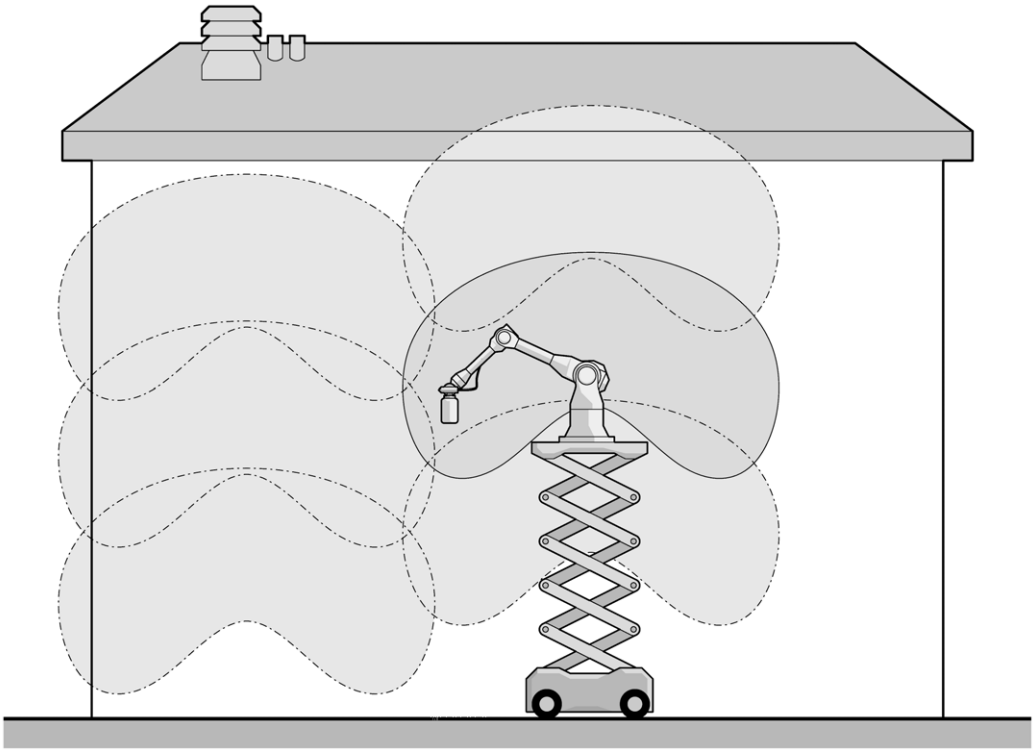

Figure 2.2: A Repetitive Workspace Robot used in the painting process of a large building's façade. The elevator base moves left, right, up and down, then holding the position, it paints the wall contained in the local workspace.

to cover the most space with the highest efficiency. It is a problem that the authors highlight as underlying all of these applications, but is never investigated directly.

From a purely mathematical standpoint, the problem which is being discussed is called Topological Covering Problem or Set Covering Problem (SCP) and conspicuous space is reserved for it in the following section.

2.2 Topological Covering Problem

In order to introduce the mathematics that support the SCP, it is useful to begin by considering the concept of *tessellation* in a topological context.

In regards to an Euclidean 2D space, we can define the tessellation as the process of covering a plane through the repetition of a single geometric shape, resulting in the absence of overlaps or gaps. The tessellation is not feasible with all possible shapes; for example, a circle cannot tessellate.

However, when the aim of the task is to cover a surface with a shape of arbitrary morphology, the expression "covering problem" is rather used [34, 35]. A covering problem, sometimes referred to as Set Covering Problem (SCP) is a classical question in computer science, complexity theory and topology. It was shown to be a NP-Complete problem in 1972 by R. M. Karp [36] and also in [37]. If a certain set A is defined, this problem questions whether another fixed set B covers set A, or if a certain number of sets B can be arranged so as to cover A.

In this section we will refer to a generalized problem, that is, considering the surface to cover as arbitrarily large. This assumption is made because the covering problem is normally applied to a pre-defined surface of size comparable to that of the primary shape, as in [38–41]. In these cases the smaller sets B are not necessarily arranged in a repetitive, evenly tiled manner. Considering the surface A as arbitrarily large implies that the influence of its border can be neglected, thus allowing[1] for a uniform tiling pattern of B. In Fig. 2.3, a comparison between the classic SCP (a) and a uniformly

[1]Note: the author does not claim that, where a surface of infinite extension is considered, an even tiling is the best possible solution for a SCP on said surface. Merely, it is used as an argument to explain how the influence of the border is inversely proportional to the size of the surface, or, in other words, to the number of repetitions. This is easy to comprehend by noting that the border of a geometric shape is always slower in growing than the area, when the size of the shape increases. In fact, if a circle is considered, and D is its diameter, the border increases by $\lambda_1 D$, while the area by $\lambda_2 D^2$, where $\lambda_{1,2}$ are two coefficients.

distributed one (b) is shown. In the former the surface A is finite and of size similar to the one of B, in the latter A is considered of infinite extension. In geometry, this repetitive and evenly tiled distribution is called lattice.

The crystallographic restriction theorem[1] states that five different types of lattice exist in the 2D Euclidean space; these are also called Bravais lattices[43], after their French discoverer, Auguste Bravais (1811–1863). The peculiarity of these groups is that the lattice is isotropic, i.e. it appears identical if viewed from any point of the lattice itself.

The rationale for considering the generalized problem, is that covering a finite and comparably small surface is a complex task that has little regard to the identification of a "pattern", which is, in fact, described by a lattice. Indeed, many of the cited solutions for these kind of problems provide highly irregular layouts. For the problem at hand this is detrimental, as will become evident from the next sections.

The formalism associated with the covering problem is less stringent compared to the one associated with the tessellation, since the former implicitly allows overlap

[1]Some recent details on the theorem can be found in [42]

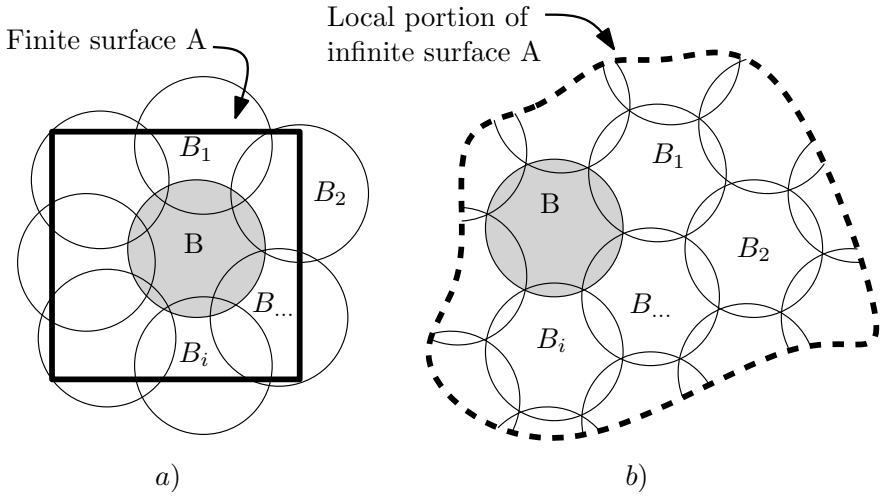

Figure 2.3: Examples of the covering problem. In a) a classic Set Covering Problem (SCP) is illustrated, where A (bold line) is a surface of finite extension, and B_1, B_2, ..., B_i are repetitions of a finite surface B. In b) a non-standard SCP is shown, where the surface A has infinite extension and B is tiled evenly according to a lattice structure. The dashed line shows a finite partition of A.

of adjacent shapes, which is, on the contrary, not allowed – by definition – in the tessellation.

2.3 Topological Covering Efficiency

We have seen how the SCP, at least in its non-generalized form, consists in determining the best possible configuration, or "pattern" of a set of shapes for the covering of a specific region of space, be it limited or non. As should be sufficiently immediate, the measure of this can be linked to the notion of efficiency.

We can thus state the SCP in other words, loosely, as: the problem of maximizing the *efficiency* in the covering of space by repetition of a specific shape. This concept is illustrated in Fig. 2.4, where two examples are given. What is immediately apparent from the same figure is that, for the same number of repetitions, six in this case, the tessellation with a square workspace (Fig. 2.4b) covers a much larger area than the one with a round workspace (Fig. 2.4c). Indeed, the overlap area is considerably larger in the case of the circular workspace. From these considerations, and assuming (for now) that the square lattice used to lay out the circles is the best option, we can infer that the circular workspace has a lower tessellation efficiency compared to the square one. We must remember that, in the case at hand we are interested in the generalized problem, so the determination of the repetition pattern is of primary importance.

It is clear that this concept of efficiency is related to the overlap, that is, that specific location in the space that is being covered, that sees the simultaneous presence of multiple base shapes. In other words, is the intersection of these base shapes. By leveraging on this concept, we can state the SCP as the problem of *minimizing* the overlap between the base shapes. We will see how this will be useful for some computations, described in the following sections.

2.4 Defining an Index for the Topological Covering Efficiency

From the considerations made up to this point, being able to formally define an index linked to this notion of efficiency seems appropriate.

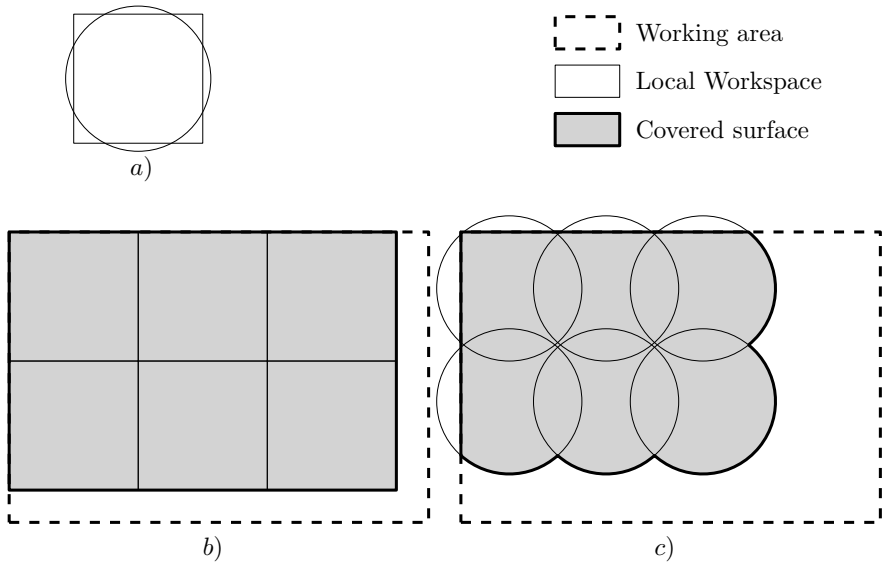

Figure 2.4: Efficiency of the tessellation (in grey) of the area to be covered (dashed line). In a) a square and a round workspace are shown; these have the same area. In b) one can see a partial tessellation of the working area resulting from the use of the square shape, whereas in c) the same is visible in case the circular one is employed

We define the efficiency index as linked to the concept of overlap. In principle, its upper bound coincides with a pure tessellation, which produces no overlap by definition, whereas the lower bound is obviously the case when the overlap area is equal to the area of the shape[1]. In the following we will discuss about covering efficiency in relation to this scale.

In order to formally define the index, we need to define the working area first; this is a connected surface (in the 2D case) contained in a plane $S \in \mathbb{R}^2$. This surface is the portion of space that the LWR must, in the end, cover completely; by referencing Fig. 2.4, the working area is delimited by the dashed line.

Let us consider the primitive cell (or basis) of a general Euclidean Bravais 2D lattice contained in the plane S. This can be univocally defined by three points, or nodes. Referring to Fig. 2.5, we can consider the point $i \in S$ to be known and coincident to the origin of the system of reference of axis $\xi, \zeta \in S$. The points $\mathbf{j} \in S$ and $\mathbf{k} \in S$

[1]Note that this case cannot arise with *simple* shapes. In order for this condition to appear, certain degenerations of the base shapes should be considered, as for example non-convex sets with infinitesimal-sized structures that span the entire domain. These are, however, of little impact to the problem that we are discussing, and can be safely let out.

can be completely defined by 4 parameters, i.e. the coordinates $j_\xi, j_\zeta, k_\xi, k_\zeta$ of the points with respect to the reference system. Hence, where covering is concerned, a complete representation of a periodical tiling on a 2D lattice structure can be defined by 4 parameters. In order to get a better link to the algorithms presented in this study, in the following we will illustrate a more suitable representation of the lattice tiling while maintaining the formal connection to the classical Bravais lattice. In particular, we will define another reference system and a set of vectors to describe the primitive cell of the lattice rather than the points **i**, **j**, **k**. Let us define another reference system, for the vector space S, with axis' unit vectors $\mathbf{X}, \mathbf{Y} \in S$ and centered in a point $\mathbf{O} \in S$, as in Fig. 2.6a. Furthermore, let $\mathbf{x}, \mathbf{y} \in S$ be the unit vectors of another reference system centered in the same point which is rotated by an angle $\gamma \in \mathbb{R}$ relative to $\mathbf{X}, \mathbf{Y}$. This angle is equal to the orientation angle of the link between the points **i** and **j**; this results in the parallelism between this link and the **x** axis.

Let now $\hat{\mathbf{v}}_\mathbf{t} \in S$ be a unit vector, as visible in the same figure; we can define a vector $\mathbf{v_t} \in S$ of modulus $s \in \mathbb{R}$ and parallel to $\hat{\mathbf{v}}_\mathbf{t}$. According to Fig. 2.6c, let $x, y \in \mathbb{R}$ be two scalar values, coherently with the following formulation,

$$\mathbf{v_t} = (x)\,\mathbf{x} + (y)\mathbf{y}. \tag{2.1}$$

Using two values of Δx, e.g. $\Delta x_1 \in \mathbb{R}$ and $\Delta x_2 \in \mathbb{R}$, with $\Delta x_1 \neq \Delta x_2$, it is now

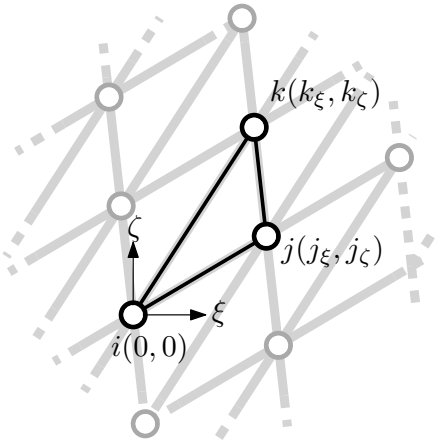

Figure 2.5: A detail of a general Euclidean 2D Bravais lattice. The points $\mathbf{i}, \mathbf{j}, \mathbf{k}$ define the primitive cell, or basis, of the lattice.

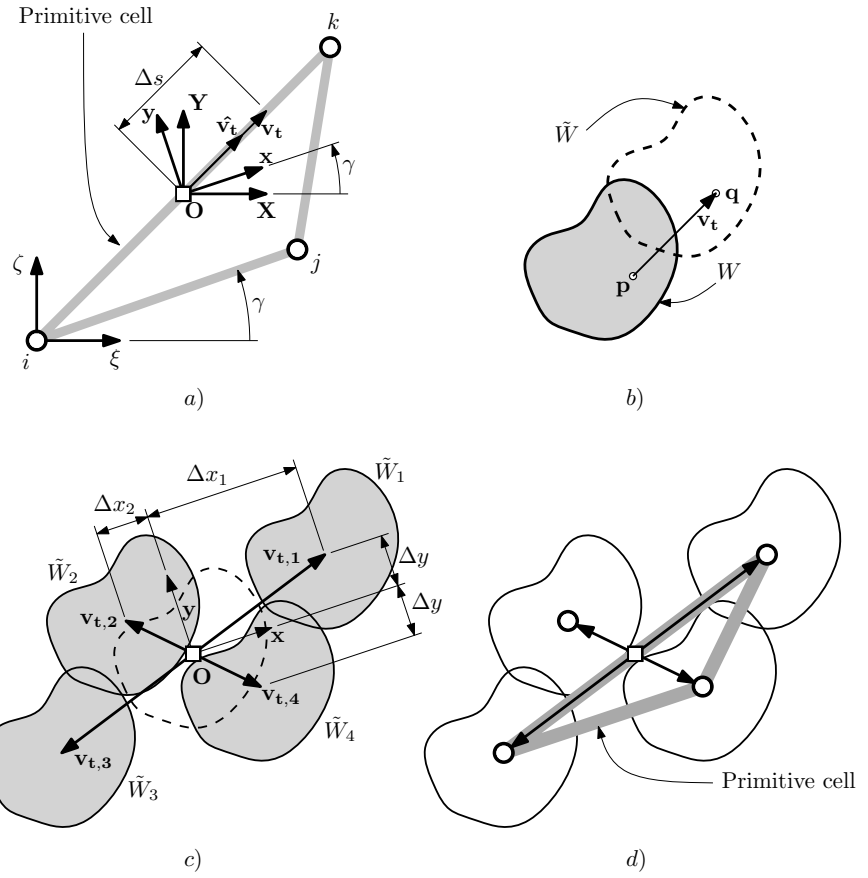

Figure 2.6: Geometrical representation of the rotation and translation of the generic workspace W. In a) ξ, ζ are defined as in Fig. 2.5 and define the primitive cell of points $\mathbf{i}, \mathbf{j}, \mathbf{k}$. Furthermore, $\mathbf{x}, \mathbf{y}$ are the unit vectors of the original coordinate system $\mathbf{X}, \mathbf{Y}$ rotated by an angular value of γ; O is the origin and is located on the middle point of the link between $\mathbf{i}$ and $\mathbf{k}$. The translation vector $\mathbf{v}_t$ is visible, along with its unit vector $\hat{\mathbf{v}}_t$ and module Δs. In b) the translation $T_{\mathbf{v}_t}$ is applied to a point $\mathbf{p} \in W$, resulting in the point $\mathbf{q} \in \tilde{W}$. In c) the translation of the workspace W into four copies $\tilde{W}_1$, $\tilde{W}_2$, $\tilde{W}_3$ and $\tilde{W}_4$, is presented, with $\Delta x_1, \Delta x_2, \Delta y$ the scalar quantities that define the vectors $\mathbf{v}_{t,1}, , \mathbf{v}_{t,4}$. In d) we can see that the W workspaces are thus arranged according to a lattice of primitive cell $\mathbf{i}, \mathbf{j}, \mathbf{k}$.

possible to define four vectors in the space S, as follows,

$$\begin{array}{rcl} \mathbf{v_{t,1}} & = & (+x_1)\,\mathbf{x} + (y)\mathbf{y} \\ \mathbf{v_{t,2}} & = & (-x_2)\mathbf{x} + (y)\mathbf{y} \\ \mathbf{v_{t,3}} & = & (-x_1)\mathbf{x} - (y)\mathbf{y} \\ \mathbf{v_{t,4}} & = & (+x_2)\mathbf{x} - (y)\mathbf{y} \end{array}. \tag{2.2}$$

The vector pairs $\mathbf{v}_{t,1}$ and $\mathbf{v}_{t,2}$, and $\mathbf{v}_{t,3}$, $\mathbf{v}_{t,4}$ are symmetric with respect to the origin $\mathbf{O}$, as follows:

$$\begin{array}{rcl} \mathbf{v_{t,3}} & = & -\mathbf{v_{t,1}} \\ \mathbf{v_{t,4}} & = & -\mathbf{v_{t,2}} \end{array}. \tag{2.3}$$

Let now $W \subset S$ be a connected space without islands. For our purpose, this is the workspace of a general robot. It is a valid assumption since robots with a non-connected workspace, or with a workspace with islands, are not common. For reference, the ABB model IRB 5500 is shown in Fig. 2.7 as an example. This is a common serial robot used in the industry in many applications. As is evident from the lateral and horizontal workspace sections, its workspace is entirely connected.

Other type of robots do have workspaces with discontinuities, an example being some planar cable robots. Even serial or parallel manipulators can show these kind of structures in their workspaces when the relevant section is choosen poorly, for example close to mid-section; this case is visible on the left in Fig. 1.2 on page 3. In general however, in the vast majority of cases, the workspace of non-planar serial or parallel robots can be sectioned so as to produce a planar workspace without discontinuities.

Nevertheless, the formalism for the index that is presented in this chapter, as well as most of the methodologies for computation, are fully capable in dealing with this kind of problem, should it arise. For simplicity and ease of computation, though, it is best to consider a workspace without discontinuities.

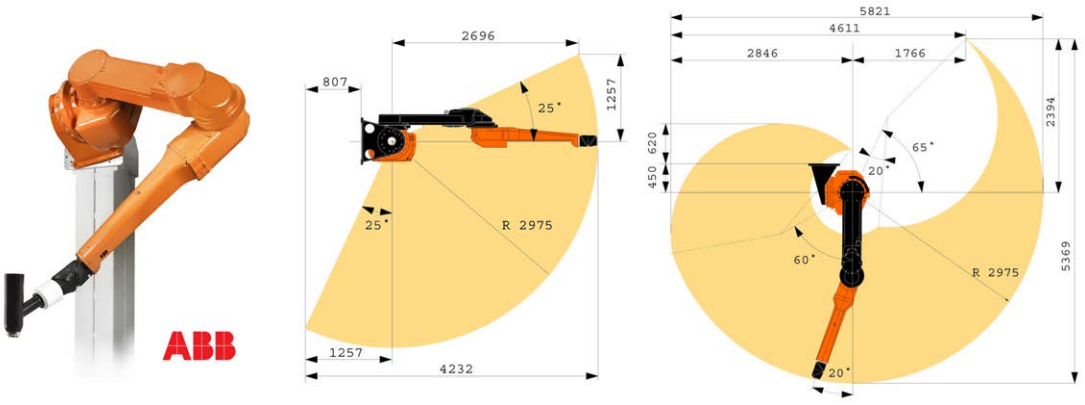

Figure 2.7: Example of the workspace of a serial chain manipulator by ABB, designed for industrial applications. The model is IRB5500.

In regards to Fig. 2.6b, being the point $\mathbf{p} \in W$, we define a point $\mathbf{q}$ which is the result of a simple translation of vector $\mathbf{v}_t$.

$$\mathbf{q} \triangleq T_{\mathbf{v}_t}(\mathbf{p}) = \mathbf{p} + \mathbf{v}_t. \tag{2.4}$$

The points thus defined constitute the locations in which the workspace W is shifted, hence defining set $\tilde{W} \subset S$, provided to apply the translation to each point $\mathbf{p}$. Formally we define a linear operator of translation $T_{\mathbf{v}_t}$ of vector $\mathbf{v}_t$, having,

$$W \xrightarrow{T_{\mathbf{v}_t}} \tilde{W}. \tag{2.5}$$

We come, at last, to the following formalism to define $\tilde{W}$:

$$\tilde{W} = \{\mathbf{q} | \mathbf{q} = T_{\mathbf{v}_t}(\mathbf{p}) = \mathbf{p} + \mathbf{v_t}, \forall \mathbf{p} \in W\}. \tag{2.6}$$

Thus, $\tilde{W} = f(W, \mathbf{v}_t)$, where f is the equivalent of the translation operator $T_{\mathbf{v}_t}$.

Similarly, we can define:

$$\begin{array}{rcl} \tilde{W}_1 & = & f(W, \mathbf{v}_{t,1}) \\ \tilde{W}_2 & = & f(W, \mathbf{v}_{t,2}) \\ \tilde{W}_3 & = & f(W, \mathbf{v}_{t,3}) \\ \tilde{W}_4 & = & f(W, \mathbf{v}_{t,4}) \end{array}. \tag{2.7}$$

The union of these sets generates a set $W_{\text{exp}} \subset S$, visible in Fig. 2.6c, in grey, and defined formally as follows,

$$W_{exp} = \bigcup_{i=1}^{4} \tilde{W}_i \tag{2.8}$$

At this point it is easy to note that the following is true:

$$W_{exp} = W_{exp}(W, \ \mathbf{v}_{t,1}, \dots \ , \mathbf{v}_{t,4}) \tag{2.9}$$

where the vectors $\mathbf{v}_{t,1}$ through $\mathbf{v}_{t,4}$ are in turn function of the parameters γ, Δx_1, Δx_2 and Δy, as follows,

$$\begin{cases} \mathbf{v}_{t,1} & = \mathbf{v}_{t,1}(\gamma, x_1, y) \\ \mathbf{v}_{t,2} & = \mathbf{v}_{t,2}(\gamma, x_2, y) \\ \mathbf{v}_{t,3} & = \mathbf{v}_{t,3}(\gamma, x_1, y) \\ \mathbf{v}_{t,4} & = \mathbf{v}_{t,4}(\gamma, x_2, y) \end{cases} \tag{2.10}$$

From this equation we can infer that the expanded workspace W_{exp} is dependent solely upon the original workspace W and upon the parameters γ, Δx_1, Δx_2 and y. Formally, we can write:

$$W_{\text{exp}} = W_{\text{exp}}(W, \gamma, x_1, x_2, y). \tag{2.11}$$

Let us note that the expanded workspace, intended as a tiling configuration is completely determined by four parameters. This claim is supported by the considerations made in the beginning of this section, about the Bravais lattice. The two representations of the lattice are therefore equivalent.

It might be worth noting that while the tiling configuration is indeed determined by only four parameters, the expanded workspace is not necessarily so. This is due to the fact that tilings deal with points, that is to say entities which have no dimensions. When, however, we associate an arbitrarily large geometric shape W_i to each point of the tiling, thus generating an expanded workspace W_{exp}, we introduce one parameter for each shape. This parameter defines the rotation of the shape with respect to the primitive cell. In the end, the expanded workspace is completely defined by 7 parameters.

In our case, since the technological aspects related to the positioning of the robots generally prevents us from having the workspace rotated in different ways, the assumption is made to consider the shifted workspaces W_i coherent in direction.

We can now conceive a dimensionless quantity which is essentially the ratio between the scalar area of the W_{exp} region and the area of the original workspace W. If we call A the area operator, we can define the scalar area A_W of the workspace W as $A_W = A(W)$, and the area of the expanded workspace as $A_{W,exp} = A\,(W_{exp})$. This dimensionless quantity, which we call Λ, can then be expressed as follows,

$$\Lambda = \Lambda(\gamma, \Delta x_1, \Delta x_2, \Delta y) = \frac{A_{W,exp}}{4A_W}, \tag{2.12}$$

with $\Lambda \in \mathbb{R}$. The scalar value 4 at the denominator is used to limit Λ in order to always keep $\Lambda \in [1/4, 1]$. The lower limit value is $1/4$, since $min(A_{W,exp}) = A_W$. A formulation which is bound to $[0, 1]$ is as follows,

$$\Lambda = \frac{A_{W,exp} - A_W}{3A_W}. \tag{2.13}$$

One must note that certain combinations of the values of the parameters γ, x_1, Δx_2 and Δy exist, whose associated W_{exp} is not a topologically connected partition of the vector space S (as in Fig. 2.6c). Furthermore, some combinations of the parameters that generate a W_{exp} with an island could exist. All of these sets do not cover a surface uniformly due to the gaps and are therefore not acceptable for the purpose of this work. Hence, the condition we want to impose is that W_{exp} is a connected space without islands. An elegant way to express this is to impose the presence of a single border, since this automatically negates the presence of islands while imposing the connectedness of the space contained in the border itself. This concept is shown in Fig. 2.8.

While it is assured that, if W is a connected shape without discontinuities, many configurations (γ, Δx_1, Δx_2, Δy) exist which are associated with single-bordered expanded workspaces W_{exp}, the same cannot be said if W has discontinuities. In this case the situation can be much more complicated. In the present research, no energies were put to the chase of this particular case, but it is worth noting that it exist and should, perhaps, be investigated in the future.

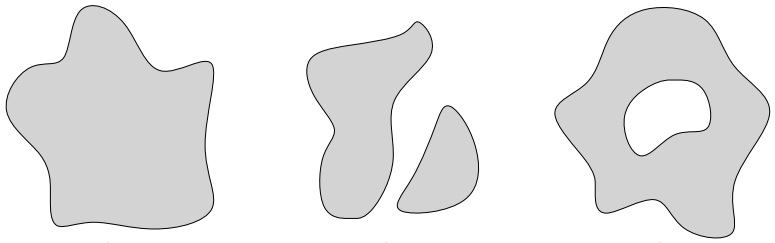

Figure 2.8: Three general types of domains are presented. In a) a connected and island-free space is shown, in b) an island-free but non-connected domain is visible, and in c) a connected space with an island is illustrated. Note that in b) and c) more than one boundary is present, while in a) there is a single one.

To apply this condition to our case, being n_b the number of borders of W_{exp}, we can define the quantity $\Lambda^{'}$ as follows,

$$\Lambda^{'} = \Lambda^{'}(\gamma, \Delta x_1, \Delta x_2, \Delta y) = \begin{cases} \Lambda(\gamma, \Delta x_1, \Delta x_2, \Delta y) & , \quad \text{if} n_b = 1 \\ 0 & , \quad \text{if } n_b > 1 \end{cases} \tag{2.14}$$

It is now possible to define the index for Repetitive Workspace Robots:

$$I_{\mathrm{RWR}} = \max\left(\Lambda^{'}(\gamma, \Delta x_1, \Delta x_2, \Delta y)\right). \tag{2.15}$$

It is now possible to compute the index for the workspaces present in Fig. 2.4, that is to say, a circular one and a square one. Namely:

$$I_{RWR,square} = 1, \tag{2.16}$$

and

$$I_{RWR,circle} = \frac{\frac{\pi}{2} + 1}{\pi} \cong 0,8183. \tag{2.17}$$

This last equation is given by simple geometrical considerations involving the area of a circular segment. The numerical results show that the index I_{RWR} is comparatively low for a circular workspace, and maximum for a square workspace. This is coherent with the expected behavior highlighted in Section 2.2.

2.5 Computation Methodologies

Some remarks have to be made at this point. The fact that the index is essentially the maximization of a function of four variables makes this fundamentally an optimization problem. This statement is based on the fact that no analytical formulation is known for the relation Eq. 2.15, since, for the problem at hand, the following is true,

$$\mathbb{R}^4 \xrightarrow{I_{RWR}} \mathbb{R}. \tag{2.18}$$

Therefore, no explicit solution can be found to determine the optimum values of the parameters γ, x_1, Δx_2 and y. Some different approaches to the problem are viable at this point, and will be discussed in the following sections.

In total, three algorithms are illustrated for the calculation of the index. Based on the consideration that the problem is inherently an optimization process, the first method is based on a genetic algorithm; this algorithm provides the correct solution, or *global maximum*. The second and third algorithms are semi-analytical and provide an approximate solution. Even with these, the solution is found by performing a search in the final solution space. In other words, a complete enumeration of a discretised

limited continuum of the solution space must be carried out. It is worth noting that this partition of the solution space cannot be defined as differentiable or even continuous, so enumerative or heuristic techniques should be used instead of general methods which use gradients (e.g. Newton-Raphson).

In fact, one of the reasons the solution of the SCP is so hard lies in the difficult definition of the base shapes, or in our case the workspaces W_i. Leaving aside trivial geometries like squares, rectangles, circles and alike, the definition of an arbitrarily complex shape, albeit 2D, is no small feat. Several methods exist to describe an arbitrarily complex shape. For example, it could be approximated with a polygon with a sufficient number of sides, or a splinegon. A splinegon is a polygon bounded by algebraic curves, which can either be defined parametrically (x and y being polynomial functions of a parameter t) or implicitly as the solution to a polynomial equation in x and y[1].

2.5.1 The Genetic Covering Algorithm (GCA)

Since the problem at hand is not explicitly solvable, numerical methodologies must be used if sufficient robustness is required. The only exact method would be the total enumeration of the possible combinations of the values of the parameters. This is clearly impracticable if a sufficient resolution is desired, due to computational costs. For this reason, to be able to provide a close approximation to the exact solution, we use a constrained genetic algorithm, as described in [44–46]. This is because, ultimately, the search for the optimal configuration (which guarantees the maximum covering efficiency) is essentially an optimization problem, as was previously highlighted.

It is worth noting explicitly that the GA serves to the purpose of finding the index I_{RWR}, and not to that of finding the maximum covering efficiency *per sé*. The latter is indeed the means to the end of determining the index.

Genetic Algorithms (GA) pertain to a specific class of methods called Differential Evolution (DE) methods, a field of evolutionary computation, as illustrated by Storn et al. in [47, 48]. These methods optimize a problem by iteratively attempting to improve a candidate solution. Such methods are known as metaheuristics since they can search very large solution spaces; this is achieved by being very restricted in the breadth of the initial conditions and assumptions that are made. The differentiability of the

[1] https://www.ics.uci.edu/ eppstein/projects/splinegon/

solution space is not required, since no gradient is employed. The same applies even for continuity. These inherent qualities make DE methods – and the GA in particular – optimal candidates for the SCP, which is a topological problem with an incredible complexity in the definition of the structure itself.

The genetic algorithm requires the definition of a fitness function f as a function of a number of variables that define the configuration to be studied. In the case of this research, these are: the rotation angle, γ; the translation coefficients in the $\mathbf{x}$ direction, Δx_1 and Δx_2; the one in the $\mathbf{y}$ direction, Δy. In mathematical terms,

$$f = f(\gamma, \Delta x_1, \Delta x_2, \Delta y), \tag{2.19}$$

It is now necessary to identify the region of W_{exp} which presents overlapping. We can define,

$$W_{\cap} = \tilde{W}_1 \cap \tilde{W}_2 \cap \tilde{W}_3 \cap \tilde{W}_4, \tag{2.20}$$

It is easily verifiable that $W_{\cap} \subset W_{\text{exp}}$. In fact, if we consider Eq. 2.8 we see that W_{exp} is the union of the $\tilde{W}_i$, thus, every intersection between these is also part of W_{exp}. If we use the area operator defined in Section 2.4, we have:

$$A_{\cap} = A(W_{\cap}). \tag{2.21}$$

It is now possible to define f',

$$f' = A_{\cap}, \tag{2.22}$$

It is now necessary to consider the condition highlighted in Eq. 2.14, that is, the possible presence of islands or of a non-connected W_{exp}. In that case, the fitness function must be corrected with a certain coefficient, since it would lead to unfeasible configurations (i.e. violating the condition in Eq. 2.14). We will call this *penalty function* and indicate it with the letters s or k, respectively if we have an island or a non-connected W_{exp}. This leads to the final fitness function,

$$\begin{cases} f &= \begin{cases} f's & \text{if an island is present in } W_{exp} \\ f'k & \text{if } W_{exp} \text{ is non-connected} \end{cases} \\ s &= A_{island} \\ k &= \left(\frac{\Delta x_1 + \Delta x_2}{2} + \Delta y + \varepsilon\right)^2 \end{cases}, \tag{2.23}$$

where $\varepsilon \in \mathbb{R}$ is an arbitrarily small value. From the equation we can see that $s = s(A_{\text{island}})$, where A_{island} is the area of the island possibly present in W_{exp}. Along the same line we see that $k = k(\Delta x_1, \Delta x_2, \Delta y)$. With this formulation, the penalty function is made proportional on the magnitude of the topological incongruence.

Being the expression of s sufficiently straightforward, for what concerns k instead, the expression in the equation is not self-evident. In fact, by referring again to the geometry of the problem that is illustrated in Fig. 2.6c, we can see that the condition of the figure is that of a disconnection of the domain, which is precisely the case when k is relevant. The first term in the parentheses is the mean between the two coefficients of expansion along the **x** axis. The second is the translation coefficient along the **y** axis. The final term, ε, serves to the purpose of making sure that $k > 0$ holds true always. It is of no theoretical importance but can help in some borderline cases of the numerical problem of optimization. Generally $\varepsilon = 1$.

Having defined the fitness function f, it is now possible to state the optimization problem as:

$$\underset{\gamma, \Delta x_1, \Delta x_2, \Delta y}{\text{minimize}} \quad f(\gamma, \Delta x_1, \Delta x_2, \Delta y), \tag{2.24}$$

Finally, to greatly reduce the generation of unfeasible configurations such as negative translations or translations which are bigger than the image itself, we apply a set of boundary constraints to the variables, as follows,

$$\begin{cases} 0 \leq \gamma \leq \gamma_{\max} \\ 0 \leq \Delta x_1 \leq \Delta_{\max} \\ 0 \leq \Delta x_2 \leq \Delta_{\max} \\ 0 \leq \Delta y \leq \Delta_{\max} \end{cases} \tag{2.25}$$

These are the variables that effectively appear in Eq. 2.24, and are those on which the genetic algorithm directly operates. The quantities γ_{max} and Δ_{max} are the absolute values of the allowed maximum rotation and maximum translation modulus, respectively. The former value has been set as: $\gamma_{max} = \pi$, the latter has been set as approximately equal to the maximum value between the width and the height of the bounding box containing the original shape W. Indeed, any value over these borderline conditions would trigger a discontinuity in the domain.

The fitness function works by calculating the translation vectors for the $\tilde{W}_1$, $\tilde{W}_2$, $\tilde{W}_3$ and $\tilde{W}_4$ workspaces and then computing the area of the intersection $A_\cap$ between

the workspaces $\tilde{W}_i$. At this point, the penalty function can be applied, if the specified conditions are met.

The other parameters and methods used in the genetic algorithm are summarized in Table I. In this research, it has been seen that a number of generations of 200 guarantees that the global maximum is reached in 99% of the runs. As for the population size, a comparatively high number (50) was being chosen because it increases the diversity in the variables. In fact, the problem at hand shows a very sparse solution space, with a large number of oscillations (local maxima), so producing the largest possible exploration of this space is paramount to a satisfactory result. This is the reason why a stochastic uniform (i.e. non-deterministic) and heuristic methods were chosen as selection and crossover respectively. In particular, heuristic crossover seems to have the ability to get easily out from local maxima, which is a feature that is very much useful in this case[49].

Parameter or method	Value or type
Selection method	Stochastic uniform
Crossover method	Heuristic
Initial population creation method	Uniform distribution
Mutation function	Gaussian
Crossover fraction	0.8
Elites	2
Maximum number of Generations	200
Population size	50
Population type	Double

Table 2.1: Parameters used in the genetic algorithm solver implemented in the MATLAB's Optimization Toolbox.

The I_{RWR} index itself is computed following yet again the formulation in Eq. 2.12, 2.14 and 2.15, in Section 2.4. Thus, we have,

$$\Lambda_{GCA,opt} = \Lambda_{\mathrm{GCA}}\left(\gamma_{opt}, \Delta x_{1,opt}, \Delta x_{2,opt}, \Delta y_{opt}\right) = \frac{A_{W,exp,opt}}{4A_W}, \tag{2.26}$$

where $A_{W,\mathrm{exp}} = A(W_{\mathrm{exp}})$ and $A_W = A(W)$; the subscript "opt" indicates that the associated variable's value is optimal as it results from the optimization process. The

condition in Eq. 2.14 is implied in the GCA via the penalty functions s and k, which leads to $\Lambda'_{\mathrm{GCA}} = \Lambda_{\mathrm{GCA}}$. Finally, we come to the definition of the actual index,

$$I_{\mathrm{RWR},GCA} = \Lambda_{GCA,opt} = \frac{A_{W,exp,opt}}{4A_W}. \tag{2.27}$$

Again, note that the index is dependent from *all* the parameters considered in Section 2.4.

2.5.2 The Uniform Expansion Covering Algorithm (UECA)

In regards to the geometrical representation of the index present in Fig. 2.6, and exploiting Eq. 2.11, we see that the parameters of the affine transformations rotation and translation are γ, Δx_1, Δx_2 and Δy, each one independent from the others. The genetic algorithm used to solve this problem (see 2.5.1) was coherent with this independence at the cost of very high computational times. To reduce the computational time we present a highly simplified algorithm; to easily compute an early approximation of the index we can reduce all the parameters to a single one. This is equivalent to selecting a specific partition of the space of the variables and discarding the rest, therefore passing from a subset of $\mathbb{R}^4$ to one of $\mathbb{R}^1$.

This is done by imposing the following conditions,

$$\begin{cases} \gamma &= 0 \\ \Delta x_1 &= \Delta x_2 = y = h \end{cases}. \tag{2.28}$$

This brings Eq. 2.12 to the following form, defining Λ_{UECA} as a simplified (or limited) version of Λ,

$$\Lambda_{\mathrm{UECA}} = \Lambda_{\mathrm{UECA}}(\Delta h) \triangleq \Lambda(0, \Delta h, \Delta h, \Delta h) = \frac{A_{W,exp}}{4A_W}. \tag{2.29}$$

Note that in this case the index will be dependent only on the parameter h. This will allow for an easy computation, where the "optimization", as derived from Eq. 2.14, is confined to the mere determination of the maximum value of Λ'_{UECA}, which is trivial and escalates with $O(n)$, with n being the dimension of the discretized Λ_{UECA}. We have:

$$I_{RWR,\mathrm{UECA}} = \max\left(\Lambda'_{\mathrm{UECA}}(\Delta h)\right). \tag{2.30}$$

Geometrically we have the structure highlighted in Fig. 2.9 where the unit vectors $\hat{\mathbf{v}}_{t,1}$ and $\hat{\mathbf{v}}_{t,2}$ (not labeled in the figure) are orthogonal and the workspace W is not rotated ($\gamma = 0$).

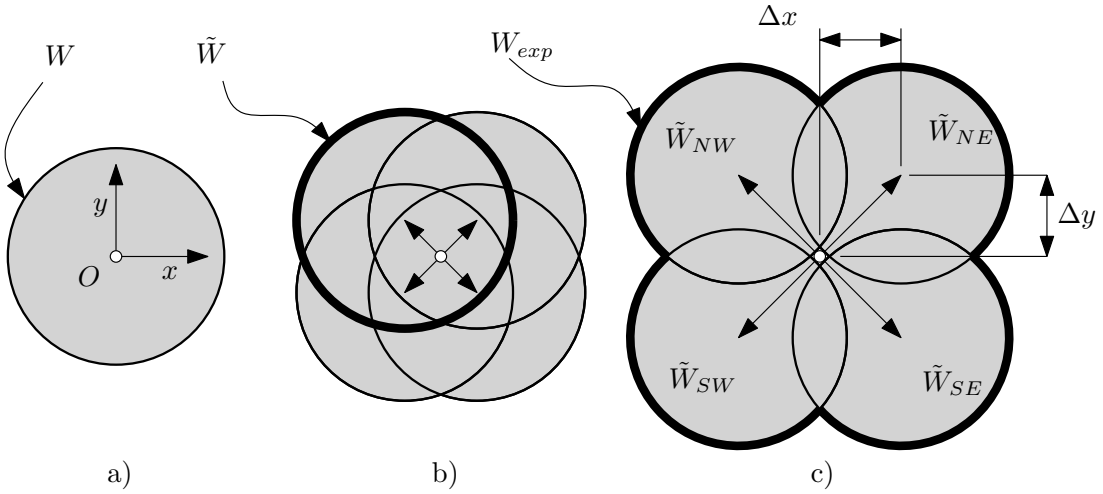

Figure 2.9: Translation of the original workspace and expansion of the union of the resulting areas. The arrows show the translation of the $\tilde{W}$ areas. The grey area shows the expanded area W_{exp}. In a) the robot workspace W is shown. In b) a general translation step is illustrated, and in c) the maximum expansion step is appreciable, with the presence of a gap at the center of the frame; this is representative of the criterion for the maximum translation (expansion) of the surface.

The algorithm is written in MATLAB. All the calculations are done with raster binary images of 500x500 pixels. Inputs have the same dimensions. It is important to stress that the original workspaces W can take up at most one third of the total width and of the total height of the entire image, so the actual workspace image is contained in a box of around 150x150 pixels. Images so small can cause some discretization errors in the process. The structure of the algorithm is split into three main parts:

i. Pre-processing,

ii. Computation of Λ'_{UECA},

iii. Determination of $max(\Lambda'_{\text{UECA}})$, which translates in the index $I_{RWR,\text{UECA}}$.

Part i. serves to the purpose of polishing the image of the workspace. Some minor operations are performed, like the exclusion of possible smaller isolated parts of the

workspace, a certain smoothing of the borders, etc. This is done to minimize errors in the algorithm.

Part ii. is based on the actual translation and union of the workspaces, following Eq. 2.8. At each step j, every point $\mathbf{p} \in W$ is translated by a certain quantity in the four directions, typically $h_j = kj$ in pixels, where $k \in \mathbb{N}^+$ is a positive constant (normally, $k = 1$) (see Eq. (9)). The resulting translated sets $\tilde{W}_j$ are then united into the expanded workspace $W_{exp,j}$. With the equations described in the preceding section, and the formulation for Λ_{UECA} used in Eq. 2.29 the value $\Lambda'_{UECA,j}(h_j)$ is calculated and stored. The computation of the topological conditions on the number of borders n_b, visible in Eq. 2.14, is done by taking advantage of a fast morphological operator that returns the Euler number of the image [50]. This analyses, for every pixel in the image, the patterns of convexity and concavities in the pixels adjacent to each probed pixel; finally, it computes the Euler number for the image: $N_E = N_{\text{Convexities}} - N_{\text{Concavities}}$.

In Part iii., the algorithm performs a backwards search on the array of values $\Lambda'_{UECA,j}$ and determines the maximum value. This means that the process starts from the maximum expansion possible of the workspaces and proceeds in the direction of *contraction*, rather than expansion.

The backwards search is advisable since for some workspaces W it can happen that, during the expansion, temporary discontinuities may arise. Furthermore, in order to make the algorithm efficient, the end-condition is set so as to exit the moment a discontinuity appears. From these considerations it is clear that the backward search guarantees that the algorithm exits when the best configuration is found, that is, the maximum expansion one.

Indeed, one could perform a forward search, and in the majority of events, a maximum expansion configuration would be detected correctly. However, as a thought experiment, let us consider an forward search for an expansion that has no end-condition. In this case, one should see the index growing as a function of the expanding workspace. However, for some type of workspace, a discontinuity could arise that whould disappear with further expansion; these we will call *transient discontinuities*. These are actually quite common in the immediate proximity of the actual maximum expansion configuration, though in this specific case they are admittedly mainly due to discretisation of the workspace. A workspace which generates this transient discontinuities very early in the forward expansion is illustrated in Fig. 2.10a. The rest of the figure shows the

discontinuity appearing (b) and disappearing (c) until maximum expansion is reached (d). Backward search in this case would make matters substantially easier, since the first configuration found that is consistent with the general condition of single border would be the one associated with maximum expansion. On the other hand, a forward search would need tracking of transient expansion to be able to rule them out and thus proceed all the way to the maximum one. It is pointless to say that this would be tremendously impractical.

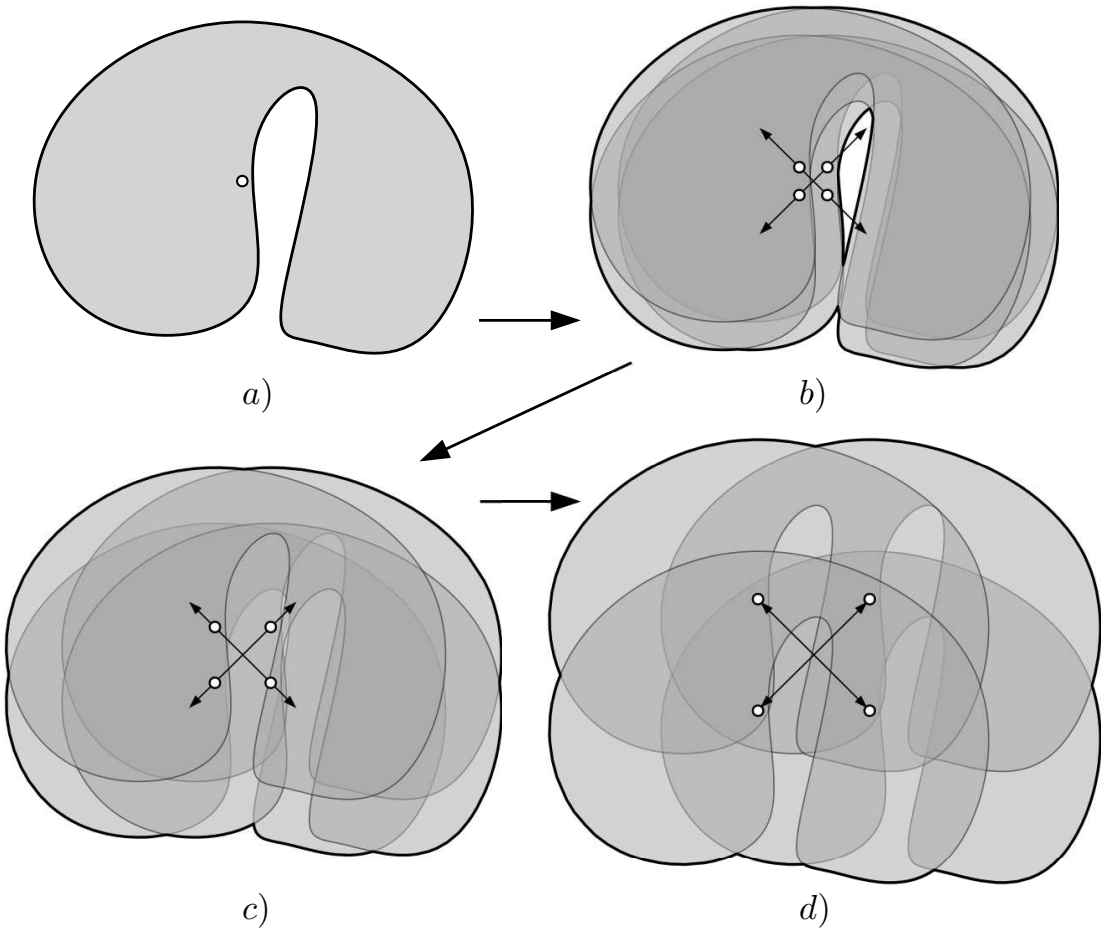

Figure 2.10: An example of expansion by a workspace that generates transient discontinuities during the process. In a) the workspace is shown, in b) the expansion is started and a discontinuity appears in the center of the global workspace, in c) the expansion continues and the discontinuity disappears, finally in d) the expansion reaches its maximum.

2.5.3 The Corrected Inertial Ellipsoid Covering Algorithm (CIECA)

As mentioned in the opening of the preceding Section 2.5.2, UECA is a highly simplified algorithm. The system in Eq. 2.28 operates a series of identities on all the various variables, which comprise expansion (Δx_1, Δx_2, Δy) and rotational parameters (γ). In this section, a set of techniques to algorithmically determine most of these variables will be illustrated. It is worth mentioning that all of these methods do not give a solution which is proven to be the one associated to the *optimum*, rather, they are an attempt to produce a satisfying approximate solution. The starting point is determination the rotational parameter γ.

The first drawback of UECA is that the $I_{RWR,UECA}$ index is not rotation-invariant. If W, for example, has a square shape, by rotating it by some angle, one would expect the index to remain constant. This is, however, not true and easily verifiable, as shown in Fig. 2.11.

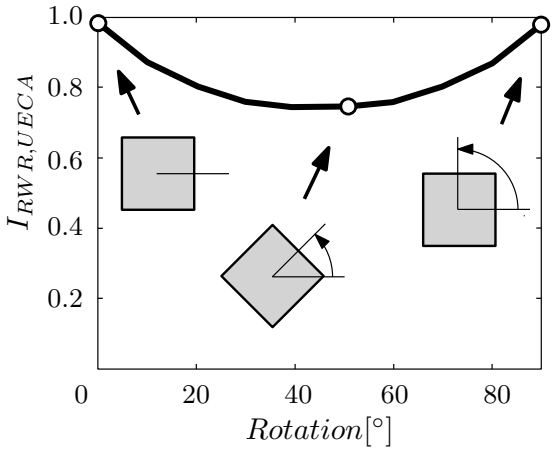

Figure 2.11: Dependence of the index $I_{RWR,\mathrm{UECA}}$ on the rotation of a square workspace W. Note that the variation magnitude can be higher than 20%.

The second limitation is related to some anomalies that can occur with specific geometries of the workspace W, like the one depicted in Fig. 2.12a. Indeed, stretched shapes which are oriented at roughly 45°, will lead to a strong probability of errors. Indeed, the expanded area W_{exp} shown in Fig. 2.12c complies with condition $n_b = 1$, as seen in Eq. 2.14. Nevertheless, as is clear from Fig. 2.12d, a more complete covering (i.e. considering a higher number of lattice-tiled workspaces), shows islands. The

obvious conclusion is that the algorithm provides a wrong result in this case. We call these "sock anomalies" from the resemblance to the homonymous garment.

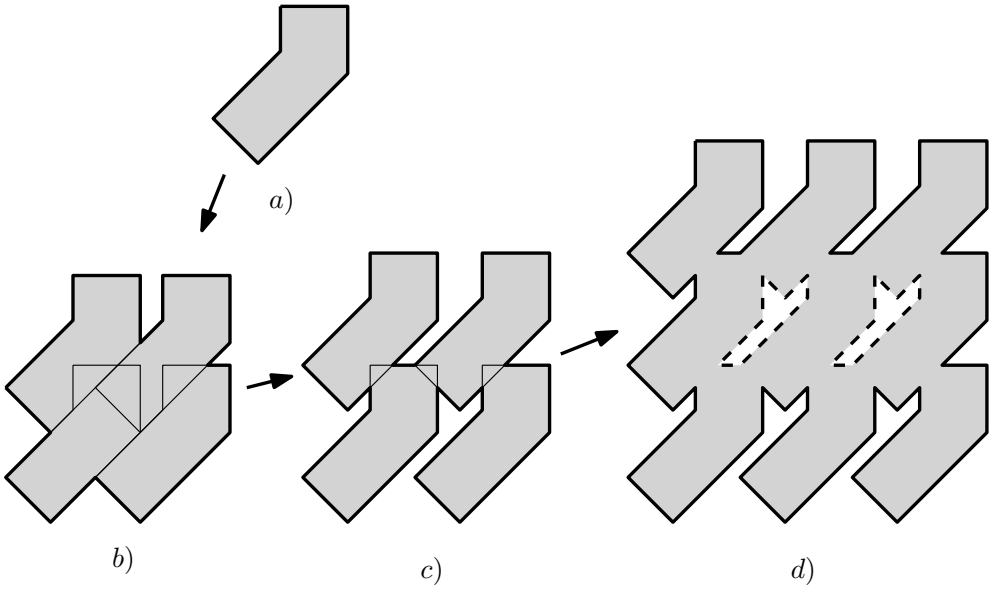

Figure 2.12: An illustration of a "sock anomaly". Workspaces with shapes similar to the one in a) can result in the non-detection of the islands visible in d) as dashed lines, if UECA were to be used. Indeed, if the expansion in b) and in c) is examined, the criterion $n_b = 1$ is still verified.

These limitations can be overtaken with the methodology we present in the following. The key premise is in the following assumption:

$$\Delta x = \Delta x_1 = \Delta x_2. \tag{2.31}$$

This introduces a simplification of the problem. In fact, a difference between Δx_1 and Δx_2 is what produces a distortion in the expansion directions that is consistent with a skewed parallelogram. If the above equation is introduced, this constrains the expansion in a rectangular pattern, hence, skewed expansion will not be possible. This is the only hard limitation for the CIECA algorithm, as will be evident from the results.

After these considerations, it follows that the index, as calculated using CIECA, will be dependent on the parameters γ, Δx and Δy. The variable space for CIECA will then be a subset of $\mathbb{R}^3$.

We can then define two sequential steps:

I. Decoupling of the variable space; the parameter γ is uncoupled from the other parameters, Δx and Δy.

II. The algorithm follows certain geometrical considerations to smartly guide the partitioning of the remaining coupled variables' space.

In the end we find ourselves having two decoupled subsets of the $\mathbb{R}^3$ space of variables; the first is a $\mathbb{R}^1$ space, whereas the second is obviously a $\mathbb{R}^2$ space. In general terms, during step I the algorithm performs a search for a value of γ that it predicts could lead to a global best solution. In step II CIECA finds a coefficient to define the ratio between Δx and Δy, thus linking the two parameters. At this point a simple search is performed in the resulting $\mathbb{R}^1$ space.

The overall methodology is loosely based on the concept of inertia ellipsoid, in fact it was inspired by it. We can compute this structure based on a polar formalization, i.e. calculating the moment of inertia along a rotating axis centred in the barycentre of the considered body.

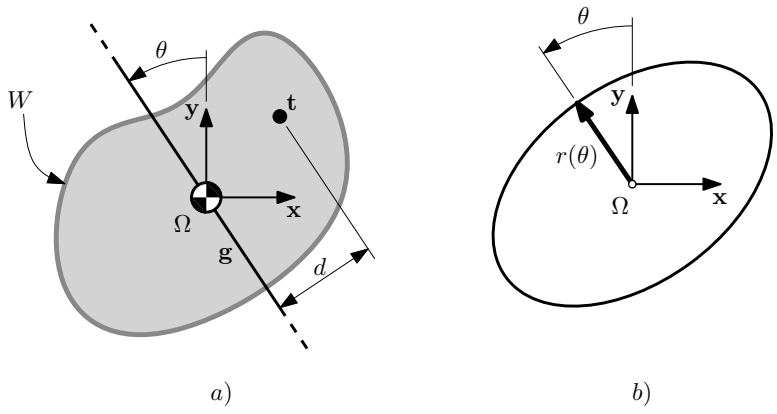

Figure 2.13: Calculation of the inertia ellipsoid with the aid of a rotating axis **g** centered in the barycenter **Ω**. In a) the 2D body W is shown. A point $\mathbf{t} \in W$ is also highlighted, as are the **x**, **y** coordinate system and axis **g**. For a specified angle θ of said axis, the minimum distance d of point **t** from the axis itself can be easily computed. In b) the resulting 2D inertial ellipse is visible, in the (r, θ) coordinates.

Formally, we have, in the polar coordinates (r, θ),

$$r_{\text{ellipsoid}}(\theta) = \frac{1}{\sqrt{I_g(\theta)}}, \tag{2.32}$$

where, looking at Fig. 2.13, we have the 2nd order momentum,

$$I_g(\theta) = \int_W \rho(\mathbf{t}) d^2(\theta) dW. \tag{2.33}$$

In this last equation, W indicates the surface of the shape in the figure, ρ the mass density in the point $\mathbf{t}$ and $d(\theta)$ the distance between $\mathbf{t}$ and the axis $\mathbf{g}(\theta)$.

What matters for our purposes is precisely $I_g(\theta)$. This moment of inertia can be computed by taking advantage of the discrete nature of the raster image we use in the process. If said image contains N pixels, assigning every pixel a "mass" m_i based on its value ($m_i = 1$ if pixel$_i \in W$, else $m_i = 0$), one can easily calculate the normal distance d of this pixel $\mathbf{t}_i$ (with $i \in [1, N]$) from the rotating axis $\mathbf{g}$ centered in the barycenter $\mathbf{\Omega}$. This is illustrated in Fig. 2.13a. The following equation for the 2nd order discrete momentum results:

$$I_g(\theta) = \sum_{i=1}^{N} m_i d(\mathbf{t}_i, \mathbf{g}(\theta))^2. \tag{2.34}$$

Repeating this process for $\theta = 0, \ldots, 2\pi$, and applying Eq. 2.32, the ellipsoid can be computed, as visible in Fig. 2.13b.

The distribution of $I_g(\theta)$ can help define the orientation of a shape as long as it has a clear difference between the inertia along the principal directions, respectively I_1 and I_2. In other words, the shape needs to be oblong for this assumption to be true. This is clearly a big limitation, since with figures like squares or some regular polygons, the resulting $I_g(\theta)$ describes a perfect circle ($I_g(\theta) = constant$), and thus no principal orientation information is detectable. This is immediately evident from the second column of the table in Fig. 2.14.

The solution we propose is to adjust the computation of this quantity by increasing the weight the distance d itself has on I_g. We thus have the 3rd order discrete momentum:

$$I_g'(\theta) = \sum_{i=1}^{N} m_i d(\mathbf{t}_i, \mathbf{g}(\theta))^3, \tag{2.35}$$

which is, indeed, very different from Eq. 2.34 because the distance term $d(\mathbf{t}_i, \mathbf{g}(\theta))$ is now raised to the power of 3.

At this point we can clearly see from Fig. 2.14 that the distribution of $I_g^{'}(\theta)$ can give us the principal orientation of the shape we are studying. We define $\tilde{\theta}$ as the value of θ for which $I_g^{'}(\theta)$ is a global maximum. Going back to Eq. 2.12 we can see that the parameter γ can be effectively estimated using $\tilde{\theta}$, thus having the following,

$$\gamma \cong \tilde{\theta}, \tag{2.36}$$

The other two parameters (Δx and Δy) can be estimated using the 1st order discrete momentum, similarly to Eq. 2.32 and Eq. 2.33

$$I_g^{''}(\theta) = \sum_{i=1}^{N} m_i d(\mathbf{t}_i, \mathbf{g}(\theta)), \tag{2.37}$$

This time the distance term $d(\mathbf{t}_i, \mathbf{g}(\theta))$ is of the first degree. The rationale for using the 1st order discrete momentum is precisely that this quantity is of the first order with respect to the distance term. Indeed, the point of this part of the algorithm is to find the coefficients of expansion in x and in y, which are – ultimately – distances.

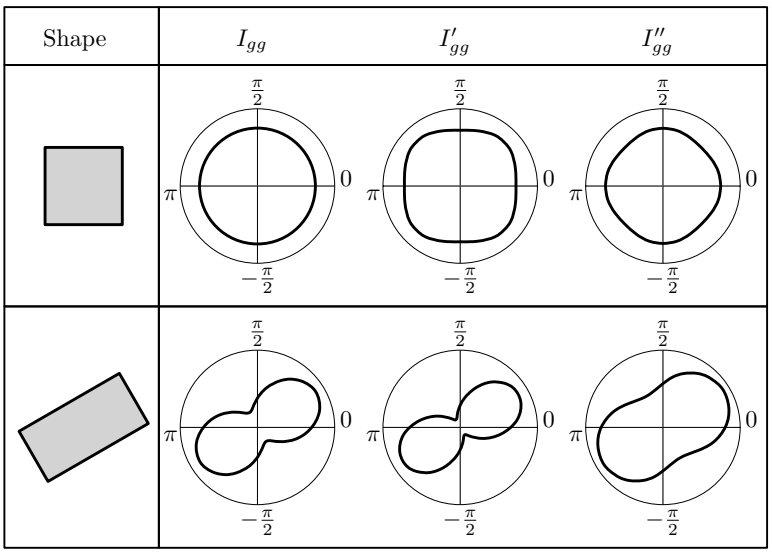

Figure 2.14: Different types of I_g computed for two different shapes¿ a square, and an oblique rectangle. In the second column $I_g(\theta)$ is visible: this is the distribution of the moment of inertia along a rotating axis. In the third column, $I_g^{'}(\theta)$, an adjusted, third degree moment of inertia is visible, and in the fourth column $I_g^{''}(\theta)$ is presented, which is a first-degree-adjusted moment of inertia. It is important to note that $I_g(\theta)$ in the first column is what leads to the usual inertia ellipsoid.

The discrete momentum of the 1st order, $I_g^{''}(\theta)$, thus provides a very precise numerical indication of this expansion.

An example computed for two different shapes is presented in Fig. 2.14, in the fourth column. We can define the following ratio:

$$\psi = \frac{I_{\mathrm{g,min}}^{''}}{I_{\mathrm{g,max}}^{''}}, \tag{2.38}$$

where $I_{g,max}^{''}$ is the maximum value among those computed in the range $\theta \in [0, 2\pi]$, with $\hat{\theta}$ such that $\max\left(I_g^{''}\right) = I_{g,max}^{''} = I_g^{''}\left(\hat{\theta}\right)$. Consequently the following applies:

$$I_{g,min}^{''} = I_g^{''}\left(\hat{\theta} + \frac{\pi}{2}\right). \tag{2.39}$$

This means simply that $I_{g,min}^{''}$ and $I_{g,max}^{''}$ are associated to axes that are orthogonal. This is a well known property of momentums, which originates from their inherently symmetrical nature.

At this point we can define a pair of multipliers, the first of which is defined as equal to one,

$$\begin{cases} \lambda_1 &= 1 \\ \lambda_2 &= \psi < 1 \end{cases}. \tag{2.40}$$

It is easy now to link together the parameters Δx and Δy of the translation vectors $\mathbf{v_t}$ as follows,

$$\frac{\Delta x}{\Delta y} = \frac{\lambda_1}{\lambda_2}. \tag{2.41}$$

This leads, after a simple manipulation, to the following formulation:

$$\Delta x = \frac{\lambda_1}{\lambda_2}\Delta y = \Delta x(\Delta y). \tag{2.42}$$

With these considerations the actual problem is reduced to a mono-parametric one similar in some respects to UECA, introduced in Section 2.5.2.

We can define the following variation of Eq. 2.12,

$$\Lambda_{\mathrm{CIECA}} = \Lambda_{\mathrm{CIECA}}(\gamma, \Delta x, \Delta y) = \Lambda(\tilde{\theta}, \Delta x, \frac{\lambda_2}{\lambda_1}\Delta x) = \frac{A_{W,exp}}{4A_W}, \tag{2.43}$$

and then determine the relevant index,

$$I_{RWR,\text{CIECA}} = \max\left(\Lambda'_{\text{CIECA}}(\Delta x)\right), \tag{2.44}$$

having care to compute Λ'_{CIECA} as prescribed by Eq. 2.14.

The algorithm itself is, in essence, equivalent to the one described in Section 2.5.2. The only difference is how the γ, Δx and Δy parameters are chosen between the two cases. In UECA these parameters are reduced to just one via an arbitrary simplification, whereas in CIECA a smarter method is used and no arbitrary choice is made.

2.6 Comparison Between the Computation Methodologies

The methods or algorithm up to this point illustrated are in general very different one from the other. Each has its own strong points and weaknesses. In this section, a general overview will be given to understand how one compares to the others.

As previously noted, the methodologies we want to evaluate are the UECA, the CIECA and the GCA, which were shown in Section 2.5 of this manuscript. In this research we considered the GCA as the baseline to compare the methodologies. In fact, the solution given by GCA comes very close to the theoretical optimum in all the tests performed in our study, and can therefore be considered optimal. Therefore, it is possible to precisely evaluate how much a method or algorithm comes close to the best solution possible, which is, in fact, the correct one by definition. The drawback of GCA, compared to UECA and CIECA, is that genetic algorithms generally require a very long time to compute, typically a couple of order of magnitudes longer.

As stated in the same section, the inputs fed to the algorithms were in the form of raster binary images of 500 by 500 pixels.

In the following sections, the two main aspects of the algorithms are discussed: accuracy or robustness and computational requirements.

2.6.1 Accuracy and Robustness

Refer to Fig. 2.15, where the results for the three methodologies are shown. First of all, looking closer to the columns pertaining to the genetic algorithm, one can appreciate

that this methodology finds the best possible covering with the provided shape: with all the shapes, with the exception of d and h, the $I_{RWR,GCA}$ is found to be nearly one, which is of course the theoretical maximum, since all these shapes tessellate.

Concerning shapes d and h, no covering is possible without overlapping. The best covering arrangement for the circle shape is the hexagonal tiling, as explained in Section 2.2. This configuration is indeed found by the genetic algorithm used in this study. Note that the same pattern is found for the hexagon (f), which was to be expected as well.

Lastly, as for the configuration originating from the use of shape h with GCA, no mathematical proof is given in this manuscript for it being the best possible, so we assumed it as our baseline optimum.

Having defined the upper limits of the problem for each shape, we can proceed to analyze and compare the methodologies.

In Fig. 2.15 we present the qualitative and quantitative results, in terms of accuracy, of our tests on UECA, CIECA and GCA. In the first column the workspace shape is shown; in the second and third column we find the expanded workspace W_{exp} and its I_{RWR} respectively, computed with GCA. In the fourth and fifth the same is visible, as computed with UECA; in the sixth and seventh columns the optimal W_{exp} is visible, along its corresponding I_{RWR}, this time computed with CIECA.

Referring to the same figure, regarding UECA, the first aspect that emerges is that this method is not rotation-invariant, as previously noted (see the beginning of Section 2.5.3). If, for example the first two shapes (a and b) are considered, one can see that, despite both being fundamentally square-shaped, the associated $I_{RWR,UECA}$ values are very different, the first being, correctly, equal to 1, while the second being equal to 0,7565, which is smaller by almost 25%. This flaw is obviously not evident for the circle (shape d), since this is an intrinsically rotation-invariant figure.

Another aspect that one can appreciate from the same figure, is that in some cases, namely those indicated by letters c, e and in particular h, the maximum expansion configuration for UECA presents the "sock anomaly" explained in section 2.5.3 and in the related Fig. 2.12, as expected. This is a major flaw since it is very hard to foresee if and when it will occur.

Upon examination, the results in columns four and six prove that the method based on CIECA has, instead, a much higher performance in regards to both accuracy and

Shape	Uniform Expansion Covering Algorithm (UECA)		Corrected Inertial Ellipsoid Covering Algorithm (CIECA)		Genetic Covering Algorithm (GCA)	
	Maximum expansion configuration	$I_{RWR,1}$	Maximum expansion configuration	$I_{RWR,2}$	Maximum expansion configuration	$I_{RWR,3}$
a		1.0000	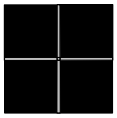	0.9750	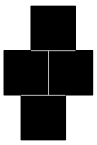	0.9938
b		0.7565		0.9812		0.9932
c	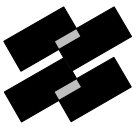	0.9453	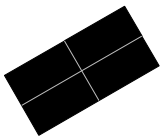	0.9895	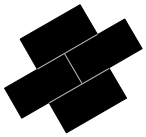	0.9893
d	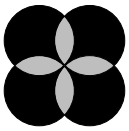	0.8296	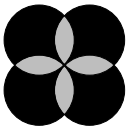	0.8250	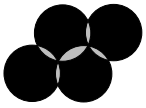	0.9400
e		0.9449		0.7604	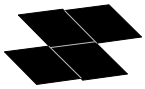	0.9957
f		0.8147		0.8275		0.9926
g	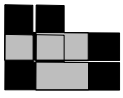	0.6409	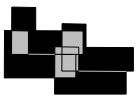	0.7945		0.9901
h		0.9992		0.9216		0.9513

Figure 2.15: Results summary for the three methodologies to calculate the I_{RWR}. In the first column the shape of the workspace is visible (letters a to h). In columns two, four and six the configuration of maximum expansion is shown for the related shape respectively for GCA, UECA and CIECA. Finally, in columns three, five and seven, the actual associated index I_{RWR} is reported. Black areas are considered as workspace, whereas the grey ones are intersections between overlapping expanded workspaces.

coherence. In all the tests we performed with this last method, the "sock anomaly" never appeared at all.

Since the ultimate objective of the algorithm is to provide the index that best approaches the *optimum* (in this work given by the GCA) for a chosen shape, and given that the indexes $I_{RWR,UECA}$ and $I_{RWR,CIECA}$ are computed essentially in the same way as ratios between areas, it follows that the higher the index, the best the tiling configuration will be for an efficient covering. So, we can observe that for every shape in Fig. 2.15 the following inequality applies:

$$I_{RWR,UECA} \leq I_{RWR,CIECA}$$

with the exceptions of the case in which the first algorithm results in the "sock anomaly" and having care to consider that a certain amount of numerical error is present (e.g. shape *d* results in a slightly bigger $I_{RWR,UECA}$, but for our purposes we can safely assume $I_{RWR,UECA}|_d \cong I_{RWR,CIECA}|_d$; the same applies for shape *a*).

In general it is apparent from the results in the same figure, that the CIECA does come very close to the *optimum* found with the genetic algorithm. Specifically, in the case of shapes *b* and *c*, if numerical error is considered, the $I_{RWR,CIECA}$ can be assumed as equal to the GCA-derived $I_{RWR,GCA}$. In case of shape *g*, a strong improvement is made with respect to the UECA methodology, going from $I_{RWR,UECA} = 0.6409$ to $I_{RWR,CIECA} = 0.7945$, which corresponds to an increase of roughly 15%. In the case of shape *h* the CIECA conveys a good approximation of the optimum value of $I_{RWR,GCA}$, with a value of $I_{RWR,CIECA}$ smaller by something less than 3%. The cases of shape *d* and *f* are the only ones in which the CIECA does not behave appreciably better in respect to the UECA. If the circle (shape *d)* is taken into account, we can see that the best possible tiling is the one shown in the third column, found with the GCA (hexagonal tiling). As explained in section 2.5.3, the CIECA and UECA topological representations cannot represent this hexagonal tiling at all, since they are forced to be symmetrical both to the **x** and the **y** axis (refer to Fig. 2.6 and consider that, in UECA and CIECA, $\Delta x_1 = \Delta x_2$). It is obvious that the same situation applies to the hexagon (shape *f* in Fig. 2.15).

As mentioned, the CIECA does not normally present the "sock anomaly". No mathematical proof of this assumption is given in this manuscript, though a preliminary consideration can be made in this direction; we observed that the "sock anomaly"

presented itself if, and only if, one of the directions of expansion (defined by the $\mathbf{v}_t$ vectors in Fig. 2.6) was roughly aligned with the main extension of the primary shape. This is clear from shape h in Fig. 2.15, where the oblique side of the shape is aligned with two of the expansion vectors that result in the configuration in the second column. This is true also for shape c and in a smaller way also for shape e. The reason behind this robustness of the CIECA may be due to the fact that the algorithm forces the shape to orient itself in a way that causes its main extension direction of the shape to not be aligned to the expansion vector, and thus not causing the anomaly in the first place.

2.6.2 Computing Time

The methodologies we presented in this chapter were extensively tested in terms of computing time. For the UECA and CIECA tests were done three times for each workspace shape. In total 24 data points were acquired for each method. Due to the long computational time, with the GCA only one test was performed for each workspace shape, resulting in 8 data points. All this was done to provide a certain degree of repeatability. In particular for UECA and GCA, each shape resulted in very consistent computing time values. The global statistics (visible in the last two rows of Table 2.2) show that the standard deviation (STD) value is sufficiently small to compare the three algorithms.

The results in Table II show that there is an important difference regarding computing time between the first two algorithms (UECA, CIECA) and the genetic-derived one (GCA). This was to be expected, since, generally speaking, evolutionary algorithms such as the one here employed, tend to take much time to converge. As for the other two algorithms, their performance can be considered similar, with the UECA slightly ahead.

However, keeping in mind the considerations about the robustness of UECA, the comparatively longer time required for CIECA to produce output seems to us as a fair price to pay, since results show that UECA can be considered adequate for the task at hand only in some cases.

2.7 Applications

Both the I_{RWR} index and the entire concept of Repetitive Workspace Robot is comparatively novel and unexplored in the field. It is then perhaps useful to show some practical implementation of the methodology in an industrial context. In order to do this, in this section two applications are shown: the former is related to the analysis and selection of robots based on their workspace aptness to be employed as RWR, the latter, more substantial, is relative to the optimization of a CDPR robot with the objective of increasing the efficiency when operating as a RWR. In other words, the workspace is optimized by employing the I_{RWR} index in order to cover the working

Table 2.2: This table illustrates the results of the time-to-compute analysis of the three algorithms. In the three columns the resulting time-to-compute are visible for the three algorithms, UECA, CIECA and GCA. In the last two rows the mean and standard deviation (STD) values for the three distributions are computed.

	Computation Time		
Shape	**UECA**	**CIECA**	**GCA**
a	3.570	11.59	2006
	3.481	11.49	
	3.499	11.53	
b	3.068	14.44	2010
	3.009	14.35	
	3.049	14.32	
c	3.045	13.81	1761
	3.061	13.93	
	3.039	13.95	
d	4.321	21.65	1708
	4.340	21.58	
	4.292	22.37	
e	4.162	21.02	1916
	4.177	21.12	
	4.170	21.39	
f	4.351	20.52	1911
	4.298	21.51	
	4.315	21.35	
g	3.939	19.23	1936
	3.963	19.49	
	3.954	19.28	
h	3.892	21.15	1834
	3.890	21.11	
	4.020	21.13	
Mean [s]	**3.788**	**18.05**	**1885**
STD [s]	**0.493**	**3.849**	**102.4**

surface more efficiently.

2.7.1 Comparing two Industrial Robots in terms of RWR efficiency

Following the general results for simple shapes presented in the section 2.15, we present an example of application of the I_{RWR} index in a practical case.

The aim is to compare a pair of industrial spray-paint robots which are similar in size and have similar workspace areas. In particular, the absolute area of the workspace is approximately the same. The robots are the ABB$^{\mathrm{TM}}$ IRB 550, and the CMA®Robotics GR 6100. See Table 2.3 for a summary of the specifications of the two robots.

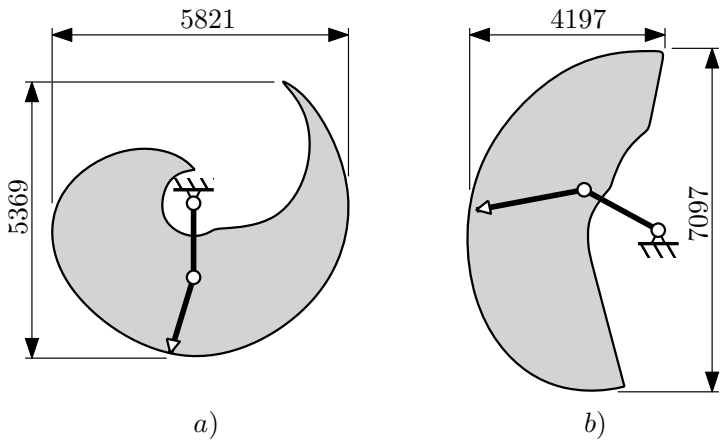

Figure 2.16: Workspaces and bulk schematics of two industrial spray-paint robots. In a) the ABB$^{\mathrm{TM}}$ IRB 550 is shown and in b) the CMA®Robotics GR 6100 is represented. Dimensions are in mm.

Note that, although the maximum reach of the first robot is considerably smaller, the robot itself has a higher range (See the workspaces in Fig. 13); this produces in fact a larger workspace area, as is apparent from Table 2.3.

The CIECA algorithm, covered in section 2.5.3, applied to the workspaces in Fig. 2.16, produces the following results for the ABB$^{\mathrm{TM}}$ IRB 550:

$$I_{RWR,2,IRB550} = 0.76. \tag{2.45}$$

For the CMA®Robotics GR 6100, the following results are found by the same

algorithm:

$$I_{RWR,2,GR6100} = 0.90. \tag{2.46}$$

It is evident, at this point, that the index $I_{RWR,CIECA}$ provides useful and somewhat counter-intuitive information on how efficient the covering process of the working area would be. In fact, the index $I_{RWR,CIECA}$, computed for the two workspaces, suggests that the GR 6100 robot provides a higher covering efficiency compared to the IRB 550. This is not immediately apparent from looking at the workspace shapes or by examining the specifications in Table 2.3. More so, considering that the IRB 550 workspace's absolute area is effectively larger than the one of the GR 6100, albeit by just over 1%.

Table 2.3: Specifications of two industrial spray-paint robots from ABB™ and CMA®Robotics.

	ABB™ IRB 550	CMA®RoboticsGR 6100
Maximum reach	2975 mm	4197 mm
Workspace area	18,050,000 mm^2	17,860,000 mm^2
Weight	540 Kg	780 Kg
Payload	13 Kg	5 Kg
N. of Axes	6	6

To support the result of the $I_{RWR,CIECA}$ analysis, it is perhaps useful to consider the maximum expanded area $A_{W,exp,max}$ in both cases. This is the area defined by $max(A_{W,exp})$ just before the $n_b > 1$ condition becomes true (see Eq. 2.14). This is a good absolute indicator of an efficient covering because it relates directly to the expansion magnitude of the shape. Larger expansions lead to less repetitions (the lattice is coarser) in the covering process because the $A_{W,exp,max}$ shape is bigger and covers more surface.

For the ABB™ IRB 550 the following results:

$$A_{W,exp,max,IRB550} = 54,720,000 mm^2. \tag{2.47}$$

On the other hand, for the CMA®Robotics GR 6100, we have the following value:

$$A_{W,exp,max,GR6100} = 64,290,000mm^2. \tag{2.48}$$

Indeed, despite being the area of the IRB 550 bigger than the one of the GR 6100 robot, the $A_{W,exp}$ values show quite the opposite with $A_{W,exp,max,GR6100}$ being bigger than $A_{W,exp,max,IRB550}$ by almost 15%. Since the $A_{W,exp,max}$ area is a good reference for the efficient covering of a surface, this proves that the $I_{RWR,CIECA}$ is a useful estimator for the covering efficiency problem discussed up to this point.

2.7.2 Optimization of a CDPR in terms of RWR efficiency

In this section we consider the optimization of some parameters of a CDPR by using the concept of I_{RWR} [51]. The robot is designed for industrial painting of a ship side, and an illustration can be seen in Fig. 2.17. Since the index provides an account on the aptitude of the robot to cover a large surface repetitively as a RWR, it can drive the optimization in order to improve the topological efficiency of the robot. In this case the UECA

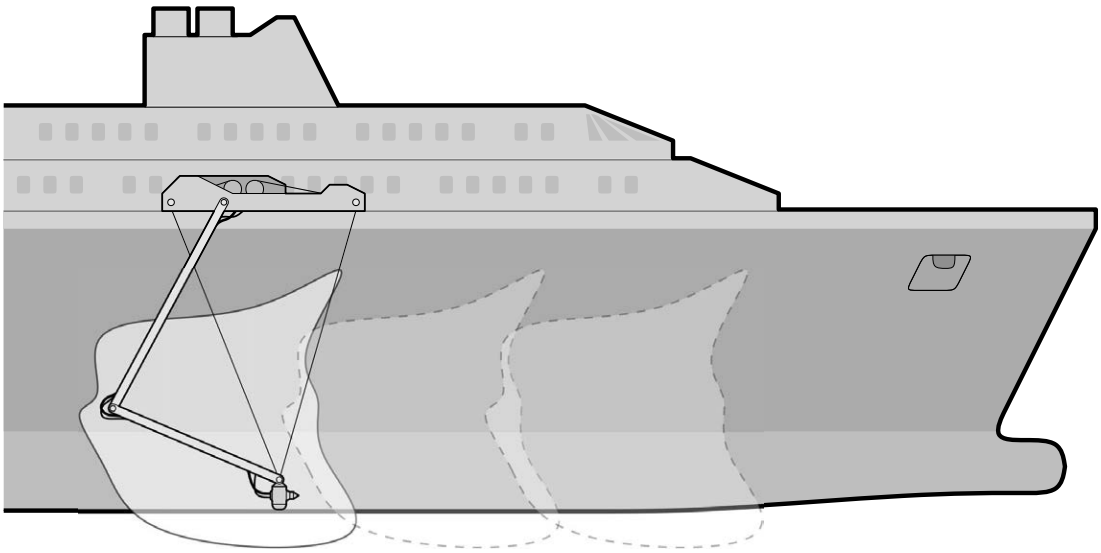

Figure 2.17: An example of the spray-painting process of the side of a ship with a cable-suspended RWR. The chassis of the robot is placed at regular intervals on the length of the ship and each time it paints the wall contained in its local workspace.

In particular, contrary to usual planar 2D CDPRs, a 2-link passive serial manipulator is coupled with the cables, to stabilize the end-effector in the vertical plane. This is necessary since planar cable robots tend to be labile in the direction orthogonal to the nominal workspace plane.

The complete system is set up by two links, two cables and two pulleys driven by two actuators and operates on a vertical plane. The 2-link serial robot is anchored on a lightweight chassis which hosts the cable pulleys as well as possible controller modules. The entire structure is lightweight and compact when stored and can be easily mounted on an external movable structure as an AWP.

The end-effector is supported by the cables and its position E on the workspace is a function of the cables angular positions ψ_1 and ψ_2. In order to avoid movements along the direction normal to the workspace plane, the end-effector is connected to the free end of a passive two-link planar two degrees-of-freedom serial manipulator by means of a revolute joint. The serial manipulator is attached to the frame in a selected point R. The CDPR's geometrical parameters and its kinematics scheme are shown in Fig. 2.18.

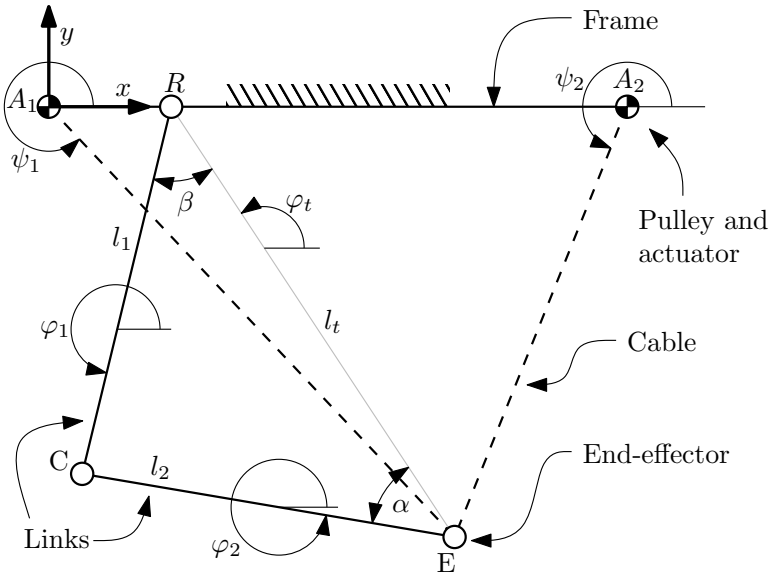

Figure 2.18: Two-links CDPR passive serial manipulator.

Finally we note that the variation of the geometrical and physical parameters of this robot produces workspaces which are considerably different in shape and dimensions

one from the other.

Following the approach described in the preceding sections and in [33], we use the Uniform Expansion Covering Algorithm (UECA) to compute the index I_{RWR}. The index is then employed to optimize the geometry of a CDPR provided with a 2-link serial passive manipulator. An illustration of the robot is shown in Fig. 2.19, whereas the actual diagram of the model used to describe the robot's behavior is shown in Fig. 2.18. We choose to calculate the index following the UECA methodology, since, contrary to the other methodologies presented in this manuscript (CIECA, GCA), this works best where the robot's workspace has a fixed orientation. In the specific case at hand, where a CDPR is considered, the rotation of the workspace is not trivial. In fact, the robot's kinematics is dependent on the gravity acceleration versor, therefore rendering the computation complex were the workspace shape to rotate. Additionally, this method allows for very fast computation time, more than 4 times CIECA and almost 500 times GCA.

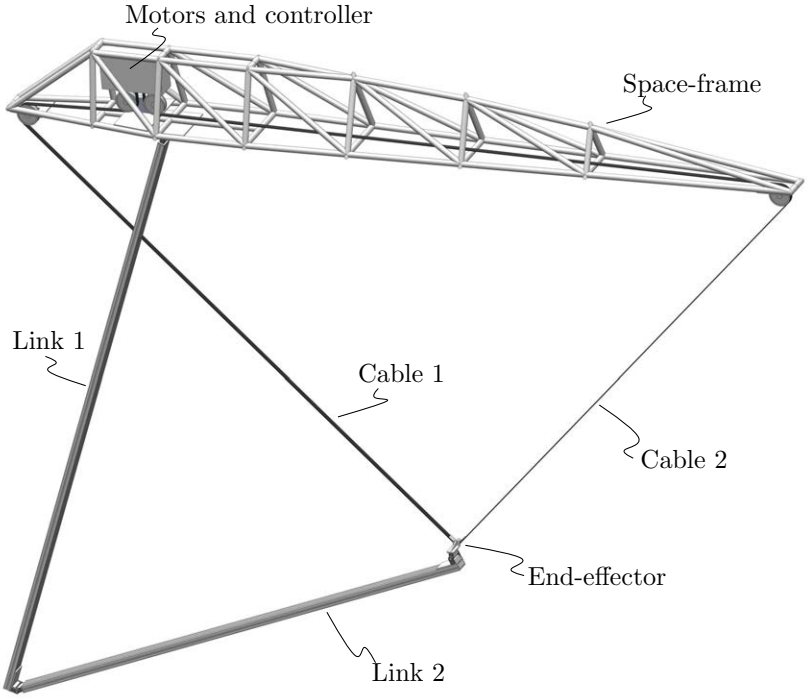

Figure 2.19: The CDPR robot equipped with a 2-link passive serial manipulator. The space-frame structure at the top provides support for the cable pulleys (upper-right and left) and for the first link, near the center. It also hosts the motors, winches and controllers for the cable maneuvering.

2.7.2.1 Kinematics of the CDPR

Referring to Fig. 2.18; φ_1 and φ_2 are the angular orientations of the RC and CE links respectively; ψ_1 and ψ_2, the angular orientations of the A_1E and A_2E cables; l_1 and l_2, the RC and CE link lengths; (x_R, y_R), (x_E, y_E), (x_{A_1}, y_{A_1}), (x_{A_2}, y_{A_2}), the coordinates of points R, E, A_1 and A_2.

Given the position $\mathrm{E}E$ of the end-effector, the inverse kinematics analysis allows to calculate φ_1 and φ_2.

The virtual vector l_t is given by

$$\varphi_t = \mathrm{atan2}((x_E, y_E), (x_R, y_R)), \tag{2.49}$$

$$l_t = \sqrt{(x_R - x_E)^2 + (y_R - y_E)^2}. \tag{2.50}$$

The angular positions of the links are,

$$\varphi_1 = \varphi_t + \pi - \beta \tag{2.51}$$

$$\varphi_2 = \varphi_t + \pi + \alpha \tag{2.52}$$

where,

$$\alpha = acos\left(\frac{l_2^2 + l_t^2 - l_1^2}{2 l_2 l_t}\right) \tag{2.53}$$

$$\beta = acos\left(\frac{l_1^2 + l_t^2 - l_2^2}{2 l_1 l_t}\right) \tag{2.54}$$

Furthermore, we can define the ratio between the length of the two links l_1 and l_2,

$$\xi = \frac{l_1}{l_2}. \tag{2.55}$$

2.7.2.2 Workspace definition

The workspace A of the two links CDPR passive serial manipulator is defined as the subset of space where the tensions on cables are both non-negative. The workspace A depends on the geometrical parameters of the robot (weight of the links and of the end-effector, motor positions, etc.).

Expanding further, it is possible to define the following relation for the workspace,

$$W = \{E \in \mathbb{R} | T_1 > 0 \wedge T_2 > 0\}, \tag{2.56}$$

where and are the cable tensions. These are obtained by means of the Newton's method, as follows,

$$X = M^{-1}B, \tag{2.57}$$

where the matrix M is

$$M = \begin{Bmatrix} 1 & -1 & 0 & 0 & 0 & 0 \\ 0 & -cos(\varphi_1) & 0 & \sin(\varphi_1) & 0 & 0 \\ 0 & 1 & -1 & 0 & 0 & 0 \\ 0 & 0 & \text{-cos}(\varphi_2) & \sin(\varphi_2) & 0 & 0 \\ 0 & 0 & 1 & 0 & \sin(\psi_1 + \pi) & \sin(\psi_2 + \pi) \\ 0 & 0 & 0 & 1 & \cos(\psi_1 + \pi) & \cos(\psi_2 + \pi) \end{Bmatrix}, \tag{2.58}$$

and X, B are,

$$X = \begin{Bmatrix} V_R \\ V_C \\ V_E \\ H \\ T_1 \\ T_2 \end{Bmatrix} \qquad B = \begin{Bmatrix} P_1 \\ \frac{1}{2} P_1 \cos\varphi_1 \\ P_2 \\ \frac{1}{2} P_2 \cos\varphi_2 \\ P_E \\ 0 \end{Bmatrix}. \tag{2.59}$$

Note that V_C and V_E are the vertical forces acting on nodes C and E. H is the internal horizontal force acting on the end-effector and on the nodes. P_1, P_2 and P_E are respectively the weights of the links and of the end-effector.

2.7.2.3 Computation of the index $\mathbf{I_{RWR}}$ varying the ξ and $\mathbf{x_R}$ parameters

Having defined the kinematics and geometrical configuration of a two link CDPR passive serial manipulator, we can easily calculate the workspace W for different sets of design parameters. Specifically, we note that two parameters, among others, greatly influence the shape of the workspace. These are the horizontal coordinate x_R of the robot node R, and the ratio between the length of the links, ξ. To define the actual length of the links, we fixate the sum of their lengths, thus having $l_{\text{tot}} = l_1 + l_2$. This

constraint allows us to vary the geometrical configuration of the links without substantial implications on the bulk and overall weight of the robot. Moreover, we are able to perform this by acting on only one parameter, ξ.

We discretize the variation span of the two parameters, thus creating a grid. By computing the workspace for each grid-point we are able to calculate the associated I_{RWR} index for the workspaces. These are shown as a surface in Fig 2.20.

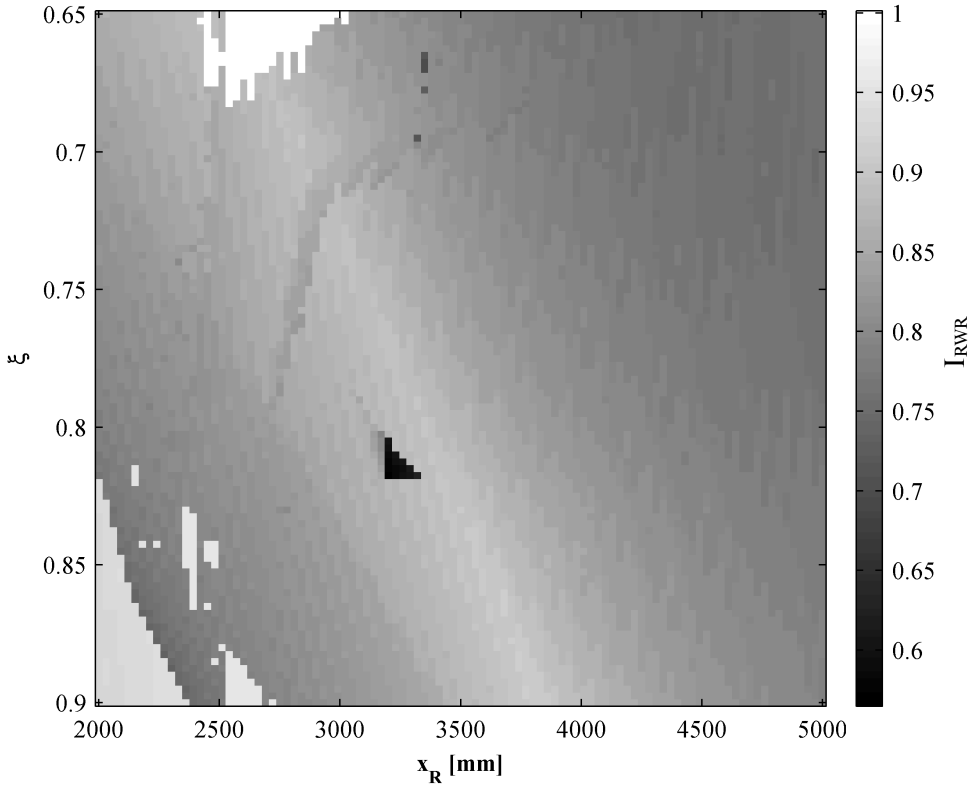

Figure 2.20: Surface resulting from the values of I_{RWR} obtained by varying the x_R and ξ parameters.

The x_R parameter varies between 2000 and 5000 mm, whereas the variation interval of ξ is $0.65 \div 0.9$. The total length of the links is $l_{\text{tot}} = 9899\ mm$. All other parameters are fixed: $x_B = 7000\ mm$, $x_A = 0\ mm$, $y_{A_1} = y_{A_2} = y_R = 0\ mm$, $P_1 = P_2 = 12\ Kg$, $P_E = 10\ Kg$. The end-effector (point E) represents a spray gun (e.g. *WAGNER Colora GA 4000ACIC*) which bulk dimensions are $129 \times 47 \times 60\ mm$, and weight is $0.678\ Kg$.

The spray stroke can vary from approximately 20 to 300 mm in diameter.

From the surface in the figure we can see that the index varies substantially in function of the parameters x_R and ξ. A general trend is evident in the form of a curved ridge where the points with the highest index lay. This shows a possible correlation between the considered parameters, although this is not investigated further in the present study. Finally, we note that in the proximity of the bottom-left and upper corners of the surface, a series of white areas are present. These are errors of the UECA algorithm known as "sock anomaly", described in Section 2.5.3. Furthermore, we note that near the center of the surface, a dark-grey spot is present. This is due to the formation, at those coordinates, of irregular structures along the edge of the workspace; these contribute to a substantial decrease in the local index value.

2.7.2.4 Computation of the Index I_{RWR} varying the x_R parameter alone

The coordinate x_R (the anchor point R of the first link (link RC), as seen in Fig. 2.18), plays a key role in the definition of the workspace shape. The x_R variable is chosen as the optimization parameter because, as previously noted in 2.7.2.3, the position of joint R on the frame is strongly influential on the resulting workspace shape for this type of robot (and therefore for its I_{RWR} index). Furthermore, this parameter is easily customizable on a robot, contrary to the length of the links (which gives the ξ ratio). Nevertheless, the variation of the I_{RWR} index can be studied for any other parameter (for example ξ, l_1, l_2, the weight of the links, etc.).

Therefore, it is interesting to calculate the I_{RWR} index for different values of the coordinate x_R. This way, according to the index, it is possible to select the value of x_R which guarantees that the workspace associated with the robot provides the maximum possible tessellation efficiency.

Results are presented in Fig. 2.21 and in Fig. 2.22. In particular the former shows the I_{RWR} index values obtained with a continuous variation of x_R; the latter, instead, allows the reader to understand the shape of the workspace for four significant x_R values, which are identified with the letters a, b, c and d.

The physical parameters of the robot are the same as those shown in 2.7.2.3, with the exception of the length of the links, which is now fixed by having $\xi = 0.78$. In fact, the plot in Fig. 2.21 is essentially a slice of the response surface visible in Fig. 2.20, at a certain ξ level.

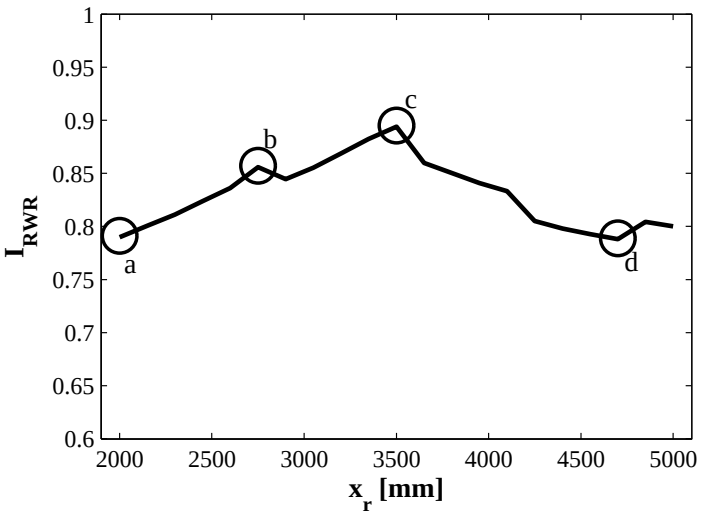

Figure 2.21: In this figure the I_{RWR} indexes of the configurations obtained varying x_R from 2000 to 5000 mm are shown. The letters *a*, *b*, *c*, *d*, indicate the cases represented in detail in Fig. 2.22

The table in Fig. 2.22 shows that configuration "*c*" ($x_R = 3500\ mm$) delivers the best I_{RWR} index, and therefore the best tessellation efficiency. One can well appreciate this, noting that the intersection area (shown in the 5^{th} column) in this case is significantly smaller than in the other cases. It can therefore be inferred that the best geometrical configuration, in terms of "efficient tessellation" of a large working area, is obtained when $x_R = 3500\ mm$. For the same reason the workspace produced by configuration "*d*" ($x_R = 4700\ mm$) has a poor efficiency, which is immediately apparent from the large intersection area. This is consistent with the related I_{RWR} index.

In general the index I_{RWR} is shown to vary against some of its parameters. As can be seen from Fig 2.7.2.3 the index is considerably more sensitive to the x_R parameter, than to the ξ parameter; in fact, once a specific ξ is selected from the map in the figure, the x_R can used efficiently to locate the maximum index value, as Fig. 2.21 and Fig. 2.22 demonstrate.

2.8 Conclusion

Whenever a large area needs to be covered by means of a robotic system, it can be worthwhile to employ a Repetitive Workspace Robot, which partitions the surface and

covers each portion one at a time.

In this section an index was introduced to evaluate the topological covering efficiency of these robots. Moreover, a set of three algorithms to compute this index were presented, the GCA, the UECA, and the CIECA, the first based on a genetic algorithm approach.

A comparison between the three methodologies was made, both in terms of accuracy and computing time. Results show that the best overall results in terms of accuracy

Rif.	x_R $[mm]$	Geometrical Configuration	Workspace (*Area* in pixels)	Maximum intersection WS	I_{RWR}
a	2000	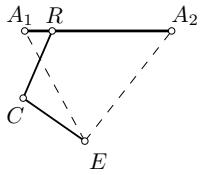	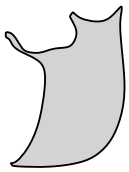 $Area = 3823$	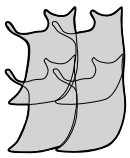	0.7911
b	2750	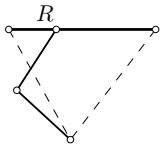	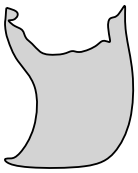 $Area = 4474$	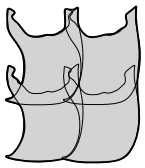	0.8571
c	3500	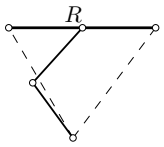	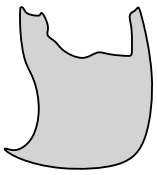 $Area = 5175$	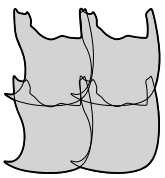	0.8950
d	4700	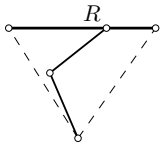	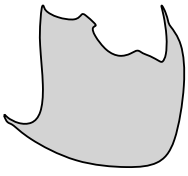 $Area = 6212$	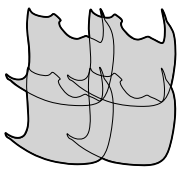	0.7889

Figure 2.22: In this figure some different configurations in terms of values of the serial manipulator anchor point x_R, noted by the letters *a*, *b*, *c* and *d* are chosen from the plot in Fig. 2.21 and the I_{RWR} index of the resulting workspace is shown. All other parameters are fixed: $l_tot = 9899\ mm$ $\xi = 0.78$, $x_B = 7000\ mm$, $x_A = y_A = y_B = y_R = 0\ mm$. The area (in pixels) of the resulting workspace is shown for each configuration.

were given by the GCA. If, however, the computing time is considered as well, the CIECA can be considered the best performer, nearly reaching the accuracy of the GCA. The GCA was used as a baseline for the optimal solution; this since it produces undoubtedly the most accurate results, though at the cost of very high computation times. In fact, the GCA is the only algorithm which considers a complete topological model and has no simplifications in this sense. The CIECA, for example, does not allow for the lattice, or grid, to be *skewed*.

In order to demonstrate the use of the index, a simple practical application example was described. We compared two 6 D.O.F. industrial paint robots: an ABB$^{\text{TM}}$ IRB 550, and a CMA®Robotics GR 6100. The method used was CIECA. Results show that, between the two robots, the I_{RWR} index is able to correctly identify the most suitable one to cover a large surface as a RWR.

Furthermore, the UECA is employed to lay down a design methodology for a specific type of RWR, where the index is used as the main design parameter for a CDPR robot. The UECA was used, since it is well suited to cope with this type of robot. Variations in the resulting I_{RWR} values for the robot are shown in relation to variations in some of its geometrical design parameters. Finally, we show how the index can be directly used to choose a design configuration for this type of robots.

It is worth noting that this index can easily be coupled to a variety of other indexes or parameters (manipulability, dexterity, etc.).

For example, as far as CDPRs are concerned, it can be combined with indexes which take into account the tension factor values so as to generate a workspace with optimized performance [12]. Nevertheless, this endeavour confirms the claims on the index' field of application, and illustrates some practical result.

3

Control Strategies

When dealing with a Large Workspace Robot, one of the main challenges is related to trajectory – or path – planning. In the general field of robotics, this is the determination of the path that the end-effector should follow in order to complete a specific task. A multitude of techniques surfaced during the last three decades, associated with various degrees of automatism.

Restricting the field to that of commercial serial and parallel manipulators, in the industrial environment the standard, today, is still manual trajectory planning, either with point to point lists strategies or by training.

The former refers to a human operator programming (not necessarily by inserting coordinates) a list of points in the robot control logic. This is common for example in some pick-and-place operations involving comparatively slow robots and large movable objects.

Conversely, the latter, i.e. training, is related to a generally advanced technique that involves an operator carrying around the end-effector, and performing the task while the robotic system records it. The robot can then repeat the sequence when requested. This methodology finds very large use in the field of industrial robotic painting [52] and welding [53, 54], jobs that generally require the repetition of a simple task for many times.

In the following we will consider the case of robotic painting, specifically of photo-realistic images. The method we outline can be used efficiently on very large surfaces [55, 56].

The best example of system used to reproduce photo-realistic images on a surface is the printer, in its various forms. The problem of this is that it operates essentially dot-by-dot, regardless of the detail sizes in the image. This translates in very long painting times if the surface is large. Moreover, the resolution is ultimately established by the hardware in the print head, which is a big limitation in flexibility. Furthermore, the scalability is limited to a certain extent, due to the print-head functioning process, which works essentially by deposition. The principles involved cannot be reproduced on a very large scale.

For these reasons, in the following pages an innovative methodology to reproduce photo-realistic images on surfaces by means of a fully automatic robotic spray-painting process is proposed. The method is centred on the concept that with a spray-painting robot we can achieve a wide range of stroke sizes; this can be exploited by using the larger strokes to paint the larger details, and the smaller strokes for the smaller details. Efficiently calibrating this process leads to virtually any outcome, from low-detail and hi-speed to slow-speed but high-detail executions. The core of the methodology is an adaptive, smart algorithm that uses techniques derived from Voronoi diagrams, convolution and ordinary least squares (OLS) methods to define a path and feed-rate to control a general robot, especially robots that are commercially available. In this article we use only grey-scale images, but extension to full color is comparatively straightforward.

3.1 State of the Art

Nowadays, robotic painting is a very important process in the industry; it spans from automotive to manufacturing, even to art. In the vast majority of applications the spray painting technique is used rather than others, i.e. brush painting. Indeed this technique couples very well with automated systems, and can be very efficient. Normally, the painting process aims at obtaining an uniformly painted surface of arbitrary shape. It is worth noting that, some aspects of robotic painting were left behind, in particular those concerning non-uniform painting. An ordinary example of this kind of painting is a photo, or a drawing. At present, no automated methodology or algorithm aimed to replicate an accurate copy of a digitized image (be it a photograph or something less realistic) on a large surface by means of an industrial spray-painting robot has been

proposed. The purpose of this work is thus to present an innovative methodology and algorithm to tackle this challenge.

Several branches in the industry could be positively affected by this methodology, especially where decorative and/or functional painting is required. Automotive and furniture industries, particularly in the high-end segments, can present the need for this type of operations, and up to now this was generally met with the aid of highly skilled artisans or with complex masking systems (which, in turn, needs other professionals as well). It goes without saying that these procedures often impose great cost and time. Another promising branch is the one involved in construction; some companies (Cité-Création[1]) use classic techniques like *fresco* and *trompe-l'oeil* to decorate buildings and homes, this mainly in an attempt to increase quality of life in crowded and dull city environments. Along the same line, in a less artistic way perhaps, industry buildings often need signs, text or warnings on walls or machinery, and while on small surfaces decals can be used, with larger surfaces this becomes impractical. The history of painted furniture is as old as society in itself, dating back to at least ancient Egypt; in modern times the interest in this kind of art has somewhat subsided due to high costs, but examples are still present. If, though, the process were to be completely automated and robotised, cost would lower substantially.

At present, the mechanics of the spray painting are well understood, for example Balkan et al. [57], Ellwood et al. [58] and Conner et al. [59] presented models for the flow rate flux of a paint gun and for the paint deposition in spray painting. Chen et al. [60] experimentally analysed the paint coating characteristics for uniform velocity with overlapping paths, whereas Fogliati et al. [61] provided a numerical CFD (Computational Fluid Dynamics) analysis of the paint deposition process. Elliot et al. [62] provided a model for the fluid-dynamics effects of spray-painting with a rotary nozzle. Atkar et al. [63] published a work on robotic uniform spray-painting in automotive. Robotic spray painting is also widely acknowledged; in normal industrial practice the manual teaching methods (see Baldwin [52]) are widely used. Chen et al. [64] propose a review of the current state of the art in the automatic path planning for industrial robotic spray-painting. Artistic, non-uniform painting by means of autonomous or automatic systems has been a subject of research in the last two decades, mainly since the work by Haeberli [65] on the virtual representation of images using pictorial, abstract

[1] Lyon, France, http://cite-creation.com

styles. A crucial reference for our work is the concept highlighted by Hertzmann [66], in which the painting is carried out (virtually) with progressive decreasing-size strokes, following the footsteps of Haeberli. A series of different artistic painting robots are presented in literature, a few examples of which are in [67–69]. All these are not adequate since they tend to produce artistic-looking, non-photo-realistic paintings.

As stated, in fact, the objective of the work which is reported in this manuscript, is the reproduction on large surfaces of photo-realistic images; in other words, given a certain target image, the intention is to accurately paint it on the canvas by using a system based on an industrial robotic manipulator and a spray gun.

3.2 Approaching the Problem Iteratively

The key concept in the proposed approach is that, in the spray-painting process, the size of the stroke is determined by the distance of the nozzle of the gun from the surface. This dimension can be adjusted by varying the distance of the end-effector (EE) of the robot from the target surface.

It is worth noting that other techniques exist to modify the diameter of the stroke; for example, there exist several types of variable-geometry nozzles; other implementations can vary the stroke by acting on the feed pressure of the paint; others still use rotary nozzles to widen the stroke, based on the speed of rotation. In this work, however, we focus on the distance, since this allows us to exploit the morphology of the paint cone originating from a standard spray-paint gun.

The morphology of the spray-paint cone originating from the nozzle is illustrated in Fig. 3.1. The Gaussian-like distributions shown at distances d_1, d_2 and d_3 are the cross-sectional paint-flow profiles of the jet. It can be noticed that these represent equally well the paint collected in a unit of time on a surface if said surface were placed at that specific distance. In other words, being density the ratio of paint-covering on the surface, the distributions represent the density profile per time unit, as this is deposited on the surface.

The main challenge of the proposed approach is to split the painting task into a series of cumulative sub-tasks with increasing detail. It is worth noting that as the level of detail increases (thus requiring lower sized strokes), the time required to perform the sub-task increases. For this reason it is crucial to perform as much work as possible in

the first steps, where the larger strokes are employed. The overall process is illustrated in Fig. 3.2.

In the figure, the target image can be seen: this is the image that needs to be painted on the canvas or the surface, in general. The image is fed into the algorithm, and the robot is controlled based upon the involved computations. For this example, a serial manipulator is considered, with a spray-gun attached at the end effector. In the first row, the system analyses the target image considering that a large stroke will be used. The algorithm creates a path and a feed adequate to the stroke; upon actuation, this leads to a layer that consists in large strokes that cover most of the surface. The remaining rows show layers at lower detail size, each likely contributing less (in terms of paint) than the previous to the overall image. Efficiency is connected to this procedure; the more paint is delivered in the first layers (with the larger strokes) compared to the subsequent, the higher will the overall efficiency be.

It is easy to understand that, in order to obtain a good result, the stroke size at each step must be chosen wisely. Furthermore, the number of steps and the size of the stroke at the last step are very important for the overall quality of the finished piece. Many methods can be made available to precisely calibrate these parameters (empirical, semi-empirical, numerical optimization), but are not of our immediate concern for the purpose of this manuscript.

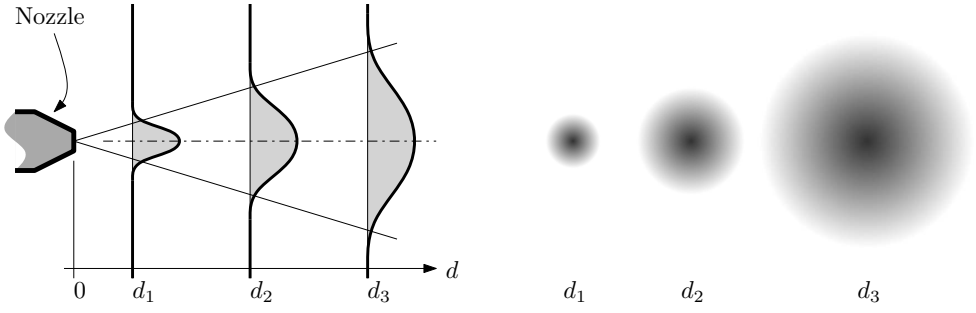

Figure 3.1: Spray-paint cone morphology. The cone originates from the Nozzle, and at various distances (for example d_1, d_2 and d_3) an indication of the cross-sectional paint distribution is visible in grey, along with the resulting stroke on the canvas (on the right). For clarity purpose, the distributions are normalized over the maximum value of each curve.

3.3 Experimental Investigation of the Spray Morphology

Preliminary experimental tests must be performed in order to analyse the physical characteristics of the painting process. The first one is aimed to identify the paint density profile shape at different distances of the nozzle from the surface, the second one is aimed to determine how the deposition of paint on the canvas varies with time. The paint density profile is crucial to precisely define how the paint will be distributed on the actual surface: it is the main parameter for the algorithm, as shown in the following sections. The deposition rate is comparatively less important than the density profile. Therefore, for the sake of simplicity a linear approximation is adopted.

The main objective of these tests is to provide a framework, and to define a procedure to evaluate the main physical properties involved in the system. The experimental

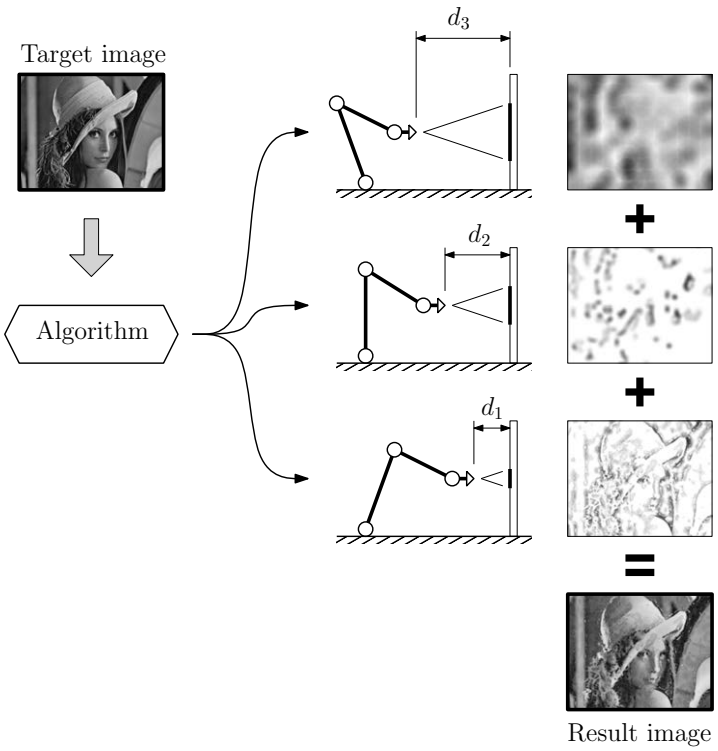

Figure 3.2: The proposed methodology. The image (upper-left) is fed into the algorithm, which, according to the spray morphology and mechanics, splits the paint execution in a series of consecutive tasks, each of which takes advantage of a different stroke size, and operates mostly on details of matching size. The progressive execution of these steps generates the resulting image. Note that $d_3 > d_2 > d_1$.

investigation conveys a general idea of the process of measurement. This ultimately leads to a better formulation of the algorithm, which is the main purpose of the endeavour.

3.3.1 Paint Density Profile

This test is done by performing a quick burst with the airbrush at fixed distances from the canvas. This approach is similar to many found in literature [57]. The paint used in the experiment was black acrylic at a 2:5 paint to water ratio. Note that the airbrush nozzle was placed orthogonal to the canvas. The resulting strokes were then digitized with a *Canon PIXMA MP280* scanner; the image was then analysed to provide a paint density profile.

The duration of each burst lasted approximately 1s; in order to precisely normalize the distribution, we exploited the audio recording associated to each burst to precisely determine its duration.

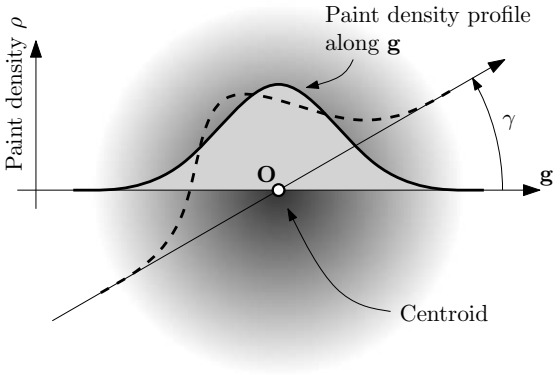

Figure 3.3: Analysis of the paint density profile ρ of the paint stroke. The centroid $\mathbf{O}$, the axis $\mathbf{g}$ (coincident with $\mathbf{O}$) and the angle γ are visible. The paint density profile is also appreciable for two different orientations of $\mathbf{g}\,(\gamma)$

Taking Fig. 3.3 as a reference, the axis $\mathbf{g}$, centred in $\mathbf{O}$ ($\mathbf{O}$ is the barycentre of the paint stroke), is progressively rotated by $\gamma \in [0, \pi]$ and the paint density along $\mathbf{g}\,(\gamma)$ is stored as $\rho\,(r, \gamma)$, where r is the radius. We can thus calculate the mean density profile by averaging the values of $\rho(\gamma)$ for each radius r value. A typical result is given in Fig. 3.4a. The process can be repeated at different distances of the nozzle from the canvas, as visible from Fig. 3.4b. Additionally, we find that the profile can be well

approximated with a Gaussian curve. It is generally sufficient to truncate the curve at 2 or 3σ.

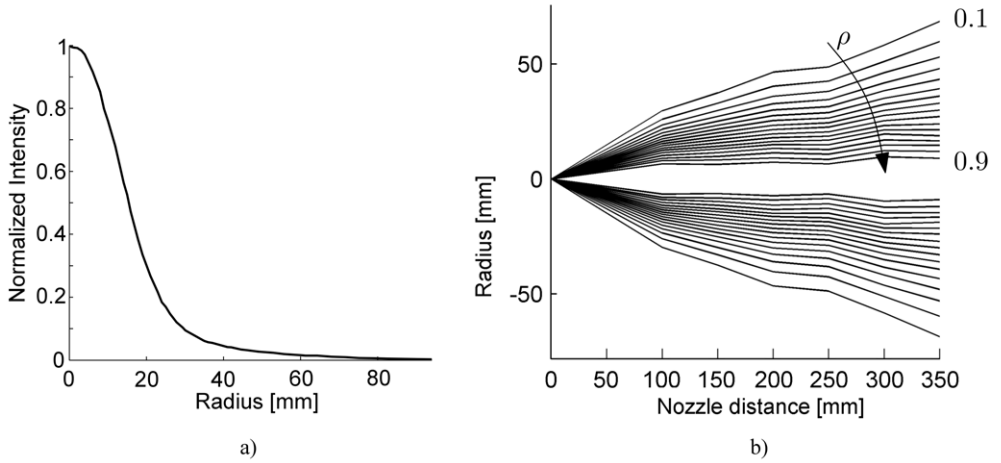

Figure 3.4: Example of experimental results for the paint density profile at various distances. In a) a density profile is visible: the nozzle-canvas distance was 100 mm. In b) one can appreciate the qualitative paint density ρ distribution along a longitudinal section of the spray-paint jet; the arrow shows the direction of increment of ρ, whereas the lines represent iso-ρ levels in the spray section; the step is $\Delta\rho = 0.5$. All the graphs are symmetric.

3.3.2 Paint Deposition Rate Law

If a small fixed region inside the boundaries of the spray-gun stroke is considered, it is possible to analyze the density of paint deposited over time; therefore, the law for the paint deposition ratio can be extracted. This was performed for a series of different points along the generic radius, and for several different distances. This experiment was performed using a video-camera (*Nikon D90*) to record the spraying process on a common paper substrate. In Fig. 3.5 a typical result of this experiment is shown. It is possible to observe that the first part of all the experimental curves is very close to linearity.

This property is important because it determines how two different layers of non-saturated paint interact with each other. If the deposition ratio is linear (or can be approximated as linear) the resulting density of two overlaying strokes of paint will be equal to the sum of their densities in each point.

An explanation to the fact that the deposition law shows a definite linear segment is given in the following. The spray-painting process breaks the flow of paint into a cloud of small droplets (atomizing). This results into a colloid suspension of fine liquid particles called *aerosol*. In the first instants of the painting process, that is, when the canvas is clear and the first particles of the aerosol hit the surface, the likelihood that a particle hits a spot where a previous particle hit, is next to zero. After the first hits, particles start to accumulate on the canvas, but, since their size is small, the likelihood of hitting a paint spot remains very low. At a certain point, this probability rises and linearity ends. The reason is that, while probability is low, the vast majority of particles will hit a clear spot, thus increasing the overall intensity; in fact, when a particle hits an already painted spot, the overall increase of intensity is null. Since these last events

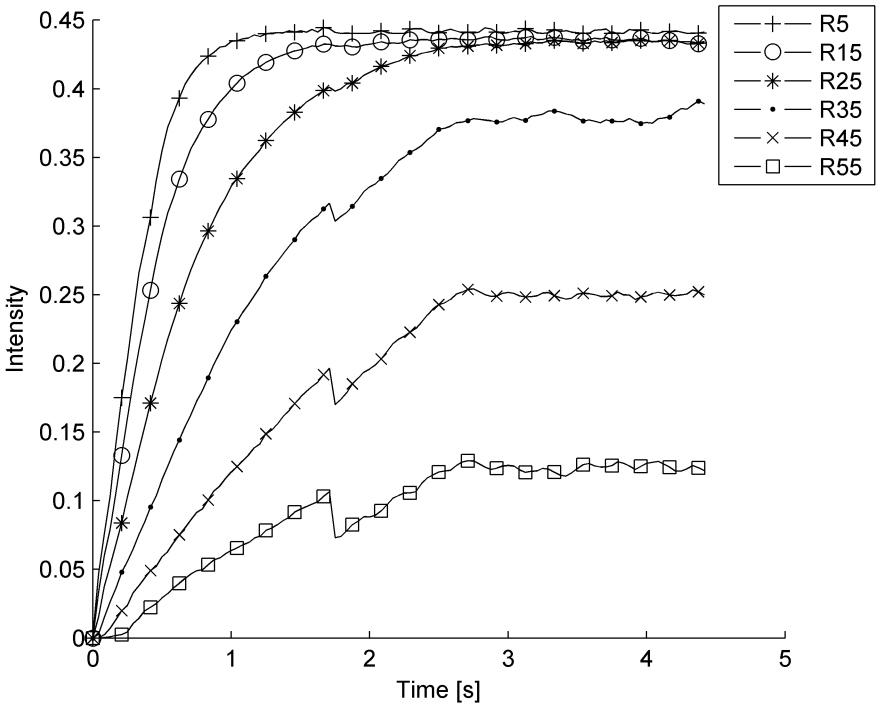

Figure 3.5: Paint deposition ratio over time. The different lines represent different points along the general radius, from 5 to 55 mm (starting from the center), as shown in the legend. It can be noticed that an intensity of approximately 0.45 is equivalent to saturation due to the video-camera setup. The nozzle-canvas distance was 100 mm. The presence of a step in the R25 through R55 lines is due to the appearance of spots on the painted surface, which are in turn caused by non-adhesion of the paint to the substrate.

are rare in the first portion of the plot, the increase is close to linear. A simulation of this behavior is reported in Appendix A on page 171.

3.4 The Algorithm

The methodology proposed in this study mainly relies on a three-step algorithm. As mentioned in Section 3.2, the idea is to perform the painting procedure on multiple levels (layers) on the canvas, each determined by a different stroke size (given by the distance, or by other means), and thus by a different detail size.

In the following sub-sections some basic definitions are provided, then the structure of the algorithm with its main operational blocks is illustrated, and finally the *timing algorithm* is described, which is the block that uses OLS to calculate the speed profile of the EE.

3.4.1 Definitions

In order to provide a consistent framework for the illustration of the algorithm, a set of definitions is given in the following.

Let us indicate Q_i as a general point of the surface and define the intensity $I(Q_i)$ as the value corresponding to the paint-density ρ when this is acquired by the acquisition system (camera, scanner, etc.). It is, essentially, the integral of the paint-flow per time unit, which was shown in Fig. 3.1, and is mapped in the 0–1 interval.

Given a specific *target image* (TI) to be painted on a canvas, for each point Q_i of the TI, a target grey-intensity $I_{grey,target}(Q_i)$ for that point can be determined. Along the same line, if the canvas is not blank (since the process is intrinsically multi-step and iterative, this happens after the first layer is deposited), a starting intensity $I_{grey,start}(Q_i)$ can be determined.

It is important to remark the concept of *over-painting*: this term means essentially over-saturation, i.e. when the coating of paint is already at its maximum density, and the spray-gun continues to apply paint; this usually translates in droplets forming on the canvas and this, in turn, leads to sub-optimal outputs. Another kind of over-painting can be defined: *grey over-painting*. This is meant in the sense that if we pick a point Q_i of the TI which has a prescribed grey-intensity level of $I_{grey,target}(Q_i) < saturation$,

every intensity $I(Q_i)$ that causes $I(Q_i) > I_{grey,target}(Q_i)$ causes grey over-painting: this obviously causes non-realistic output images as well, yet it might not cause droplets.

Thus, for each point Q_i of the canvas and TI, a distance$\Delta I_{grey,i}$ from the target to the starting grey-level. This translates in the following,

$$\Delta I_{grey,i} = I_{grey,target}\left(Q_i\right) - I_{grey,start}\left(Q_i\right). \tag{3.1}$$

Furthermore, for every Q_i we can define a saturation velocity $I^{'}\left(Q_i, Q_t\right)$, which is derived from the experimentally determined paint deposition rate law, illustrated in Section 3.3.2. This is as follows,

$$I^{'}\left(Q_i, Q_t\right) = I^{'}_{i,t} = I'\left(\|Q_i - Q_t\|\right) = \frac{dI_{grey,i,t}}{dt}, \tag{3.2}$$

where Q_t is the barycentre of the stroke (tool-centre).

It is important to recall that this relation can be sufficiently approximated as linear, hence the $I^{'}$ can be considered constant in the time domain, and function of Q_i alone.

Finally, S can be defined as a Cartesian map of the stroke of the spray-gun which was previously defined in polar coordinates $\rho(r, \gamma)$ in Section 3.1. The stroke map S is defined as a collection of $I^{'}\left(Q_i\right)$ saturation velocities. Operatively, S is a matrix of coordinates (ζ_1, ζ_2) which arbitrarily discretizes the $\rho(r, \gamma)$ profile. In the algorithm a 2σ truncated Gaussian approximation is used.

3.4.2 Main Structure of the Algorithm

Since the painting process is split into different layers, at each stage the algorithm has to take into account the areas which are already saturated or have reached the prescribed intensity, in order to produce respectively neither over-painting nor grey-overpainting. In order to comply with this, critical points are determined at each step, and are used to limit the paint coating in order to prevent over-painting.

In Fig. 3.6 an overview of the proposed methodology is presented. The general layout is illustrated in Fig. 3.6a. The algorithm starts with the first layer at the maximum distance, it acquires the target image into the *core algorithm* and from the output image it investigates if there are any other regions still to be painted at this detail level; eventually it sub-iterates the process. If no regions are left, it can proceed to the next layer (at a closer distance) and iterate until the last layer is reached. The

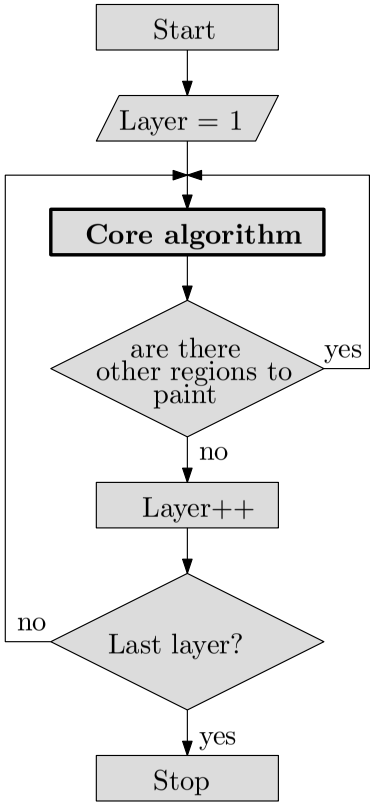

a)

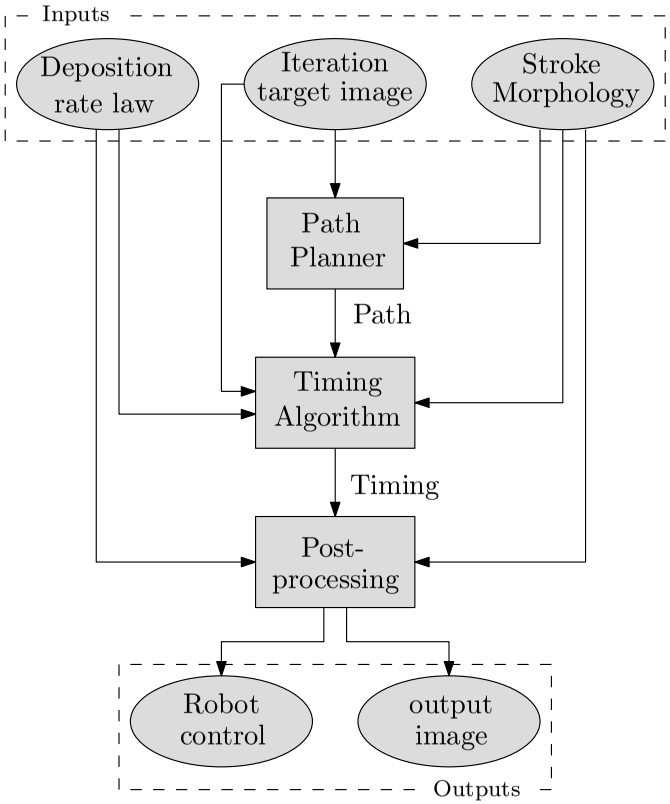

b)

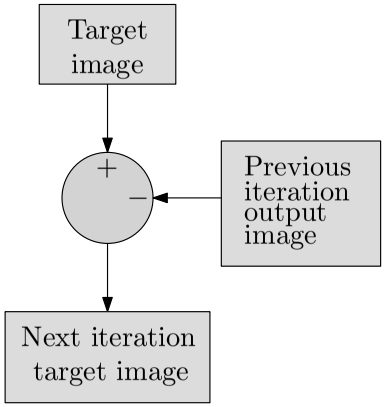

c)

Figure 3.6: The algorithm used to perform automatic path-planning for a photorealistic painting robot. In a) the general methodology is visible, the *Core algorithm* block is visible in b), with highlighted inputs and outputs; lastly, in c) the generation of the *iteration target image* (see b)) is visible.

core algorithm is visible in Fig. 3.6b; it requires three main inputs: the deposition rate law, the stroke morphology (the size and shape of the stroke) and the *Iteration Target Image (ITI)*. The first two inputs are contained in the stroke map S. This image is obviously coincident to the target image in the first sub-iteration of the first layer, but at the following steps it is found following the diagram in Fig. 3.6c. An illustration of the described concept is given in Fig. 3.7.

It is worth noting at this point, that in case the feedback loop uses not the output of a simulated layer, but a real-time camera system, the "Output image" term will be the acquired image via the CCD. In that case the system will likely compensate better for execution errors that would otherwise build up during simulation and *offline* execution.

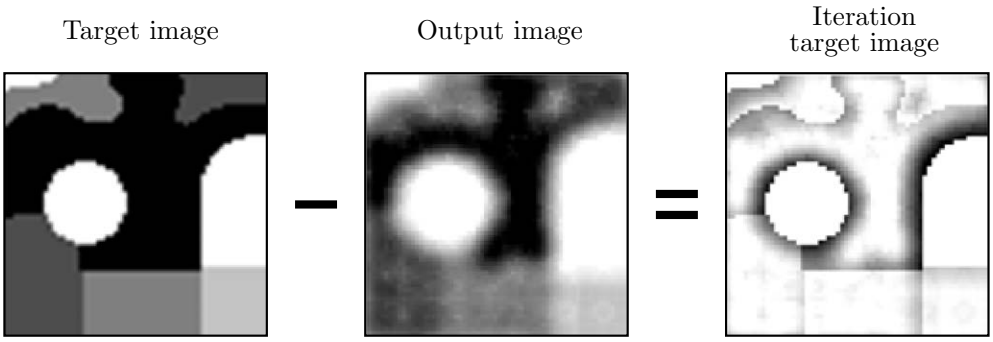

Figure 3.7: Generation of the iteration target image. During a general step of the algorithm the *iteration target image* (ITI) is found by subtracting the *output image* (resulting from the preceding step) from the *target image*. Black areas are to be painted.

The three main operational blocks are illustrated in Fig. 3.6b. The *Path-planner* blockis based on an algorithm which uses offsets computation via Voronoi diagrams [70–72]. The boundaries for the calculation are chosen by a basic thresholding technique applied to the *Iteration target image*. The output of this process is a hierarchical collection of offsets, which is ultimately the *tool-path*; in the following, the tool-path will be referred as as the vector L. The most important block is the *Timing algorithm*. This calculates the time the spray-gun must "rest" over each point of the tool-path, which easily translates into a *speed profile* along the path. The detailed procedures will be thoroughly explored in the following section. The complete process in the elaboration of a generic layer is summarized in Fig. 3.8.

The *post-processing* generates the projected output image at the current layer, following the timing profile along the tool-path. This provides the next iteration image,

as can be seen from Fig. 3.6b and c. This last step can be executed either by virtual representation or simulation (convolution of the stroke S with the tool-path), or by acquiring real-world results during the process (CCD camera, etc.).

3.4.3 Linear System (LS) Structure

As mentioned before, the timing algorithm is based on the solution of a linear system (LS) using the OLS method. This produces a speed profile for the EE to follow during the implementation of the tool-path provided by the path-planner block.

Let the LS be in the following form:

$$At \leq B, \tag{3.3}$$

where A is the matrix of coefficients, and B is the known terms vector. The t term is the vector of the variables; in order to better define it, let us consider a generic vectorial tool-path L generated by the *path-planner* block and juxtaposed over the image we are processing (the ITI). By using the Bresenham line algorithm [73], we can rasterize this path; the resulting succession of points P_i corresponds to pixels belonging to the image and constitutes the discrete path $\tilde{L}$. Each of these pixels is effectively related to one variable in the LS, which is the time the end-effector is required to remain in that specific pixel boundaries. It follows that the number of variables in the LS can be (initially) assumed to be equal to the number of pixels belonging to the path $\tilde{L}$.

The matrix of coefficients A can be built according to the following rules: each column relates to a specific point $P_i \in \tilde{L}$, whereas each row is relative to each point

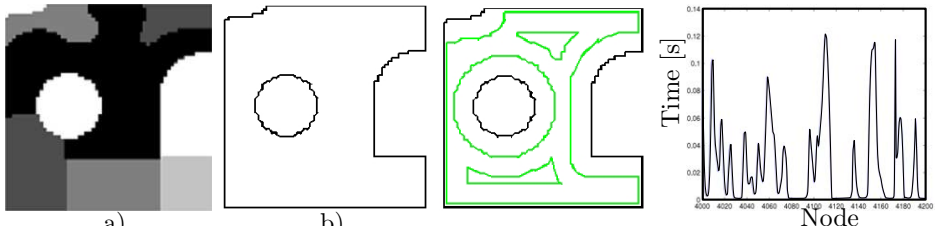

Figure 3.8: Generation of the tool-path and speed profile for the robotic system. In a) a simple target image is visible, in b) the contours of the paintable area are detected; the computed offsets which form the actual tool-path are presented in c). Finally in d) one can see the speed profile along a partition of the tool-path.

Q_j of the ITI. Since the number of Q_j is exceptionally large, a significant number of equations would arise from this formulation. Therefore, an approach based on a restricted collection of critical points K_η is exploited. The definition and selection of these critical points will be discussed in the following sections (3.4.4 and 3.4.5). The values are the previously described saturation velocities $I'(K_\eta, P_i) = I'_{\eta,i}$ of the critical points.

Finally, the known terms matrix B contains the target I_{grey} for the same critical Q_η points that were taken into account during the assembly of A, that is to say $I_{\text{grey}}(Q_\eta)$.

3.4.4 Critical Points: definition and determination

A critical point K_η is defined as a point which, during a specific layer painting process, is substantially more prone to over-painting or grey over-painting than the majority of the other points of the ITI. Two kinds of K_η exist in our problem, and are related to their selection process: *global* critical points $K_{\eta,global}$ and *local* critical points $K_{\eta,local}$.

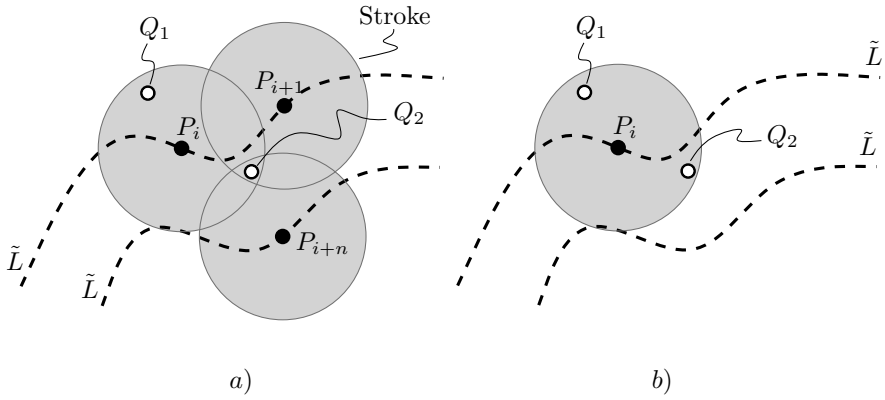

Figure 3.9: Selection of critical points inside the Timing Algorithm. In a) the global potential critical points $K_{\eta,\text{global}}$ selection is shown, whereas in b) the local $K_{\eta,\text{local}}$ selection process is shown. These K_η critical points are the result of the selection between points Q_1 and Q_2.

3.4.4.1 Global critical points

Let us start by illustrating the selection process of the *global* critical points by referring to Fig. 3.9a. As an example, let us consider the 2σ-truncated stroke centred in $P_i \in \tilde{L}$; let Q_1 and Q_2 be two generic points included in the boundaries of the stroke, which are

potential critical points. The inclusion principle requires that $\|Q_j - P_i\| \leq R_{2\sigma}$, where $R_{2\sigma}$ is the radius of the 2σ-truncated stroke.

these are painted by different strokes. Specifically, whereas Q_1 is painted solely by the stroke originating by the EE placed in P_i, Q_2 is instead painted additionally by strokes centred in P_{i+1} and P_{i+n} as well, (note: here, n is an arbitrary number ≥ 2). The algorithm has to decide which one is (more) critical. In order to comply with this, it has to calculate the saturation velocity $I^{'}(Q_1) = I_1^{'}$ and $I^{'}(Q_2) = I_2^{'}$ and the distance $\Delta I_{grey,1}$ and $\Delta I_{grey,2}$ at point Q_1 and Q_2, following Eq. 3.1 and 3.2.

At this point it can finally calculate the time necessary to reach $I_{grey,target}(Q_j)$ at points Q_1 and Q_2, as follows,

$$\tau_j = \tau(Q_j) = \frac{I_{grey,j}}{\sum_i (I^{'}(Q_j, P_i))}. \tag{3.4}$$

The selected critical point will then be $Q_{\text{sel}} = Q_j$, where Q_j is the point with the lowest time, i.e. $\tau_j = min(\tau_1, \tau_2)$. Note that the calculation of τ_j is carried out for *every* point Q_j included in the boundaries of the 2σ-truncated stroke centred in P_i, thereby extending the reasoning explicated for points Q_1 and Q_2. It follows logically that Q_{sel} will belong to the stroke area of effect.

In other words, the algorithm calculates the time each point in the considered boundaries will require to reach grey over-painting, and selects the one with the lowest time. This is marked as a global critical point.

Operatively, this process is carried out by calculating the convolution C of the path $\tilde{L}$ with respect to the stroke of the spray-gun, as follows,

$$C(\xi_1, \xi_2) = \sum_{\zeta_1=-\infty}^{+\infty} \sum_{\zeta_2=-\infty}^{+\infty} S(\zeta_1, \zeta_2)\, L(\xi_1 - \zeta_1, \xi_2 - \zeta_2), \tag{3.5}$$

where, ξ_1 and ξ_2 indicate respectively the column and row of the generic ITI, and S is the already defined stroke characteristic, with ζ_1 and ζ_2 coordinates. The convolution C essentially maps the intensity per time values, that is to say, the saturation velocity $I^{'}(Q_j, P_i)$, where $Q_{i,j}$ is the collection of all the points or pixels contained in the ITI. Note that C is the same for each point of the path L. In practical terms, C resembles a stroke that follows the tool-path $\tilde{L}$.

Finally, by solving Eq. 3.4 the algorithm is able to determine the timing map (τ_j) and thus select the relevant $Q_{sel,j}$, which is finally labeled as a global critical point $K_{\eta,global}$.

3.4.4.2 Local critical points

The selection process for *local* critical points is similar. The difference lies in the different way the intensity velocity map $I^{'}(Q_j, P_i)$ is defined. In this case, in Eq. 3.5, the term $\tilde{L}$ is replaced by the term $\tilde{L}^{'}$, which is function of the point P_i we are considering. To clarify, let us consider point P_i; the matrix originating from term $\tilde{L}^{'}$, in this case, will be equal to a matrix of zeroes with the only non-zero value corresponding to point P_i. The convolution will result in a single stroke centred in that point. The points that are being determined are thus labelled $K_{\eta,local}$.

3.4.4.3 Speed During Critical Points Selection

It is worth noting that in this phase we assume the tool-path $\tilde{L}$ to have a prescribed constant speed of arbitrary value.

3.4.5 Critical Points: selection

In this phase, inside a general layer, a pair of $K_{\eta,local,i}$ and $K_{\eta,global,i}$ critical points are determined for each point P_i of the tool-path $\tilde{L}$. The methodology prescribes that for each pair, only one is selected and the other is discarded. In order to comply with this, a LS containing both objects is assembled and preliminarily solved using OLS. For each point, the algorithm compares the value resulting from the convolution of S along $\tilde{L}$ (that is, the simulation of the painting process with the speed-profile resulting from the OLS LS's solution), and selects the point which shows the larger deviation from the target value defined in the ITI. This process is contextually carried out for all points $P_i \in \tilde{L}$; the result is a collection of K_η points, which is equal in number to points P_i.

It's worth to note that this computationally intensive 2-step process is necessary and propædeutical for the iterative phase, which will be illustrated in the following section.

3.4.6 Iterative Refinement

This last phase consists in the adaptive iterator used to refine the results of the process described in the previous sections. The main objective is to drastically limit over-painting and grey over-painting inconsistencies. The procedure is laid down in the following:

i. Definition and selection of critical points K_η,

ii. Assembly of the LS and solution with OLS,

iii. Analysis of the results and identification of over-paint areas (OPAs),

iv. Determination of the points P_i which associated critical point K_η is contained in an OPA,

v. 5% Reduction of the LS's known term B associated to all points P_i determined in the previous step,

vi. Addition of one line in the LS relative to the most over-painted pixel in each OPA.

vii. Iteration of steps ii–vi, until one of the following termination conditions are reached:

- No more OPAs are detected.
- The maximum number of iterations is reached (this is an arbitrary parameter).
- The global over-painting effect (GOP) increases, which leads to divergence.

The GOP is defined as the cumulative sum of all over-painted pixels in the resulting image, when this is compared to the ITI.

3.5 A Practical Application

In this section we propose, as an example, a practical case based on the famous 1973 "Lena" standard test image [74]. In Fig. 3.10a the actual 800×800 pixels image at a resolution of 1 pixel/mm is presented. For the test we used 3 progressively decreasing

Figure 3.10: The target image, the "Lena" standard test image [74].

distances, which translated into the following stroke diameters and relative layers: layer 1, 81 pixels; layer 2, 27 pixels; layer 3, 9 pixels. The shape of the stroke profile was approximated as a 2σ-truncated Gaussian curve. The "intensity" of the paint flow was assumed as 0.3 $^{I}/_{s}$, where $I \in [0, 1]$ is the intensity of the image. For the intensity, a global tolerance of $I_{\text{tol}} = {}^{1}/_{255}$ was used in the algorithm. A speed limit of 1 $^{m}/_{s}$ was imposed to the *timing algorithm*.

In Fig. 3.11 we show the results of the *path planner* block for each iteration and sub-iteration. It can be seen that the smaller the size of the stroke gets, the smaller the distance between the offsets gets, and the higher the number. This translates into quite long computation and execution times.

Furthermore, one can see that the plots in Fig. 3.11*a*, *c* and *e* are, in general, more packed. This is due to the fact that these are sub-iteration steps, and do not need to carry out much work in order to complete the corresponding layer.

The OLS method (*timing algorithm*) highlighted in Fig. 3.6 computes the time that the nozzle should rest over each point of the generated tool-path L. This easily translates into a speed profile, as shown in Fig. 3.12. Note that the speed remains always under 1 $^{m}/_{s}$, as prescribed.

Finally, in Fig. 3.13 is illustrated the progressive cumulative result after each of the tool-paths shown in the corresponding letter in Fig. 3.11 was fed into the *post-processing*

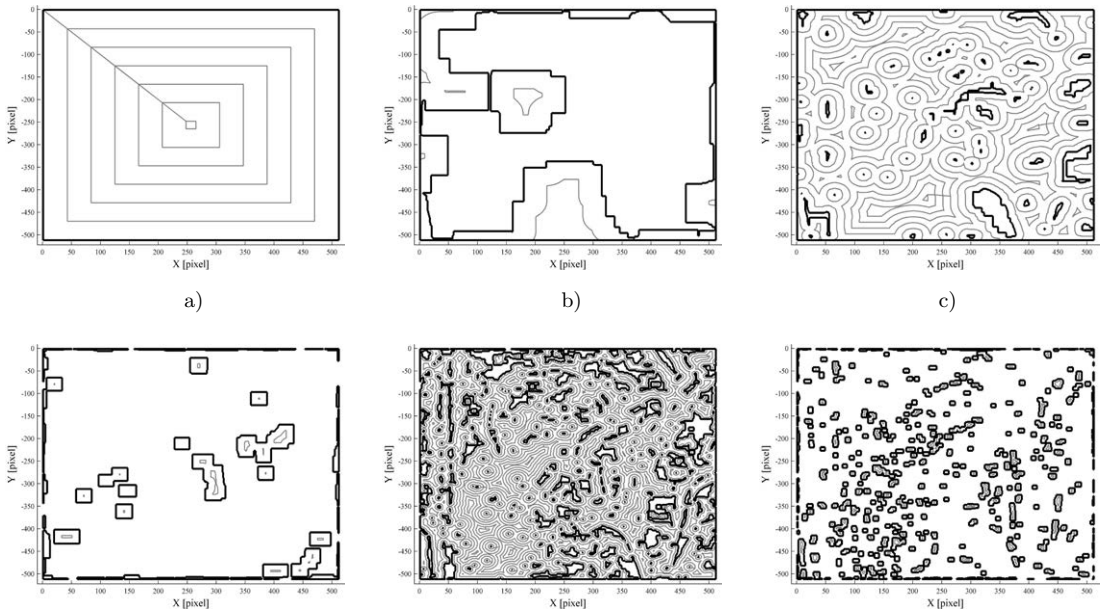

Figure 3.11: Tool-paths generated via Voronoi diagram and offset computation by the *path planner* algorithm; the area to be painted is shown with a solid black contour, whereas the tool-paths L are in grey. Since the general algorithm performs some sub-iterations, some of the steps presented in this figure belong to the same layer. In fact, *a)* and *b)* are relative to *Layer 1*, c) and d) to *Layer 2*, and *e)*, *f)* to *Layer 3*.

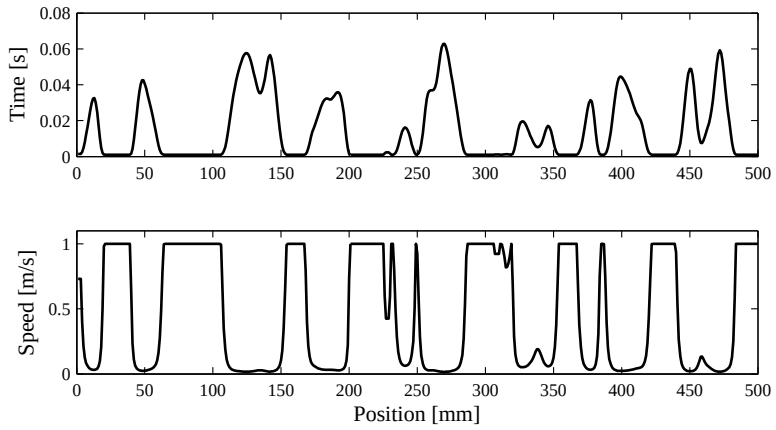

Figure 3.12: Timing and Speed profile of the tool-path generated by the *timing algorithm*. This is a partial result from the tool-path in Fig. 3.11a limited to the first 500 *mm*.

block, along with the stroke parameters, the tool-path and the speed profile.

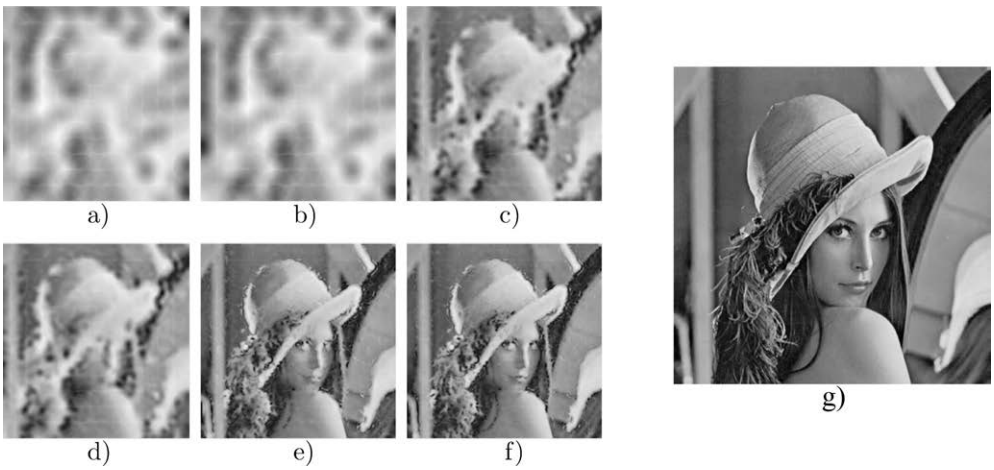

Figure 3.13: Progress of the output image at completion of the various layers. *a)* and *b)* are relative to the 1st and 2nd sub-iterations of *Layer 1*, *c)* and *d)* belong to *Layer 2* and *e)*, *f)* to *Layer 3*. Finally g) is the target image, which is here shown for comparison.

From the same figure one can immediately appreciate that the difference between the pairs *a*-*b*, *c*-*d* and *e*-*f* is not very significant; this is due to the sparseness of the sub-iterations tool-paths (which *b*, *d* and *f* are indeed). Nevertheless, the final output image (Fig. 3.13f) is very close to the target image (Fig. 3.13g), despite of the limitation of the number of iterations.

The time required for the robot to complete the painting was calculated using the speed-profile and resulted in 2692 s. Moreover, an estimate can be computed of the time that a Cartesian printer-like methodology would require completing the same painting with a similar resolution. Assuming that this Cartesian printer performs as our robot does when at the nearest distance from the canvas (smallest stroke size), the resulting execution time is 15251 s, more than 5 times the one needed by the proposed approach.

3.6 Conclusion

The proposed methodology provides an efficient solution to perform photographically realistic paintings of digital images on large surfaces by means of a robotic system like an industrial spray-painting robot. The developed method promises to outperform

normal printer-based methods where the result does not require a very high degree of detail, both in terms of costs and of execution time.

A general framework for the characterization of the spray-gun's spray morphology was described, which consisted in the measurement of the paint density profile shape and the paint deposition ratio. Both these are critical to correctly operate with the presented algorithm.

This innovative approach promises several applications in the field of industrial and artistic spray-painting, allowing the complete automation of tasks previously limited to the world of craftsmanship or assisted robotics.

Important steps should be made in the future to further refine the methodology, especially in the field of optimization (tool-path, timing, etc.) and in the actual control of the robotic system (i.e. maximum acceleration control).

4

Design and Actuation of LWRs

Robots with large workspaces have unique requirements for what concerns their design and actuation. Being mass a major variable in these systems, as from the definition in Eq. 1.1, some assumptions must be made. For example, special kinds of actuators should be considered, as opposed to traditional ones already widely employed in industrial practice. These, for example, should have a very large elongation ratio, or stroke, with limited weight and bulk dimensions.

The actuation of large and light structures is a topic that has had only marginal interest. In the usual industrial practice, robotised systems are bulky and heavy, for they are designed to operate in a highly accurate and reliable way. One can argue, on the other hand, that the tasks traditionally associated to robotics simply all fall in this class of problems.

Aside from the matters relative to hardware, the geometry of these systems is a most important aspect. Modularity or collaborative robotics are ways to address the issues associated with LWRs, in the sense that they allow large systems to be assembled without relying on a single support structure.

Being able to define a design and analysis paradigm for LWR means also to discover which technologies are best to tackle the challenges that arise, rather than trusting blindly what traditional practice, with ordinary industrial robots, have taught us. For this reason, in the following, a series of technologies and design modalities are explored that could contribute heavily in defining the overall paradigm for LWRs.

In particular, attention is focused on three distinct aspects. The first deals with actuators that are based on thin, light, deployable structures, called STEMs (Storable

Tubular Extendible Members); they provide immense strokes while keeping a compact size. Secondly, another kind of actuators are shown, this time exploiting cable systems, and specifically variable radius drums (VRD); linear actuators can be synthesized by exploiting these mechanisms. Finally, the third topic revolves around a deployable, modular cable robot, for use during exploration on planetary bodies.

4.1 STEM-based Parallel Robot

The purpose of this section is to present an innovative type of robot [75] that unites the concept of vertical planar cable parallel robot to the concept of Storable Tubular Extendible Members, or STEMs. In the following, these two distinct aspects of the research will be covered fully.

In the field of Robotics, two general sets of robots exist: parallel and serial manipulators. Parallel manipulators are robots which are constituted by a number of links arranged in parallel; the synchronized motion of these links produces the desired motion of the end-effector. Serial manipulators, on the other hand, are robots where the links are arranged serially. In general, parallel manipulators tend to be lightweight, stiff and accurate, while the biggest disadvantage normally consists in a small workspace and limited manipulability indexes inside its envelope; serial robots, instead, tend to be heavy and less stiff, leading to less accurate positioning and motion, while, on the other hand producing larger workspaces and considerably higher manipulability indexes.

In fact, in the realm of the industry, serial robots find applications virtually everywhere, from welding, to assembly, from inspection to handling; conversely, parallel robots, in view of their small workspace and limited flexibility are seldom used, showing a good spread in few areas, notably pick-and-place tasks.

A peculiar type of parallel robot is the Cable Direct Driven Robot (CDDR), or Cable Driven Parallel Robot (CDPR). This class of machines is characterized by a system of cables that supports and manoeuvres the end-effector. A general description is given by Lamaury et al. [76]. Many variations exist in literature; Gallina et al. [4] show a possible application of CDDRs to haptic interfaces; Tadokoro et al. [3] employ a 3D parallel CDDR for a virtual acceleration base; furthermore, Albus et al. [14] describe the NIST (National Institute of Standards and Technology) *Robocrane* setup which exploits a CDDR and Campbell et al. [77] show a cable robot for space and

terrestrial applications. Another popular example is *SkyCam* [78], a robotic camera system widely used in stadiums around the world.

As Williams et. al [79, 80] point out, the CDDR's major advantage lies in the fact that, since their primary structure is made out of lightweight, high load-bearing cables, the resulting system can be lighter, safer, stiffer, and more economical than traditional parallel robots. Additionally, the workspace can be much larger. Furthermore, as Trevisani et al. [10] remark, a peculiar benefit of some of these robots is the fact that they efficiently exploit gravity to keep their correct configuration; in fact, gravity can be made to act on the mechanism in the same way a cable pulling towards the ground would.

On the other hand, as the very same Trevisani [11], Williams [79, 80] and Pigani [81] et al. point out, these features are achieved through often severe limitations in manipulability; in fact their manipulability indexes vary considerably inside the boundaries of their reachable, kinematic or dynamic workspace. The reason for this behaviour lies chiefly in the inability of cables to sustain compressive loads; this ultimately translates in the major constraint that some degree of positive tension must be present in the cables at all times. When gravity stabilized robots are considered [10, 78, 82, 83], this has the effect of causing the end-effector to be unable to deliver downwards forces other than its own weight, thus greatly limiting practical applications.

For the same inability with compression loads, dynamics can be a big problem. In fact, one of the strong points of parallel robots in general is speed. Their structure is generally very light compared to serial manipulators, which makes them prone to high accelerations. The problem with CDPRs based on gravity is that very high speeds of actuation generally induce rebounds and require time to decelerate in order to avoid the cables loosing tension. This has greatly detrimental effects on the speed of the overall system.

In the present case, we focus on a subset of these robots: *planar vertical CDDRs*. For example, Pigani et al. [81] describe a vertical planar CDDR robot to be used in industrial spray-painting processes; these types of robots tend to have an additional drawback, which is out-of-plane instability. As Pigani [81] and Trevisani [10] et al. point out, the structure of these robots does not explicitly constrain the end-effector in the direction orthogonal to the workspace plane; this invariably causes some degree of out-of-plane sag. Some solutions are given by these authors, in form of passive

serial manipulators applied to a state-of-the-art planar vertical CDDR. These, however, present some drawbacks as well; the workspace can become irregular as a consequence of adding a complex system on top of the robot, and the overall inertia is inevitably bound to increase by much.

The planar parallel 2-d.o.f. robot that is proposed takes advantage from the CDDR's structure, while at the same time exploiting a special type of actuator in place of the cables, to increase the workspace and the manipulability indexes, and to increase stability along the normal to the workspace plane, thus avoiding out-of-plane motions. This actuator is based on the Storable Tubular Extendible Members (STEM) technology first described by Groskopfs in his patent [84]. A STEM is a type of component which is based on two distinct concepts. The first is the structural stability and stiffness of a curved sheet of material, albeit thin. In fact, thin sheets generally tend to offer low stiffness values when compression or bending is concerned. In the case of STEM, this is overcome thanks to the increase in the area moment due to the curving nature of the thin section; this is the same concept which is applied with hollow tubes, which the extendible STEM mimics. The second aspect is that, by using thin sheets the structure can be un-bent and rolled up. An illustration of the STEM founding concepts is shown in Fig. 4.1.

Normally these type of structures are used in the aerospace and space industry; they are exploited in deployable booms and masts aboard space-faring apparati [85, 86]. Typical uses regard deployment of solar panels, large antennae and detectors. Another less common use is for artificial satellite gravity-gradient stabilization [87].

Commercially available STEMs are made in a variety of materials, from stainless steel, to composite materials like carbon, glass or kevlar fiber. Mono- and multi-layered polymeric STEMs exist. In general the structure is made to be bi-stable by imprinting it with internal tensions that work towards this goal.

A few examples of similar applications that regard actuators are available in literature, for example Blanchard et al. [88] exploit spread-bands actuators for deployable telescopes; similarly, Aridon et al. [89] show a deployable Steward-Gough platform for space applications, as do Guinot et al. [90]. However it is generally not a common solution, especially in the field of planar robots.

As for the evaluation of the robot, we perform a kinematics and workspace analysis based on the concept of polytopes [91]. Some examples of kinematics for a CDPR are

given by Trevisani et al. [10, 11] and Bahrami et al. [7]. A workspace analysis done via a polytope formulation was carried out by Gallina et al. [92]. Several other examples of CDPR kinematics and workspace evaluation are present in literature [8, 9, 12].

In the following sections the robot is described, a mathematical model is produced to the extent of evaluating the manipulability indexes of the system and a prototype is described and presented. In order to evaluate the performance of the robot, a methodology is described to analyse the maximum force that the end-effector is capable of delivering in a given direction. Finally, some results are illustrated and discussed.

4.1.1 Robot description

As stated, the proposed planar robot is constituted by a pair of STEM structures which, combined, are manoeuvred to drive the end-effector. The STEM actuators (see Fig. 4.2a) are linked to the frame by means of a revolute joint; two actuators are used to extend the STEMs and an additional one is made to actively drive one revolute joint. Indeed, there is an actuation redundancy, since the system uses 3 actuators for 2 d.o.f; this serves to the purpose of removing the singularity which would otherwise be present

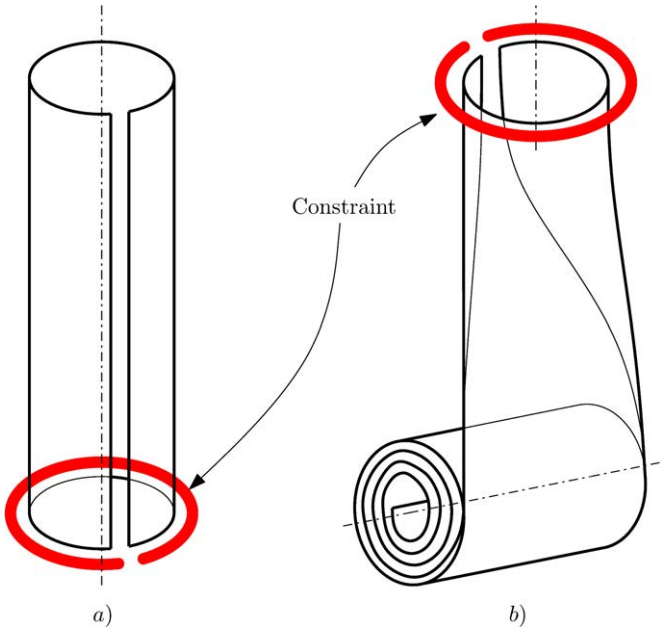

Figure 4.1: Storable Tubular extendible Member (STEM). In a) the extended structure is visible, whereas in b) the folded or rolled-up configuration is shown. The constraint shown in the figure shows the "connection" of the structure in a) and in b).

when the 2 links are co-linear. In the prototype, the actuators drive the STEM via a friction puller driven by a NEMA17 stepper motor.

In order to experimentally evaluate the performance of the proposed robot, a prototype of a STEM actuator was built, and is shown in Fig. 4.3b. The STEM is kept rigidly in place thanks to a set of low-friction Polytetrafluoroethylene (PTFE) guides. Their free extremities are equipped with a pressure cap, which provides a no-warp constraint to the structure. The spool which stores the sheet is driven by a passive spring mechanism. This is necessary since this specific STEM model is not bi-stable, and thus requires a certain effort to be kept rolled up. Ultimately this can easily be addressed by using a bi-stable structure. The STEM is made of a narrow band of polyethylene terephthalate (PET), which was thermoformed at 160 °C for 5 hours, to the desired tubular shape.

Contrary to state-of-the-art materials for STEMs, we used PET thanks to its availability. In particular we used a camera film as the sheet.

The robot prototype is shown in Fig. 4.2. Note that the layout of the two links is staggered; this is to increase the workspace area of the robot. In fact, where the links aligned, collisions would happen in every configuration where the end-effector was to be aligned to the joints, with the exception of the area included between the joints themselves. This solution is expected to cause a certain moment in the links, but should not appreciably increase out-of-plane instability or the structural integrity of the system, while at the same time greatly increasing the workspace.

In the following sections the kinematics and structural model of the proposed robot will be covered, and the methodology for its evaluation will be defined as well.

4.1.2 Kinematics analysis

The kinematics of the system is similar in some aspects to some planar CDDR geometries. By looking at Fig. 4.4 one can appreciate a schematic diagram of the 2 d.o.f. over-actuated planar robot.

Given the position of the revolute joints $\mathbf{H}_1$ and $\mathbf{H}_2$ in respect to the frame of reference $\mathbf{O}$, we can define the position of the end-effector E in function of the geometrical parameters and a pair of independent coordinates, i.e. (l_2, ψ_2). In fact this problem is

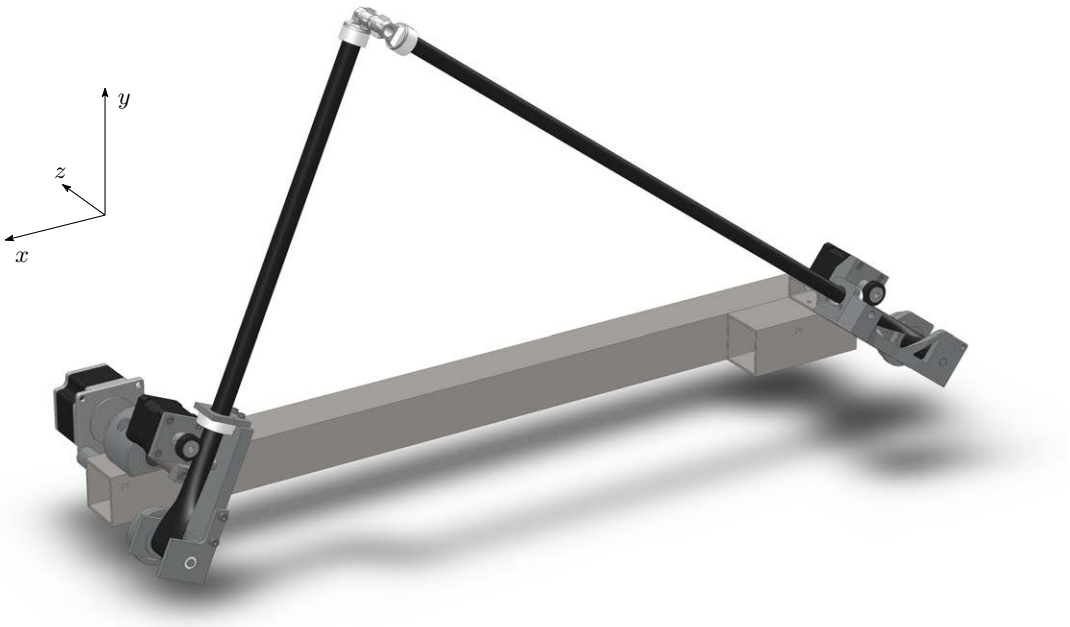

a)

b)

Figure 4.2: The 3D model of the planar STEM parallel 2 d.o.f. robot. In a) the active revolute joint is visible on the left. In b) a side-view shows the staggered layout of the links.

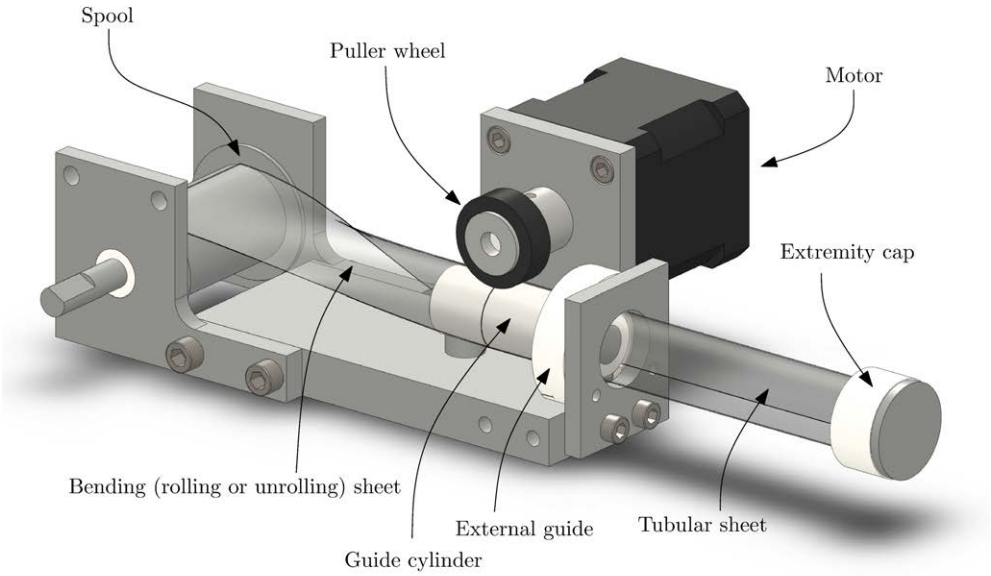

a)

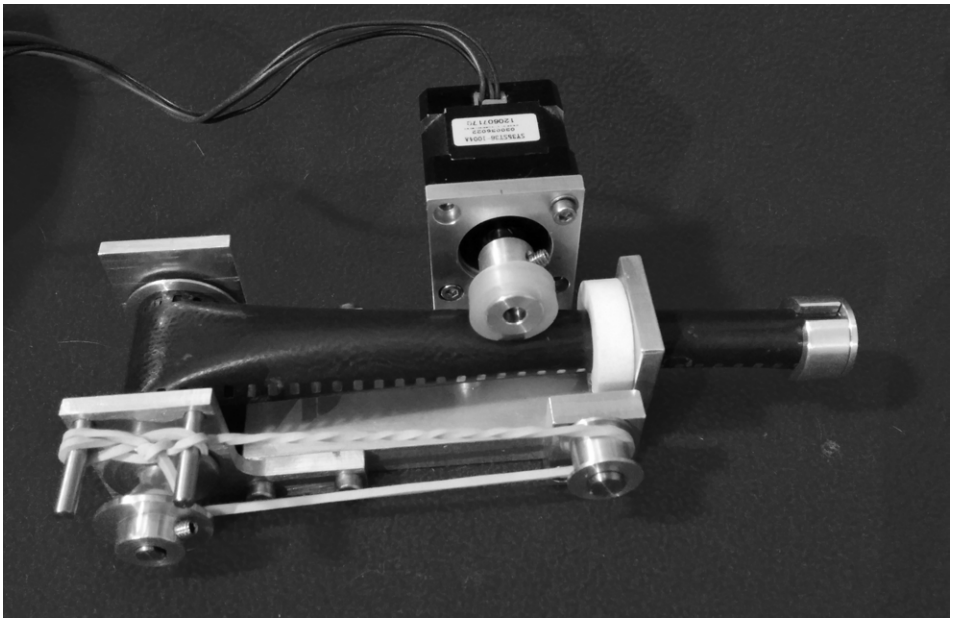

b)

Figure 4.3: A STEM actuator. In a) we can see a 3D model of the actuator, whereas in b) the actual prototype is shown. The tubular sheet is aligned and guided by a PTFE guide cylinder and external guide. A stepper motor provides motion to the sheet by means of a friction puller wheel. The sheet is rolled up on a spool which is driven by a passive spring mechanism (shown in b, in a temporary version).

over-actuated. As already pointed out we have 3 actuators and 2 d.o.f., which translates in the fact that, provided that the two independent coordinates are given, the third (i.e. l_1) follows as a combination of the first two:

$$l_1 = f(l_2, \psi_2). \tag{4.1}$$

The direct kinematics equation is,

$$\mathbf{E} = \mathbf{H}_2 + l_2\hat{\mathbf{l}}_2 \ = \mathbf{H}_2 + l_2 \begin{bmatrix} \cos\psi_2 \\ \sin\psi_2 \end{bmatrix}. \tag{4.2}$$

Conversely, the inverse kinematics equations are as follows,

$$\begin{cases} l_2 &= \|\mathbf{E} - \mathbf{H_2}\| \\ l_1 &= \|\mathbf{E} - \mathbf{H_1}\| \ = \sqrt{\left(H_{2,x} - H_{1,x} + l_2\cos\left(\psi_2\right)\right)^2 + \left(H_{2,y} - H_{1,y} + l_2\sin\left(\psi_2\right)\right)^2} \end{cases}. \tag{4.3}$$

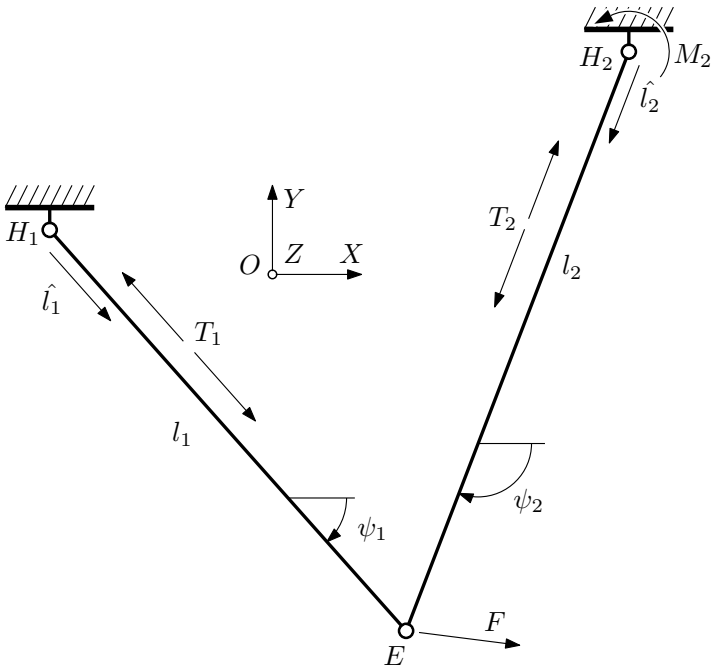

Figure 4.4: The 3D model of the planar STEM parallel 2 d.o.f. robot. In a) the active revolute joint (A_2) is visible on the left. In b) a side-view shows the staggered layout of the links.

and, as for the orientation of the second link,

$$\psi_2 = \text{atan2}\left(\hat{\mathbf{l}}_2 \bullet \mathbf{Y}\ ,\ \hat{\mathbf{l}}_2 \bullet \mathbf{X}\right). \tag{4.4}$$

4.1.3 Structural Model

In order to validate and analyse the performance of the proposed robot, we define a structural model. In the following sections we will break up the model in a series of separate considerations, for clarity.

The first section will cover the asymmetrical effects that are related to the structures STEMs are part of. Afterwards, in the following section it will be reported on the finite element model that is used to model the links. Furthermore, the third section will present a criterion for maximum applied loads. Along the same lines, the fourth section will illustrate the methodology for the out-of-plane stiffness analysis. Finally, an experimental evaluation of asymmetrical bending is presented.

4.1.3.1 Asymmetrical effects

Being the STEM a longitudinally cut cylinder with single-axis section symmetry, similarly to a C-section, it is prone to strongly asymmetric bending and 3-dimensional secondary effects like torsion. This happens mainly when loaded along a non-symmetry plane, or when internal forces are present (e.g. localized heating). These phenomena are generally uncommon in beam-theory applications; in fact, in the majority of cases they are either not present or neglected.

In general, asymmetric bending can be modelised using De Saint-Venant (DSV) beam theory [93, 94], whereas secondary torsion cannot. Indeed, DSV beam theory does not consider the phenomenon known as restrained warping. Perhaps the best known attempt to successfully model this phenomenon is Vlasov torsion theory [95, 96].

In the case at hand, both asymmetric bending and torsion are present and non-negligible; in fact the magnitude of these effects can be compared to the simple bending deformation. However, since Vlasov theory can be very complex, a simplified numerical-empirical formulation based on DSV theory is illustrated and used in this research.

The starting point of the simplified DSV formulation is the fact that the C-section of the STEM, visible in Fig. 4.5, has one symmetry axis (axis $\mathbf{y}$); when a bending moment or force produces a deformation along this axis, the structure can be considered as a

DSV beam. In fact, the asymmetrical effects (deviated bending and torsion) are not present at all, or, more rigorously, they cancel each other out.

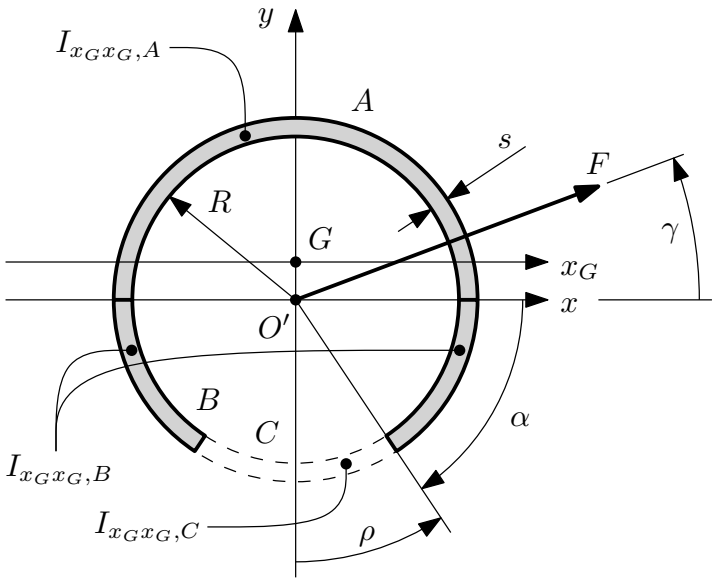

Figure 4.5: A generic cross-section of the structural part of the STEM. In the figure the origin O' is shown, along with the barycenter G and the main geometrical parameters, the internal radius R, the gap – or slit – angle ρ and the sheet thickness s. Letters A, B, C indicate the various parts of the section, which are used to calculate the area moments of inertia of the section, $I_{x_G x_G,A}$, $I_{x_G x_G,B}$ and $I_{x_G x_G C}$. Finally, γ denotes the angle between the x axis and the F force vector, which is applied on the origin O'.

The starting point is to define the static moment of inertia along the x_G axis; we will call this quantity $I_{x_G x_G}$. The following equation stands,

$$I_{x_G x_G} = I_{x_G x_G,A} + I_{x_G x_G,B}, \tag{4.5}$$

referring to the caption of Fig. 4.5 for the relevant definitions.

At this point, we can define,

$$I_{x_G x_G,B} = I_{x_G x_G,A} - I_{x_G x_G,C}, \tag{4.6}$$

thus having,

$$I_{x_G x_G} = 2I_{x_G x_G,A} + I_{x_G x_G,C}. \tag{4.7}$$

By applying Huygens-Steiner principle we can write,

$$I_{x_G x_G,A} = I_{xx,A} + A_A G_y^2, \tag{4.8}$$

where the following applies,

$$G_y = \frac{Rsin(\frac{\pi}{2} + \alpha)}{\left(\frac{\pi}{2} + \alpha\right)}. \tag{4.9}$$

Note that,

$$I_{xx,A} = \frac{\pi \mathrm{s} R^3}{2}. \tag{4.10}$$

Along the same line, as seen in Eq. 4.8, the following stands,

$$I_{x_G x_G,C} = I_{xx,C} + A_C G_y^2, \tag{4.11}$$

where, this time, the following applies,

$$I_{xx,C} = sR^3 \left(\rho + \frac{(\sin 2\rho)}{2}\right), \tag{4.12}$$

with $\rho = \frac{\pi}{2} - \alpha$.

The quantities A_A and A_C are the areas of the section's sub-sectors A and C respectively.

We define Δ as the general deflection on the STEM beam. As numerical investigations will show in the next sections, a linear relation exists between the values $\Delta_{\max}$ and $\Delta_{\min}$. We can assume that in the majority of practical implementations $\Delta_{\min}$is the deflection when the force vector loading the beam lies in the symmetry plane (along the y axis), i.e. $\Delta_{\min} = \Delta\,(\gamma = 0)$, whereas the $\Delta_{\max}$is relative to a force vector which is orthogonal to the previous, i.e. $\Delta_{\max} = \Delta\,(\gamma = 90)$. In order to allow an estimate of the structural behaviour outside symmetrical loading conditions, an experimental ratio was defined as $\mu_\Delta = \frac{\Delta_{\max}}{\Delta_{\min}}$, thus,

$$\Delta_{\max} = \mu_\Delta \Delta\,(\gamma = 0)\,. \tag{4.13}$$

4.1.3.2 Finite element model of the links

To evaluate the structural stiffness of the robot and the compliance of the end-effector, we produced a model based on a 2-element linear FE analysis. In fact, since the system is hyperstatic, this is a sensible option which can be scaled up in case other links were put into place in parallel to the existing one. Referring to Fig. 4.4, the model features a 2-d.o.f. translational constraint in the $\mathbf{H}_1$ node, and a 3-d.o.f. translational and rotational constraint in $\mathbf{H}_2$, to account for the active rotational drive of the $\mathbf{H}_2$ actuator. The FE model outputs the moment on node $\mathbf{H}_2$ and the reaction forces $\mathbf{R}_1$ and $\mathbf{R}_2$ on nodes $\mathbf{H}_1$ and $\mathbf{H}_2$, from which the tensions of the STEMs are computed as follows,

$$\begin{cases} T_1 = -\left(R_{1,X}\cos\psi_1 + R_{2,X}\sin\psi_1\right) \\ T_2 = -\left(R_{2,X}\cos\psi_2 + R_{2,Y}\sin\psi_2\right) \end{cases}. \tag{4.14}$$

Note that the moment on node $\mathbf{H}_2$ represents the maximum moment applied along link 2, which is, incidentally, the only one theoretically subject to bending stresses.

To operate the FE model we need to define some parameters of the structure, namely the cross-sectional static moment of inertia along the loaded axis and the cross-sectional area. The C-section of the STEM, visible in Fig. 4.5, is oriented so as to have its $\mathbf{y}$ axis lay in the robot's workspace plane (X, Y), and its $\mathbf{x}$ axis orthogonal to the same plane.

The cross-section has one symmetry axis (axis y); when a bending moment or force produces a deformation along this axis, the structure can be considered as a DSV beam. In fact, the asymmetrical effects are not present at all. This, along with the fact that the bending stiffness is maximum along the y axis of the cross-section, were paramount in the choice of the orientation of the links cross-section in respect to the robot structure. On the other hand this configuration leads to the structure being rather prone to out-of-plane instability.

4.1.3.3 Maximum admissible loads

Axial loads can be tensile or compressive. When the load is tensile, no instability occurs, and the maximum load is given by the ultimate tensile stress of the material

along with the minimum cross-sectional area; this is given by,

$$T_{\text{lim}} = \max\left(F_{\text{max,tensile}}\ ,\ F_{\text{max,puller}}\right), \tag{4.15}$$

where, if $\sigma_{\text{max}} = 80\ MPa$ is the maximum admissible stress of the PET (polyethylene terephthalate) used for the STEM, then,

$$F_{\text{max,tensile}} = \sigma_{\text{max}} A_{\text{cross - section}}, \tag{4.16}$$

and $F_{\text{max,puller}}$ is a parameter that expresses the maximum force that the puller wheel is capable to provide, considering both the power of the motor and the dragging friction force between the wheel and the STEM.

When, on the other hand, the load is compressive, structures like these are prone to an instability phenomenon called *buckling*. In this case we perform a simple analysis on the stability against a load directed along the **z** axis, sometimes called Euler buckling. The structure's lower part is fixed, whereas the upper is free; the load is applied on the barycentre **G** of the uppermost section. The buckling load F_{buckling} is given by the Euler formula, as follows,

$$F_{\text{buckling}} = \frac{\pi^2 E I_{min}}{4L^2}, \tag{4.17}$$

where L is either l_1 or l_2, E is the Young's module of elasticity for the STEM material, and I_{min} is the minimum static moment of inertia in the plane of the cross-section. In our case this coincides with $I_{x_G x_G}$.

The maximum axial load is thus given as follows,

$$C_{lim} = F_{\text{max,compressive}} = \min\left(F_{\text{buckling}},\ F_{\text{max,tensile}},\ F_{\text{max,puller}}\right), \tag{4.18}$$

Please note that here the absolute value of the various forces is considered.

From elasticity theory we learn that the maximum moment is related to the ultimate tensile stress σ_{max} in the following form,

$$M_{lim} = \frac{\sigma_{max} I_{x_G x_G}}{y_{max}}, \tag{4.19}$$

where y_{max} is the maximum distance along the **y** axis of the cross-section from the barycentre **G**.

4.1.3.4 Out-of-plane stiffness analysis

Given that the robot relies solely on the structural bending stiffness of the links to overcome out-of-plane motions of the end-effector, the model should account for this effect. A methodology is proposed, based on a classical linear Finite Element (FE) analysis of a STEM, along with experimental measurements on the actual structure. In Appendix C the complete FE investigation is reported. The model itself is based on a STEM beam (one of the links) which is completely constrained at the base and free on the other end. The load is applied along the **x** direction, on the free-end. Note that this load does not rest inside the symmetry plane of the cross section; as stated, this causes the presence of secondary torsion and bending.

It is important to specify that in the actual robot the free-end is not, in fact, free, but rather coupled via a revolute joint to the other link. However, by considering it free we place ourselves into a conservative position, since, in some cases, the free-end constraints tend to oppose warping and thus secondary torsion and deflection.

By exploiting the experimental relation in Eq. 4.13, we can evaluate the out-of-plane bending without complex analytical formulations.

From the out-of-plane deflection of the i-nth beam,

$$\Delta Z_i = \Delta x_i = \mu_\Delta \Delta y_i = \mu_\Delta \left(\frac{F l_i^3}{3 E I_{x_G x_G}} \right), \tag{4.20}$$

we can write the equivalent stiffness of the corresponding beam,

$$k_{Z,i} = \frac{F}{\Delta Z_i}. \tag{4.21}$$

Since the two beams are arranged in parallel we have that the total deflection of the system is,

$$\Delta Z_E = \frac{F}{k_{Z,eq}} = \frac{F}{k_{Z,1} + k_{Z,2}}, \tag{4.22}$$

which leads to the following relation,

$$\Delta Z_E = \frac{\mu_\Delta F}{3 E I_{x_G x_G} \left(\frac{1}{l_1^3} + \frac{1}{l_2^3} \right)}. \tag{4.23}$$

A graphical summary of one single case of the analysis is visible in Fig. 4.6, as an example; the mesh and deformed results are shown.

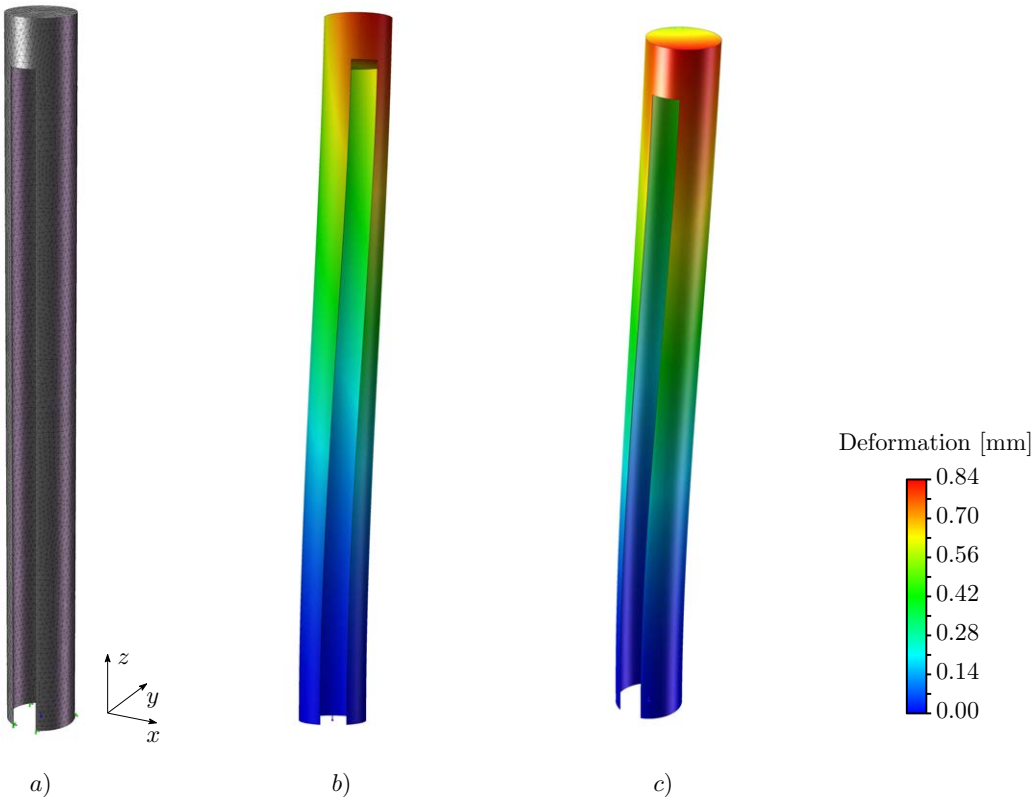

Figure 4.6: FE analysis of a STEM. In a) we show the mesh used in the case with parameters $L = 140\ mm$, $\rho = 23.37$ and $s = 0.15\ mm$. In b) and c) the deformed result is shown, with a 10x effect magnification on deformation. The load is at a 45° angle in respect to the **y** axis.

The complete aggregated results of the FE analysis are shown graphically and Fig. 4.7; it is apparent that the deflection value increases the more the load vector gets closer to being parallel to the **y** axis, that is, the more it gets orthogonal to the symmetry plane of the STEM. The maximum deflection is located indeed at $\gamma = 90°$, as expected.

From the presented results, we can see that the FE analysis produces a deflection coefficient value of $\mu_\Delta = 1.5560 \pm 0.0735$ with measurements taken at a STEM length of 70, 140 and 210 mm, different thickness of the sheet ($s = 0.15,\ 0.225,\ 0.30\ mm$), and gap angular width ($\rho = 10,\ 23.37,\ 36.75$). Indeed, since the standard deviation is this small, the value appears to be very consistent against possible variations of the main geometrical parameters.

4.1.3.5 Experimental evaluation of asymmetrical bending

In this section, an experimental investigation is carried out to determine some of the properties of the STEM structure. In Appendix C a complete record about the investigation on the structure is reported. As was noted in Sec. 4.1.3.1, loading the STEM structure orthogonally to the symmetry plane (for example along the **x** axis), produces complex behaviours linked to constrained warping. This results in deflections and torsions which are not predictable with the theoretical ground work presented in this manuscript. In particular, we are interested in the deflection values along the **z** direction; for this purpose a simple experimental analysis was carried out on a prototype of STEM actuator (visible in Fig. 4.3b).

The experimental setup consists in a vertically mounted STEM actuator, which is loaded along the **z** direction, as visible in Figures 4.8 and 4.9; note that the Z axis corresponds to the **y** axis of the C-section. The structure is extended to a desired length and a 2-axis Cartesian system, equipped with a digital readout (with a nominal resolution of 0.01 mm), is used to measure its displacements (indicated by the ΔZ symbol in Fig. 4.9). The measurements are taken on the center $\mathbf{O}'$ of the uppermost section of the beam, which corresponds to point $\mathbf{P}_1$ in Fig. 4.8. The structural and geometrical main parameters of the STEM are shown in Table 4.1.

ID	s $[mm]$	α $[\,^\circ\,]$	L $[-]$	E $[MPa]$	F $[N]$
1			70		
2	0.15	53.25	140	3000	0.2
3			210		

Table 4.1: Structural and geometrical parameters of the experimental STEM setup

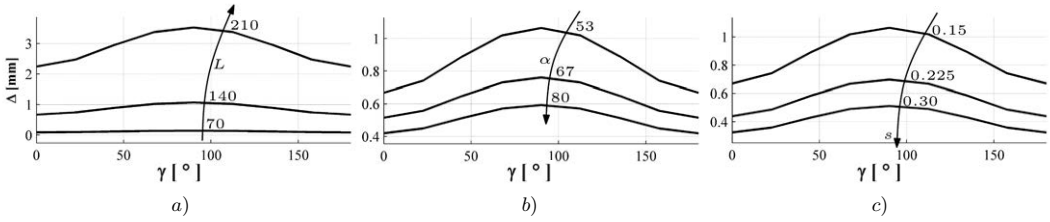

Figure 4.7: FE analysis results for deflection in function of parameters s, L and α. The angle γ defines the orientation in the x, y plane of the force vector in respect to the **y** axis.

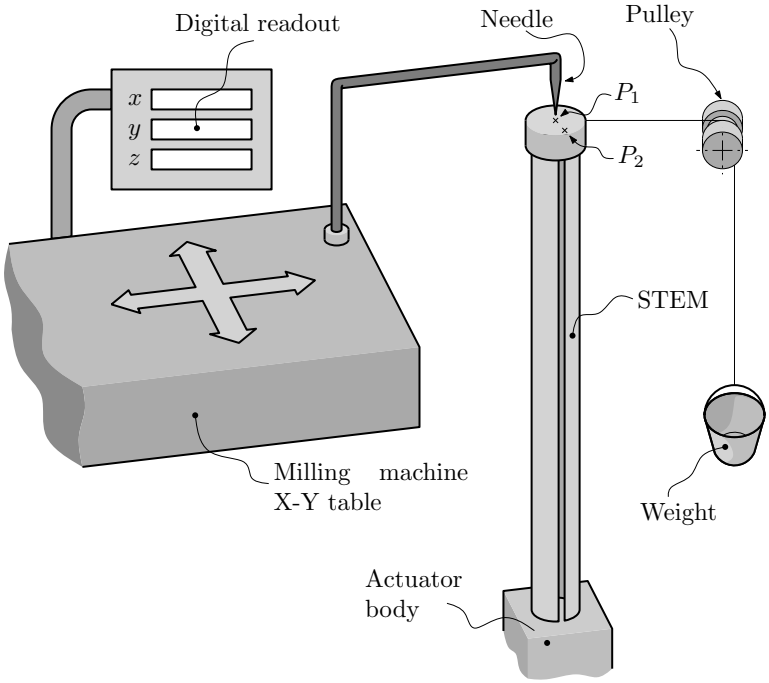

Figure 4.8: Experimental setup for asymmetrical bending.

Experimental evaluation show a value of $\mu_\Delta = 1.323 \pm 0.2413$, which is sufficiently in accordance with the value resulting from the FE analysis, shown in Sec. 4.1.3.2, corresponding to $\mu_\Delta = 1.5560 \pm 0.0735$; the two values differ by about 15%. The non-negligible difference between experimental and numerical results is largely due to a non-perfect constraint at the base of the STEM in the actuator prototype. In fact, since a certain degree of warp is allowed, the beam tends to behave more like a DSV beam, as opposed to an asymmetric bending beam with strong 3D secondary effects as is, nominally, our case. For the purpose of this work, in our simulations we considered the numerical value instead of the experimental one, since we deem appropriate to approach the problem in a conservative manner by selecting the worst case.

4.1.4 Manipulability Index and Workspace

In order to evaluate the performance of the robot, two indexes are defined: the maximum force that can be produced along every direction in the workspace plane, and the maximum admissible weight. Then an arbitrary envelope of the workspace is discretised and the indexes values along this surface are mapped. For the first index, this is done

thanks to polytopes computation [92]. Finally, we define a manipulability workspace by imposing an index threshold.

In order to define the first index, we introduce the concept of polytope in relation to our work case. Let us imagine, by referring to Fig. 4.4, to apply a load **F** to the end-effector **E**. By exploiting the FE model described in Sec. 4.1.3.2 and the buckling model in 4.1.3.3, from **F** we can compute the axial loads along the links (Eq. 4.14) and the maximum moment applied along link 2. At the same time, the maximum compression force given by buckling (Eq. 4.15) and the maximum extension force given by simple normal stress (Eq. 4.18) can be computed. Normally, if $F_{\text{max,puller}}$ is disregarded, $F_{\text{max,extension}}$ tends to be orders of magnitude higher than $F_{\text{max,compression}}$; the latter, thus, generally dominates.

A scheme of a polytope is visible in Fig. 4.10. The polytope boundary is defined by n points, as follows,

$$\mathbf{F}_{max,1},\ \ldots,\ \mathbf{F}_{max,j}\ ,\ \mathbf{F}_{max,j+1}\ ,\ \ldots,\ \mathbf{F}_{max,n}, \tag{4.24}$$

where the point $\mathbf{P}(x, y)$ is taken as the position of the end-effector. In our case this is obviously discretised in a certain number n of constant angular intervals. The F_{max} value is easily visualized as the radius of the largest circle (dashed line, in the figure), centred in **P**, that is completely contained in the polytope boundary. Note that this is the maximum force that the robot is guaranteed to withstand – or to exert – in every

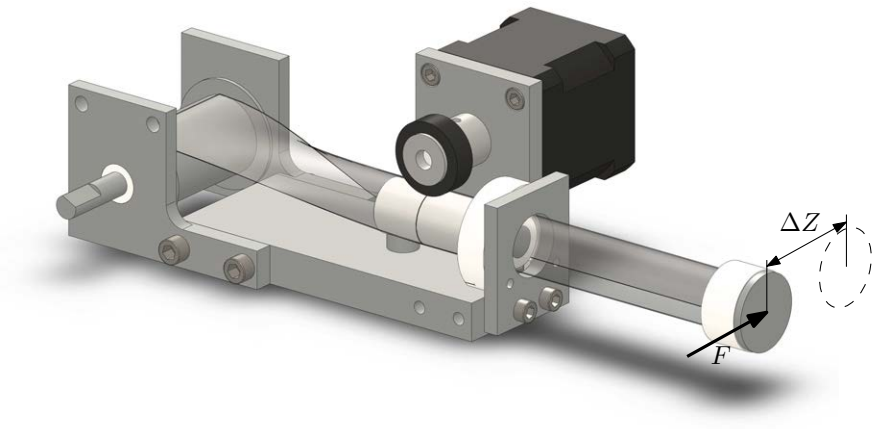

Figure 4.9: Asymmetrical bending measurement.

direction, not the maximum among the forces around the polytope. In fact, F_{max} is essentially the minimum value of those forces; this will be clarified in the following paragraphs.

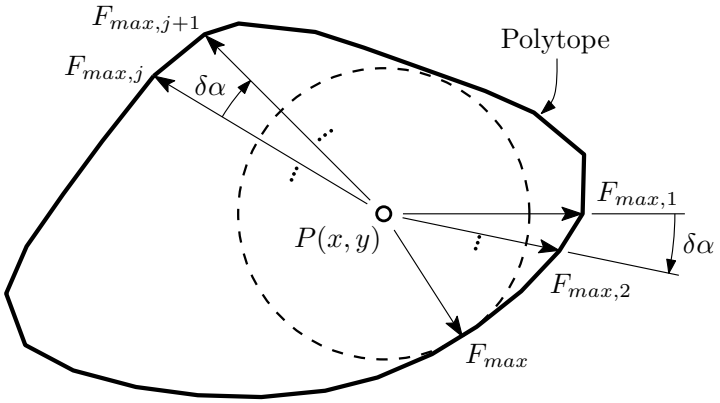

Figure 4.10: Polytope and $F_{\max}$ definition.

Firstly, it is necessary to define a failure ratio for the i^{th} link tensions and moment, as follows,

$$\begin{aligned} K_{T,fail,l_i} &= \begin{cases} \frac{T_i}{T_{lim}} & \text{if } T_i \geq 0 \text{ (compression)} \\ \frac{-T_i}{C_{lim}} & \text{if } T_i < 0 \text{ (tension)} \end{cases} \quad . \\ K_{M,fail} &= \frac{\|M_2\|}{M_{lim}} \end{aligned} \tag{4.25}$$

These values are essentially the tensile and moment loads on the structure which has been normalized in the $0-1$ interval; they are defined to allow the identification of the structurally dominant load type in a specific robot configuration.

In essence, when analysing the structure, we want to know what is the type of stress that is closer to the limit, and that is thus likely to cause a failure. The formalism presented in these paragraph serves to the purpose of normalizing – in a broad sense – the load level of the structure over the failure limits of each type of load. This ultimately allows the definition of a normalized ratio, which indicates how close to failure the structure *as a whole* is.

To exploit this in a quantitative and formal way, we define,

$$max_K = max(K_{T,fail,l_1},\ K_{T,fail,l_2},\ K_{M,fail}), \tag{4.26}$$

and we provide the following comparison chart,

$$\begin{cases} \text{if } \max_K = K_{T,fail,l_1} \\ \quad \implies L_{\text{dominant}} = |T_1| \ , \ L_{\text{lim,dominant}} = \begin{cases} T_{lim} & \text{if } T_i \geq 0 \text{ (compression)} \\ C_{lim} & \text{if } T_i < 0 \text{ (tension)} \end{cases} \\ \\ \text{if } \max_K = K_{T1,fail,l_2} \\ \quad \implies L_{\text{dominant}} = |T_2| \ , \ L_{\text{lim,dominant}} = \begin{cases} T_{lim} & \text{if } T_i \geq 0 \text{ (compression)} \\ C_{lim} & \text{if } T_i < 0 \text{ (tension)} \end{cases} \\ \\ \text{if } \max_K = K_{M,fail} \implies L_{\text{dominant}} = |M_2| \, , L_{\text{lim,dominant}} = M_{\text{lim}} \end{cases} . \tag{4.27}$$

This allows us to determine the quantities L_{dominant} and $L_{lim,dominant}$, which will serve to compute the value of $\mathbf{F}_{max,j}$ and ultimately F_{max}. The procedure to calculate the applicable $\mathbf{F}_{max,j}$ and F_{max} values in point $P(x, y)$, is summarized in these steps:

i. Impose an arbitrarily small $\|\mathbf{F}_j\|$ load to the FE model in a specified direction,

ii. Compute the normal tensions T_1, T_2 on the links and the moment M_2 at $\mathbf{H}_2$,

iii. Define the structural limits of the structure, T_{lim}, C_{lim} and M_{lim},

iv. Define a failure ratio for the links tensions ($K_{T,fail,l_1}$ and $K_{T,fail,l_2}$) and moment ($K_{M,fail}$),

v. Compare the failure ratios following the chart in Eq. 4.27,

vi. Calculate $\mathbf{F}_{max,j} = \mathbf{F}_j \left(\frac{L_{lim,\text{dominant}}}{L_{\text{dominant}}} \right)$,

vii. Repeat steps *i.* through *vi.* for $j = 1, \ldots, n$. This effectively builds the polytope.

viii. Finally, we can identify $F_{\max} = \min \left(\|\mathbf{F}_{max,j}\| \right)$.

Polytopes, as defined up to this point, are a very convenient methodology to represent the manipulability of robotic systems, serial or parallel indifferently. Once determined for a specific point in the workspace, it can be analysed and can offer a whole set of values or indices related to the force acting on the end-effector. This is analysed in the following sections.

4.1.5 Workspace Analysis and Results

In Fig. 4.11 we show an array of $\mathbf{F_{max,j}}$ polytopes in the surroundings of the robot's frame. This is computed following the outlined procedure with steps *i–vii*.

It is worth noting at this point that the workspace was evaluated without taking in consideration auto-collision events. In fact, as was already mentioned, the links are staggered; while this means that on one side the links can travel one on top of the other (right side looking at Fig. 4.2 on page 83), it leads to collisions happening on the other side. Indeed, the right link would definitely collide with the left joint assembly. This was not considered in the analysis because it goes beyond the scope of the research at this stage.

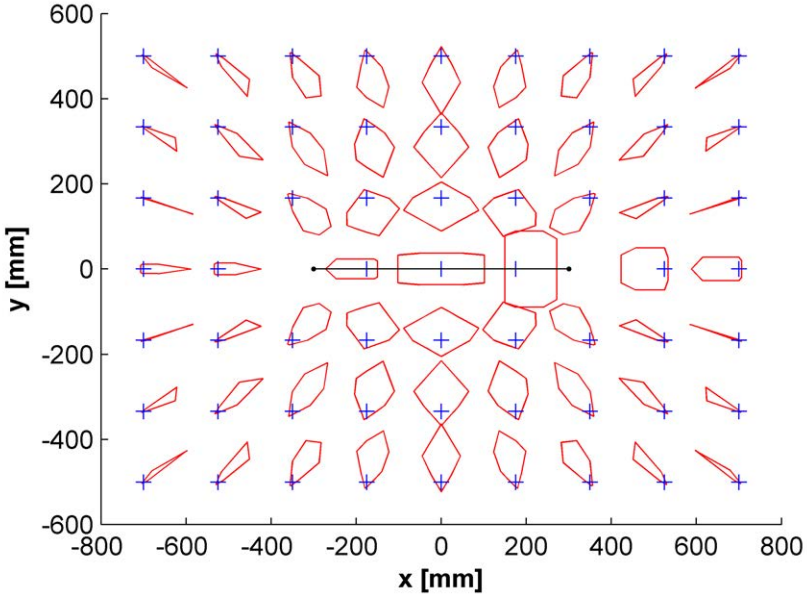

Figure 4.11: An array of workspace's load polytopes. These show the maximum force that the end-effector is capable to produce in each direction.

It is apparent that the load profiles represented by the polytopes are very unsymmetrical. This is primarily due to the great difference that exist between compressive and tensile maximum loads. This can reach 2 to 3 orders of magnitude in some points of the workspace. However, in the central range shown in the figure these are compara-

ble. Note that when talking about compressive loads, buckling tends to be the limiting factor, more than the compressive yield limit.

It is worth noting that the limits of actuation were not considered in this endeavour. With this term we indicate essentially two aspects; the potential slip of the puller wheel against the STEM when the force acts axially to the structure, and the yielding of the actuator on the rotation-active joint. In fact, we assume that the motors have enough torque and the friction force is sufficient as well, in order to avoid yielding.

Perhaps the most important fact is that the vertical load along the points at $Y = 0$ is non-null. This is entirely thanks to the rotation-active actuator; indeed, if both the links were rotation-passive, there would be a singularity at $y = 0$, and the admissible load in the vertical direction would be exactly zero. This peculiarity allows the robot to effectively double its workspace, by letting it travel across the singularity without having to exploit dynamic effects.

Dynamic effects are mentioned because, where the joint actuator not present, the only way to bridge the singularity-originated gap between the lower workspace and the upper one would be to exploit them. It is conceivable that the end-effector could travel through the singularity by accelerating upwards while in the lower workspace and letting inertia do the job of reaching the top workspace. It should be noted that the top-workspace is stable because it relies on the compressive strength of the links. By comparison, this is not possible with a CDPR.

4.1.5.1 Manipulability workspace

The manipulability workspace can be defined as the locus of end-effector points where the robot can apply a certain force of value $F_{\max}$ in all directions.

Remember that $F_{\max}$ is represented by the radius of the smallest circle centred in point **P** and completely included in the polytope. This is carried out by the *viii*$^{\text{th}}$ step described in Section 4.1.4 on page 94.

In Fig. 4.12a we present a contour plot of the $F_{\max}$ values in different points of the workspace, and in Fig. 4.12b a plot showing the workspace defined by a force threshold of 1 N. From this last plot in particular, it is apparent how the singularity does not appear, and the robot possesses a sufficient manipulability index to overcome the $y = 0$ level both between node $\mathbf{H_1}$ and $\mathbf{H_2}$ and in the region on the immediate right of node $\mathbf{H_2}$. This definitively proves that the robot has a connected large workspace.

It goes without saying that, depending on the force threshold level which is selected, the morphology of the workspace can change, even drastically. Indeed, by choosing an appropriately large force, the central part of the workspace could even disappear and lead to a non-connected workspace.

4.1.5.2 Maximum Admissible Weight

To evaluate the maximum weight $F_{max,weight}$ that the end-effector can withstand without the structure collapsing, the polytopes array described in Section 4.1.4 can be used. This is done by considering the maximum load directed along the $-\mathbf{y}$ direction, as follows,

$$F_{max,weight} = \max\left(\mathbf{F_{max,j}} \bullet (-\hat{\mathbf{y}})\right). \tag{4.28}$$

In Fig. 4.13a a contour plot of the maximum admissible weight is shown. It is apparent how the admissible weight is rather high in the lower region of the workspace, and low in the upper part. In fact, in the lower region the links are primarily tensioned, whereas in the upper part they tend to be compressed; the distribution in figure follows naturally, since normally $T_{\text{lim}} \gg C_{\text{lim}}$.

However, it is important to note that, in the middle region the singularity is non-existent, and the load level is non-null; the same is valid in the region on the immediate right side of node $\mathbf{H_2}$ (right node). This is consistent with what was expected from the polytope analysis.

4.1.5.3 Out-of-plane stiffness analysis

The out-of-plane stiffness level is an important result in the evaluation of the robot's workspace. In this section we will present a response surface of the z-translation $\Delta Z_{\mathbf{E}}$ of the end-effector E, when a nominal load of $F_{z,nominal} = 0.1\ N$ is applied transversally along the $\mathbf{Z}$ axis. Results are shown in Fig. 4.14, where a contour plot can be examined.

As expected, the contours grow towards an elliptic shape, with the distance from the robot's frame increases. Numerically, the values seem to remain sufficiently low even at a distance of 0.5 m, where, as a comparison, the frame width ($\overline{H_1H_2}$ segment) is 0.4 m.

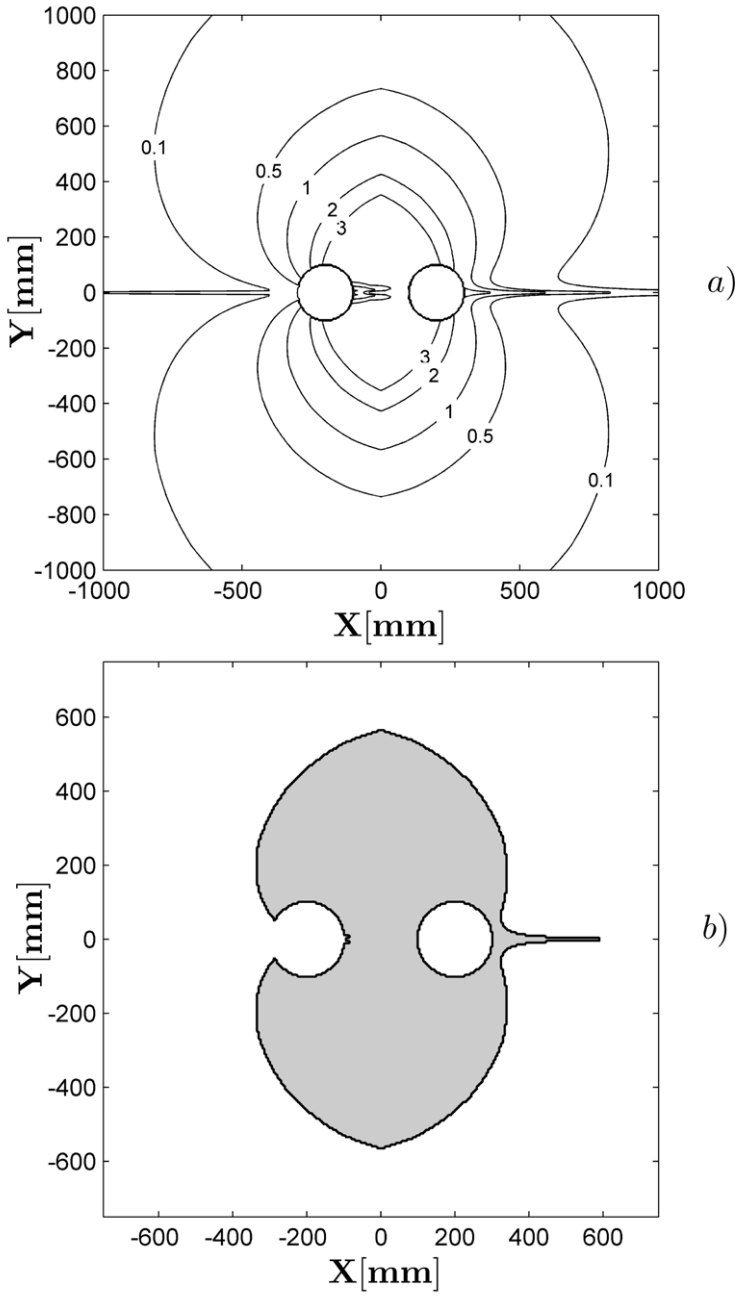

Figure 4.12: Manipulability index in the reachable workspace. In a) the contour plot is shown, with the maximum load which can be produced in all directions, whereas in b) a workspace with an all-direction load level of 1 N is shown.

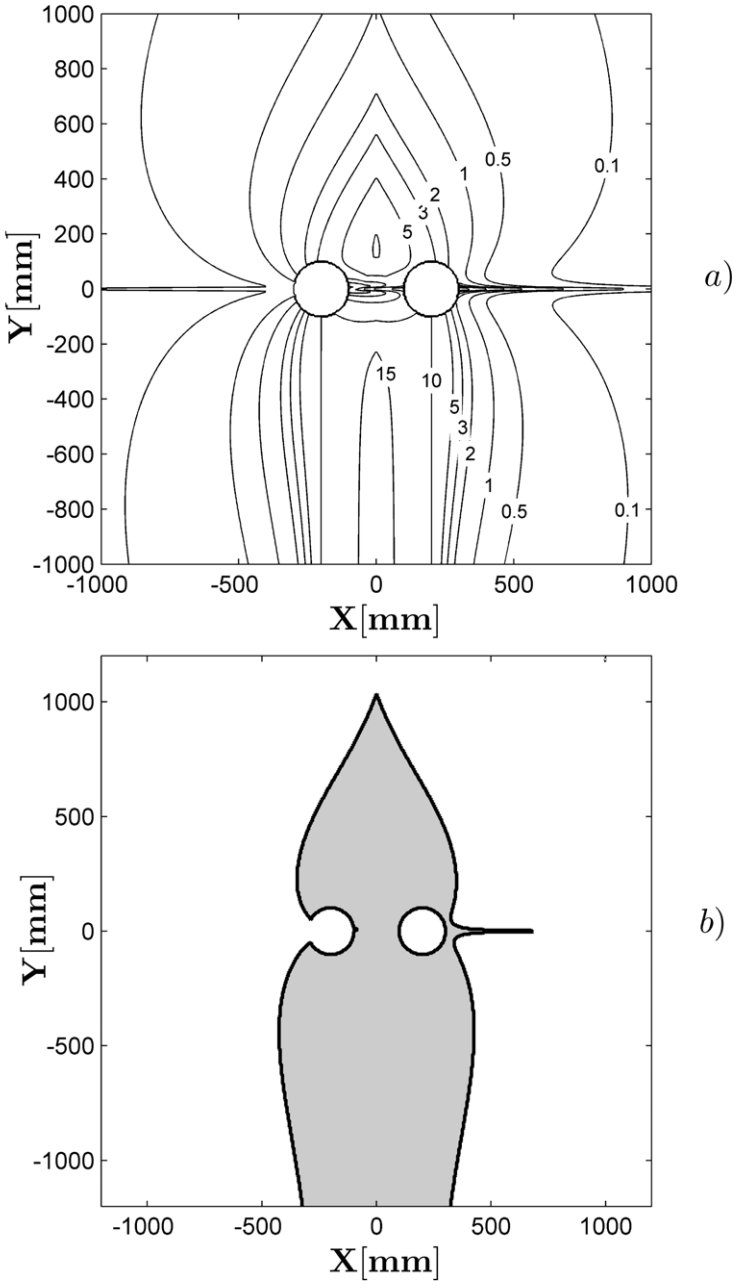

Figure 4.13: Admissible weight. In a) the contour plot of the admissible weight is shown, whereas in b) a workspace with a admissible weight of 1 N is shown.

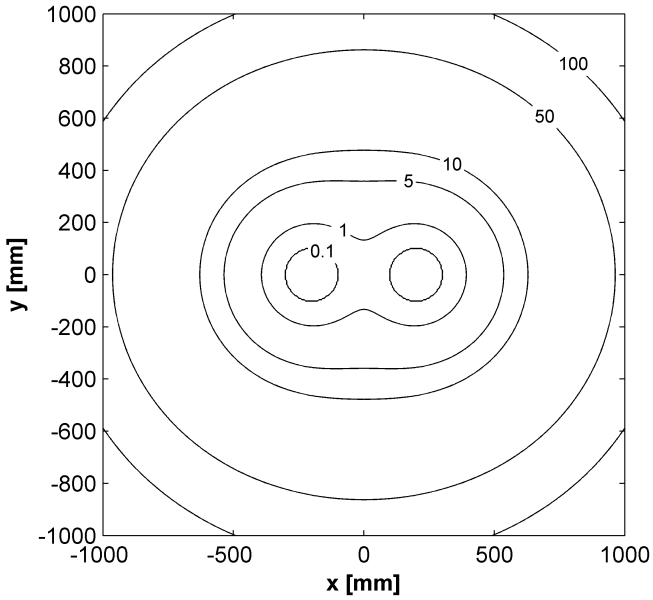

Figure 4.14: Out-of-plane stiffness response surface. Contour values are in mm. The applied force is $F_{z,nominal} = 0.1\ N$.

4.1.6 Conclusion

In this section an innovative type of 2-link, 2-d.o.f. planar parallel robot was presented, which uses a pair of STEM actuators as links. In order to evaluate the robot and aid in the design process a complete model was defined. The model takes advantages of analytical, numerical and even experimental investigations. The kinematic model that was produced in this study is closely based on CDDRs theory, the numerical part was carried out with a state-of-the-art FE solver, and the experimental investigation was performed on a prototype of one actuator which was built for the occasion. The evaluation phase was carried out by exploiting the concept of force polytope as an index of manipulability; maximum force in all direction, maximum admissible weight and out-of-plane stability were thus tested.

The resulting data shows that the robot has indeed a large connected workspace that responds well to all the key requirements. By comparing it to a planar CDDR, it shows remarkable improvement in the overall performance, while at the same time maintaining some of the cable robot's advantages like lightness, speed and a large workspace. Since, unlike cables, STEM links are able to deliver compressive loads, the robot easily allows the end-effector to travel beyond the height of the links anchor points; as said, this almost doubles the available workspace. In addition, still compared to CDDRs, this

system is much more independent from dynamic effects, thus the maximum speed and acceleration is higher in several sets of manoeuvres.

It is important to note that, by using state-of-the-art STEM structures, the performance of the robot could be increased in most aspects by several orders of magnitude.

4.2 Synthesis of VRDMs as actuators

As stated in this chapter heading, our objective is to design actuators with very large strokes and workspaces compared to the bulk and weight of the mechanism as a whole. In this section a novel technology is shown to allow this kind of actuators. It is based loosely on the concept of cable robots, and to a special kind of Variable Radius Drum (VRD). Combining these technologies gives birth to a mechanism (VRDM) [97] that can effectively be used as an actuator in larger mechanisms or robots.

In particular, this actuator can be used as the main axis of a overhead crane. In general, these structures are immovable or need to be built onto the base structure, e.g. a warehouse, depot or industrial plant.

In the next sections a complete analytical formulation of the problem is illustrated, and an example of linear actuator is shown. Furthermore, the linear actuator concept is exploited in the design of a novel kind of overhead crane.

Figure 4.15: An industrial state-of-the art overhead crane. Image credits *Demag Cranes AG*.

4.2.1 State of the Art

A drum is an elementary mechanical system that has been used throughout history in numerous applications. Also known as spool, in its simplest form it consists of a spindle with flanges, around which a cable is wound. The cylindrical surface of an ordinary drum has a constant radius [98].

A winch [99] is a typical device which employs an ordinary drum. It essentially consists of a movable drum around which a cable is wound so that rotation of the drum produces a drawing force at the end of the cable. Winches are normally equipped with a ratchet wheel and a pawl to prevent slippage of the load [100].

Drums are essential mechanical elements in hoist cranes. A hoist crane is mounted so as to be movable (as in a travelling crane). Winches and hoists are widely used in cargo handling, e.g., in ships, factories, and warehouses, and also function as the power unit in derricks [101, 102], power cranes, and power shovels. All the drums employed in these applications have a constant radius.

While traditionally the drum is used in application where little to no control or accuracy is needed, there have been some development in precise movement and position control applications [98, 100, 103, 104].

In this research we introduce the concept of Variable Radius Drum (VRD), a mechanical element consisting in a drum where the radius varies along its profile. As the VRD rotates of an angle α, the cable is released or wound. The length of the released (or wound) cable can be expressed by a non-linear relationship $g = g(\alpha)$, which is affected by the VRD's profile.

VRDs, with respect to constant radius drums, present the following advantages:

- It is possible to define a specific profile shape of the VRD in order to obtain the desired target relationship $g = g(\alpha)$. Note that in an ordinary drum of radius r, the released cable is given by the linear relationship $g = \alpha\, r$.

- It is possible to define a specific profile shape in order to modify the value of the torque generated by the cable on the VRD. In this case, in literature, VRDs are often referred to as Variable Radius Pulleys [105].

A Variable Radius Drum Mechanism (VRDM) is a mechanism (i.e. a linkage mechanism, or a cable-driven mechanism) which contains at least one VRD.

In literature, some examples of VRD have been studied and employed.

Shin et. al. [105, 106] combined pneumatic artificial muscles (PAMs) in a Muscle-based Antagonistic Actuation System. A pair of PAMs are connected antagonistically via a VRD to generate a bidirectional torque. The produced torque is the result of difference in applied muscle forces on each side of the VRD. The VRD has been synthesized in order to adjust the torque produced at every VRD angular position.

Tidwell et al. illustrated a synthesis methodology of the so-called wrapping cams [107], mechanisms used to generate non-linear torques or forces. Kilic et al. used the same concept to design an adjustable stiffness mechanism for use in prosthetics [108]. A non-linear rotational spring mechanism was developed by Schmit et al. following a similar methodology [109]. Furthermore, Kim et al. proposed a non-constant radius pulley for antagonistic springs [110] which are validated through gravity compensation both of an inverted pendulum and a 2-link robotic arm.

Okada proposed a mechanism with non-circular pulleys and springs for an inner pipe inspection robot to generate uniform contact forces on pipe surfaces [111]. Endo et al. and Ulrich et al. employed VRDs and linear springs to achieve passive gravity compensation [112, 113]. Kljuno et al. [114] applied a VRD to the locomotion of a legged robot. The knee is activated by two cables. The objective of the VRD was to compensate for the difference in the cable length increase on one side and the cable length decrease on the other side of the corresponding joint.

A numerical algorithm was proposed to synthesize a pulley profile that improved the output torque of a shape memory alloy actuator [115]. Some developments in the field of mechanical transmissions have seen the application of pulleys with non-constant radii [116]. From a kinematic point of view, the problem of the VRD synthesis was previously approached on a particular case of rocker-belt mechanism [117].

In this section a general kinematic analysis of a VRD is carried out analytically. Moreover, the synthesis problem, which is related to the solution of a non-linear Volterra equation, is addressed and analytically solved. To the best of my knowledge, such a theory has never been presented in previous literature.

In order to show the practical benefits of VRDMs, the theory of synthesis is then applied to a real case consisting of a mechanism which can support and guide a load along a horizontal linear path, and that can be taken advantage of as a 1-d.o.f. linear actuator.

4.2.2 Kinematic Analysis of a VRD

Let us introduce the parameters involved in the kinematic analysis of a VRD. A simple sketch of a VRD is given by Fig. 4.16. The VRD is fixed to the frame in $\mathbf{O}$ by means of a revolute joint. On the right, an idler pulley is fixed to the frame at the point $\mathbf{P_b}$ by means of another revolute joint. One end of a cable is fixed to the end of the VRD profile at the point $\mathbf{F}$. Finally, the cable is wound around the VRD profile. In its initial condition, as in Fig. 4.16a, the cable leaves the VRD at the tangent point $\mathbf{P_t}$. Let us define $\mathbf{A}$ as that point coincident with $\mathbf{P_t}$ at the initial condition and integral to the VRD profile; as the VRD rotates, $\mathbf{A}$ rotates accordingly. The cable is then wound around the idler pulley; points $\mathbf{C_0}$ and $\mathbf{E}$ represent the tangent points of the cable with the idler pulley.

Dotted segment represents an angular marker fixed with respect to the frame of the VRD. α gives the angular position of the VRD with respect to the inertial reference frame. α is assumed positive when the VRD rotates clockwise.

The VRD is sketched in two different configurations, namely when $\alpha = 0$ (Fig. 4.16a) and when $\alpha > 0$ (Fig. 4.16b). Let us consider the two configurations separately.

a) $\alpha = 0$.

   The length of the free cable (not wound around the VRD) at the right of the VRD, from point $\mathbf{A}$ to point $\mathbf{P_0}$, is referred to as l_0. In other words, l_0 is the length of the free cable when the VRD is at its initial position $\alpha = 0$. l_0 is the sum of an arc and two segments, namely,

$$l_0 = \|\mathbf{AC_0}\| + \overset{\frown}{\mathbf{C_0E}} + \|\mathbf{EP_0}\|. \tag{4.29}$$

   Let us assume that the system is in equilibrium, i.e. there exists a proper torque acting on the VRD along the counter-clockwise direction and a proper force pulling the cable in such a way that the mechanism is always balanced. For sake of simplicity equilibrium of forces is not considered.

b) The VRD has rotated clockwise of angle $\alpha > 0$.

   In this situation a segment of cable is wound around the VRD along the curved segment $\overset{\frown}{\mathbf{AP_t}}$. In the following, the symbol $\overset{\frown}{*}$ will be employed to address arcs

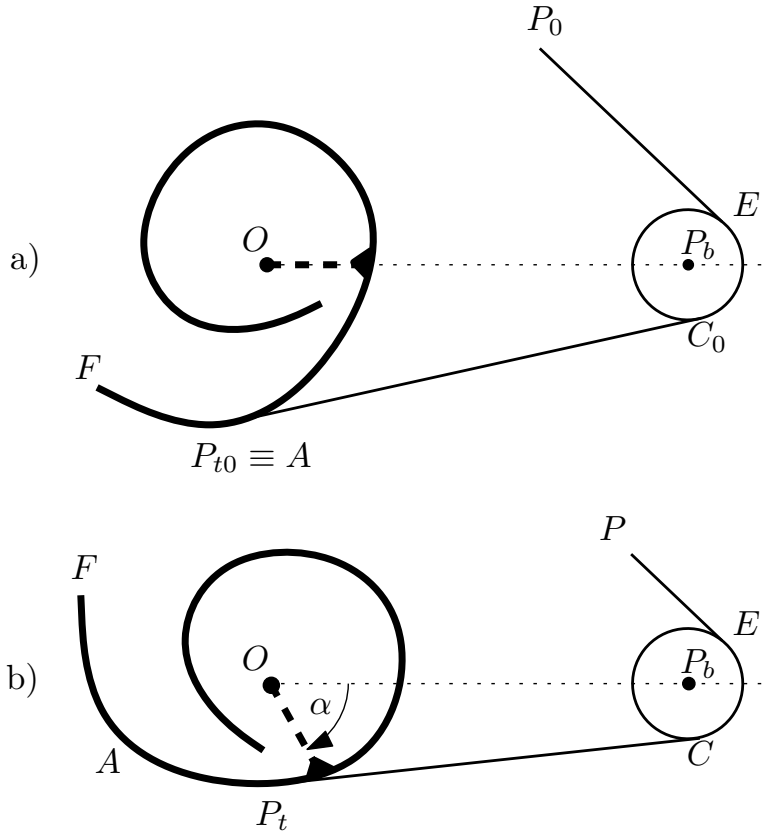

Figure 4.16: Sketch of a VRD

as well as curved VRD segments. The length of the segment of cable $\|\mathbf{PE}\|$ is a function of the angular position of the VRD and it depends on the shape of the VRD. It yields

$$\|\mathbf{P_tC}\| + \widehat{\mathbf{CE}} + \|\mathbf{EP}\| = l_0 - \widehat{\mathbf{AP_t}} \,. \tag{4.30}$$

Let us define,

$$g = g(\alpha) := \|\mathbf{EP_0}\| - \|\mathbf{EP}\|. \tag{4.31}$$

$g(\alpha)$ represents the cable wound by the VRD during its rotation. It is therefore a function of its angular position. Replacing Eq.s (4.29) and (4.30) into (4.31), it yields

$$g(\alpha) = (\|\mathbf{P_tC}\| - \|\mathbf{AC_0}\|) + \left(\widehat{\mathbf{CE}} - \widehat{\mathbf{C_0E}}\right) + \widehat{\mathbf{AP_t}} \,. \tag{4.32}$$

The equation emphasizes the contributions of the three addends: the difference between the segments of the cable tangent to the VRD and the idler pulley when $\alpha \neq 0$ and $\alpha > 0$; the difference between the arcs on the idler pulley when $\alpha \neq 0$ and $\alpha > 0$; and the curved profile of the VRD which has wound the cable. Note that $g(\alpha)$ contains neither $\|\mathbf{EP}\|$ nor $\|\mathbf{EP_0}\|$.

4.2.2.1 Direct Kinematic Analysis (DKA)

The problem of the DKA consists of calculating the relationship between the wound cable length function $g(\alpha)$ and the angular position of the VRD α, given the geometry of the VRD profile. Let us define $\phi = \phi(\alpha)$ the angle of the tangent point $\mathbf{P}_t$ measured with respect to the horizontal line (positive when clockwise).

The geometry of the profile of the VRD can be expressed in polar coordinates $\rho = \rho(\beta_r)$. The angle β_r is assumed positive if it rotates counter-clockwise with respect to the frame fixed to the VRD (relative reference frame).

The KDA can be carried out by calculating the integral of the VRD curve,

$$g(\alpha) = (\|\mathbf{P_tC}\| - \|\mathbf{AC_0}\|) + \left(\widehat{\mathbf{CE}} - \widehat{\mathbf{C_0E}}\right) + \int_{-\phi(0)}^{\alpha-\phi(\alpha)} \sqrt{\rho^2 + (d\rho/d\beta_r)^2}\, d\beta_r \quad . \tag{4.33}$$

Note that both the addends $(\|\mathbf{P_tC}\| - \|\mathbf{AC_0}\|)$ and $\left(\widehat{\mathbf{CE}} - \widehat{\mathbf{C_0E}}\right)$ are non-linear functions of the angular position of the VRD. Their computations depend on the function $\rho(\beta_r)$ and need to be analyzed case by case.

4.2.2.2 VRD Synthesis

As the VRD rotates clockwise, an observer on the drum sees the idler pulley rotating of the same angle in the opposite direction, as shown in Fig. 4.17. Unit vectors $\mathbf{x}$ and $\mathbf{y}$ define the absolute reference frame while unit vectors $\mathbf{X}$ and $\mathbf{Y}$ define the rotating (with respect to the VRD, of an angle α) reference frame fixed to the idler pulley center ($\mathbf{X}$ points $\mathbf{P}_b$). As a first approach to the problem, the idler pulley is assumed to be pointlike, that is to say, the associated radius is zero. c_d is the distance between the idler pulley center and the VRD center, l_t is the distance between the point $\mathbf{P}_t$ and the idler pulley center and γ is the angle between the segment $\mathbf{OP}_b$ and the minimum

distance between the cable and the VRD center. The goal of the synthesis consists of calculating the profile of the VRD, given the function $g = g(\alpha)$.

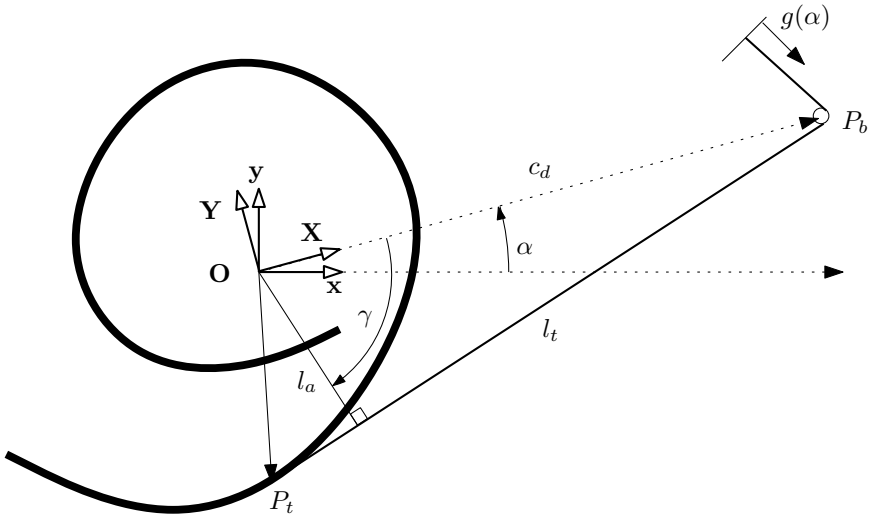

Figure 4.17: Geometric parameters associated to the VRD

Using a matrix notation and local coordinates, $\mathbf{P}_t$ can be expressed as a sum of vectors, the first one from the VRD center to the idler pulley $\left\{ \begin{array}{cc} c_d & 0 \end{array} \right\}^T$ and the second one from the idler pulley to the VRD profile $\left\{ \begin{array}{cc} l_t & 0 \end{array} \right\}^T$,

$$\mathbf{P}_t = \mathbf{T}(\alpha) \left\{ \begin{array}{c} c_d \\ 0 \end{array} \right\} + \mathbf{T}(\alpha)\,\mathbf{T}(-\gamma)\,\mathbf{T}\left(-\frac{\pi}{2}\right) \left\{ \begin{array}{c} l_t \\ 0 \end{array} \right\}, \tag{4.34}$$

where the operator $\mathbf{T}(x)$ represents the rotation matrix from two reference frames rotated of an angle x, namely,

$$\mathbf{T}(x) = \left[\begin{array}{cc} cos(x) & -sin(x) \\ sin(x) & cos(x) \end{array} \right]. \tag{4.35}$$

Note that,

$$\frac{d\mathbf{T}(x)}{dx} = \mathbf{T}\left(x + \frac{\pi}{2}\right). \tag{4.36}$$

The differentiation of Eq. (4.34) against the VRD rotating angle α, considering property (4.36), produces

$$\begin{aligned}\frac{d\mathbf{P}_t}{d\alpha} =& \frac{d\mathbf{T}(\alpha)}{d\alpha}\begin{Bmatrix} c_d \\ 0 \end{Bmatrix} + \frac{d\mathbf{T}(\alpha)}{d\alpha}\mathbf{T}(-\gamma)\,\mathbf{T}\left(-\frac{\pi}{2}\right)\begin{Bmatrix} l_t \\ 0 \end{Bmatrix} \\ & - \frac{d\gamma}{d\alpha}(\alpha)\frac{d\mathbf{T}(-\gamma)}{d(-\gamma)}\mathbf{T}(\alpha)\,\mathbf{T}\left(-\frac{\pi}{2}\right)\begin{Bmatrix} l_t \\ 0 \end{Bmatrix} \\ =& \mathbf{T}\left(\alpha+\frac{\pi}{2}\right)\begin{Bmatrix} c_d \\ 0 \end{Bmatrix} + \mathbf{T}(\alpha)\,\mathbf{T}(-\gamma)\begin{Bmatrix} l_t \\ 0 \end{Bmatrix} \\ & - \frac{d\gamma}{d\alpha}\mathbf{T}(\alpha)\,\mathbf{T}(-\gamma)\begin{Bmatrix} l_t \\ 0 \end{Bmatrix} \\ =& \mathbf{T}\left(\alpha+\frac{\pi}{2}\right)\begin{Bmatrix} c_d \\ 0 \end{Bmatrix} \\ & + \mathbf{T}(\alpha)\,\mathbf{T}(-\gamma)\left(1-\frac{d\gamma}{d\alpha}\right)\begin{Bmatrix} l_t \\ 0 \end{Bmatrix}\end{aligned} \quad . \tag{4.37}$$

The unit vector normal to VRD profile at the contact point $\mathbf{P}_t$ is,

$$\mathbf{n} = \mathbf{T}(\alpha)\,\mathbf{T}(-\gamma)\begin{Bmatrix} 1 \\ 0 \end{Bmatrix} \tag{4.38}$$

Since the vector $\frac{d\mathbf{P}_t}{d\alpha}$ must point at any time along the tangent line $\mathbf{P}_t\mathbf{P}_b$, it is normal to the unit vector $\mathbf{n}$. Orthogonality leads to the relationship,

$$\mathbf{n}^{\mathbf{T}}\frac{d\mathbf{P}_t}{d\alpha} = 0 \tag{4.39}$$

By replacing Eq.s (4.37) and (4.38) into (4.39), and using the property of orthogonal matrices $\mathbf{T}^T\mathbf{T} = \mathbf{I}$, one gets,

$$\begin{aligned}&\begin{Bmatrix} 1 & 0 \end{Bmatrix}\mathbf{T}^T(-\gamma)\,\mathbf{T}\left(\frac{\pi}{2}\right)\begin{Bmatrix} c_d \\ 0 \end{Bmatrix} + \\ &\left(1-\frac{d\gamma}{d\alpha}\right)\begin{Bmatrix} 1 & 0 \end{Bmatrix}\begin{Bmatrix} l_t \\ 0 \end{Bmatrix} = 0 \\ &c_d sin(-\gamma) + \left(1-\frac{d\gamma}{d\alpha}\right)l_t = 0\end{aligned} \quad . \tag{4.40}$$

On the other hand, the relationship between the unrolled cable length, the VRD rotation and the lever arm l_a is

$$l_a = \frac{dg}{d\alpha}. \tag{4.41}$$

From Fig. 4.17, it can be seen that,

$$c_d \cos(\gamma) = l_a, \tag{4.42}$$

and, by the previous relationship,

$$c_d \cos(\gamma) = \frac{dg}{d\alpha}. \tag{4.43}$$

Differentiating, and replacing $c_d \sin(\gamma) = \sqrt{{c_d}^2 - {l_a}^2}$, produces,

$$\frac{d\gamma}{d\alpha} = -\frac{\frac{d^2g}{d\alpha^2}}{\sqrt{{c_d}^2 - \left(\frac{dg}{d\alpha}\right)^2}}. \tag{4.44}$$

In conclusion, the VRD profile, in Cartesian coordinates, is given by Eq. (4.40), where,

$$l_t = \frac{c_d \sin\gamma}{1 + \frac{\frac{d^2g}{d\alpha^2}}{\sqrt{{c_d}^2 - \left(\frac{dg}{d\alpha}\right)^2}}}, \tag{4.45}$$

and,

$$\gamma = \cos^{-1}\left(\frac{1}{c_d}\frac{dg}{d\alpha}\right). \tag{4.46}$$

A necessary condition for the existence of a solution is the continuity of the function $g(\alpha)$ and its derivative. From Eq. (4.45), $\frac{dg}{d\alpha} < c_d$ has to hold. This last condition suggests that the idler pulley has to be located at proper distance with respect to the VRD; the higher is the slope of $g(\alpha)$, the higher the distance of the idler pulley from the VRD has to be.

4.2.2.3 VRD Synthesis without neglecting the radius of the idler pulley

Let us consider now the effect of the idler pulley radius r and the thickness of the cable $2f$ as shown in Fig. 4.18. Note that r includes the radius of the idler pulley plus half of

the cable thickness. In this case the VRD profile (similarly to Eq. (4.34)), is expressed by,

$$\begin{aligned}\mathbf{P}_t =&\mathbf{T}(\alpha)\left\{\begin{array}{c} c_d \\ 0 \end{array}\right\}+ \\ &\mathbf{T}(\alpha)\,\mathbf{T}(-\gamma)\,\mathbf{T}\left(-\frac{\pi}{2}\right)\left\{\begin{array}{c} l_t \\ 0 \end{array}\right\}+\chi(\alpha)\end{aligned}, \tag{4.47}$$

where,

$$\chi(\alpha)=\mathbf{T}(\alpha-\gamma)\left\{\begin{array}{c} r \\ 0 \end{array}\right\}-\mathbf{T}(-\gamma+\alpha)\left\{\begin{array}{c} f \\ 0 \end{array}\right\}. \tag{4.48}$$

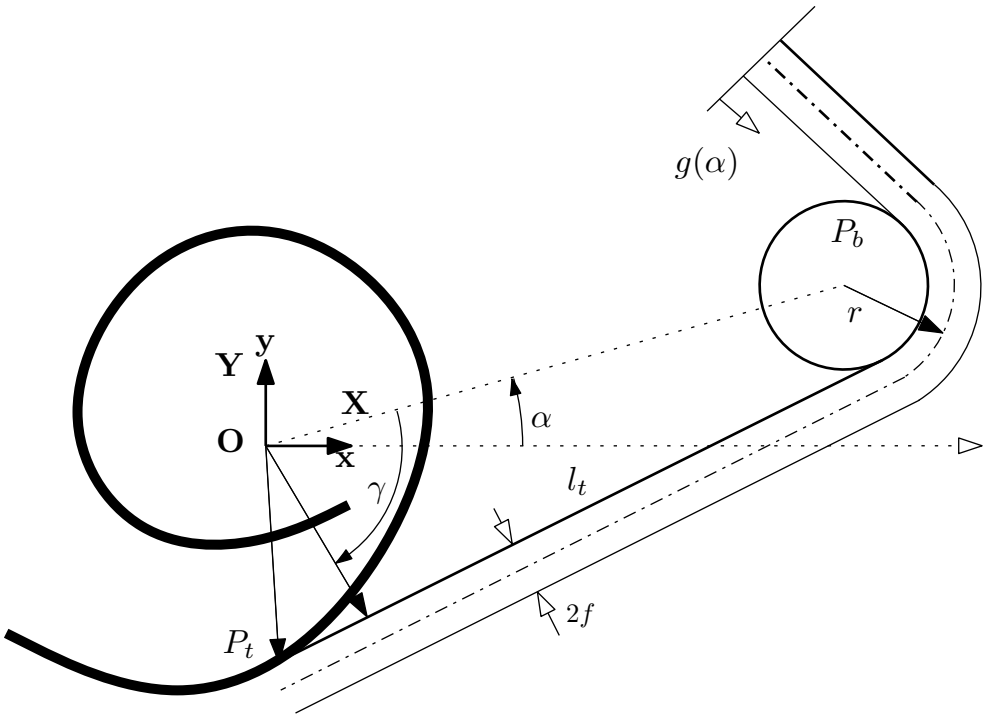

Figure 4.18: Geometric parameters associated to the VRD in case of a non pointlike idler pulley and cable with a thickness of $2f$.

The vector tangent to the profile in $\mathbf{P}_t$ is given by,

$$\begin{aligned}\frac{d\mathbf{P}_t}{d\alpha} =& \frac{d\mathbf{T}(\alpha)}{d\alpha}\begin{Bmatrix} c_d \\ 0 \end{Bmatrix} + \frac{d\mathbf{T}(\alpha)}{d\alpha}\mathbf{T}(-\gamma)\,\mathbf{T}\left(-\frac{\pi}{2}\right)\begin{Bmatrix} l_t \\ 0 \end{Bmatrix} + \\ & - \frac{d\gamma}{d\alpha}(\alpha)\mathbf{T}(\alpha)\frac{d\mathbf{T}(-\gamma)}{d(-\gamma)}\mathbf{T}\left(-\frac{\pi}{2}\right)\begin{Bmatrix} l_t \\ 0 \end{Bmatrix} + \frac{d\chi(\alpha)}{d\alpha} \\ =& \mathbf{T}\left(\alpha+\frac{\pi}{2}\right)\begin{Bmatrix} c_d \\ 0 \end{Bmatrix} + \\ & \mathbf{T}(\alpha)\,\mathbf{T}(-\gamma)\left(1-\frac{d\gamma}{d\alpha}\right)\begin{Bmatrix} l_t \\ 0 \end{Bmatrix} + \frac{d\chi(\alpha)}{d\alpha}\end{aligned}, \tag{4.49}$$

since,

$$\begin{aligned}\frac{d\chi(\alpha)}{d\alpha} =& \frac{d\mathbf{T}(\alpha-\gamma)}{d\alpha}\left(1-\frac{d\gamma}{d\alpha}\right)\begin{Bmatrix} r \\ 0 \end{Bmatrix} + \\ & - \frac{d\mathbf{T}(\alpha-\gamma)}{d\alpha}\left(1-\frac{d\gamma}{d\alpha}\right)\begin{Bmatrix} f \\ 0 \end{Bmatrix} \\ =& \mathbf{T}\left(\alpha-\gamma+\frac{\pi}{2}\right)\left(1-\frac{d\gamma}{d\alpha}\right)\begin{Bmatrix} r \\ 0 \end{Bmatrix} + \\ & \mathbf{T}\left(\alpha-\gamma+\frac{\pi}{2}\right)\left(1-\frac{d\gamma}{d\alpha}\right)\begin{Bmatrix} f \\ 0 \end{Bmatrix}\end{aligned}. \tag{4.50}$$

Note that Eq. (4.49) is equal to Eq. (4.37). Therefore, the orthogonality condition of Eq. (4.39) leads to the same results of Eq.s (4.45) and (4.46). In fact,

$$\mathbf{n}^{\mathbf{T}}\frac{d\chi(\alpha)}{d\alpha} = 0. \tag{4.51}$$

The following results,

$$l_t = \frac{c_d \sin\gamma}{1+\frac{\frac{d^2g}{d\alpha^2}}{\sqrt{{c_d}^2-\left(\frac{dg}{d\alpha}\right)^2}}}, \tag{4.52}$$

and

$$\gamma = \cos^{-1}\left(\frac{1}{c_d}\frac{dg}{d\alpha}\right). \tag{4.53}$$

In conclusion, the VRD profile, in Cartesian coordinates, is given by Eq. (4.47), combined with Eq.s (4.48), (4.52) and (4.53).

4.2.3 Design of a VRDM-based Overhead Crane

In this section, the VRDM theory is applied to a real problem: moving a load along a linear path, parallel to the x axis, employing just cables, a regular drum and a VRD.

Many applications exist where it is required to move a load in space trough a cable system. Sky-cams (or spider-cams) are cable-suspended and cable-maneuvered camera systems operating over a large area such as a stadium [21, 78]. Several cable suspended parallel robots have been studied and implemented [13, 118]. In a simplified scenario, moving a load along an horizontal linear path through cables could be useful as well, such as the case with short funicular railways, rope-way conveyors and overhead travelling cranes.

Let us consider conventional cable-driven systems that are planar, act in the vertical plane (x, y) and are subject to gravity; these are, in general, 2 degrees of freedom (DoFs) mechanisms. The configuration of these systems is in the form of a triangle, where the load is suspended through two cables between the respective motor-drums. Gravity is needed for the cables to be in tension. If a load is then required to be moved along a linear path that is, for example, parallel to the ground (while still in the (x, y) plane), the two actuators would normally need to be coordinated to achieve the desired trajectory of the point mass load. In other words, given the complex geometry, the path-planner module would need to act on the 2 DoFs of the system. The proposed mechanism is capable of reaching the same goal with just 1 DoF.

The schema of the proposed VRDM is shown in Fig. 4.19. The mechanism is capable of maintaining the load, represented by a little gray rectangle, horizontal by employing just pulling cables, pulleys and revolute joints. Note that no prismatic joints are required and neither are links.

The mechanism is made up of a constant radius drum (its radius is r_1) a VRD, two idler pulleys and the load. The load, at the point **L**, has mass m. The mechanism is located on a vertical plane. Therefore gravitational force is acting on the mass m. Two cables are connected at the point **L**. Cable thickness is assumed to be null. The green cable goes around the idler pulley on the right and is then wound around the constant radius drum (in green). The blue cable goes around the idler pulley on the left and is then wound around the VRD (blue). VRD and drum are connected one to the other (they have same angular position α). The idler pulleys (each one of radius r) are fixed

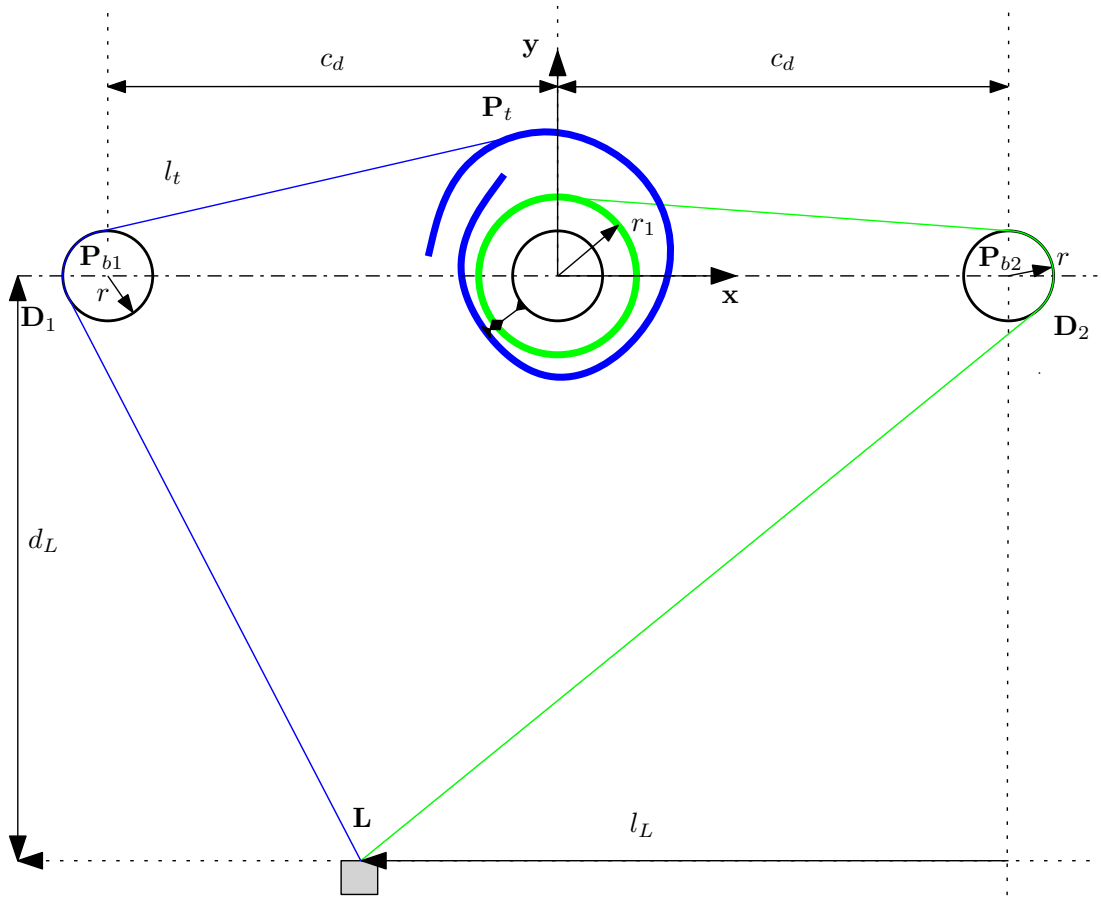

Figure 4.19: Sketch of a VRDM for horizontal motion.

to the point $\mathbf{P}_{b1}$ and $\mathbf{P}_{b2}$. The distance between the centres of the idler pulleys and the center of the VRD is c_d. The distance between the nominal horizontal linear path of the load and the x axis is d_L. l_L is the distance of the load from the vertical segment intersecting the point $\mathbf{P}_{b2}$.

Let us consider the mechanism in its initial condition, that is, when the load is on the right (Fig. 4.20a)): $\alpha = 0$ and $l_L = 0$. In this situation, the coordinates of point $\mathbf{L}$ are $\{c_d, -d_L\}^T$. As the drum/VRD rotates clockwise, a segment of the green cable is released and, at the same time, an other segment of blue cable is wound around the VRD profile.

If D_1 and D_2 are the tangency points formerly indicated with P_t, the input function

for the solution of the synthesis of the VRD profile is given by,

$$g(\alpha) = \mathbf{D}_1(0)\widehat{\mathbf{D}}_1(\alpha) + \left(\|\mathbf{L}(0) - \mathbf{D}_1(0)\| - \|\mathbf{L}(\alpha) - \mathbf{D}_1(\alpha)\|\right), \tag{4.54}$$

where,

$$\begin{aligned}\|\mathbf{L}(0) - \mathbf{D}_1(0)\| &= \sqrt{\|\mathbf{L}(0) - \mathbf{P}_{b1}\|^2 - r^2} \\ &= \sqrt{(2\,c_d)^2 + d_L^2 - r^2}\end{aligned}, \tag{4.55}$$

and

$$\|\mathbf{L}(\alpha) - \mathbf{D}_1(\alpha)\| = \sqrt{(2\,c_d - l_L(\alpha))^2 + d_L^2 - r^2}, \tag{4.56}$$

$l_L(\alpha)$ provides the relationship between the horizontal translation of the load and VRD rotation, namely

$$\begin{aligned}l_L(\alpha) &= \sqrt{\|\mathbf{L}(\alpha) - \mathbf{P}_{b2}\|^2 - d_L^2} \\ &= \sqrt{\|\mathbf{L}(\alpha) - \mathbf{D}_2(\alpha)\|^2 + r^2 - d_L^2}\end{aligned}, \tag{4.57}$$

where,

$$\begin{aligned}\|\mathbf{L}(\alpha) - \mathbf{D}_2(\alpha)\ | &= \|\mathbf{L}(0) - \mathbf{D}_2(0)\| + r_1\,\alpha - \mathbf{D}_2(0)\widehat{\mathbf{D}}_2(\alpha) \\ &= \sqrt{d_L^2 - r^2} + r_1\,\alpha - \mathbf{D}_2(0)\widehat{\mathbf{D}}_2(\alpha)\end{aligned}. \tag{4.58}$$

In the following, the arcs $\mathbf{D}_1(0)\widehat{\mathbf{D}}_1(\alpha)$ and $\mathbf{D}_2(0)\widehat{\mathbf{D}}_2(\alpha)$ are assumed to be null. Eventually, by backwards replacing all the terms into Eq. (4.54), one obtains the analytical input function to be exploited in the synthesis.

Table 4.2 shows the values of the geometrical parameters used in the synthesis.

Table 4.2: Values of parameters employed for the synthesis of the horizontal moving mechanism. Values are expressed in m.

r	r_1	c_d	d_L
0.05	0.2	1.3	1.1

Function $g(\alpha)$ provided by Eq. (4.54) has been derived numerically. The profile of the VRD, given by the calculation of $\mathbf{P}_t$ Eq. (4.47), is traced in blue in Fig. 4.20.

The four subfigures show the VRDM kinematic configurations for 4 different values of α. Fig. 4.21 shows the plot of the derivative $ds/d\alpha$ versus α. Note that the maximum value of the derivative is always lower than c_d ($c_d = 1.3m$).

4.2.4 Prototype experimental evaluation

It is important to note that the manufacturability of the VRD is a critical aspect, since the shape of the drum belongs to that general class of objects which surfaces can be loosely considered free-form in nature. In this section we report the fabrication of a working prototype by using a FDM approach, which copes well with these type of geometries.

The prototype itself is built against the case of horizontal motion described in Sec. 4.2.3.

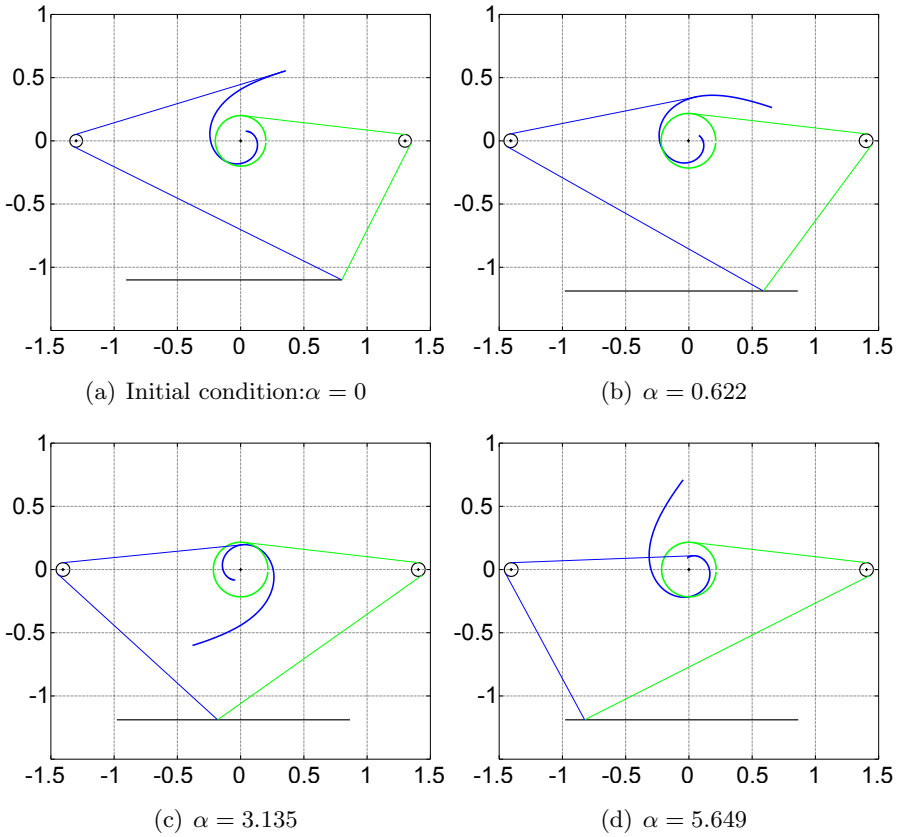

(a) Initial condition:$\alpha = 0$ (b) $\alpha = 0.622$

(c) $\alpha = 3.135$ (d) $\alpha = 5.649$

Figure 4.20: Kinematics configurations for the VRDM at different α values.

A schematic of the experimental setup is illustrated in Fig. 4.22, whereas some pictures can be seen in Fig. 4.23. As is visible in the figures and in the schematics, the drums are not planar, rather they are in the form of an helicoid and a cylinder. This, though introducing a small error, solves the practical problem of manufacturability; indeed, in general, purely planar VRDs have impossible-to-manufacture geometries, except where the spiral angle is less than 360°.

In order to evaluate the performance of the mechanism, one must consider that the theory produced in this research is related to a planar mechanism. Conversely, the prototype is inherently non-planar. As can be seen in the figure, the pulleys and drums are not co-planar; indeed, if the pulleys are aligned between one and the other, the VRD and the constant radius drum (CRD) are not. In fact, since they are mounted on the same axis, they are slightly offset with respect to the idler pulleys' plane. This misalignment causes a certain deviation due to the fact that the cable is forced at an angle. However, this effect can be easily quantified using basic trigonometry and starting from the values of k_{CRD} and k_{VRD}. It should be noted that k_{CRD} and k_{VRD} are measured directly, rather than inferred from the nominal geometry of the drums.

The performance of the system can be evaluated in terms of the deviation either from the nominal path P_n (horizontal, linear) or against the corrected path P_c (considering the deviation caused by the offset of the drums). For our purpose, we will call D_n the former and D_c the latter. In either case, the height of the end-effector is measured

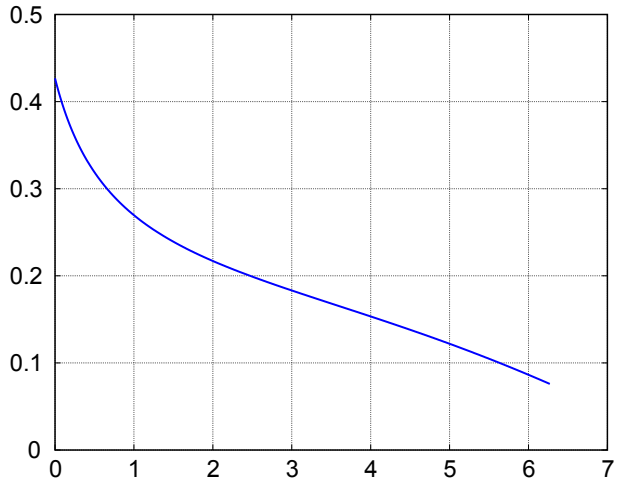

Figure 4.21: $ds/d\alpha$ versus α.

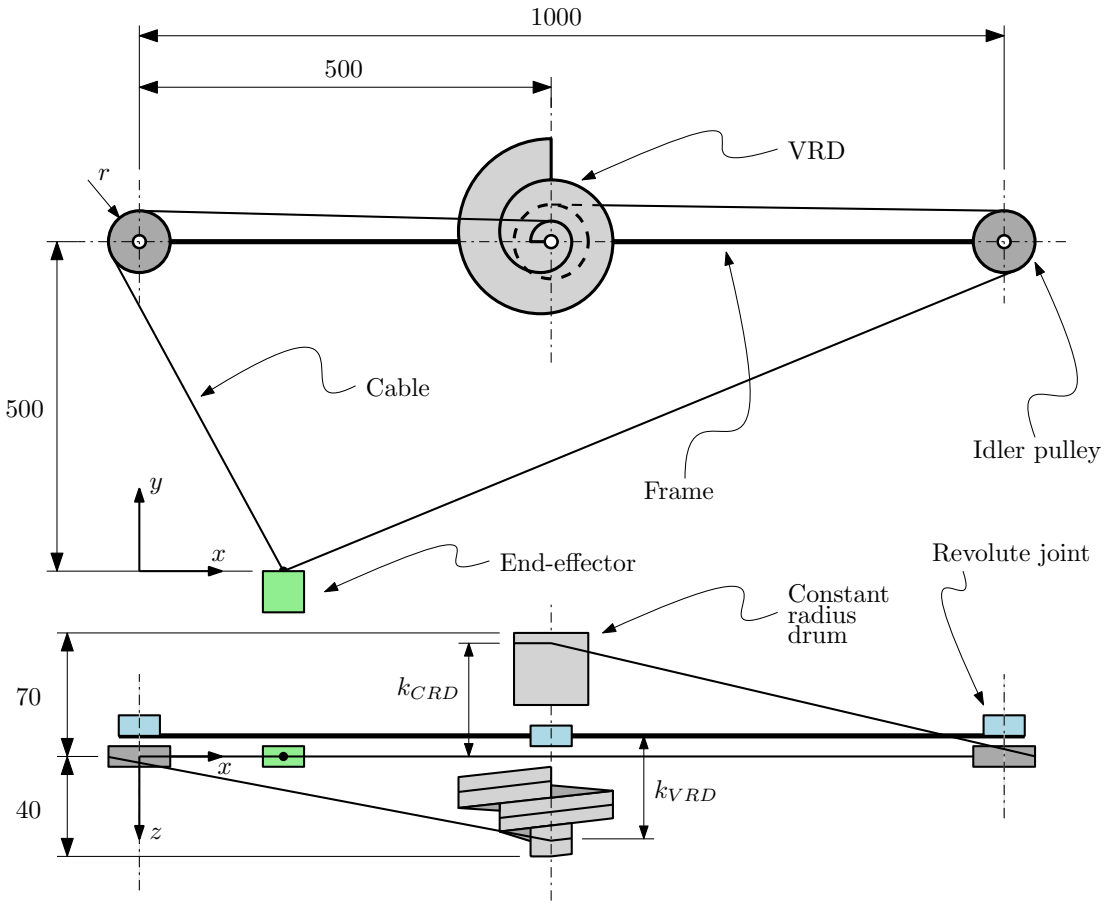

Figure 4.22: Experimental setup (measures in mm). The figure shows the front and top view of the prototype. The VRD is shown in the middle, along with the constant radius drum. The frame is aligned horizontally. The end-effector is suspended 500 mm below the frame and is to move parallel to the frame, towards the right-hand direction.

experimentally along the path (x axis direction) at $50mm$ intervals, starting at $x = 150mm$ and ending at $x = 850$. This is then compared against the reference value.

The D_n deviation is important because it gives a general understanding of the accuracy of the system when the drums' offsets are not analytically considered; it is a worst-case scenario. On the other hand, the D_c allows us to isolate the error due to the inevitable discrepancies that can arise in practice; in our case, these can account for slippage, cable elongation, bending of the structure, low manufacturing quality, thermal effects and so on.

The results are illustrated in graphic form in Fig. 4.24. The plot shows the values

Figure 4.23: A set of pictures of the experimental setup and prototype. In the upper-left corner the VRD and CRD assembly are shown; on the right and below the whole assembly is visible.

of P_n, P_c, D_n and D_c at each measure point.

Aggregate values are reported in Table 4.3. It is immediately appreciable how the maximum relative error is indeed very small, both for D_n and D_c, and well below the 1% threshold.

Results of the prototype experimental evaluation have shown that the system is capable of acceptable precision and accuracy, even in these early stages of development. Furthermore, the drums' offsets are proven not to produce worrying effects on the performance of the system. Given that the parts were manufactured mainly using a very basic FDM technology, and provided that more accurate manufacturing methods are exploited, the D_c deviation could be dramatically reduced. The geometry of the VRD

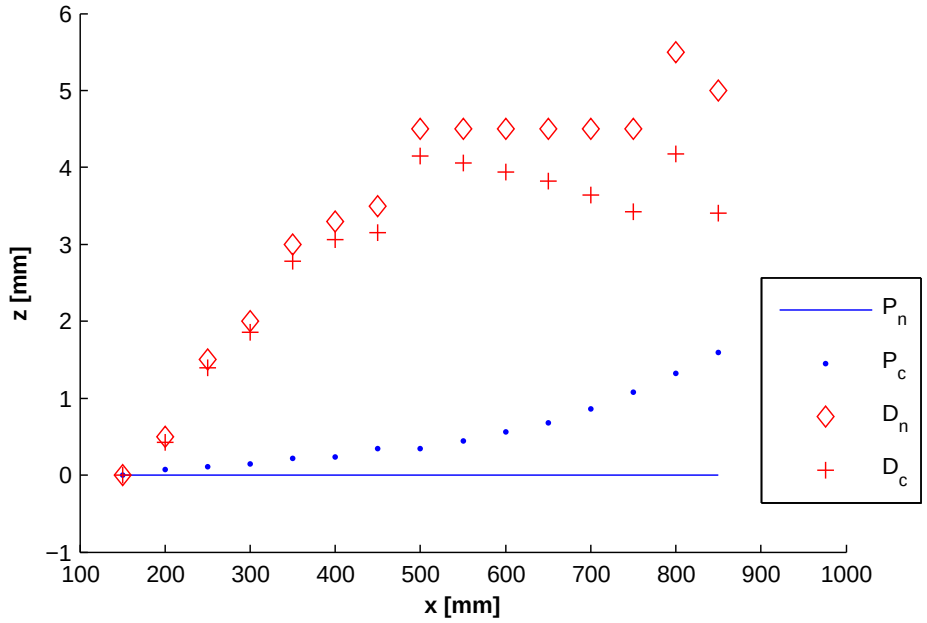

Figure 4.24: Experimental results for the horizontal path. The nominal path is shown in blue, whereas the corrected nominal is dotted in the same color. Experimental values are in red (diamond for raw measurements, cross for corrected).

allows for CNC 4-axis milling machine manufacturing, or even 3-axis ones, provided, in this last case, that special tools are used. For example, the helicoid constituting the VRD could be milled on its sides, from the top, with custom-profile slot end-mills with simple contour machining paths.

This prototype shows once more the advantages of using a VRD as opposed to more traditional approaches with CRDs, the first and foremost being the simplicity in the

Table 4.3: Aggregate results. The first two columns present the average and peak values for the three main experimental series. The last column shows the error relative to the total path length (700mm).

	Mean value	Peak	Max. relative error
P_c	0.53	1.59	0.23%
D_n	3.42	5.50	0.79%
D_c	2.89	4.18	0.60%

required control system. In fact, to produce a linear trajectory alike that performed in this evaluation, one would need at least a pair of CRDs with a coupled control system to drive them synchronously. The VRD, on the other hand, requires only to compensate for the varying radius of the pulley, in order to produce a pre-determined speed (or torque) output.

4.2.5 Application

As hinted in the opening of this section, the key application of VRDMs as actuators is in the design of lightweight overhead cranes. State-of-the-art systems are normally cumbersome, heavy, and in most cases cannot be assembled and disassembled easily; instead, they are meant to remain as a fixed asset in an industrial plant.

As Fig. 4.15 shows, the overhead crane is an assembly of three main components:

- a main set of rails, which allows it to travel along the lenght of the warehouse in which it is found,
- the structure of the crane, generally in the form of a beam-type frame,
- a secondary rail, which provides transversal movement, e.g. along the beam itself,
- a hoist mechanism, generally based on a wire rope and a motorized winding device.

These provide the necessary load hoisting and manoeuvring capabilities inside industrial plants.

As is perfectly evident, the largest inconvenience is the presence of the main rails, which are heavy and cumbersome components that in most cases need to be mounted on the structure of the building along its entire length.

In the this section, a overhead crane concept is presented, which uses VRDMs in place of the main rails. An illustration of an early prototype model is visible in Fig. 4.25. The VRDMs are used to provide the longitudinal motion, and require only one motor, compared to CDPRs, which would need the coordinated motion of two of them. In fact, the motor visible on the right is coupled to both CRDs and both VRDs, so as to control the manoeuvring of the blue cable, as well as the red one. This synchronous

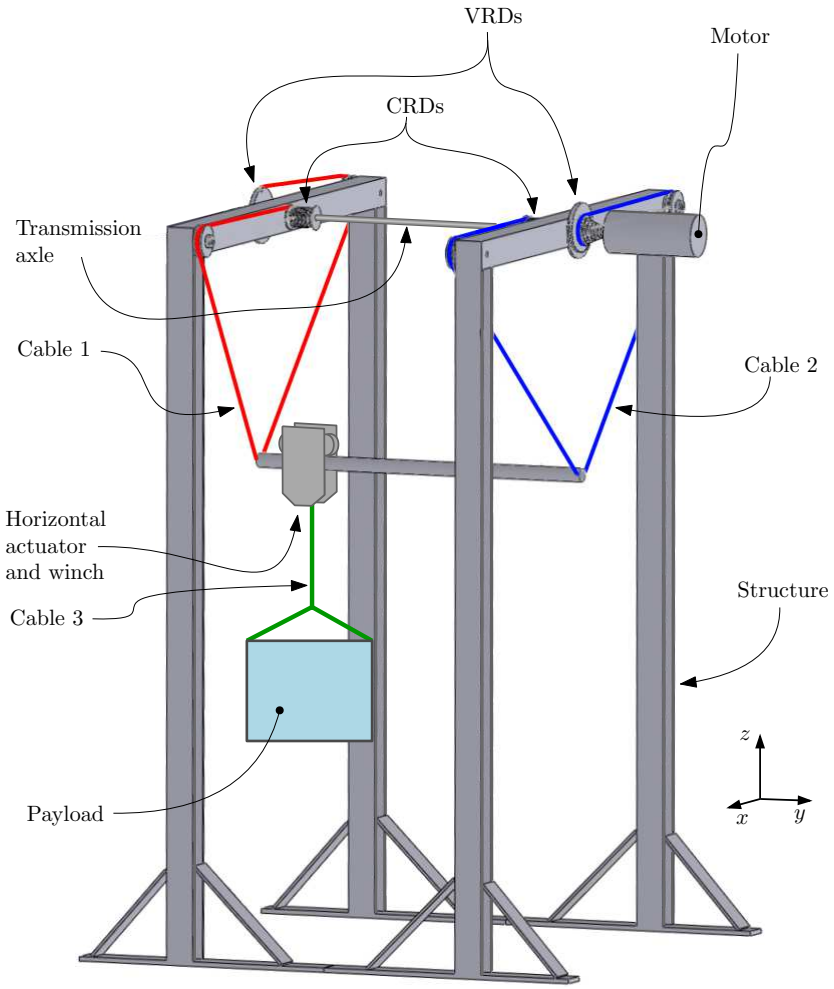

Figure 4.25: Concept of a overhead crane based on VRDMs.

motion provides the motion of the horizontal rail, on which an horizontal carriage is located which hosts the hoisting device (shown in green).

It is worth noting that in the presented embodiment, a certain degree of lability is present in the horizontal, transversal direction. This is due to the geometry of the cables. A more complex arrangement can indeed be made to account for this problem, for example by replacing one of the VRDM actuators with a pair of actuators placed at an angle. This would keep the transversal rail from oscillating.

Compared to the system shown in the figure, which is in the prototype phase, a real world system could consist in modules that could be either fixated to a base structure (as the columns of the building) or kept in place with assembled towers. In particular, four of these would be necessary, one for each pulley, as the VRDs and CRDs can be

placed closer to the pulleys, on the same column. One must note, finally, that the model presented in the figure has a certain degree of lability in the direction normal to the planes of the cables. This should be taken care of, for example by extending the 2D formulation to a 3D one, which is well in reach; in that case, stability would be excellent.

Some limitations exist:

- Large vertical encumbrance; the cables must drop at a certain angle in order to keep tensions to a minimum,
- Higher maintenance; cable systems need to be checked, certified, and replaced according to a precise schedule; in general they can be more prone to failures,
- Manufacturing of the VRD is not straightforward and needs special care,
- The mechanism needs to be calibrated in order to provide a smooth and coherent translation.

This being said, the comparable portability – or at least ease of assembly and disassembly – of such systems is unparalleled by other fixed solutions which are used in the industry. Even mobile hoist cranes have strong limitations, in particular with covering large volumes.

4.2.6 Conclusion

This section introduced and analyzed the concept of Variable Radius Drum Mechanisms (VRDM), the core of which is based on the Variable Radius Drum (VRD) mechanical element. Properties of such a devices have been discussed, as well as the kinematic analysis and synthesis. An analytical solution of the VRD synthesis has been determined. To show the benefits of VRDMs, two practical implementations have been presented and discussed, the first being a mechanism to guide and move a load along a predetermined horizontal linear path, and the second an overhead crane made of a pair of these actuators.

Furthermore, a 3D printed prototype was presented and evaluated experimentally against the horizontal path case, showing good accuracy and precision regarding the actual trajectory of the end-effector.

The research has shown that there is progress to be made in the field of efficient manufacturing of the complex VRD's geometries. Since the system relies on cables positioned on drums with a certain precision, a complete sensitivity analysis would be useful to evaluate potential issues. Moreover, with further efforts, an extension in 3D space could well be within reach, and could possibly provide interesting real-world applications, as hinted in Section 4.2.5.

As far as applications in the field of LWRs goes, it has being shown that VRDMs can be used in the design of portable overhead cranes, with clear advantages over fixed ones. Disadvantages were pointed out and a conceptual model was illustrated.

4.3 CDPR for Inspection and Light Manipulation for Space Applications

The exploration of planets and other celestial bodies has been, up to this point in history, carried out by the use of small, solitary, one-package probes [119, 120]. Since the first soft landing performed by the Soviet's Luna 9 in 1966 on the Moon, many landers have been deployed all around the solar system, e.g. Mars [121], Venus, even Jupiter's moon Titan with ESA's Huygens probe [122] in 2005, or, more recently, the partially successful landing of ESA's probe Philae [123] on comet 67P/Churyumov–Gerasimenko. A subset of these probes are the so-called rovers, robotic vehicles designed to travel across the surface of planets or, more generally, unexplored, and possibly hostile, environments. Notable examples are Lunokhod 1, deployed on the moon in 1970, which kept operating for 11 months, the mars rovers MER-A and MER-B, the latter still in operation after more than 11 years from its landing, and finally the most recent Mars Science Laboratory (MSL) rover [26]. Future planned rovers include ISRO's Chandrayaan-2 [25], ESA's ExoMars [24] and Mars 2020 Rover Mission from NASA [23]. As it is clear from reviewing all these missions, the focus is on the scientific payload that is on-board the rover. This calls the robot to be conceived primarily as a mobility and support structure for the several instruments that need to probe the environment in different locations. This rationale results in a system that needs to be as self-contained as possible, to be efficient and to save weight. A partial deviation in principle is represented by landers made by an autonomous base and a rover. An example is NASA's Sojourner, part of the Mars Pathfinder mission [27], in 1996–7, or the recent Chang'e 3, with its partially successful rover Yutu [28], in 2013.

The design of rovers has thus been geared towards mere carriers of scientific instruments. Indeed, modularity in its broad sense has seen, up to now, extremely limited practical development in the field of space exploration, mainly for the mentioned lack of necessity. In the last decade, though, with the prospect of entering into a new phase of exploration – especially of Mars and the Moon – a new paradigm is starting to take form [124, 125]; one where rovers and robots are not simple carriers, but actually constitute and support a modular, multi-expertise environment for complex planetary activities that can go from sample extraction, collection and processing, to the preparation of a base for manned exploration or resource gathering [126–131].

Despite the lack of an implementation in the real space environment, there is ongoing development on the subject of integrated robotic exploration; for example, Fink et al. [132] describe a framework for the robotic exploration of lava tubes of which there is strong evidence both on the Moon and on Mars.

Cordes et al., with the LUNARES project [133], describe the development of a framework for collaborative robotics with the intent of lunar craters exploration; static, wheeled, and legged robots are implemented.

Modular robotics applied to celestial bodies exploration has been also investigated by the RIMRES project [134], which describes the collaborative operations of several heterogeneous autonomous robots. In particular, a wheeled rover with a serial manipulator is used to load, carry to target and deploy immovable modules on the ground that can contain scientific instrumentation, experiments or other devices like radio beacons.

A supervised autonomy telerobotics experiment [135] under the METERON project demonstrated the use of the DLR's (Deutsches Zentrum für Luft und Raumfahrt) wheeled anthropomorphous robot Justin, for the maintenance of a solar array deployed in a space environment.

In this section, a novel application of cooperative and modular robotics is presented, to the field of space exploration [136]. This consists in a series of 3 modules that, when deployed, constitute a 3-links Cable Driven Parallel Robot (CDPR) that can perform efficiently tasks which require a large workspace and a lightweight structure. The modules themselves are arranged and deployed by a rover equipped with a serial manipulator with a docking interface instead of a conventional gripper.

4.3.1 Description of the system

The system consists of 3 types of components: the modules, the rover and the end-effector. Initially, these are separate and possibly stowed. The deployment process consists of positioning the 3 modules, and connecting the end-effector to the cables attached to each module; this procedure is carried out by the rover.

The CDPR, as mentioned in the introduction, consists in the 3 deployed modules, which provide the active winches that operate the cables. In the following subsections the module and the end-effector subsystems are presented. Finally, the deployment procedure is outlined, along with a general description of the rover.

4.3.1.1 The Module

Each base module, as seen in Fig. 4.26, is a device which must be stable on rough terrain, provide structural integrity to the system, and perform its hardware control functions. In this work we focus on a module which is not fixed to the ground, but simply lies on top of it, relying on friction with the ground to keep its position.

In order to coordinate the feed of the cables, a master-slaves configuration is advisable, where one module acts as the master, and the rest as its slaves; the master module provides all of the high-level functions, e.g. path-planning, vision, communication with the slaves, etc., whereas the slaves themselves will perform the lower-level functions, i.e. control of the winches, relative position control, etc.

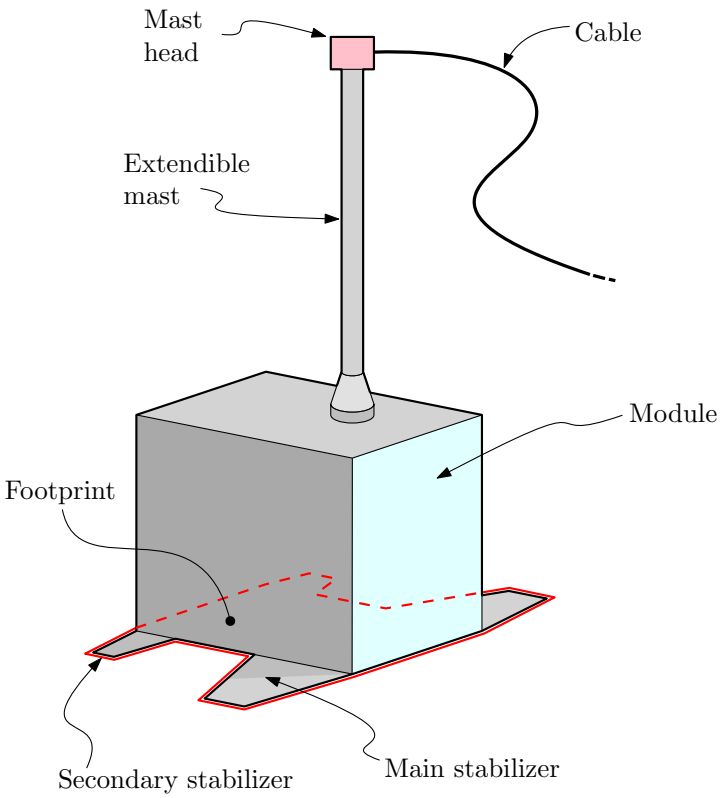

Figure 4.26: A module of the 3-cable CDPR robot. The prism at the bottom contains the actuator for the extendible mast and the control system. The main and secondary stabilizers are illustrated at the very bottom, and the footprint is highlighted

Since the module is not fixed to the ground, a fundamental characteristic of it is its footprint, since it contributes to its stability when loads are applied by the cables. In

this section we discuss three different types; by looking at Fig. 4.26, one can see that two pairs of stabilizers exist, the "Main" and the "Secondary stabilizer". These are lightweight deployable structures that widen the footprint of the module, thus making it less prone to tilting and ultimately toppling. We call "A" the situation where no stabilizer is present, "B" where only the main ones are deployed, and "C" where both the main and the secondary are open.

4.3.1.2 The end-effector

The end-effector that we propose as an example in Fig. 4.27, consists of a body frame on which a pan-tilt camera is mounted. Since the component must be allowed to be disconnected from the cables, a docking system is employed for the connection. Since the cables should incorporate data and power transmission functions, the docking adapters must employ a coaxial or similar connector.

From the figure it is easy to locate the arm docking interface; this is the means by which the arm of the rover picks up and manoeuvers the end-effector during the deployment of the robot. A solution like this is advisable since conventional grippers can be less reliable and deterministic. In fact, some sort of advanced positioning system would be needed to locate precisely the end-effector once it is gripped by the arm. This is necessary in order to perform the docking with the cables.

In general, the only major limitation on the typology of end-effector is weight, as will become evident in the following sections.

4.3.1.3 Deployment Procedure

The deployment procedure consists mainly in two steps:

1. Positioning and setup of the 3 modules,

2. Connection of the end-effector to the cables' endpoints.

By referring to Fig. 4.28a one can appreciate how the modules can be carried around by the rover; a docking adapter is used in place of a conventional gripper, increasing robustness in the whole process. The same concept is used to manipulate the end-effector depicted in Fig. 4.27, which carries a docking adapter as well.

In order to fully describe the various phases of deployment, along with some possible paths of the rover, a schema is shown in Fig. 4.28b. In the figure, the area to cover is shown, along with the desired positions of the modules $P_1^{'}$, $P_2^{'}$ and $P_3^{'}$, around it.

To position the modules, the rover has to drive through path $t_a \rightarrow t_b \rightarrow t_c$, incrementally. At this point the modules' stabilizers deploy.

The placement of the end-effector is substantially more complex since it involves connecting and driving a tethered component; the procedure is as follows:

1. The rover picks up the end-effector from storage, by docking it to the arm,
2. It follows path segment t_d,
3. In $P_1^{'}$, the rover maneuvers the end-effector to connect to the cable of module 1 through the plug visible in Fig. 4.27. It is worth noting that the cables can be locked in place by the feed mechanism, and thus offer a rigid connection point during the docking performed by the arm with the end-effector.

At this point, the rover is effectively tethered to module 1, and the path planner must account for any constraints posed by such connection.

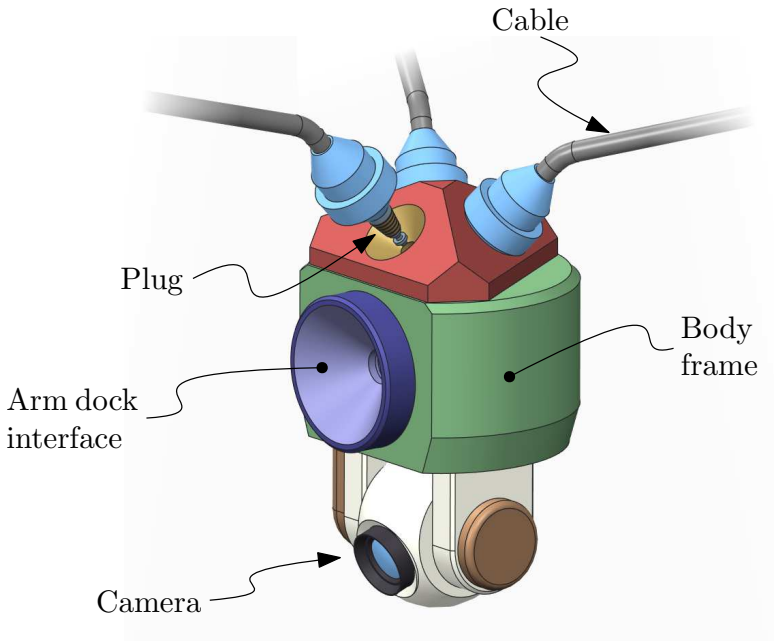

Figure 4.27: The end-effector. The cables are connected through small lockable docking adapters which can host an electrical connector or plug.

1. The rover drives through segment t_e,
2. In proximity of $P_2^{'}$ it connects the cable of module 2 to the end-effector,

The rover is now tethered to both module 1 and 2. This effectively means that the path planner must coordinate the feed of the cable of the two modules to follow the end-effector, which is moving along with the rover.

1. The rover drives through segment t_f,
2. At $P_3^{'}$, it connects the end-effector to the last cable,
3. The rover undocks the end-effector,
4. The masts of the modules extend.

The CDPR is now in place and the rover can be released to perform other tasks, possibly unrelated to the cable robot.

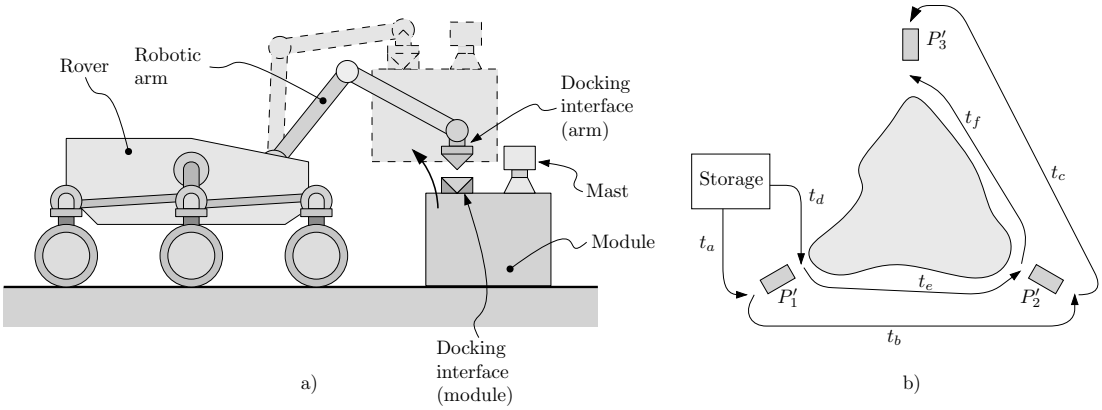

Figure 4.28: Deployment procedure. In a) the interaction of the rover with the module is shown. The docking interface on the arm side locks itself in the counterpart on the module and allows the module to be lifted and driven in place. In b) the possible paths of the rover are shown as t_a through t_f. The grey area visible in b) represents the workspace that is needed.

4.3.2 Model of the CDPR

The CDPR is the heart of the integrated system. In order to analyze feasibility and performance, in the following sections, a full analytical model is given, along with the tools to evaluate it.

It is worth noting that the model is based on simplified straight-line undeformable cables, as opposed to cables that sag under the effect of gravity. An study on the influence of this is shown in Appendice D on page 189.

4.3.2.1 Kinematics

The kinematics of the CDPR is illustrated in Fig. 4.29. The system is defined by the following governing vector equation,

$$\mathbf{F} + T_1\hat{\mathbf{v}}_1 + T_2\hat{\mathbf{v}}_2 + T_3\hat{\mathbf{v}}_3 = 0, \tag{4.59}$$

Where $\hat{\mathbf{v}}_i$ is the versor of the i-th cable, defined as $\hat{\mathbf{v}}_i = \|P_i - Q\|$.

Assumed the force $\mathbf{F}$ on the end-effector $\mathbf{Q}$ is known, in order to calculate the cable tensions $T_{1,2,3}$, these terms must be rendered explicit. Eq. 4.59 can be manipulated into this form,

$$\begin{bmatrix} v_{1,x} & v_{2,x} & v_{3,x} \\ v_{1,y} & v_{2,y} & v_{3,y} \\ v_{1,z} & v_{2,z} & v_{3,z} \end{bmatrix} \begin{Bmatrix} T_1 \\ T_2 \\ T_3 \end{Bmatrix} = \begin{Bmatrix} F_x \\ F_y \\ F_z \end{Bmatrix}, \tag{4.60}$$

which is of the $Ax = b$ type, meaning it can be easily inverted as $x = A^{-1}b$; hence,

$$\begin{Bmatrix} T_1 \\ T_2 \\ T_3 \end{Bmatrix} = \begin{bmatrix} v_{1,x} & v_{2,x} & v_{3,x} \\ v_{1,y} & v_{2,y} & v_{3,y} \\ v_{1,z} & v_{2,z} & v_{3,z} \end{bmatrix}^{-1} \begin{Bmatrix} F_x \\ F_y \\ F_z \end{Bmatrix}. \tag{4.61}$$

The layout of the modules is illustrated in Fig. 4.30. We can, at this point, define the cable's tensions vectors, as $\mathbf{T}_i = -T_i\hat{\mathbf{v}}_i$, for the i-th module. These are applied to the cable's feed mechanism on top of the mast of the module, that is to say, to point $\mathbf{P}_i$, and can cause the module to topple over if certain conditions are met. This will be discussed in depth in the next section.

4.3.2.2 Stability Polytope Analysis

The stability of a rigid body which is placed on the ground in a still condition, is subject to gravity and to a general external force $\mathcal{F}$, can be defined as the subset of $\mathcal{F}$ for which the body is in a stable condition, i.e. remains still indefinitely.

The main factors that come into play are the footprint of the body, the center of mass $\mathbf{G}$ position, the mass m itself of the body, the point of application of $\mathcal{F}$ and its

magnitude. We do not consider possible sliding of the module on the ground. These are illustrated in Fig. 4.31, where, notably, $\mathcal{F}$ is represented by $\mathbf{T}_i$ (i.e. the cable tension) and the footprint is defined by the polygon of vertices $\mathbf{p}_1, \ldots, \mathbf{p}_j, \ldots, \mathbf{p}_n$. Note that the footprint seen in Fig. 4.31 is the planar convex hull of the original footprint of the module found in Fig. 4.26; this is a general requirement of the method.

It is possible to calculate the momentum that $\mathbf{T}_i$ generates along the versors $\hat{\mathbf{e}}_j$. Let us call $\mathbf{r}_{T,j}$ the projection of $\mathbf{P}_i - \mathbf{p}_j$ on a plane for which $\hat{\mathbf{e}}_j$ is the normal; similarly, let $\mathbf{r}_{G,j}$ be the projection of $\mathbf{G}_i - \mathbf{p}_j$ on the same plane. Then we have,

$$\begin{cases} \mathbf{M}_{T,j} &= \mathbf{r}_{T,j} \times \mathbf{T}_i \\ \mathbf{M}_{G,j} &= \mathbf{r}_{G,j} \times m_i \mathbf{g} \end{cases} . \tag{4.62}$$

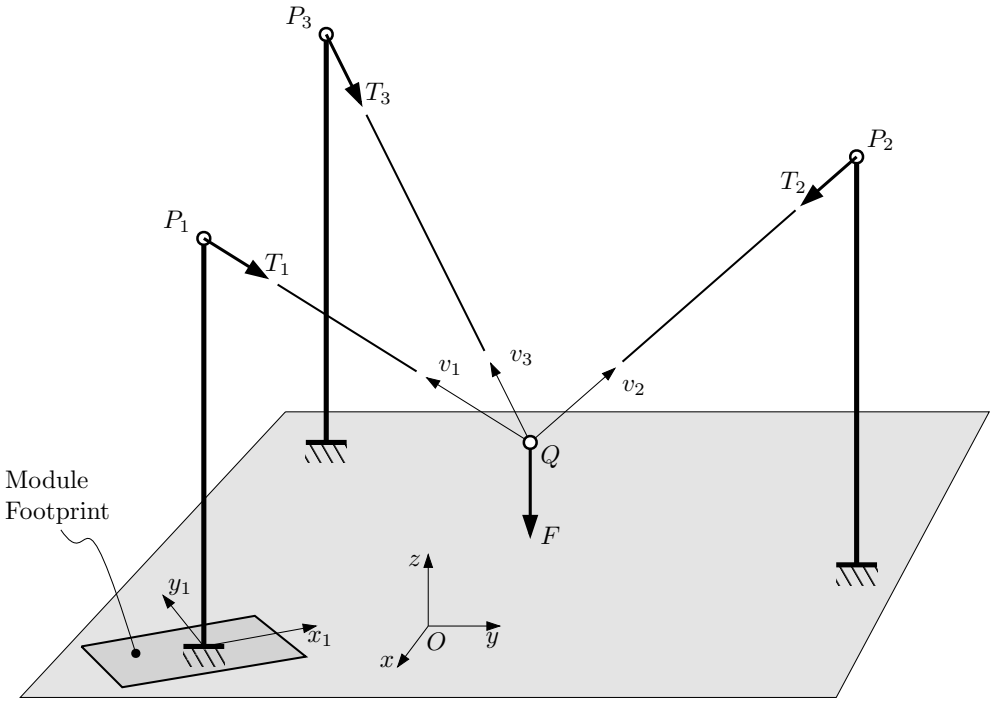

Figure 4.29: Illustration of the kinematics scheme of the modular CDPR. The end-effector Q is suspended by the three cables of versors $v_{1,2,3}$, with tensions $T_{1,2,3}$ to the cable feed mechanisms located in $P_{1,2,3}$. The force Fcaused by gravity is applied to Q. The module footprints are referred to the modules local coordinate systems (x_1, y_1, z_1), (x_2, y_2, z_2) and (x_3, y_3, z_3), the last two of which are not shown.

The condition for stability can be expressed as,

$$(\mathbf{M}_{T,j} + \mathbf{M}_{G,j}) \bullet \mathbf{e}_j \leq 0, \forall j \in 1, \ldots, n. \tag{4.63}$$

In other words, stability is achieved when the momentum $\mathbf{M}_{T,j}$ generated by $\mathcal{F}$ applied in $\mathbf{P}_i$ is counteracted entirely by the momentum $\mathbf{M}_{G,j}$ generated by the gravity acceleration on the center of mass $\mathbf{G}$, that is to say, when $\mathbf{M}_{G,j} > \mathbf{M}_{T,j}$.

As previously stated, the general requirement for which Eq. 4.30 – and the relative methodology – is applicable, is that the footprint must be a convex polygon. In fact, the footprint does not necessarily coincide with the geometry of the lower face of the body; it is rather the convex hull of this geometry.

In Fig. 4.32 a possible polytope computation is visible for three different footprint polygons. In this case, the external force $\mathcal{F}$ is placed at an height of 1 m over the ground, and oriented towards the ground by $-45°$, $-30°$ and $-10°$, to account for the

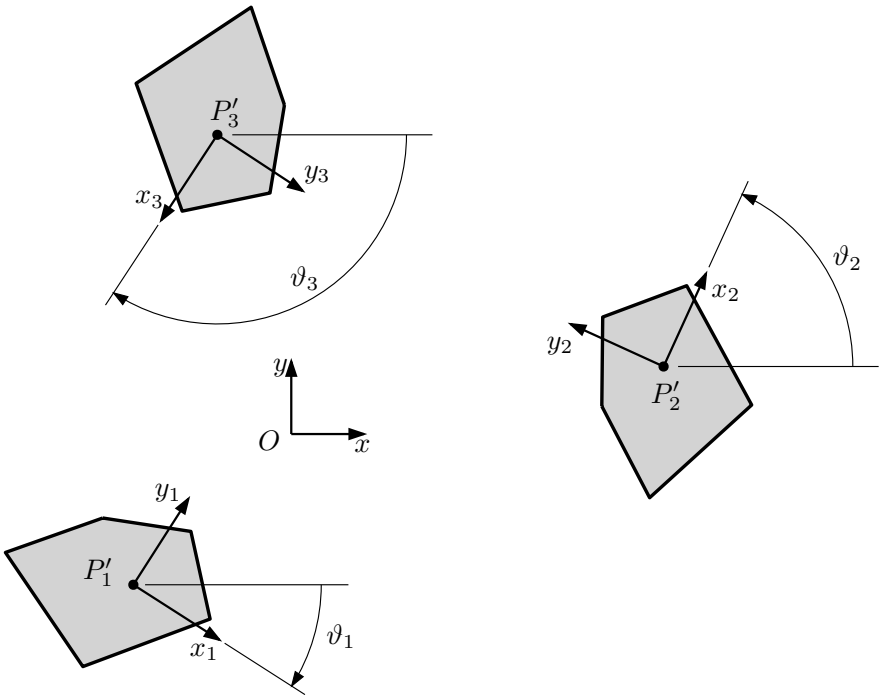

Figure 4.30: View from the top of the footprints of the modules. The polygon representing the footprint is identical in the three cases, and is positioned in points $P'_{1,2,3}$, with a rotation along the $y_{1,2,3}$ axes of angles $\vartheta_{1,2,3}$ respectively.

cables usual orientation. Where φ is the angle between the force vector and the y axis of the module, the general point of the polytope is as follows,

$$\rho(\varphi) = \min\left(-\frac{(\mathbf{r}_{G,j} \times m\mathbf{g}_j) \bullet \mathbf{e}_j}{\left(\mathbf{r}_{T,j} \times \hat{\mathbf{T}}_i(\varphi)\right) \bullet \mathbf{e}_j}\right), \tag{4.64}$$

Where $\hat{\mathbf{T}}_i(\varphi) = \frac{\mathbf{T}_i}{\|\mathbf{T}_i\|}$, and $j = 1, \ldots, n$.

The $\rho'(\varphi)$ value represents the minimum normalized force, oriented along the direction given by φ, required to hinder the stability of the rigid body. This, represented in polar form, is visible in Fig. 4.32 on the right. It is important to note that this is dependent on other parameters, e.g. the center of mass G_i location, and the location of point P_i. For this example, the G_i is located in the geometrical center, at a height of 0.2 m, whereas point P_i is in the same location but at a height of 1 m.

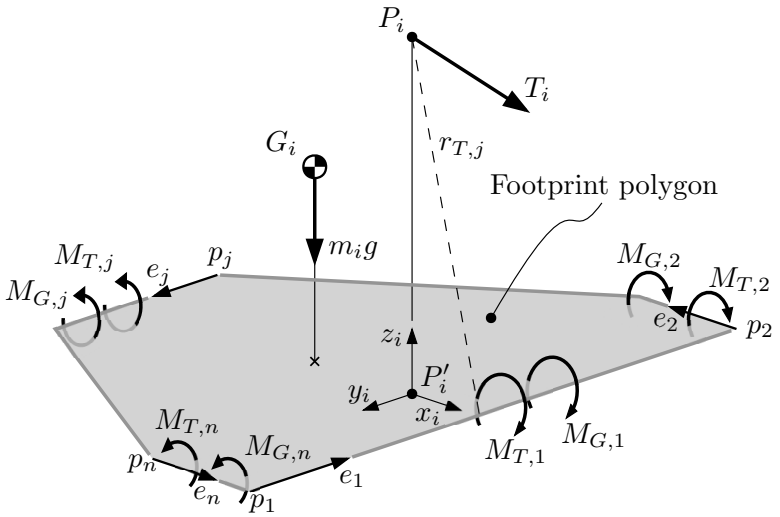

Figure 4.31: Stability analysis quantities. For each module i the cable tension $\mathbf{T}_i$ is applied to $\mathbf{P}_i$ and generates momentums $\mathbf{M}_{T,i,j}$ around the footprint polygon $\mathbf{p}_{i,(1,\ldots,n)}$ sides versors $\hat{\mathbf{e}}_{i,j}$. The same applies to the force of gravity $m_i\mathbf{g}$, which, applied to the center of mass $\mathbf{G}_i$ generates $\mathbf{M}_{G,i,j}$. Note that in the figure, some occurrences of the index i were neglected, in order not to clutter.

4.3.2.3 Workspace Analysis of the CDPR

When viewed from above, the *reachable* workspace W_r of a 3-link CDPR subject to gravity has a triangular shape with the vertices coincident with the cable anchor points.

This is a result of the following condition on the cables' tensions,

$$T_i \geq 0, \tag{4.65}$$

which applies to Eq. 4.61.

Within the reachable workspace, depending on the position of $\mathbf{Q}$, $\mathbf{P}_1$, $\mathbf{P}_2$ and $\mathbf{P}_3$, and the force $\mathbf{F}$, the values of T_i can change considerably. One can define a *manipulability* workspace W_m, where the stability of the modules is guaranteed for each point $\mathbf{Q} \in W_m$. As stated in Section 4.3.2.1, this is given when Eq. 4.63 holds.

It might be useful to define an index I_t to better evaluate the closeness to tilting; if we take into consideration the moments defined in Eq. 4.62, we can write the following,

$$I_t\left(\mathbf{Q},\mathbf{P}_i,\mathbf{F},m,\mathbf{p}_{i,j}\right) = \max\left(\frac{\mathbf{M}_{T,i,j}}{\mathbf{M}_{G,i,j}}\right), \tag{4.66}$$

where j represents, as usual, the j-th side of the footprint polygon $\mathbf{p}_j$, i the i-th module and m the mass of the module.

The tilt index I_t is defined in the $[0,+\infty]$ interval, hence the following holds,

$$\begin{cases} I_t \in [0,1] & \text{Stability} \\ I_t \in [1,+\infty] & \text{Instability} \end{cases}. \tag{4.67}$$

4.3.3 Results and Discussion

Since I_t is, in general, a very high dimension hypersurface, a completely coupled analysis would be impractical, impossible to visualize and computationally too expensive. It is though convenient to slice I_t along some of the most interesting dimensions, namely the configuration of angles ϑ_1, ϑ_2 and ϑ_3. In order to simplify this we assign the following constraint,

$$\vartheta^* = \vartheta_1 = \frac{\pi}{3} + \vartheta_2 = \frac{2\pi}{3} + \vartheta_3. \tag{4.68}$$

The other parameters are fixed and their values are summarized in Table 4.4.

By means of Equations 4.59, 4.62 and 4.66, it is possible to define the values of $I_t\left(\mathbf{Q},\,\vartheta^*\right)$ for every $\mathbf{Q} \in W_m$; If $\mathbf{Q}$ is selected always at the same height from the ground, this produces a set of surfaces $\mathbf{S}\left(\vartheta^*\right) = \bigcup I_t\left(\mathbf{Q},\,\vartheta^*\right),\ \forall \mathbf{Q} \in W_m$, one for each value of ϑ^*. It is then possible to discretize $\vartheta^* = 0,\ldots,2\pi$, in order to analyze the

Table 4.4: Fixed parameters for the CDPR robot. Note that the value $\mathbf{Q}_z$ denotes the height in the z-direction at which the workspace is computed.

Parameter	Value	Unit
m_{module}	20	Kg
$m_{end-eff}$	1	
$\mathbf{F}$	$[\,0\;0\;-9.81]$	N
$\mathbf{Q}_z$	0	m
$\mathbf{P}_i$	$P_1 = [\;\;,0 \quad 0, \quad 3\;]$	
	$P_2 = [\;\;,5 \quad 10\cos(\pi/6) \quad 3\;]$	
	$P_3 = [\;-5 \quad 10\cos(\pi/6) \quad 3\;]$	
$\mathbf{p}_j\vert_A$	$\mathbf{p}_1 = [\;-0.09 \quad 0.5 \quad 0\;]$	
	$\mathbf{p}_2 = [\;0.09 \quad 0.5 \quad 0\;]$	
	$\mathbf{p}_3 = [\;0.09 \quad 0 \quad 0\;]$	
	$\mathbf{p}_4 = [\;0.09 \quad 0 \quad 0\;]$	
$\mathbf{p}_j\vert_B$	$\mathbf{p}_1 = [\;-0.49 \quad 0.5 \quad 0\;]$	
	$\mathbf{p}_2 = [\;0.49 \quad 0.5 \quad 0\;]$	
	$\mathbf{p}_3 = [\;0.49 \quad 0.4 \quad 0\;]$	
	$\mathbf{p}_4 = [\;0.09 \quad 0 \quad 0\;]$	
	$\mathbf{p}_5 = [\;-0.09 \quad 0 \quad 0\;]$	
	$\mathbf{p}_6 = [\;-0.49 \quad 0.4 \quad 0\;]$	
	$\mathbf{p}_7 = [\;-0.49 \quad 0.5 \quad 0\;]$	
$\mathbf{p}_j\vert_C$	$\mathbf{p}_1 = [\;-0.49 \quad 0.5 \quad 0\;]$	
	$\mathbf{p}_2 = [\;0.49 \quad 0.5 \quad 0\;]$	
	$\mathbf{p}_3 = [\;0.49 \quad 0.4 \quad 0\;]$	
	$\mathbf{p}_4 = [\;0.29 \quad 0 \quad 0\;]$	
	$\mathbf{p}_5 = [\;-0.29 \quad 0 \quad 0\;]$	
	$\mathbf{p}_6 = [\;-0.49 \quad 0.4 \quad 0\;]$	
	$\mathbf{p}_7 = [\;-0.49 \quad 0.5 \quad 0\;]$	

impact the angle ϑ^* has on the workspace morphology and index. For example, we can define the following quantity,

$$I_{t,max}\left(\vartheta^*\right) = \max\left(\mathbf{S}\left(\vartheta^*\right)\right), \tag{4.69}$$

which can be determined for each and every ϑ^*. The values are plotted in Fig. 4.33 for the three footprint configurations A, B and C, visible in Fig. 4.32 and defined in Table 4.4.

By looking at the curves, it is immediately apparent how configuration A is the least stable, with the majority of angular positions ϑ^* resulting in tilting or toppling ($I_t > 1$) for the parameters used in this setup. Configurations B and C show, instead, good stability for every angular position, while the global minima of I_t is reached by configuration C at $\vartheta^*_{\text{best}} \cong 0.6\pi$, with $I_t\left(\vartheta^*_{\text{best}}\right) \cong 0.3$.

A map of the workspace defined by the stability index I_t is visible in Fig. 4.34; it is relative to the height of $\mathbf{Q}_z = 0$ and shows the stability configuration along the entire working area. The deep-blue area outside the central triangle is considered forbidden because the system would not be stable. In fact, should the end-effector lie there, a situation in which at least one of the cable tensions T_i would be negative. Since this cannot happen because of the structural nature of the cables, that location cannot be – at least statically – reached. Quantitatively, at this height the robot is very stable, with a maximum value of $I_{t,max} = 0.31$; in fact, approximately 77% of the area in the central triangle pertain to the interval between $I_t = 0.2$ and $I_t = 0.3$. In Fig. 4.35 it can be seen how the stability and workspace morphology changes in response to different heights of the end-effector $\mathbf{Q}$. In particular, in the last row of the grid, it is clear that the workspace *erodes* very fast, approaching the 2.5 m level. This is due to the structural and geometrical characteristics of the CDPR; sure enough, the cables' tensions rapidly grows to a level where the momentums generated on the modules are so high that stability is compromised in at least one module.

4.3.4 Applications

As mentioned in the introduction, if complex structures or arrays of constructs are deployed on the surface of celestial bodies like Mars or the Moon, steps must be taken towards making maintenance and inspection of these systems possible and efficient. Automating these tasks is of paramount importance even in case of a manned presence, since extravehicular activities are generally to be avoided wherever possible.

Let us consider a possible solar panel array. Since size is, in this case, directly proportional to energy production, the ground area should conceivably be very large. The modular CDPR presented in this work could provide an affordable and efficient

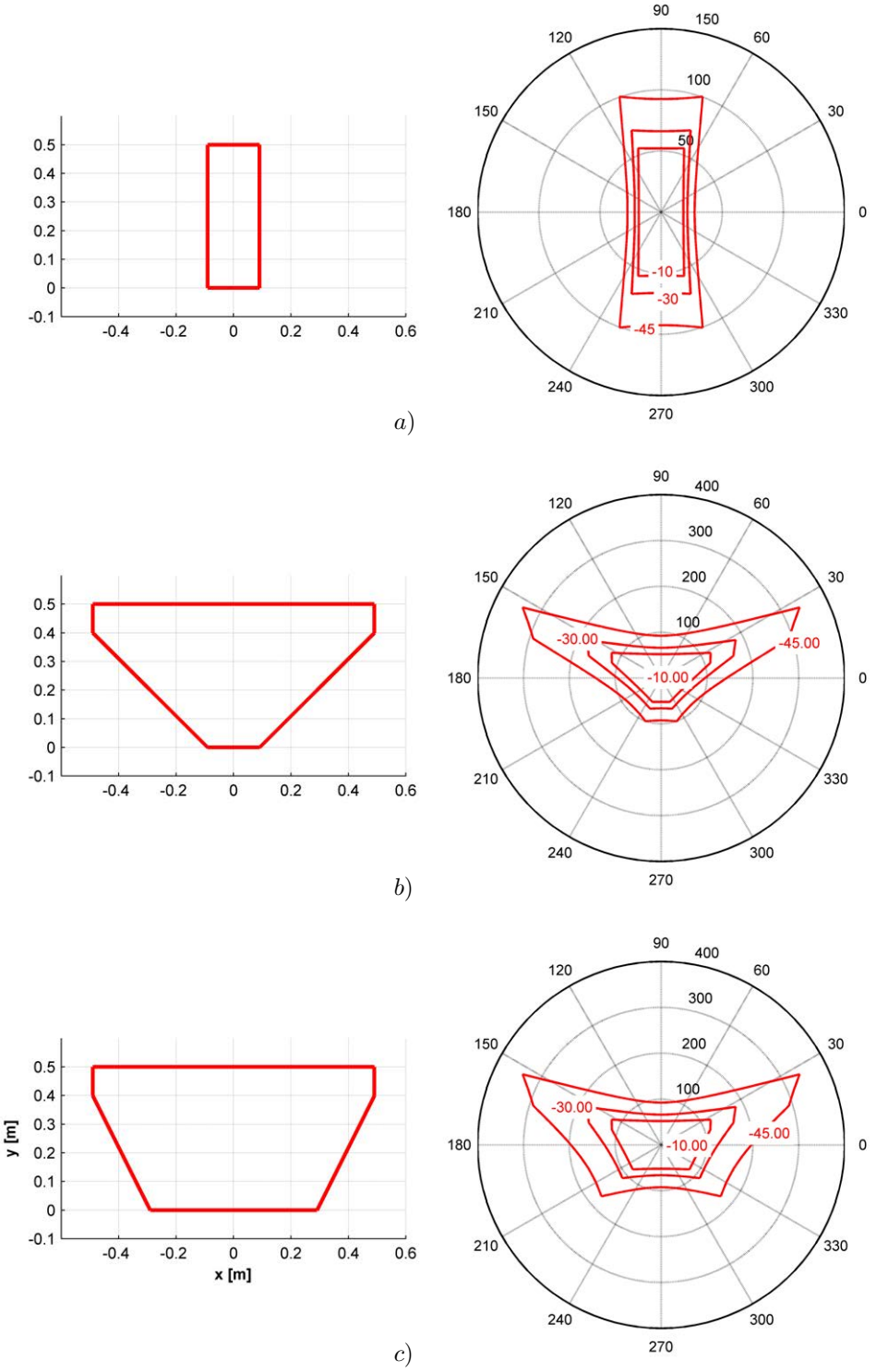

Figure 4.32: Shape of the stability polytopes for different footprints $\mathbf{p}_j|_A$, $\mathbf{p}_j|_B$ and $\mathbf{p}_j|_C$ which are visible respectively, on the left, in a), b) and c). For each footprint three different deflection angles from the horizontal plane are shown: $-45°$, $-30°$, $-10°$,.

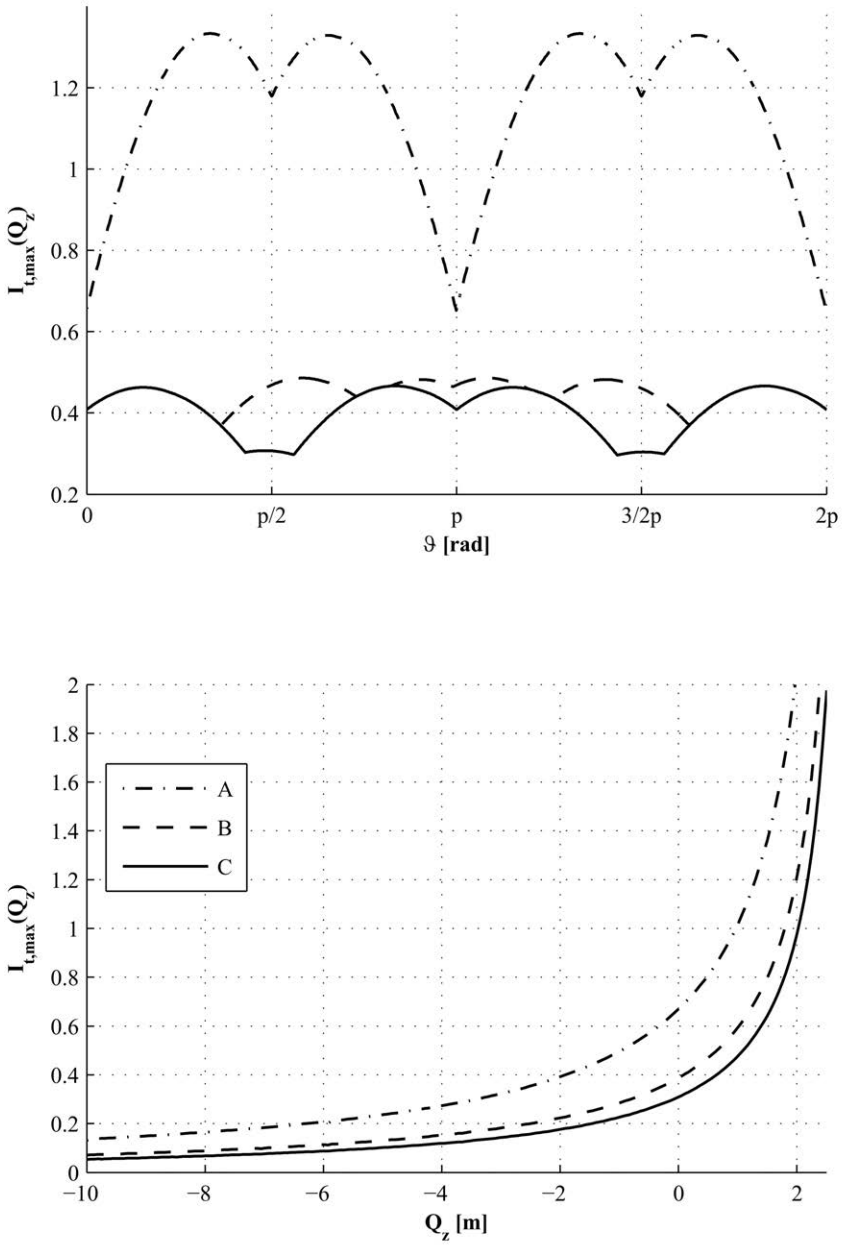

Figure 4.33: Characterization of the tilting index. The top plot shows the relation between the angle ϑ of the modules and the tilting index $I_{t,max}$ for the different footprints. The discretization steps are $\delta\vartheta = 2\pi/1000$ and $\delta x = \delta y \cong 0.47\ m$. The bottom plot shows $I_{t,max}(Q_z)$. Discretization is $\delta x \cong 0.17$, $\delta y \cong 0.15\ m$ and $\delta Q_z \cong 0.06\ m$.

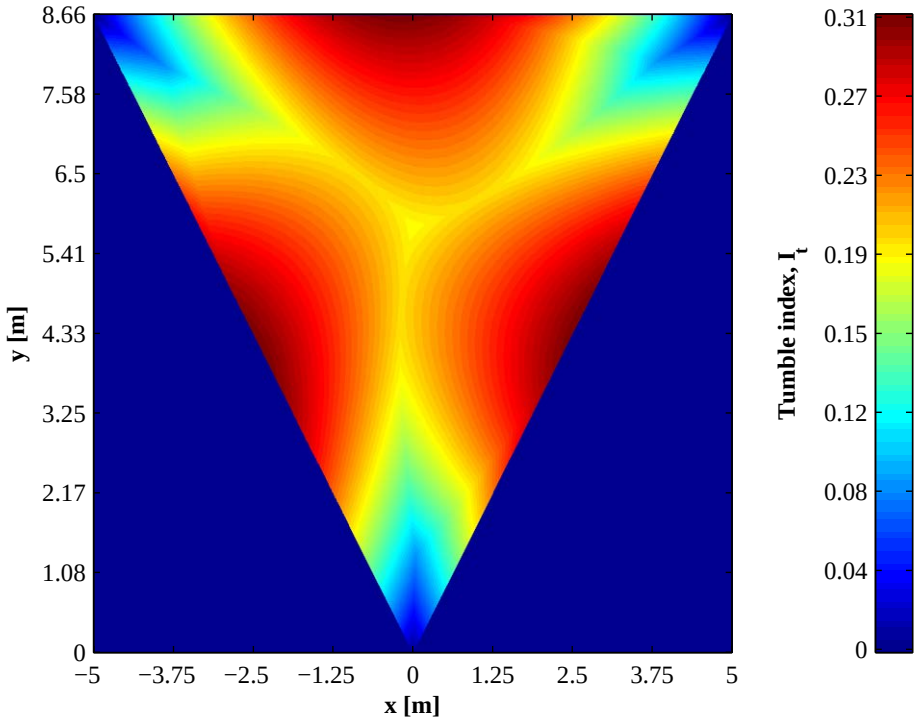

Figure 4.34: Map of the workspace of the modular CDPR at ground level. The angular position of the modules is $\vartheta^* = 1.384\pi$. Spatial discretization of the domain is, in this case, $\delta x = \delta y = 0.01\ m$.

mean to inspect this structure, as visible in Fig. 4.36. Furthermore, as the last two decades of exploration on Mars with Pathfinder, MER-A, MER-B and MSL rovers from NASA demonstrate [137–139], dust deposition over time is a major problem. To mitigate this problem, the modular CDPR, equipped with a simple wiping device, could be used for the removal of the dust.

Regarding this particular application, the DLR tackled the problem with an approach [135] based on a wheeled anthropomorphous robot called Justin which could perform both the inspection and maintenance of the system. However, this procedure is very complex in relation to the task to be carried out, especially for the inspection. Perhaps a joint approach would be more efficient, where the modular CDPR acts as the inspection device, and the wheeled robot as the manipulation and maintenance system. This would limit very much the overall complex activity of the latter, increasing the

global efficiency.

A very promising concept for a possible base on Mars or the Moon are inflatable structures [127–129]; one major issue for these is the structural integrity of the shell. Frequent inspections by rover or other conventional device (or even manned) would be hard, especially on the top portions of the dome. The modular CDPR could be deployed around the dome and provide fast inspection capabilities to the most inaccessible parts

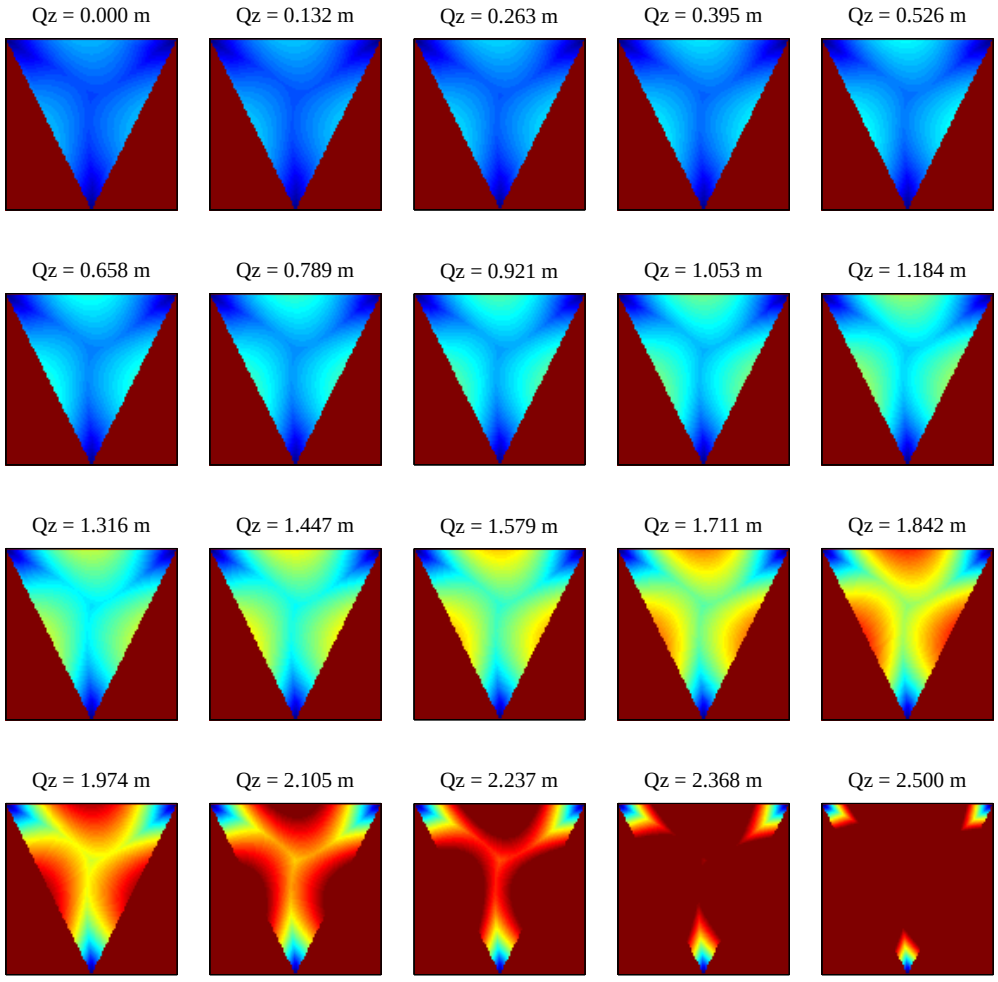

Figure 4.35: Mosaic of the configurations of the workspace at varying height from the ground. Note that the colour red represents $I_t \geq 1$ (instability) – and is infact used as a threshold – while blue stands for $I_t = 0$ (stability).

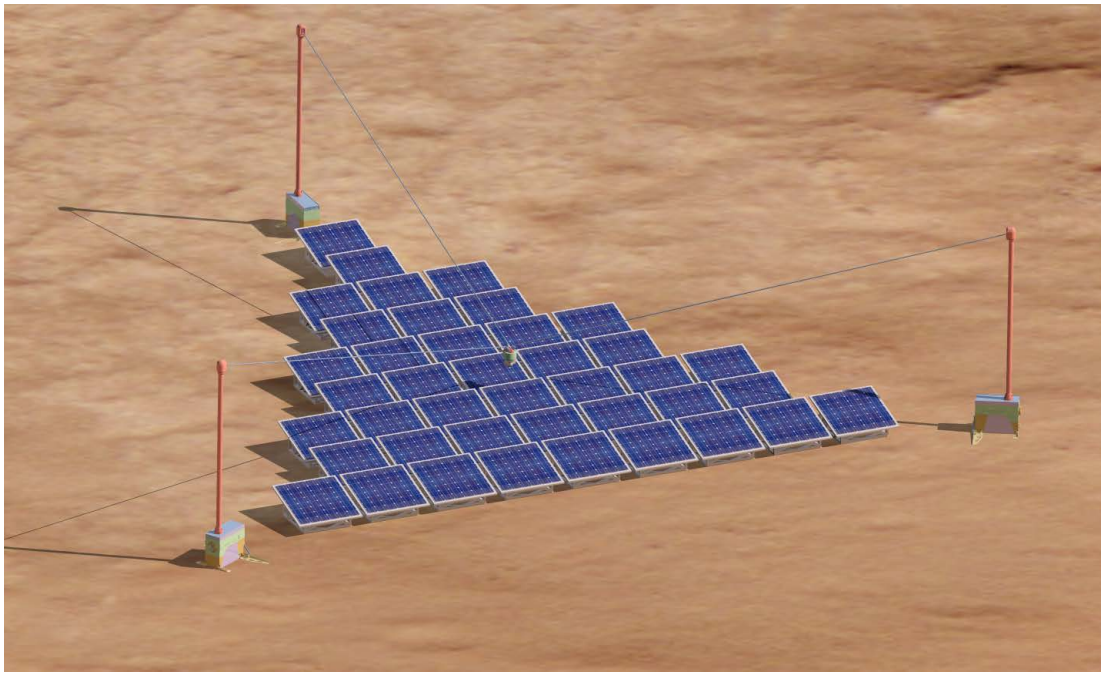

Figure 4.36: Application of the modular CDPR for the maintenance of a large ground-deployed solar array.

of the structure.

Celestial body ground geological surveys seek a collection of samples from large extensions of the surface to provide a representative set. This, in turn, requires a close-up investigation of potential sampling locations [131], which can be very inefficient and time-consuming with a conventional rover. A modular CDPR could allow a first inspection of a large surface (e.g. around 100 m^2 referring to Table 4.4) with relative ease.

Along the same lines, it could be exploited for the exploration of lava tubes [132], as visible in Fig. 4.37, either through simple visual inspection or as a deployment system for small rovers. Furthermore, some craters show very steep walls, which pose the same challenges [133] to exploration. In fact, in Fig. 4.33 one can see that a configuration where the load is lower than the ground level (such as is the case of any depression) has a very low tilting index $I_{t,max}$, which would increase stability and payload capacity.

As a last application example, the modular CDPR could be used as an efficient means of transport between the modules of a robotic or manned base, without the need to erect complex and un-reconfigurable structures for transportation.

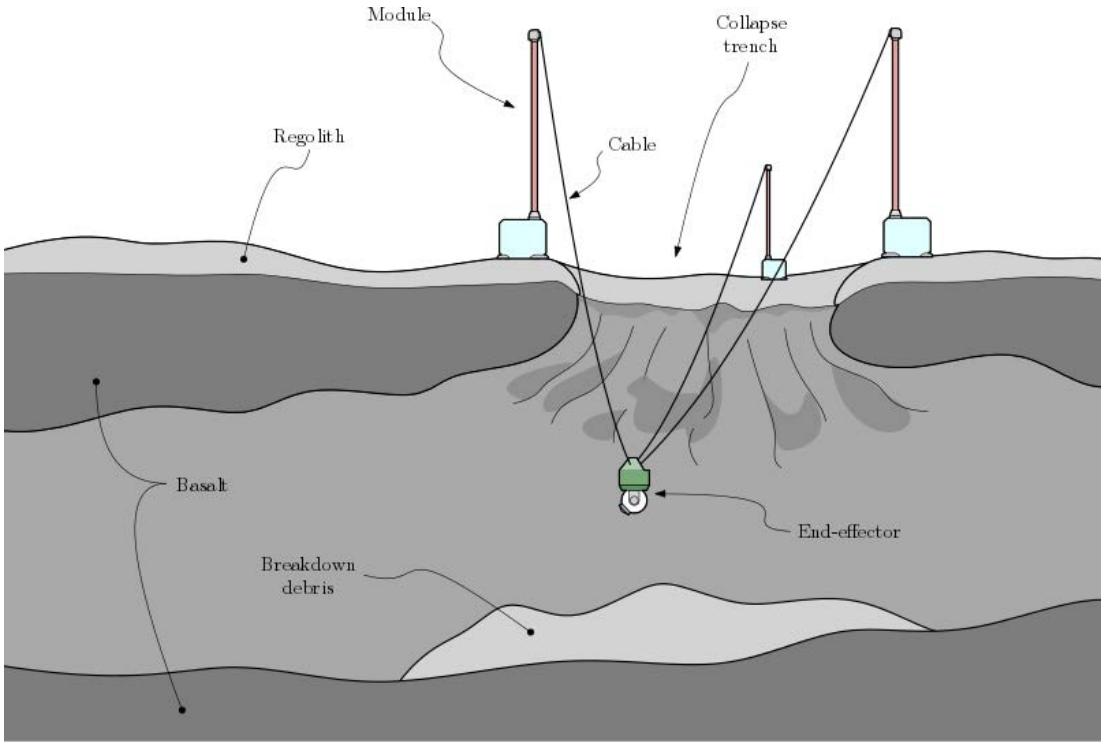

Figure 4.37: Application of the modular CDPR to the exploration of lava tubes on celestial bodies. The end-effector shown is in the form of a pan-tilt camera system.

5

Applications and Future Developments

We have decomposed the topic of Large Workspace Robots in three main parts, covering topological efficiency, path planning and hardware actuation, design and analysis. The complete methodologies or systems were illustrated in detail, with each method individually validated either experimentally, numerically or both.

In this chapter, the focus is in the integration of these algorithms, methodologies and procedures, in order to provide a coherent framework for the design and analysis of LWRs.

In particular three main topics will be discussed. The first sees the coexistence of the topics discussed in Chapters 2 on page 9 and 3 on page 55; specifically, the exploitation of the index for Repetitive Workspace Robots (RWR) is shown to be possible and useful in combination with robotised painting of large, photorealistic images. The second topic analyses topological efficiency concepts related to RWRs in the context of the modular CDPR presented in Section 4.3 on page 128 in Chapter 4. The last argument regards the more broad subject of the technical solutions applicable to the same CDPR; in particular stabilizer designs and mast actuation are discussed.

5.1 Topological Efficiency in Large Surface Robotised Painting

In Chapter 2 on page 9, the concept of topological covering efficiency was described, and an index, I_{RWR}, was defined for the purpose of quantifing the the associated value. In order to compute this, three algorithms were described: the uniform expansion covering algorithm (UECA), the corrected inertial ellipsoid covering algorithm (CIECA) and the genetic covering algorithm (GCA).

As mentioned in the same chapter, one of the main application is the field of robotized industrial painting. The outlined theory can work with these kind of problems without further modifications or improvements when uniform painting is concerned. In fact, the example given in Section 2.7.2 on page 45 refers to an industrial painting robot for use in the ship-building industry.

In general, when uniform covering is concerned, one needs not bother with matching patterns between local (repetitive) workspaces. This is not true, for example, when certain non-uniform kind of painting are considered. One example of these processes is described in Chapter 3 on page 55, photorealistic painting of large workspaces.

In Fig. 5.1 an example is shown involving the painting of a large urban complex. Operations alike can lighten considerably the cities landscapes, particularly in degraded neighbourhoods.

Figure 5.1: A simulation of an urban building complex painting with a lifelike pattern resembling a cloud-peppered sky.

5.1.1 Combining RWRs and Photographic Painting on Large Surfaces

In chapter 3 on page 55, we emphasize the fact that the process involves different layers, each at increasing level of detail. The first layers take care of larger, less detailed parts of the picture, while the final layers are all about the finishing touches.

Up until now, it was assumed that each layer was taken care of by the same robotic system, for example an industrial serial manipulator. A consequence of this line of thought is that the workspace associated to each layer was to be exactly the same. This is adequate when the difference between the size of details is comparatively small in the target image.

On the other hand, in principle, this means that a large – even the largest – portion of the image could be worked upon with a very large robot, e.g. a planar CDPR, characterized by high speed and large stroke size at the cost of a reduced accuracy. Other areas would then be worked upon with smaller robots: slower, but with increased precision. For example, in the case illustrated in Fig. 5.2, one can see that large sky-blue areas are present on the building façade, as well as complex shapes where clouds appear.

Conceivably, one could utilize a LWR in the form of a CDPR to cover the blue large semi-uniform areas, and a RWR like a serial manipulator mounted on an AWP to cover the smaller details found in the clouds.

Being it so, the methodology highlighted in Chapter 3 could be used without substantial modifications, to cover the first part of the process, while the methods presented in Chapter 2 might be exploited to complete the detailing in an efficient way.

5.1.2 A First Glance at the Procedure

In principle, a general procedure can be broken up in three phases:

I. Painting of the uniform coloured background,

II. Painting of the large-size non-uniform details,

III. Incremental detail painting.

Since the area to cover in the first steps is very large – possibly in the order of hundreds of square meters – a suitably large spray gun or similar end-effector should

be selected for phase I. Composite systems could be conceived, as, for example an array of spray guns; other possibilities could be related to traditional uniform wall-painting techniques, as a painting roller or large brush. These systems can help in covering very large surfaces when the majority of the surface is of uniform color. Along the same lines a suitable LWR capable to cover the entire surface should be selected for maximum efficiency. The algorithm presented in Chapter 3 can perform satisfactorily with these systems, provided that the correct parameters and coefficients are applied. Uniform covering can be useful in the first couple of layers, depending on the type of image to be reproduced on the wall, and the degree of uniformity of colour.

Phase II would require a spray gun or array thereof, in order to be able to complete the larger details of varying colour intensity. During this phase the end-effector can

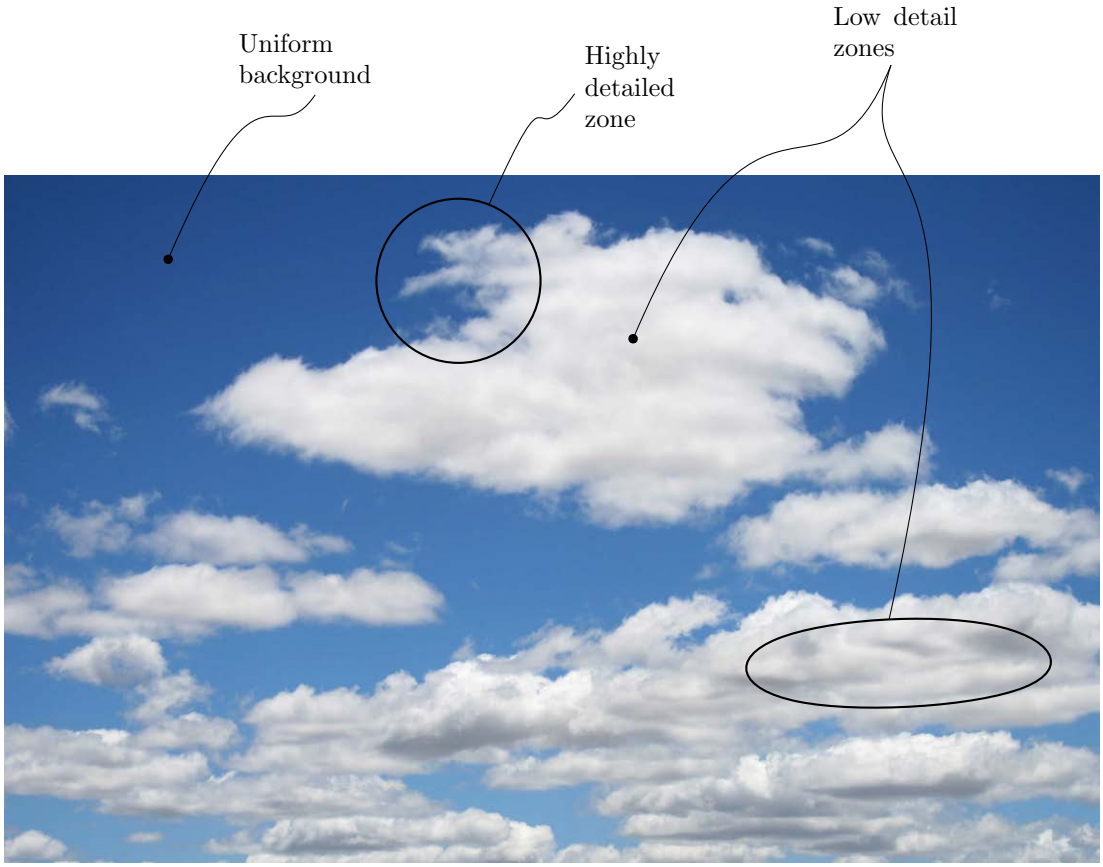

Figure 5.2: Detail zones. In the figure, which is cropped from the image used for Fig. 5.1, three main zones can be seen: the almost uniform background, some low-detail zones in the clouds' bulk, and high-detail zones on their borders.

be still attached to the LWR used in phase I, as accuracy is not yet a main concern. However, if the details at this phase are already very small one should consider employing a smaller robot. In this case, the rest of the process shall be carried out following the approach of a RWR, i.e. partitioning the areas that contain the details yet to be painted, and addressing them sequentially.

Phase III is characterized by the maximum accuracy, and the detail level is typically so high that accuracy becomes a major factor in the process. The RWR approach is in this case recommended.

It should be noted that the path-planning algorithm presented in Chapter 3 works by defining a ITI (Iteration Target Image) at the beginning of each layer, as the difference between the TI (Target Image) and the current state of the canvas. From this, it follows that the process described in phase II and III if a RWR paradigm is considered, can be completed either layer by layer or by local workspaces. In the former case, one should paint the entire building façade in one layer, partitioning the area as necessary, and then get to the next layer and resume work in each partition but with a higher level of detail. In the latter, one could partition the canvas and proceed, in each local workspace, to complete the remaining layers, sequentially. In general, the former case would be efficient whenever different tools were needed between one layer and the other (e.g. different nozzle sizes), while the latter would be best with geometrically active nozzles, or when varying the spray gun distance from the canvas to achieve the correct stroke size.

5.2 Topological Efficiency of a Modular, Reconfigurable CDPR

In Section 4.3 on page 128, a modular reconfigurable CDPR was presented for use in harsh environment like Mars and the Moon. It was shown that the robot is made of three modules which are individually deployed by a rover. The end-effector is then connected to the cables.

In this section the exploitation of the RWR methodology described in Chapter 2 in conjunction this type of CDPR is investigated. In particular, two very different approaches are taken into consideration:

- Imperfect efficient covering,
- Complete covering of a surface.

The following sections will outline the process and the possible issues of each approach.

5.2.1 Imperfect Covering

The CDPR workspace shape can be seen in Fig. 5.3, highlighted in grey; it resembles a roughly triangular shape. This shape can be seen mainly from Fig. 4.35 on page 144, in the last configurations (from $Q_z = 2.105\ m$ onwards).

Pure periodic tessellation with triangular tiles can always be made. However, since the workspace is not perfectly triangular, but has some degree of "erosion" around its boundary, if the usual triangular lattice is employed, an incomplete tessellation will result. This is visible in Fig. 5.3. If the left-out area can be made sufficiently small by acting on the geometry of the robot, this can still be a satisfactory result for some applications.

The procedure by which this is achieved is, in principle, simple, and is illustrated in the figure. The rover in charge of moving the modules should pick up the module in $\mathbf{P}_1$ and move it along the r_1 path. This generates the 2^{nd} workspace. At this point the procedure can be repeated by moving the module in $\mathbf{P}_2$ along r_2 and so on.

The complexity of the procedure escalates with $O(n)$, where n is the number of repetitions in the process. This is because it is possible to cover a surface of arbitrary size with this exact procedure, although this is not demonstrated in this work.

For example, when doing prospecting in preparation for sample-collection over very large surfaces. The sample-collection in itself is a task which is routinary during the operations of the rovers presently on Mars, however, due to the impossibility of covering large surfaces easily, in order to decide the best spots to sample, the team operating the rovers must confide solely in the long-range capabilities of the cameras or similar optical instruments that are present on the rover.

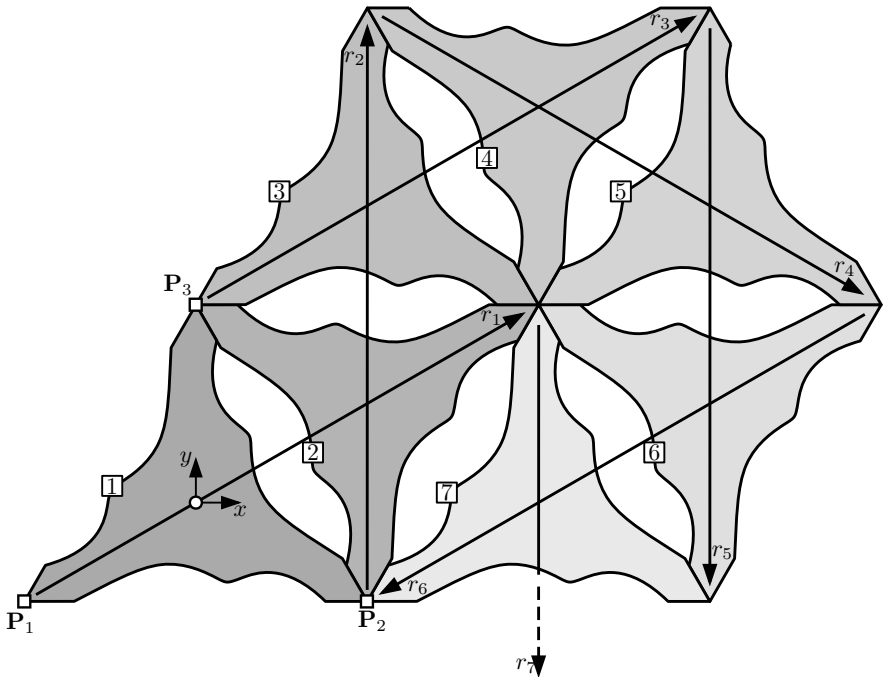

Figure 5.3: Incomplete covering of an arbitrarily large surface through tessellation with local workspaces. The tiling can be achieved by "flipping" the robot along the r_i vectors. The numbers in the rectangular boxes indicate the sequence at which the workspaces are "generated".

5.2.2 Complete Covering

Contrary to what summarized in the preceding section, the need to have a complete covering of a large workspace can arise in some scenarios. In this case a more conventional approach using RWR can be exploited.

Referring to Fig. 5.4a, it can be noted that there is one important difference compared to the methodology illustrated in Chapter 2, that is, when the workspace has

the general shape of a triangle, the most efficient covering pattern is where there is an alternation of the direction of the tilings.

However, the algorithms presented in Chapter 2, do not allow for these kind of pattern. In principle, the GCA can be modified in order to work correctly, but UECA and CIECA cannot without *substantial* rework.

There is, on the other hand, a workaround which can lead to coherent results. This is shown in Fig. 5.4c. Starting from the concept of tessellation, as visible in *c)*, it is apparent that the tiling can be done with a composite tile which is made from the original workspace and its rotated copy. This produces a shape which can "tessellate" – or better, efficiently *cover* – the surface.

Extending this concept to the covering problem, the original workspace, a roughly triangular shape, can be united to a 180° rotated workspace, which is translated in a way to create a composite workspace that satisfies the conditions stated in Eq. 2.14, in Chapter 2. In essence, this means having a connected shape with no holes, or discontinuities. This composite workspace can be seen in 5.4b. Indeed, this is very similar in concept to what can be seen in *c)* of the same figure, although with simple triangles; note that the triangles are alternatively rotated by 180° (the workspaces are shown with different shades of grey, in the figure, based on their orientation).

This approach allows a complete covering of the target surface by means of the modular CDPR. However, it must be noted that the efficiency of the overall system is hindered by the fact that all three modules that define the CDPR's workspace need to be moved at each step. This was not necessary with the preceding methodology of imperfect covering.

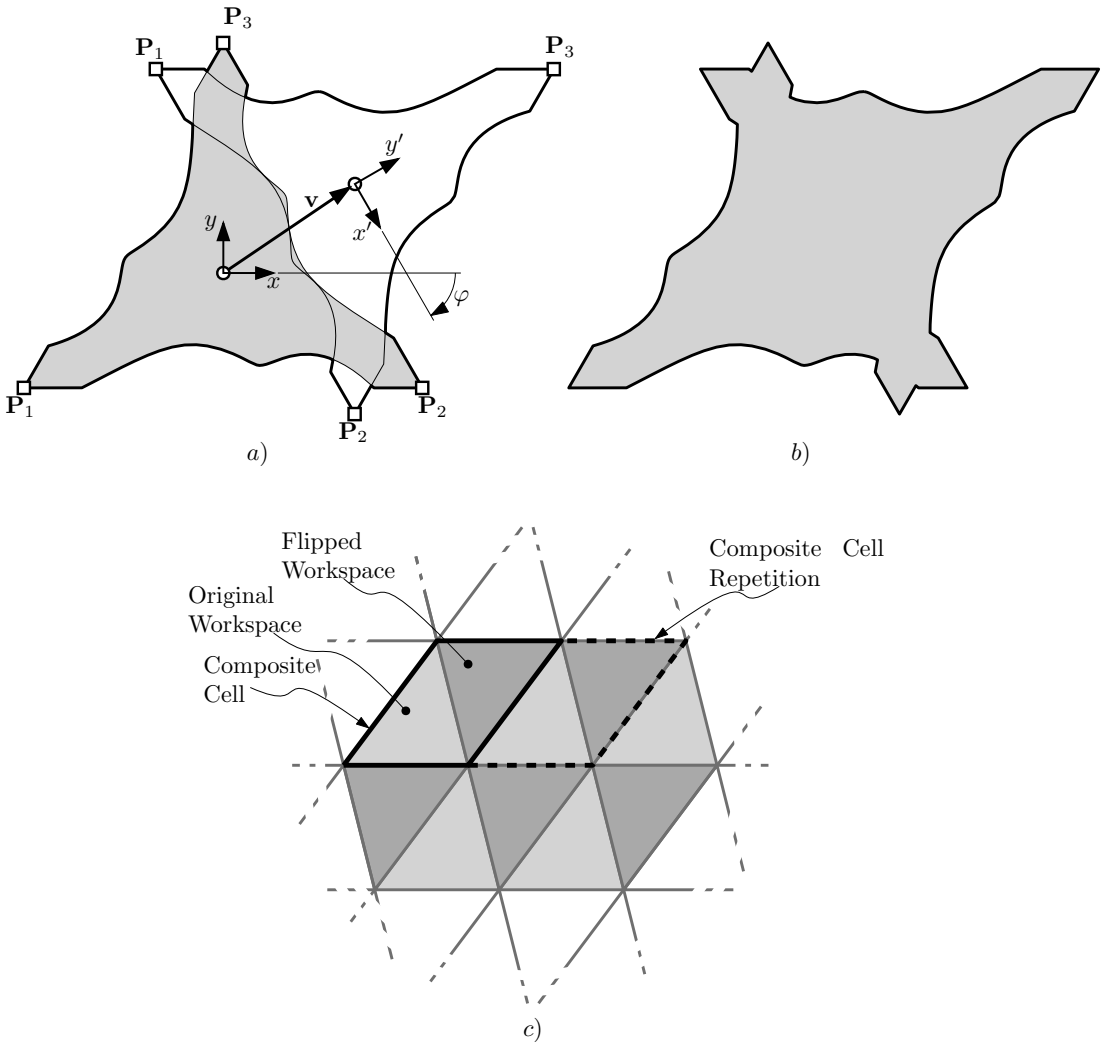

Figure 5.4: Workspace of the modular CDPR. In a) the actual workspace is shown, whereas in b) the composition of two workspace is visible. The composition is made to allow the I_{RWR} index to be computed. Finally, in c) a composite tiling is shown as would be if simple triangles were chosen.

5.3 Technical Solutions for the Deployable Modular CDPR

Similarly as in the preceding section, we once again consider the modular CDPR presented in Section 4.3. In this section focus will be given to some aspects of the actuation of the robot, namely, the possible technical solutions for the mast and stabilizers deployment.

In Fig. 5.5 a version of the module is illustrated, so as to provide reference in the

sections that will follow.

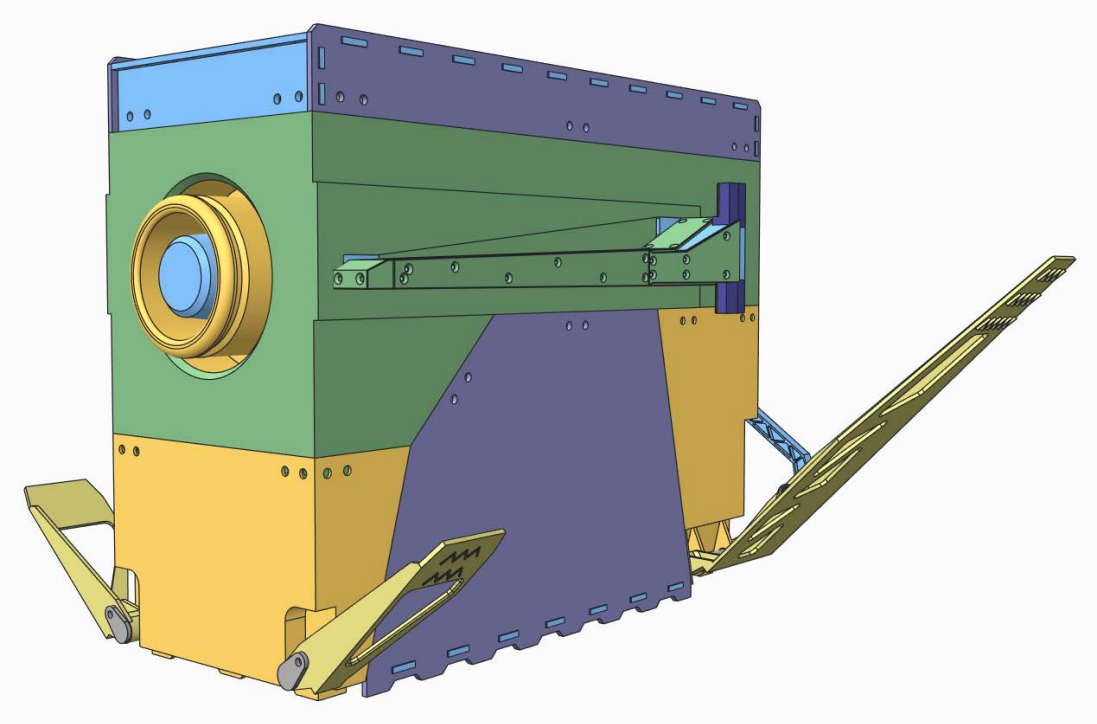

Figure 5.5: A module of the deployable CDPR. In this example version, the module has both main and secondary hinged stabilizers. A docking adapter is visible as well. The mast assembly is not included in the Figure.

5.3.1 Mast Actuation and Considerations on the Center of Mass

The modules that are deployed on the surface of interest are, in principle, not anchored firmly to the ground. In fact, as was illustrated in the relevant sections, each module leans on the friction between itself and the soil and the inherent stability given by its footprint and the height of the center of mass (CM).

In the theoretical model presented in Section 4.3.2 on page 133 the general assumption was that the ground was parallel to the horizontal plane. However, this is a gross simplification, in that often the ground is not planar but tilted in some way. What keeps the module stable in this condition relates directly to the height of the CM, since it affects the stabilizing moment created by the force of gravity acting on the CM location.

At this point it is easy to spot that one solution to mitigate and keep under control this problem is to keep the CM as low as possible. However, as is clear from the results of the workspace analysis, the higher the masts are, the higher tends to be the stability of each module. In fact, this relates to the fact that the cables tend to get closer to vertical, and so does the direction of the pulling force acting on the top of each mast. This obviously translates into a lower toppling moment. This is illustrated in Fig. 5.6. In the figure two cases are illustrated, indicated with the subscripts *1* and *2*, respectively related to a low CM and a higher one. The stabilizing moment $\mathbf{M}_{G,k}$ results higher in the first case, this due to the lower CM G_1 projection $\mathbf{G}'_1$ being farthest to the fulcrum side $\mathbf{e}_k$.

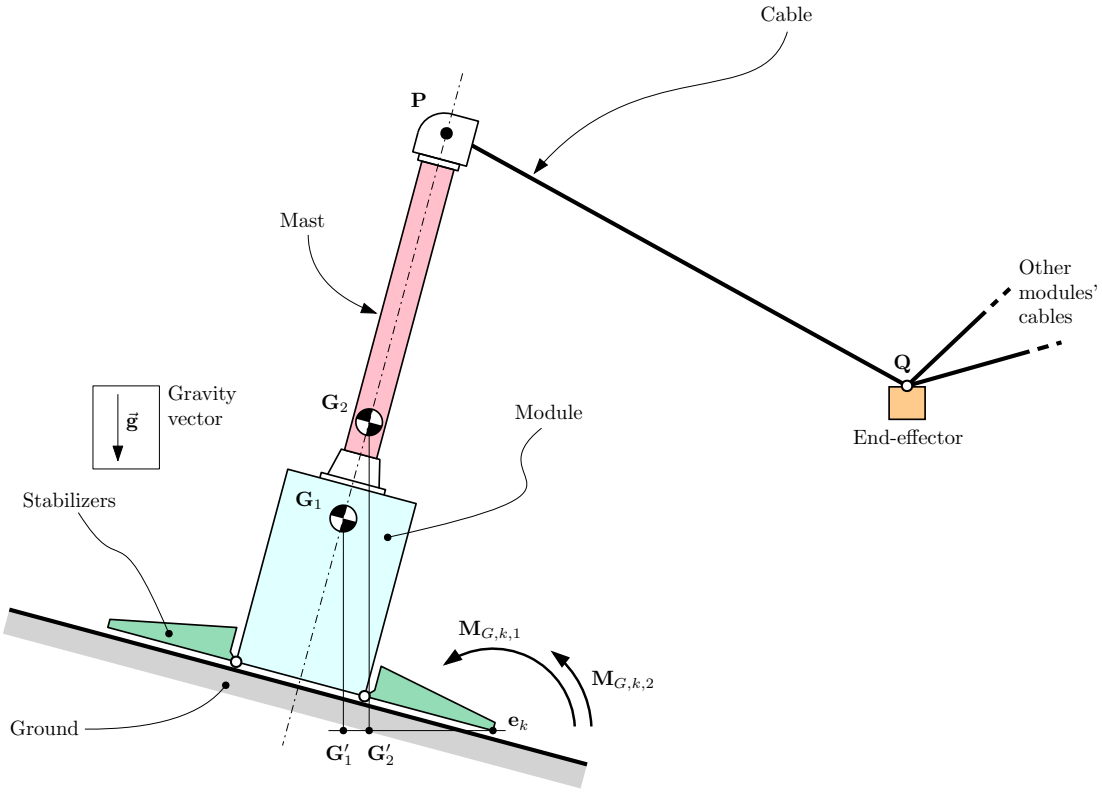

Figure 5.6: A module deployed on a slope. The figure shows the relation between the height of the center of mass (CM) of the system and the stabilizing moment $\mathbf{M}_{G,k}$ in two cases, 1 and 2. The gravity vector field direction is indicated in the figure as $\vec{\mathbf{g}}$.

In order to keep the CM low, steps can be taken in the technological choices made in the design of the mast. One example can well be STEM structures, as illustrated in

depth in Section 4.1 on page 78 in Chapter 4. The high elongation and compactness of the STEM actuators, united with the extreme lightness of the erected structure, make these the perfect choice for this kind of application. Besides, since the most part of the mechanism and actuation is in the base of the actuator, the CM can be kept very low even with high translations. On top of this, STEM structures are best used when marginal bending moment is present, which is the case in this embodiment.

5.3.2 Stabilizers' Designs

The stability of the module is best described by the polytopes seen in Section 4.3.3 which are based on various geometrical parameters, among which the most important is the shape of the footprint. The stabilizers, which were introduced in the same chapter, are deployable light structures used to expand the footprint of the module, thus greatly increasing the stability of the overall system.

In the following, some possible designs, which were considered in the conceptualization of the modular CDPR, are illustrated.

5.3.2.1 STEM-based Stabilizers

As all Space-based systems the modules have the need to keep mass at a minimum. For this reason, the approach of using STEM based actuators proves to be effective, as was illustrated in Section 5.3.1.

Referring to Fig. 5.7, a schematic of the system can be appreciated. The idea is using two STEM actuators placed either on one end of the module or in its middle, oriented at an angle towards the ground. This configuration keeps bending moments – which tend to be somewhat critical to STEMs – to a minimum while at the same time keeping weight under control. By making some simple geometrical considerations, an angle of roughly 45° (with respect to the vertical plane) can be considered adequate, provided that the feet of the stabilizers do not slip across the soil. In fact, this would generate a bending moment on the STEM. Larger angles tend to increase the likelihood of this happening.

5.3.2.2 Hinged Stabilizers

Hinged stabilizers are a promising choice in terms of ease of manufacturing, reliability, re-usability and strength. A glance at parts of this mechanism could already have been

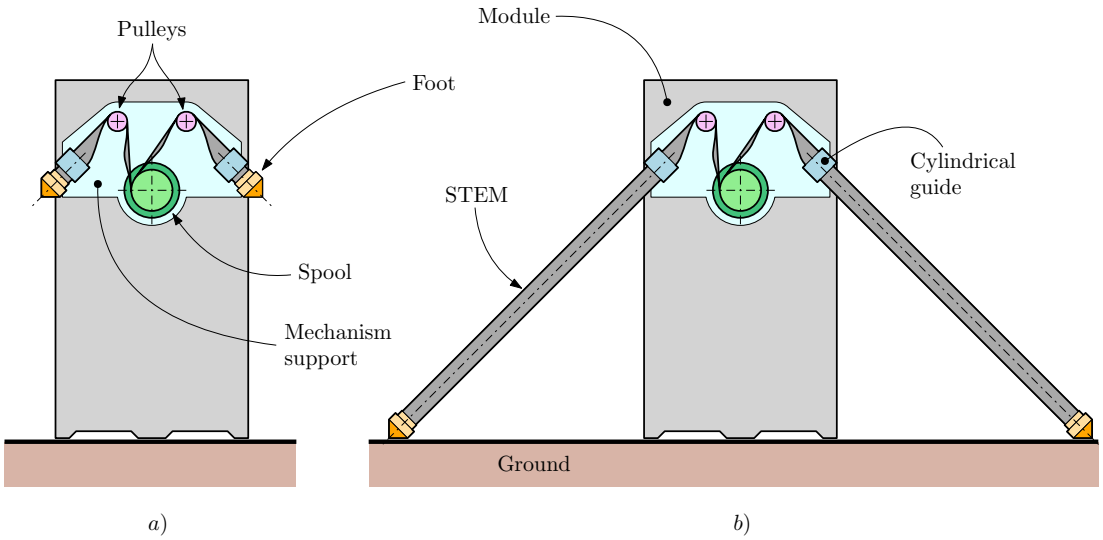

Figure 5.7: STEM-based stabilizers for the modules of the deployable modular CDPR. In a) the retracted configuration is shown, whereas in b) the fully deployed one is illustrated. Note that the mast and other systems are not depicted in order not to clutter the figure.

given when referring to Fig. 5.5. The goal is to keep the mechanism as thin and light as possible, while taking advantage of one actuator unit alone.

Initially, a motorised hinge system was considered; however, this poses several disadvantages:

- Large torque on the hinge actuators and structure,
- Either the use of at least two actuators (one for each side of the module), or the use of a mechanical transmission between the hinges,
- Contact between the actuators and the soil (possible contamination).

For this reason, a solution based on a coupled double quadrilateral mechanism to operate the stabilizers was proposed. This is shown in Fig. 5.8, where the actuator is shown in red, the stabilizers in yellow and the push-rods in blue. The motion is transferred to the secondary stabilizers through the main-secondary shaft, which effectively connects rigidly these to the main stabilizers. A complete analysis of the system is given in Appendix B.

Figure 5.8: Module with hinged stabilizers and deployment mechanism. In a) the complete mechanism is visible in an intermediate position, while in b) the deployed configuration is shown. Note that the mast and other systems are not depicted in order not to clutter the figure.

6

Conclusion

The proposed definition of the class of Large Workspace Robots (LWR) is one way to address industrial and scientific requirements by focusing on efficiency in its broadest sense. This was given in the Introductory chapter (Ch. 1 on page 1) of this research.

As was discussed throughout this manuscript, there is, at present, no description of procedure or approach which is tailored on robotic systems characterized by large working volumes or areas. On one hand, in the field of medium- to small-sized workspaces, robotics has a plethora of methodologies, approaches and hardware to take advantage of; on the other, when faced with larger spaces, the general tendency is at best to adapt – scaling up – smaller systems, or use hybrid systems that require considerable additional work to be operationally viable.

In this research, some answers were given – or were attempted – to some of these problems. The main topic was divided into three parts, with a first one dedicated to an in-depth analysis of some topological methods on surface covering, a second part that provided an algorithm for industrial painting of large surfaces, and, finally, a third part consisting of a description of several practical solutions and technologies that shine in this particular field.

As such, in the following sections, we will explore the main points and conclusions of each part, and provide a final conclusion to this research

6.1 Topology

In Chapter 2 on page 9, we closely examine the topology of Repetitive Workspace Robots (RWR); these consist in a robotic system that operates in a sequential manner on space. The system comprises a robot with a workspace of an arbitrarily small size, and a – in principle – disjointed mechanism to move it around space. This last can be another robotised system, a semi-autonomous one, a manned vehicle, and so on. Geometrically, the region of space that needs to be worked upon is partitioned into a series of smaller regions, coincident with the local workspace of the small robot.

However, since the shape of most robot's workspace tends to be irregular, the partitioning of the surface – or of space for that matter; however, here we focus on a planar case – can be defined with some difficulty. In fact, in the vast majority of cases this problem has no analytic solution. The problem, in its most generalized abstraction, is called Set Covering Problem (SCP) and is part of the NP-Complete set of problems, for which a fast solution is not currently known (or as is theorized, doesn't exist at all).

In order to address this problem in a manner that is technologically viable, an index, referred to as I_{RWR}, was defined to describe the aptitude of a robot, or rather of its workspace, to be employed as a RWR. In the interpretation described in this manuscript, a pattern of repetition was used in the form of a lattice, or grid. This allows for indefinite repetition. Three methodologies were determined for its computation. The first is based on a genetic algorithm, called Genetic Covering Algorithm (GCA); this serves to the purpose of calculating the index and providing a baseline value that has the maximum likelihood of being correct. The solution space of this method belongs to $\mathbb{R}^5$.

The second methodology, the Corrected Inertial Ellipsoid Covering Algorithm (CIECA), is based on the concepts of area moment of the 1^{st} and 3^{rd} order. After a first simplification which transforms the solution space into $\mathbb{R}^4$, these are used to partition the GCA solution space into a simple 1D space, which allows for fast search methods to find the actual solution.

The third, and last, method, called Uniform Expansion Covering Algorithm (UECA), is characterized by its speed. This is achieved at the cost of a larger simplification than what was employed by CIECA. In fact, the solution space in this case is natively $\mathbb{R}^1$, which allows the same search methods to be used to compute the solution.

In general, there is strong evidence – supported by literature on the subject, as well – that the GCA is able to find the correct solution, so it provides a fair baseline for a comparison of the other two methodologies. The time of computation, however, proves to be very long, in the order of 10^2 times compared to CIECA, and 10^3 times against UECA. It is though able to detect skewed lattices, contrary to the other two algorithms.

Several different workspace shapes were tested in order to evaluate the algorithms performance. In particular, the CIECA algorithm proved to be the best compromise between accuracy and time of computation. UECA can be used in some special cases thanks to the underlying simplifications that were exploited. In fact, it can be used to convey a really fast approximation when large problems need to be investigated.

Two real-world applications were presented in the research. A CDPR was described and its design was shown to be greatly improved thanks to the use of the I_{RWR} index computed with UECA. A response surface was computed to show the influence of two design parameters on the index. This is feasible, in fact, precisely because of the speed of the UECA algorithm.

The CIECA algorithm was then used to determine and compare the aptitude of two industrial painting robots to act as RWR. In fact, it showed that the best of the two was the one with the smaller workspace area, which is a counter-intuitive solution.

6.2 Control

In Chapter 3 on page 55 focus is given to an innovative methodology for the path-planning of industrial painting. Two peculiarities characterize this approach: the size of the workspace, and the fact that the painting is not uniform but in grey-scale.

An in-depth literature analysis shows that, when robotic systems are concerned, the only painting tasks which are commonly performed revolve around either uniform painting (e.g. automotive, furniture industry) or artistic-looking painting. The only field where photo-realistic painting is present is in the printing industry. Additionally, we develop a methodology that gives its best when the surface to be painted is large, in the order of hundreds of square meters.

The method itself revolves around the iterative partitioning of the target image by an algorithm based on an Ordinary Least Squares (OLS) solution approach. The

partitioning itself is not spatial, but rather by detail level. In essence, the image is decomposed in layers with an increasing level of detail. For each layer, starting from the large details, a path is planned both geometrically and speed-wise. The process repeats iteratively with smaller and smaller details. The crucial point is that the dimension of the paint-tool (e.g. a spray gun), is defined based on the size of the details at the current level. This allows to paint the large areas of the picture where details are scarce or absent with very large strokes.

The algorithm that was developed takes advantage of Voronoi diagrams and offset calculation for the determination of the geometry of the path, and uses OLS to compute the speed profile of the trajectories of the end-effector. Some techniques pertaining to the image analysis field are used in the segmentation of the image. The OLS system is build taking into account special critical points that can be local or global depending on their relation with the stroke path. These effectively build the coefficient matrix used in the system.

In order to prove the efficacy of the methodology, the famous Lena test image was employed. Results of simulations show that the methodology presented in this chapter would be able to complete a 1 square meter representation of the picture in approximately 45 minutes, whereas a Cartesian printer with a similar resolution and a similar nozzle geometry, would have employed more than 4 hours.

6.3 Actuation

In Chapter 4 on page 77 a more practical approach was illustrated towards the topic of LWRs. Actuation and design of these system can pose several challenges, since state-of-the-art actuators and technological features are normally designed for robots with different characteristics than those related to LWRs.

In principle, LWRs need actuators which are light and have exceptionally large strokes (when of the linear type), while at the same time limiting bulk dimensions as much as possible.

The first technology that was investigated is based on Storable Tubular Extendible Members, or, in short, STEM. These are collapsible structures that can be exploited into linear actuators that are light, compact and provide extremely large elongations. They are used abundantly in the space industry to deploy antenna booms, solar panel arrays,

or sensor masts. A semi-analytical model was developed, a prototype of a STEM-based actuator was designed, tested and built. Exploiting these a planar, STEM-based parallel robot was designed and analysed, demonstrating many advantages over similarly structured CDPRs.

Following an entirely different approach, the concept of Variable Radius Drum Mechanisms (VRDM) was explored. In essence, these are based on the Variable Radius Drum (VRD) element, which is a drum where the radius is not constant but follows a mathematically defined function. The research that was carried out stemmed the ideation of a novel class of actuators based on this mechanism. As an example, a robotised overhead crane design was shown that utilizes two cable-based VRDMs in parallel to achieve the translational movement on the larger axis. A working prototype of the linear actuator was produced using 3D printing techniques, and was evaluated, showing remarkable accuracy.

Finally, a complex deployable and reconfigurable modular CDPR was designed for space applications on the Moon or Mars. The architecture is composed of three stand-alone modules, an end-effector, and a rover with a robotic manipulator. In the relevant sections, the deployment procedure was illustrated in detail, and the main sub-systems were described in detail. A complete model of the CDPR was presented, taking advantage, among others, of the stability polytopes of the modules; this was used to perform a preliminary workspace analysis and to show the main design parameters. Possible applications are in the field of visual inspection and light manipulation. For example, a setup for inspecting a large solar panel array (in the order of 100 m^2) was described; furthermore, it is exploitable to investigate lava tubes and possibly as a deployment device for smaller rovers in these natural structures.

6.4 Applications and Future Developments

Some possible applications which employ combinations of the methodologies described in the previous sections were explored and some future related developments are described.

In the first section, two different approaches were described, related to the industrial painting of very large surfaces. This encompasses both the field of Repetitive Workspace

Robots as well as that of the path planning and image detail decomposition for photo-realistic painting. It is discussed how the layer decomposition can be made independent on the tool used by the end-effector, so as to employ different kinds of robots for the different detail-levels present in the image. For example, it is described how the larger details can be worked upon by a large CDPR while the smaller ones can be addressed by a conventional industrial painting serial manipulator employed as a RWR.

Secondly, a way to couple RWR operations to the modular CDPR for space operations was illustrated. Two kinds of covering of a surface are described, the former being an imperfect covering scheme, and the latter a complete covering one using roughly triangular workspaces (as is the case of the described modular CDPR). The strong points of the first one is that it allows the robot to cover an arbitrarily large surface by using a specific "flip" pattern. The obvious downside is that this provides a limited covering, thus leaving "empty spots" in the overall workspace. The second methodology is an extension of the topological methodologies presented in Chapter 2, in that it provides the foundation concept for generating a triangular latex in place of the parallelogram one that is the basis for the I_{RWR} index.

Finally, some technical solutions are described for the modular CDPR for space applications. These are based essentially on the STEM technology and provide a response to some critical issues, namely the cable-feed mast actuation and the stabilizers of the modules. For the former, a solution using STEM actuators is described and finds confirmation in literature. Regarding the stabilizers, two ways were explored: STEM-based linear stabilizers and hinged, crank-rod actuated stabilizers.

6.5 Tying it all Together

The field of Large Workspace Robots is a broad one; it is also one that was never evaluated organically as a whole. In the research presented in this manuscript, a definition of LWR was given as the starting point, and the most important aspects of these kind of systems were investigated: topology of the workspace, path- and speed-planning, actuation and design and practical, within-reach technological solutions.

This allowed to provide a general framework to the design and analysis of Large Workspace Robots. Several examples of practical applications are described, from common industrial practice (industrial painting), to high-technology (space applications),

showing that this particular field is substantial and should be considered in the design process, whenever geometrically large endeavours are concerned.

As it is a newly defined field, much work has yet to be done to examine all the possible ramifications. Some directions were explored, particularly the one of RWR, where the methodologies described in the presented research show potential and some issues yet to be addressed. Another possible road is that that was opened by path-planning for photo-realistic painting, and was later expanded by describing decoupling methodologies for the layers, thus allowing collaborative robotics between different systems or tools.

Appendices

Appendix A

Simulation of the Paint Deposition Law

The law that underlines the phenomenon of the deposition of paint on a substrate is a matter of interest for the study that is presented in this manuscript. Some experimental results were shown in Section 3.3.2 on page 62.

In order to support these results, a simulation was performed on the same phenomenon. Therefore, the scope was to simulate in a realistic manner the process of paint-deposition on a surface by means of spray-paint. The paint is considered as an atomized fluid, thus composed of small droplets of liquid that impact against a substrate.

An analysis is performed on the impacts, both from a microscopic point of view as well as from a macroscopic one. Saturation constraints are considered, obviously. Furthermore, we consider a process called "splat", where droplets that hit previously impacted points on the surface – which are thus already covered by fresh paint – cause the affected droplets (both the old one and the new) to expand by a certain factor. This is made to account for the fact that, being paint fresh, it will "overflow" and cover a larger area, rather than stay where it landed. Quantitatively, this is determined by the radius of each droplet; in fact, these are considered as spheres (and half-spheres when they are in contact with the canvas), so the volume of liquid pertaining to each is easily computable using basic 3D geometry. The intersection volume is computed as well, and is then added to the droplets, thus generating the adequate expansion.

The algorithm structure is based on steps and sub-steps. Inside each step, a certain

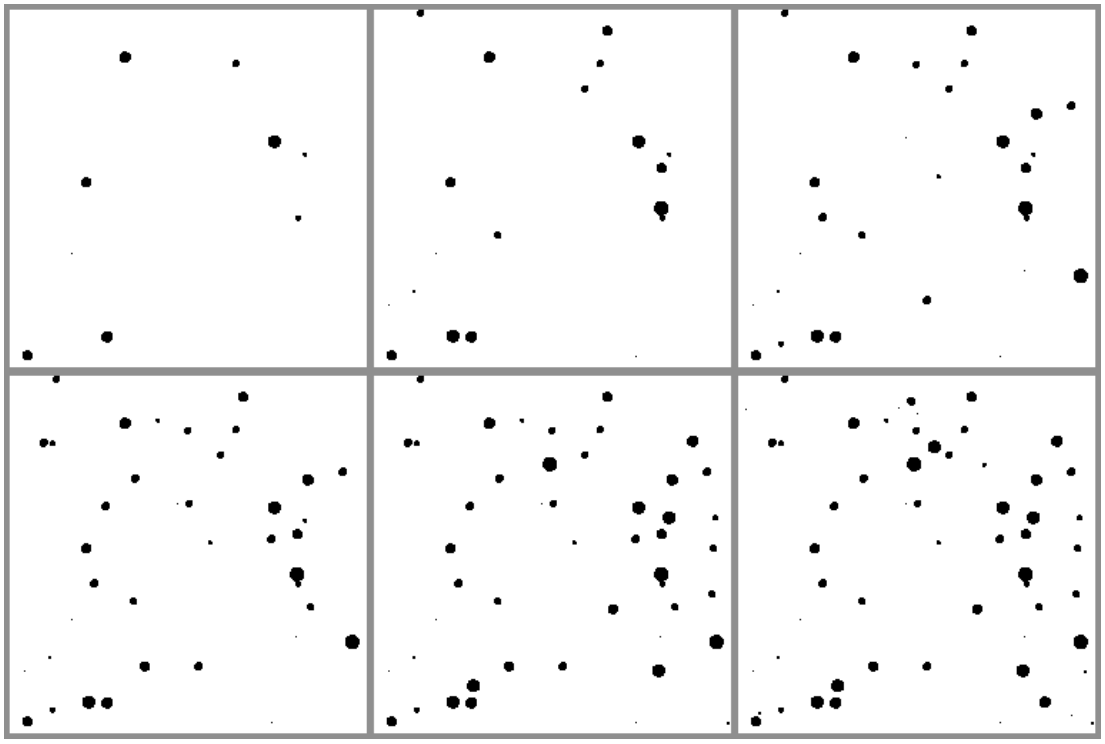

Figure A.1: Illustration of the paint deposition's first 6 layers for a 500x500 pixel canvas, 10k steps, 10 drops/step, alpha 1.0 (100% opaqueness).

number n_{blobs} of circular droplets is applied to the canvas (each sub-step is dedicated to one drop). The position of each drop is determined using an uniform distribution. Drops are, moreover, uniform in density, and have a diameter that is randomly generated using yet another uniform distribution limited between 0 and a certain value $R_{\max}$. The number of droplets per each step, and therefore, the number of sub-steps, is constant, and is indeed n_{blobs}.

More in-depth, whenever a droplet of radius R is created on the canvas, the algorithm checks if it touches a previously painted area, that is, if overpaint points exist. In general, whenever this occurs, an intersection will generate where the value is > 1, that is, overpaint happens. Operatively, the algorithm will compute the volume of the just plotted drop by considering it as a hemisphere ($V = {}^2\!/_3\pi R^3$). At this point, the volume associated with the intersection is computed (this is a section of the previously existing drop, so the volume must be computed considering that) using an approximation. This volume will then be added to the original drop by computing the radius R' associated

to the volume of the original drop plus the intersection volume. Finally, the original drop is replaced by the one with a radius of R'. This procedure repeats iteratively sub-step after sub-step and step after step.

In order to visualize the increase of intensity, an average is performed on each pixel of the image at each step, and is then plotted into a chart. This is visible in Fig. A.2. The first 6 steps of the canvas are visible in Fig. A.1.

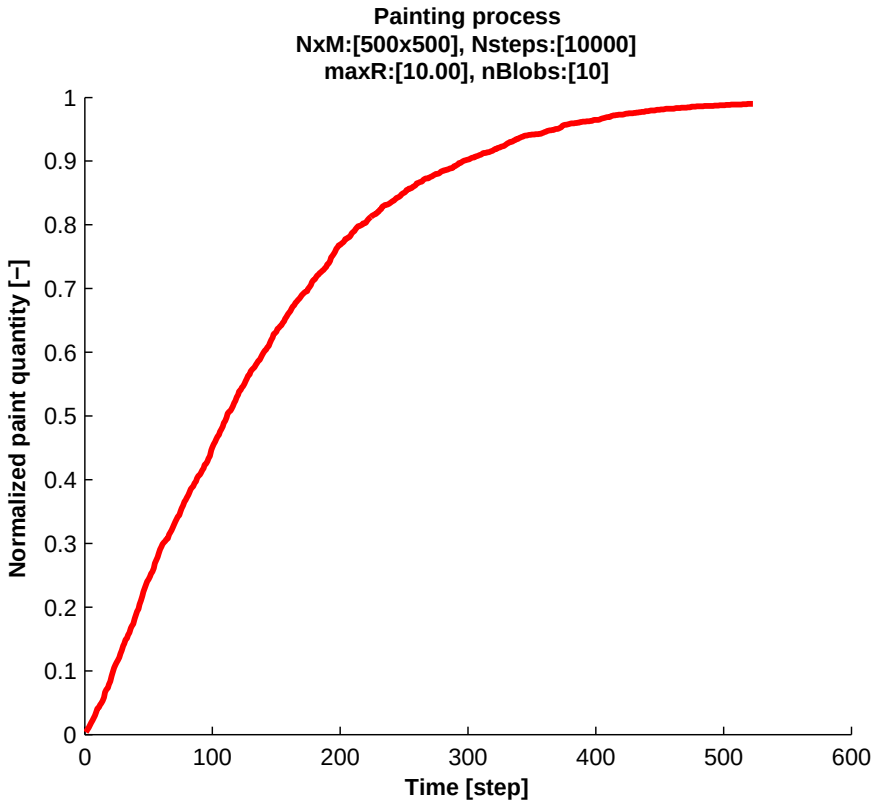

Figure A.2: Plot of the paint deposition for a 500x500 pixel canvas, 10k steps, 10 drops/step, alpha 1.0 (100% opaqueness).

The results, specifically the average intensity plotted trend, show that, despite a constant flow of paint is applied (n_{blobs} is constant at each step, and although a randomized factor appears in the size of the generated droplets, statistically this cancels out), the increase in intensity is very much not constant. This reflects very well the experimental findings which were presented in Section 3.3.2 on page 62. Moreover, a definite quasi-linear portion is discernible in the first part of the plot (between intensities

0 and 0.6, approximately). This supports once more the experimental results and the assumptions on the linearity of the deposition law.

Appendix B

Deployment of Hinged Stabilizers

One main concern of the module is stability, especially in rough terrain. Deployable stabilizers were investigated to this purpose.

B.1 Design parameters

The following were considered:

i. Ability to straighten up a 20Kg module from a side-laying position,

ii. Deployment with the simplest possible actuation (1 d.o.f.),

iii. Deployment possible even while docked to the rover,

iv. Requires a minimal amount of space,

v. Light structure,

The maximum straightening moment at the hinges of the deployable legs is $M_{\text{hinge}} = \mathbf{g}m \ \ \mathbf{G}|_z$, where $\mathbf{g}$ is the gravity acceleration module, m is the mass of the module, and $\mathbf{G}|_z$ is the height of the center of mass $\mathbf{G}$ in the system of reference of the module.

With the most up-to-date concept of module, provided that $\mathbf{G}$ lays in the geometrical center, we have $\mathbf{G}|_z = 200\ mm$, $m = 20\ Kg$. On Earth this translates in a moment $M_{\text{hinge}} = 39.24\ Nm$ which is a comparatively high value given our weight concerns (large actuator, etc.).

B.2 Mechanism

In the following, the mechanism is illustrated and a model is produced for the its kinematics. Finally, an evaluation of the static forces is performed.

B.2.1 Mechanism Principle

A compromise solution is to use a coupled double quadrilateral mechanism to operate the stabilizers. Given the definitions in Fig. B.1, the geometry equations are the following:

$$\begin{cases} r_1 &= \frac{\sqrt{(k+w/2\ )^2+k^2}}{2} - \frac{w}{4} \\ r_2 &= \frac{2k^2+wk}{w+(2k+w)\cos\xi_{2,dpl}-2k\sin\xi_{2,dpl}} \\ k &= k_1 = k_2 \\ \xi_{2,dpl} &= \operatorname{acos}\left(\frac{\left(\frac{w}{2}+k\right)}{l_2+r_2}\right) \\ l_2 &= r_2+\frac{w}{2} \\ l_1 &= r_1+\frac{w}{2} \end{cases}, \tag{B.1}$$

where w is the distance between $\mathbf{H}_1$ and $\mathbf{H}_2$. Notice that $\xi_{2,dpl}$ is the angle formed by $\mathbf{H}_2\hat{\mathbf{R}}_2\mathbf{Q}_2$ when $\gamma_2 = \gamma_1 = 0$, that is, when the stabilizers are fully deployed. In general, $\xi_i = f(\gamma_i) = g(\varphi)$, where φ is the angular position of the crankshaft. Additionally, the following is defined:

$$\boldsymbol{\Omega}|_z = k, \tag{B.2}$$

The rationale for this last relation is that it allows the highest reduction ratio in the less advantageous position, during the up-straightening of the PM. This may be clearer by looking at Fig. B.1b: the system in this configuration is in a singularity condition, which translates in the following: $\left.\frac{\partial\varphi}{\partial\gamma}\right|_{\gamma=90} = \infty$.

Since, in general, w is defined by the width of the PM (200 mm), the geometry is defined entirely by the parameter k.

B.2.2 Static forces analysis

The moment M on hinge i is given by the following relation,

$$M_i = m\left\|\mathbf{g}_{\text{loc}} \times (\mathbf{G}-\mathbf{H}_i)\right\|, \tag{B.3}$$

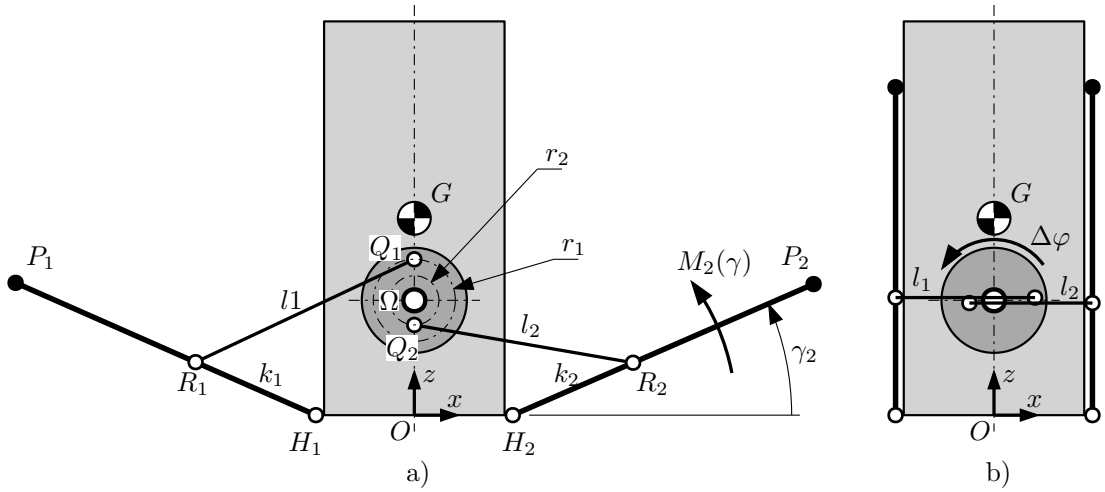

Figure B.1: General schema of the PM deployable stabilizers geometry. In a) a general intermediate position is shown, whereas in b) the "stored" configuration is shown. Note that b) also represents the geometry when the PM is laying on its side.

where $\mathbf{g}_{\text{loc}}$ is the gravity vector $\mathbf{g}$ in the x, y, z local frame of reference of the PM; it is thus $\mathbf{g}_{\text{loc}} = M_{\text{rot}}(\gamma)\,\mathbf{g}$.

The axial force on link i is given by:

$$F_{i,ax} = \frac{M_i}{K_i}, \tag{B.4}$$

Lastly, the required actuator torque is given by:

$$M_{act,i} = r_i F_{i,ax} \cos(\phi_i), \tag{B.5}$$

Where the following are true as well,

$$\begin{array}{rcl} \phi_i & = & \chi_i - \varphi - \alpha_i - \frac{\pi}{2} \\ \chi_i & = & atan2\,(\mathbf{Q}_i - \mathbf{R}_i) \\ \alpha_1 & = & \pi - \xi_{2,dpl} \\ \alpha_2 & = & -\xi_{2,dpl} \end{array} . \tag{B.6}$$

This finally translates in the results shown in Fig. B.2.

In general, it is evident that there is a strong discrepancy regarding the values of r_i and $M_{act,i}$ between the two sides of the module. This is due to the intrinsic asymmetry of the mechanism, which is well visible in Fig. B.1a.

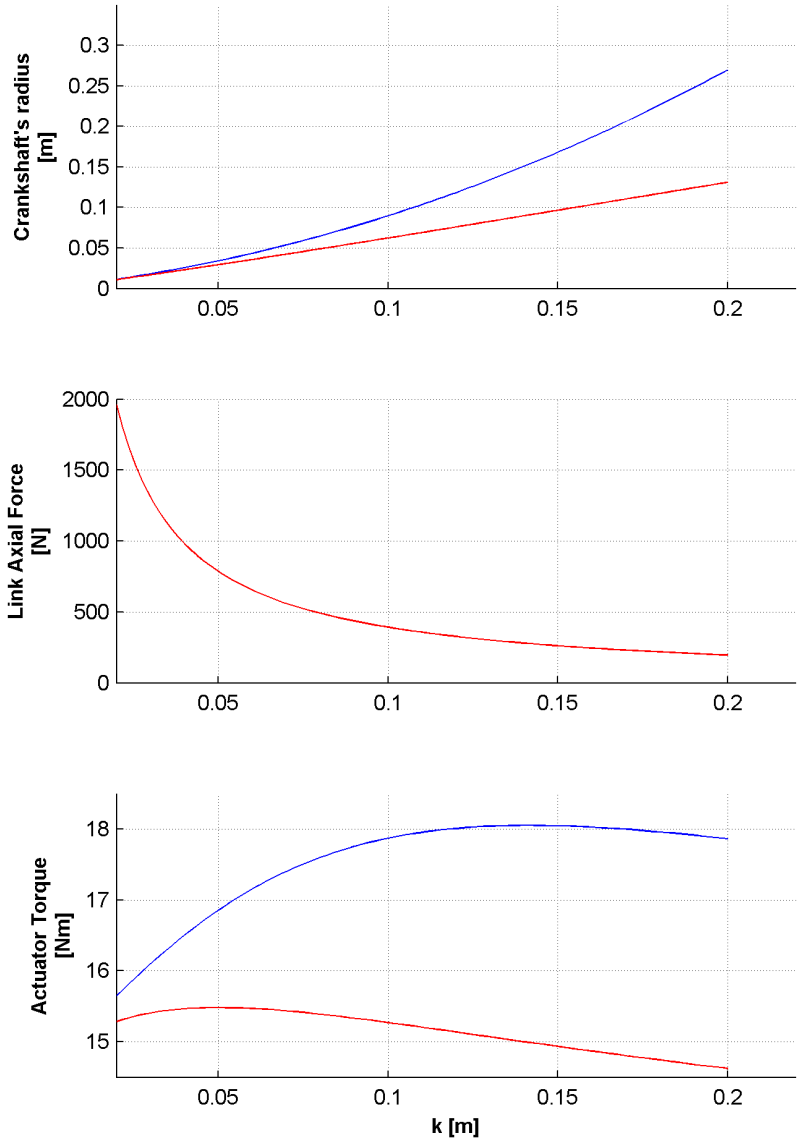

Figure B.2: Parametric analysis of k. Values for r_i and Maximum values for $F_{ax,i}$ and M_{act} are computed for $|k|_{0.02}^{0.2}\, m$ with a $\Delta k = 0.002m$ interval. Blue shows values for link 1, whereas red for link 2.

From a purely geometrical standpoint, given that the module's width is 200 mm, it would be impractical to have a major radius $r_1 > 200$; this is then a hard constraint of our problem.

More importantly, the shorter the k is, the lower the actuator torque $M_{act,1}$ gets. At the same time, though, the $F_{i,ax}$ grows, and accordingly, the stress on the stabilizers' structure.

A good compromise would be a value of $k = 80$ mm. Results for this configuration are given in Table B.1.

Table B.1: Static analysis results for $k = 80$ mm.

k [mm]	r_1 [mm]	r_2 [mm]	$F_{i,ax}$ [N]	$M_{act,1}$ [Nm]
80	64.837	48.941	490.5	17.601

B.3 Implementation A

Implementation A, visible in Fig. B.3, consists of only a pair of stabilizers, positioned in the back part of the PM.

A potential issue arises when the center of mass G of the PM is somewhat higher than the geometrical center.

As visible from Fig. B.4, the stability stance of the PM while toppled over is given by the area (shaded in red) contained in the quadrilateral defined by $\mathbf{H_2P_2P'_2H'_2}$. The condition for stability is that the projection of $\mathbf{G}$ on the ground in the direction of the gravity vector must be inside the stability stance. If this does not happen, the up-righting of the module will be impossible using the stabilizers.

A partial solution to this problem is given in Implementation B.

B.4 Implementation B

This second implementation, visible in Fig. B.5 helps with mantaining a high center of mass, for the purpose discussed above. In fact, since the stance area increases, stability will be best.

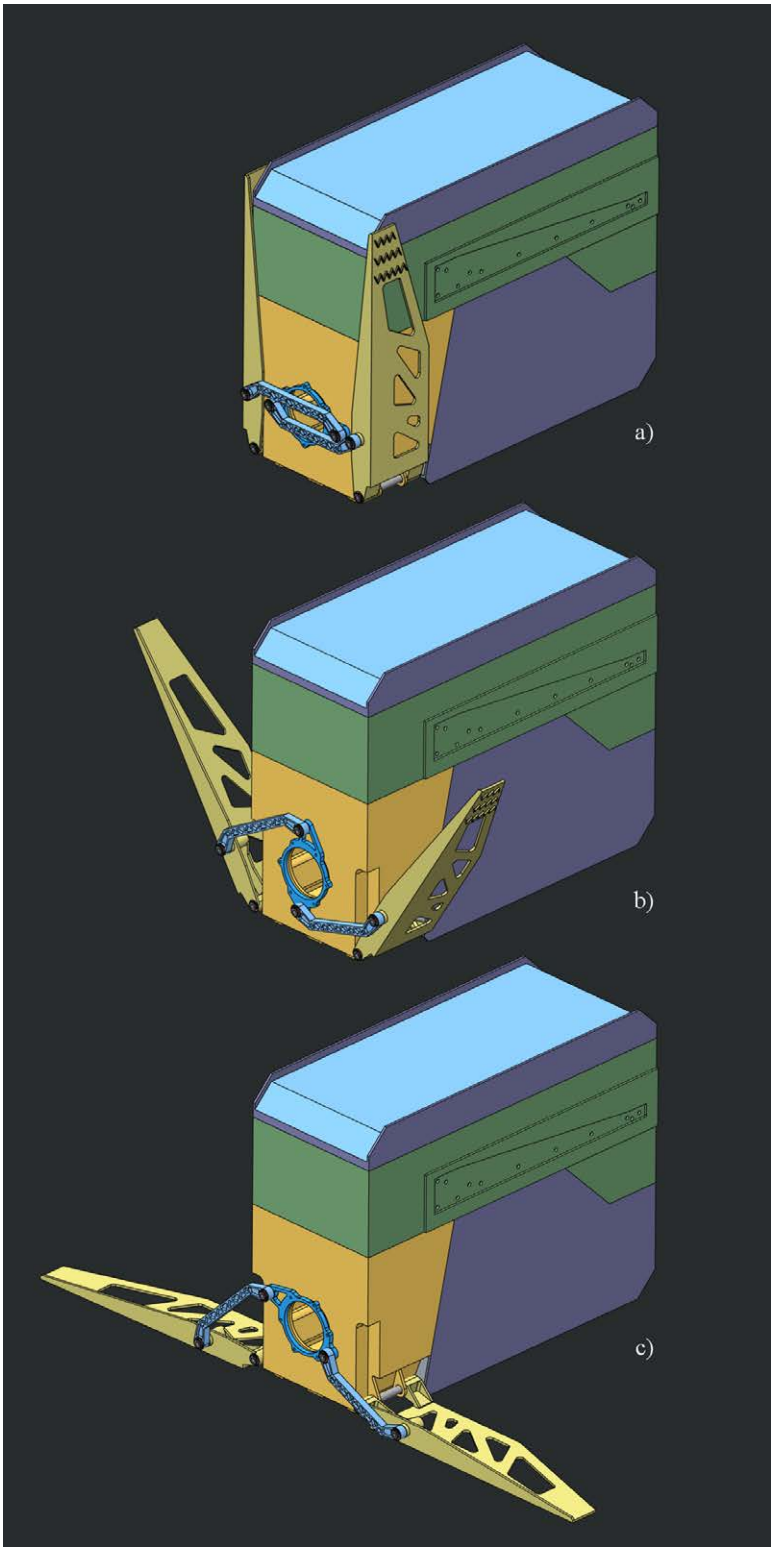

Figure B.3: Deployable stabilizers of the module: deployment sequence. In a) the "stored" configuration is shown, in b) an intermediate step is visible and in c) the fully deployed configuration is illustrated.

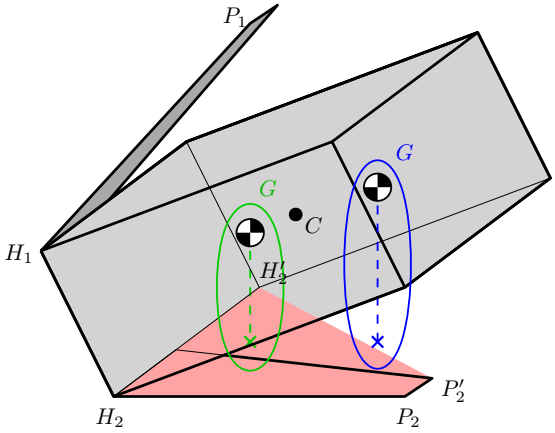

Figure B.4: Stance of the PM while being straightened up by the deployable stabilizers. The green case is when the center of mass **G** is lower than the geometric center **C** of the module, while in the blue case it is higher.

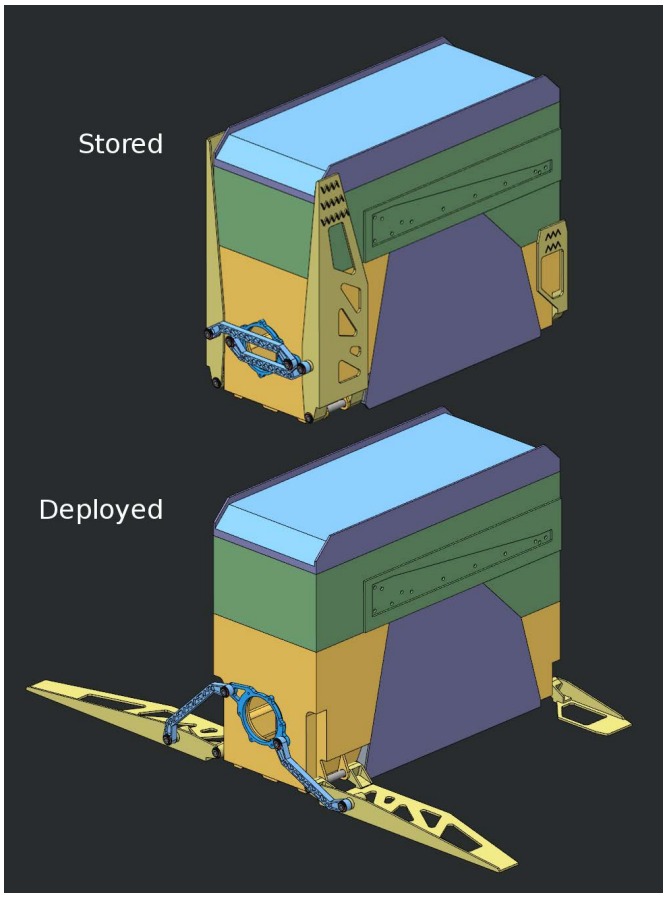

Figure B.5: Implementation B. Note the additional stabilizers on the back of the module.

Appendix C

Investigation of a STEM Actuator Structure

The STEM is a complex structure; as a longitudinally-cut cylinder with single-axis section symmetry, similarly to a C-section, it is prone to strongly asymmetric bending and 3-dimensional secondary effects like torsion. These phenomena are generally uncommon in beam-theory applications. In the majority of cases they are either not present or neglected.

Conversely, asymmetric bending can be modelized using De Saint Venant (DSV) beam theory [93], whereas secondary torsion cannot. Indeed, DSV beam theory does not consider the phenomenon known as restrained warping. Perhaps the best know attempt to successfully model this phenomenon is Vlasov torsion theory [95]. In the case at hand both asymmetric bending and torsion are present and non-negligible; in fact the magnitude of these effects can be compared to the simple bending deformation. However, since Vlasov theory can be very complex, a simplified formulation based on DSV theory is illustrated here. The complex effects will be illustrated using the Finite Element (FE) model.

C.1 Model Description

In Fig. C.1 the geometry of the bending is shown, along with the main variables associated to the various degrees of freedom or quantities. A force F is applied to point O'; the force is parallel to the plane (x, y) and its direction is determined by γ. The cut

is determined by angle α. The bending that occurs as a consequence of the application of F is directed along $\overline{O'O''}$, which is measured by angle φ. The deviation between this and the direction of the force F is parameterized as ϕ. Torsion is accounted by the variable ξ. Gross deformation of the structure is measured either by δx and δy or by Δ and φ. Note that, as visible in a), the deformation occurs on a plane parallel to (x, y); this is to simplify measurement and the model, but is sufficiently accurate, because the deformation itself is of limited extent compared to the length L of the STEM. The experimental setup is visible in Fig. 4.8 on page 94.

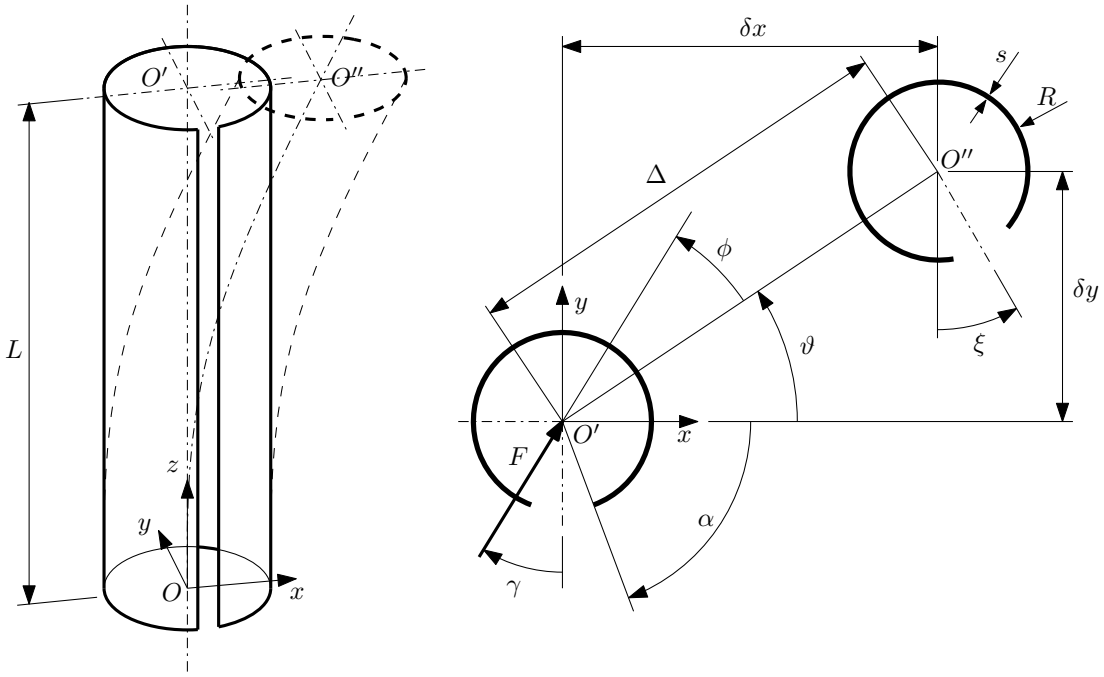

a) b)

Figure C.1: Geometry of the bending of the STEM model.

A FE model for the STEM was developed using the software SolidWorks 2010 (Dassault Systemes). A linear solver was used to keep the computation time as low as possible, given the great number (63) of different configurations that were studied. This choice was justified by the fact that involved deformations are small, and, additionally, no post-buckling analysis is necessary. The elements used were tetrahedral.

Nine different configurations were considered, and are shown in Table C.1. These are grouped in three subsets; each subset contains 9 different load condition, defined

by the angle γ.

Table C.1: The nine different configurations considered during FE analysis. Note that each configuration was studied for 9 different load angles γ: 0, 22.5, 45, 67.5, 90, 112.5, 135, 157.5, 180°.

ID	Group	s $[mm]$	α [°]	L $[-]$	N_{el} $[-]$	E $[MPa]$	F $[N]$
1				70	84,797		
2	I	0.15		140	161,417		
3			53.25	210	171,926		
4	II	0.225		140	90,336	3000	0.2
5	III	0.30		140	161,417		
6	IV	0.15	66.63	140	88,233		
7	V	0.15	80	140	188,019		

C.2 Results

This section consists in two stages, the former being the validation of the models, and the latter the discussion on the structural behaviour of the actuator. The validation of the analytical and FE models is based on a series of experimental measures that closely match the load and geometry considered in the FE analysis. In the discussion we show how the structural properties of the STEM extended portion of the actuator changes in respect to the main parameters that were studied.

C.2.1 Validation of the Model

To validate the models, a series of comparisons are made between them and the experimental results. Results are summarized in Table C.2 on the following page and Table C.3 on the next page.

The comparisons show a good affinity between the FE and the analytic model, for what concerns the simple deflection Δ, with an average error just below 10%. Large error is, on the other hand, detected when comparing the torsional and the deviational values ξ and ϕ. These yield average error values of 57.76% and 58.95% respectively.

Table C.2: Comparisons of the deflection value Δ with $\gamma = 0°$. The numerical and analytical entries are for the ID 2 configuration (see Table C.1 on the previous page).

	Deflection Δ			Error		
ID	Analytic	FE	Experimental	An-FE	An-Exp	FE-Exp
1	0.075	0.0866	0.13	14.32%	53.66%	40.11%
2	0.599	0.6690	0.58	11.04%	3.22%	14.25%
3	2.022	2.2430	2.07	10.36%	2.35%	8.02%
4	0.393	0.4389	–	11.03%	–	–
5	0.290	0.3239	–	11.04%	–	–
6	0.494	0.5158	–	4.32%	–	–
7	0.412	0.4201	–	1.95%	–	–
			Average	**9.15%**		

C.2.2 Discussion

Please refer to Fig. C.2 on page 188, which is a graphical overview of the parametric analysis (ID 17) done via the FE model. As one can appreciate from the figure, the plots consider the three main results values: the displacement Δ, the torsion ξ, and the deflection deviation ϕ.

From the plots shown in Fig. C.2a, one can see that the deflection and torsion values corresponding to the $\gamma = 90°$ angle are at their peak. This corresponds to a load case where the force is applied perpendicularly to the symmetry axis of the section of the STEM. The analytical formulation produces reliable results only for the $\gamma = 0°$ or 180° conditions, which, by looking at the same plots, are in fact the lowest points

Table C.3: Comparisons of the torsion ξ and deflection deviation ϕ values between the FE model and the experimental results.

ID	Torsion ξ [mm]		Error	Defl. dev. ϕ [mm]		Error
	FE	Experimental		FE	Experimental	
1	-0.42	-0.64	35.01%	13.60	4.76	64.96%
2	-3.12	-12.45	74.95%	12.92	6.87	46.79%
3	-10.17	27.73	63.32%	12.58	4.39	65.09%
		Average	**57.76%**		**Average**	**58.95%**

in the curves, as predicted. In the Δ plot we can extrapolate that $\mu_\Delta \cong 1.5919$ (see Eq. 4.13 on page 88). Furthermore, the same ratio was calculated for all the other plots present in Fig. C.2, yielding a value of $\mu_D elta = 1.5560 \pm 0.0735$. Since the standard deviation is so low, the methodology can be considered a good estimator for the maximum deflection Δ_{max}.

As shown in Fig. C.2b, one can appreciate how, predictably, all Δ,ξ values are proportional to the magnitude of the cut (i.e. inversely proportional to α). With the aid of some curve-fitting techniques we find that the following experimental relation closely approximates the deflection in function of the angle $\alpha : \Delta(\alpha) \cong p\alpha^(- q)$, where $p = 273.0$ and $q = 1.4$.

In Fig. C.2c, the curves are parameterized according to the length L of the pillar; we find that the following relation applies with a small deviation ($\cong 1\%$): $\Delta(L) \cong L^3$, where $a = 3.80E - 07$. This is expected, since the coefficient μ_Δ is almost entirely independent of L.

In Fig. C.2d, a parametrization on the thickness of the sheet is shown on the curves. Aside from the trivial effects (rigidity is proportional to thickness), we note that the trend is not linear, with the tendency to reach a plateau. In fact, we find that the trend can be closely approximated by the following quasi-hyperbolic relation: $\Delta(s) \cong bs^{-c}$, with $b = 6.997$ and $c = 1.06$.

The torsion parameter shows a parabolic behaviour which is function of the load direction γ. As expected, the torsion is null when the load is applied along the symmetrical axis. Furthermore, still predictably, this effect tends to become less of importance the more the thickness s and the cut angle α rise. On the contrary, higher lengths L produce opposite effects.

The deflection deviation angle, ϕ, on the other hand, shows a remarkable independence to the main parameters α, L and s; it shows, instead, a solid relation to the load direction parameter γ, exhibiting a sinusoidal shape with a value of approximately $\pm(13.26 \pm 0.34)^\circ$ on the positive and negative apices.

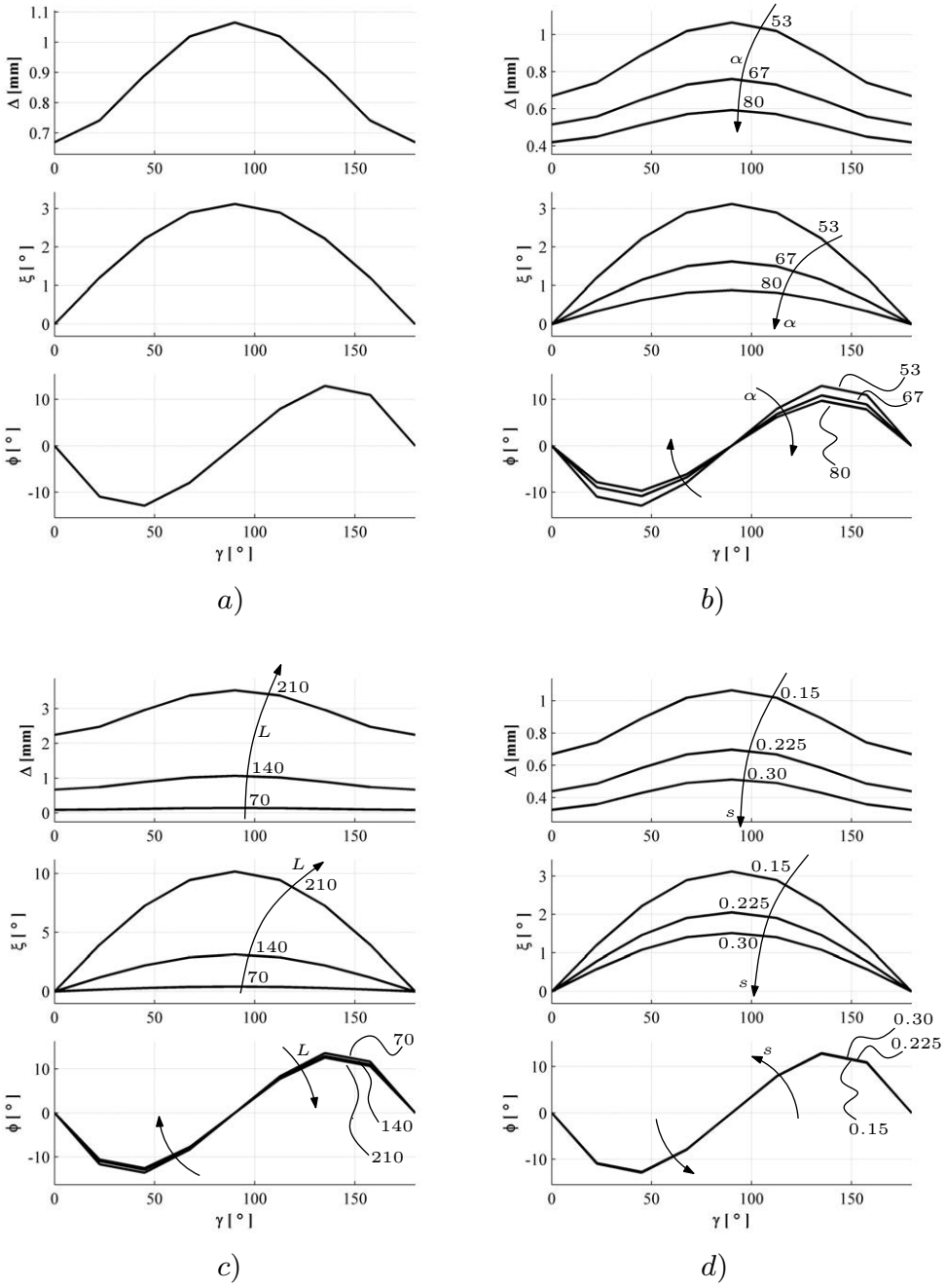

Figure C.2: Graphical form of the results. In a) a general shape of the plots is shown. In b), IDs 2, 6 and 7 are plotted to show the variation of the "slit" angle α; in c), IDs 1, 2 and 3 show the variation of length L; in d), IDs 2, 4 and 5 show the variation of thickness s in the sheet.

Appendix D

Notes on the CDPR for space applications

D.1 Power draw

The power-requirement of each module is, for the purpose of this work, based on the winches used for the cables. Considering a maximum speed of $0.5ms^{-1}$, and a mass of $1Kg$ on the end-effector, this translates into approximately $5W$, relative to the worst possible load condition, in Earth gravity. Considering all possible losses, this figure could easily grow to $10 - 50W$.

The power-consumption of the end-effector is estimated in approximately $100W$ at full draw.

D.2 The cables

The cables are a central asset for the modular CDPR. Although the aim of this paper is not to provide a detailed design for the system, some technical insight might be useful to correctly frame this work. Given the power requirements of the end-effector, and considering a 48 V line for the supply, the cables linear mass can be assumed at $0.016Kg/m$, for an AWG 17 cable, with a voltage drop of only 3.5% over 10 meters. Regarding the structural strength, we chose an aramidic fiber braid (e.g. Kevlar). Since the projected maximum tension of the cables is in the order of 50 N, this brings to a minimum diameter of a mere 0.1 mm, and a linear mass of $4.72E - 5Kg/m$. This can be considered negligible compared to the power-supply cables.

D.3 A catenary-based model for the cables

For the computations regarding the pseudostatics and the workspace analysis, presented in Section 4.3.2 on page 133, the model for the cables is approximated as a straight line with negligible mass and zero deformation. This enhances computability at the cost of some accuracy. In order to determine the loss related to the sagging, a catenary-based model for the cables is presented and its results are compared with the ones given by the straight-line approximation. Along the same line, a model for the deformation of the cable under tension is illustrated.

The general planar parametric equation for a catenary curve of linear mass ρ, subject to a gravity acceleration of module g, can be written [140] as,

$$\xi' = \frac{H}{\rho g}\left(cosh\left(\frac{\rho\zeta}{H}\right) - 1\right), \tag{D.1}$$

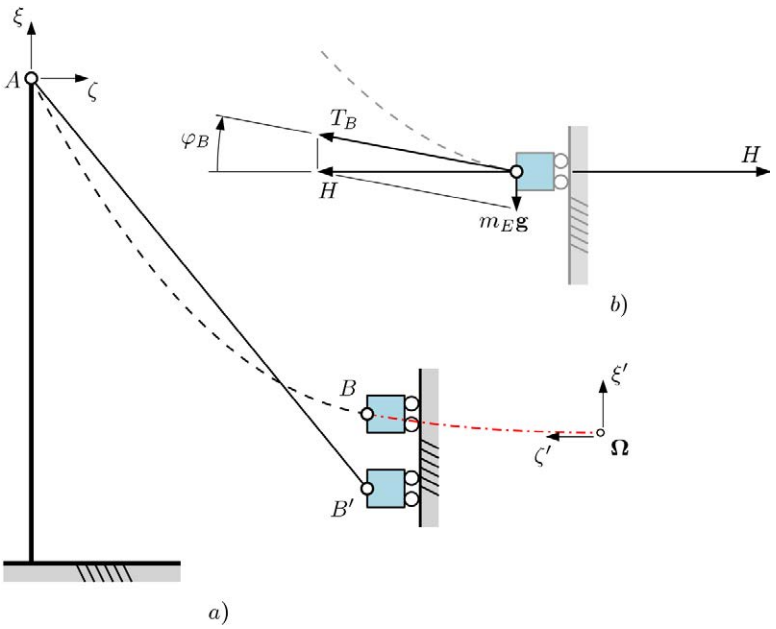

Figure D.1: Catenary-based model for the cables of the CDPR. In a), the general definitions are given, considering the end-effector as a mass m_E suspended by cable $\overset{\frown}{AB}$. The straight-line model is shown as comparison ($A\bar{B}'$). The cylindrical symmetry of the three-cable system is represented by the vertical linear constraint on point B and B. In b) the forces acting on B' are shown.

where, as shown in Fig. D.1, H is the horizontal constraint reaction on the supports and is constant along the entire assembly. It is useful to determine a "virtual" coordinate system (ξ',ζ'), which also mirrors (ξ,ζ). In order to couple the mass m_E, an artifice can be used where the mass of the dash-dotted segment $\overset{\frown}{B\Omega}$ of the catenary is defined as equal to m_E. Hence, this follows,

$$B_{\zeta'} = \frac{H}{\rho g}\, asinh\Big(\frac{m_E g}{H}\Big). \tag{D.2}$$

Furthermore, $A_{\zeta'}$ can be computed, since, in this instance, the distance $\bar{AB}$ projected on ζ is a starting parameter. The remaining coordinates of points A and B are determined as follows,

$$\begin{array}{l} B_{\xi'} = \frac{H}{\rho g} cosh\big(asinh\frac{m_E g}{H}\big) - 1 \\ A_{\xi'} = cosh\frac{A_{\zeta'}\rho g}{H} - 1 \end{array}. \tag{D.3}$$

D.4 A deformable model for the cables

Given that the length of the cables can reach large values, we show how this effect can impact accuracy. Leaning on elasticity theory, we see that the elongation of a cable is $\Delta L_i = (T_i L_{i,0})/\tau$, where $L_{i,0} = \big\|Q - P_i\big\|$, and $\tau = E_k S_k + E_{cu} S_{cu}$, with E_k and E_{cu} being the Young's modulus of Kevlar and copper respectively. S_k and S_{cu} are the cross-sectional areas for the two components. Finally, using the straight-line model, one can compute the error,

$$\varepsilon_{y,d} = \sqrt{((L_{i,0} + \Delta L_i)^2 - \big\|Q - P_i\big\|_x^2)} - \sqrt{(L_{i,0}^2 - \big\|Q - P_i\big\|_x^2)}. \tag{D.4}$$

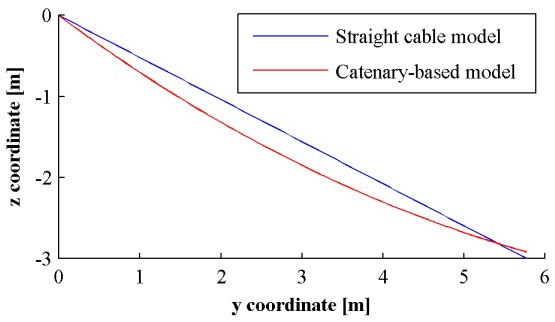

Figure D.2: Comparisons between the catenary-based and the straight cable model.

Fig. D.2 shows the results of the comparison between the catenary- and straight-line based models. This particular configuration corresponds to the one where the end-effector is in the center of the triangular workspace shown in Fig. 4.34 on page 143. A certain amount of sag in the cable exists, which causes a raise in the height of the end-effector. Given the value ρ given in Section D.2, the geometry shown in Fig. 4.34 on page 143 and a height of $3m$ from the end-effector to the top of the mast, a discrepancy $\varepsilon_{y,c} = 0.081m$ or, relatively to the width of the workspace, $\varepsilon_{y,c,\%} = 0.8\%$.

It can be shown that, for the same conditions, the error between the straight-line and the deformable-cable models is $\varepsilon_{y,d} = 0.009m$, or $\varepsilon_{y,d,\%} = 0.08\%$ relative to the width of the workspace. We find that the small size of the relative errors fully justifies the approximate straight-line model highlighted in Section 4.3.2 on page 133. Moreover, the two errors act in the opposite directions, with the cables' sagging contributing to a general increase in the height of the end-effector, and the deformation of the cables to a comparable decrease.

Finally, one should consider that, while the cables indeed add mass to the suspended portion of the robot, the tension acting on the top of the masts tends to be directed downwards by both the sag of the cable and its deformation. This has a positive effect on the stability of the modules.

D. NOTES ON THE CDPR FOR SPACE APPLICATIONS

Bibliography

[1] L. Tsai, *Robot Analysis: The Mechanics of Serial and Parallel Manipulators*. Wiley John and Sons, 1999. 1, 4, 5

[2] R. Verhoeven, M. Hiller, and S. Tadokoro, "Workspace of tendon-driven stewart platforms: Basics, classification, details on the planar 2-dof class," in *International Conference on Motion and Vibration Control MOVIC 1998;3*, pp. 871–6. 4

[3] S. Tadokoro, T. Matsushima, Y. Murao, H. Kohkawa, and M. Hiller, "A parallel cable-driven motion base for virtual acceleration," in *Proceedings of IEEE/RSJ International Conference on Intelligent Robots and systems* (H. . Maui, ed.), pp. 1700–5. 4, 78

[4] P. Gallina and G. Rosati, "Manipulability of a planar wire driven haptic device," *Mechanism and Machine Theory*, vol. 37, pp. 215–28, 2002. 4, 78

[5] I. Dulbe and I. Karcz-Dulba, "Planning motion of manipulators with local manipulability optimization," *Lecture Notes in Control and Information Sciences*, vol. 422, pp. 365–75, 2012.

[6] T. Watanabe, "Effect of torque-velocity relationship on manipulability for robot manipulators," *Journal of Mechanisms and Robotics*, vol. 3, p. 041007, 2011. 4

[7] A. Bahrami and M. Nikkhah-Bahrami in *Proceedings of the 2nd IASTED International Conference on Robotics*, pp. 345–52, Robo, 2011. 4, 81

[8] C. M. Gosselin and G. Barrette, "Kinematic analysis of planar parallel mechanisms actuated with cables," in *Proceedings of Symposium on Mechanisms*, (Quebec, Canada), pp. 41–2, Machines and Mechatronics, 2001. 4, 81

[9] P. Bosscher and I. Ebert-Uphoff, "Wrench-based analysis of cable-driven robots," in *Proceedings of IEEE Conference on Robotics and Automation*. 4, 81

[10] A. Trevisani, P. Gallina, and R. L. Williams, "Cable-direct-driven robot (cddr) with passive scara support: theory and simulation.," *Journal of Intelligent and Robot Systems*, 2006. 4, 79, 81

[11] A. Trevisani, "Underconstrained planar cable-direct-driven robots: A trajectory planning.," *Mechatronics*, 2010. 79, 81

[12] C. B. Phama, S. H. Yeob, G. Yangc, and I. M. Chen, "Workspace analysis of fully restrained cable-driven manipulators," *Robotics and Autonomous Systems*, 2009. 54, 81

[13] J. Pusey, A. Fattah, S. Agrawal, and E. Messina, "Design and workspace analysis of a 6-6 cable-suspended parallel robot," *Mechanism and Machine Theory*, vol. 39, no. 7, pp. 761 – 778, 2004. 4, 116

[14] A. James, B. Roger, and D. Nicholas, "Nist robocrane," *Journal of Robotic Systems*, vol. 10, no. 5, pp. 709–724, 1993. 4, 78

[15] N. G. Dagalakis, J. S. Albus, B. Wang, J. Unger, and J. D. Lee, "Stiffness study of a parallel link robot crane for shipbuilding applications," *Journal of Offshore Mechanics and Arctic Engineering*, vol. 111, no. 3, pp. 183–193, 1989. 4

[16] S. Kawamura, W. Choe, S. Tanaka, and S. R. Pandian, "Development of an ultrahigh speed robot falcon using wire drive system," in *Proceedings of the IEEE International Conference on Robotics and Automation*. 4

[17] A. Pott, "An algorithm for real-time forward kinematics of cable-driven parallel robots," *Advances in Robot Kinematics: Motion in Man and Machine*, 2010. 4

[18] A. Pott, T. Bruckmann, and L. Mikelsons, "Closed-form force distribution for parallel wire robots," *Computational Kinematics*, 2009.

[19] A. Pott, C. Meyer, and A. Verl, "Large-scale assembly of solar power plants with parallel cable robots," in *Proceedings of the 41st International Symposium on Robotics and the 6th German Conference on Robotics (ROBOTIK 10)*, p. 16, 2010.

[20] A. Pott, H. Mutherich, W. Kraus, V. Schmidt, P. Miermeister, T. Dietz, and A. Verl, "Cable-driven parallel robots for industrial applications: The ipanema system family," 2013. 4

[21] R. Cravotta, "Flying over the action," *EDN*, vol. 48, no. 15, pp. 30–34, 2003. 4, 116

[22] J. Izard, M. Michelin, and C. Baradat, "Fusion reactor handling operations with cable-driven parallel robots," *Fusion Engineering and Design*, vol. 98-99, pp. 1505–1508, 2015. 4

[23] J. F. Mustard, M. Adler, A. Allwood, D. S. Bass, D. W. Beaty, J. F. Bell Iii, W. B. Brinckerhoff, M. Carr, D. J. Des Marais, B. Drake, K. S. Edgett, J. Eigenbrode, L. T. Elkins-Tanton, J. A. Grant, S. M. Milkovich, D. Ming, C. Moore, S. Murchie, T. C. Onstott, S. W. Ruff, M. A. Sephton, A. Steele, and A. Treiman, "Appendix to the report of the mars 2020 science definition team," *Exploration Program Analysis Group (MEPAG)*, p. 51pp, 2013. 4, 128

[24] J. Vago, B. Gardini, G. Kminek, P. Baglioni, G. Gianfiglio, A. Santovincenzo, S. Bayn, and M. Van Winnendael, "Exomars: Searching for life on the red planet," *European Space Agency Bulletin*, vol. 126, pp. 16–23, 2006. 128

[25] J. N. Goswami and M. Annadurai, "Chandrayaan-2 mission," *42nd Lunar and Planetary Science Conference, The Woodlands, Texas*, vol. 1608, p. 2042, March 2011. 128

BIBLIOGRAPHY

[26] J. P. Grotzinger, J. Crisp, A. R. Vasavada, R. C. Anderson, C. J. Baker, R. Barry, D. F. Blake, P. Conrad, K. S. Edgett, B. Ferdowski, R. Gellert, J. B. Gilbert, M. Golombek, J. Gmez-Elvira, D. M. Hassler, L. Jandura, M. Litvak, P. Mahaffy, J. Maki, M. Meyer, M. C. Malin, I. Mitrofanov, J. J. Simmonds, D. Vaniman, R. V. Welch, and R. C. Wiens, "Mars science laboratory mission and science investigation," *Space Science Reviews*, vol. 170, pp. 5–56, 2012. 4, 128

[27] M. P. Golombek, R. A. Cook, T. Economou, W. M. Folkner, A. F. C. Haldemann, P. H. Kallemeyn, J. M. Knudsen, R. M. Manning, H. J. Moore, T. J. Parker, R. Rieder, J. T. Schofield, P. H. Smith, and R. M. Vaughan, "Overview of the mars pathfinder mission and assessment of landing site predictions," *Science*, 1997. 128

[28] W. Ip, J. Yan, C. Ouyang, and Z. Li, "Preface: The chang'e-3 lander and rover mission to the moon," *Research in Astronomy and Astrophysics*, 2014. 4, 128

[29] A. Papachristou, H. Valsamos, and A. Dentsoras, "Optimal initial positioning of excavators in digging processes," *Proceedings of the Institution of Mechanical Engineers*, vol. 224, pp. 835–844, 2010. 4, 11

[30] A. Stentz, J. Bares, S. Singh, and P. Rowe, "A robotic excavator for autonomous truck loading," in *Proceedings of the IEEE/RSJ International Conference on Intelligent Robotic Systems*, 1998. 4, 11

[31] S. J. Lorenc, B. E. Handlon, and L. E. Bernold, "Development of a robotic bridge maintenance system," *Automation in construction*, vol. 9, pp. 251–258, 2000. 5, 11

[32] Y. S. Kim, M. H. Jung, Y. K. Cho, J. Lee, and U. Jung, "Conceptual design and feasibility analyses of a robotic system for automated exterior wall painting," *International Journal of Advanced Robotic Systems*, vol. 4, pp. 417–430, 2007. 5, 11

[33] G. A. Seriani S, Gallina P, "A performance index for planar repetitive workspace robots," *Journal of Mechanisms and Robotics*, 2014. 10, 47

[34] R. Kershner, "The number of circles covering a set," *American Journal of Mathematics*, vol. 61, pp. 665–671, 1993. 12

[35] C. Uhlery and S. J. Wright, "Packing ellipsoids with overlap," *Transactions of the IRE Professional Group on Audio*, 2012. 12

[36] R. M. Karp, "Reducibility among combinatorial problems," *Complexity of Computer Computations, New York: Plenum, pp.*, vol. 85, 1972. 12

[37] R. J. Fowler, M. S. Paterson, and S. L. Tanimoto, "Optimal packing and covering in the plane are npcomplete," *Information Processing Letters*, vol. 12, no. 3, pp. 133–137, 1981. 12

[38] J. B. M. Melissen and P. C. Schuur, "Improved coverings of a square with six and eight equal circles," *Electronic Journal of Combinatorics*, vol. 3, no. 1, pp. 1–10, 1996. 12

[39] A. Heppes and H. Melissen, "Covering a rectangle with equal circles," *Periodica Mathematica Hungarica*, vol. 34, pp. 65–81, 1997.

[40] J. B. M. Melissen and P. C. Schuur, "Covering a rectangle with six and seven circles," *Discrete Applied Mathematics*, vol. 99, pp. 149–156, 1997.

[41] K. J. Nurmela, "Conjecturally optimal coverings of an equilateral triangle with up to 36 equal circles," *Experimental Mathematics*, vol. 9, no. 2, pp. 241–250, 2000. 12

[42] J. Bamberg, G. Cairns, and D. Kilminster, "The crystallographic restriction, permutations, and goldbach's conjecture," *American Mathematical Monthly*, 2003. 13

[43] A. Bravais, "Mmoire sur les systmes forms par des points distribus regulirement sur un plan ou dans l'espace," *Journal de l'Ecole Polytechnique*, vol. 19, pp. 1–128, 1866. 13

[44] D. E. Goldberg, *Genetic Algorithms in Search, Optimization and Machine Learning.* Addison-Wesley, 1989. 23

[45] A. R. Conn, N. I. M. Gould, and P. L. Toint, "A globally convergent augmented lagrangian algorithm for optimization with general constraints and simple bounds," *SIAM Journal on Numerical Analysis*, vol. 28, pp. 545–572, 1991.

[46] A. R. Conn, N. I. M. Gould, and P. L. Toint, "A globally convergent augmented lagrangian barrier algorithm for optimization with general inequality constraints and simple bounds," *Mathematics of Computation*, vol. 66, pp. 261–288, 1997. 23

[47] R. Storn, "On the usage of differential evolution for function optimization," in *Biennial Conference of the North American Fuzzy Information Processing Society (NAFIPS)*, pp. 519–523, 1996. 23

[48] R. Storn and K. Price, "Differential evolution - a simple and efficientheuristic for global optimization over continuous spaces," *Journal of Global Optimization*, vol. 11, pp. 341–359, 1997. 23

[49] P. Jog, J. Y. Suh, and D. van Gucht, "The effects of population size, heuristic crossover and local improvement on a genetic algorithm for the traveling salesman problem," in *Proceedings of the Third International Conference on Genetic Algorithms*, (San Francisco, CA, USA), pp. 110–115, Morgan Kaufmann Publishers Inc., 1989. 26

[50] *Digital Image Processing.* John Wiley & Sons, Inc., 1991. 29

[51] S. Seriani, M. Seriani, and P. Gallina, "Workspace optimization for a planar cable-suspended direct-driven robot," *Robotics and Computer-Integrated Manufacturing*, vol. 34, pp. 1–7, 2015. 45

[52] S. Baldwin, "Robotic paint automation: The pros and cons of using robots in your paint finishing system," *Metal Finishing*, 2010. 55, 57

[53] J. Aviles-Viñas, R. Rios-Cabrera, and I. Lopez-Juarez, "On-line learning of welding bead geometry in industrial robots," *International Journal of Advanced Manufacturing Technology*, 2015. 55

[54] Y. Liu and Y. Zhang, "Supervised learning of human welder behaviors for intelligent robotic welding," *IEEE Transactions on Automation Science and Engineering*, 2015. 55

[55] A. Cortellessa, S. Seriani, P. Gallina, S. Carrato, M. Sortino, S. Belfio, and G. Ramponi, "Automatic path-planning algorithm for realistic decorative robotic painting," in *3rd International Conference, Production Engineering and Management, PEM, Trieste*, 2013. 55

[56] S. Seriani, A. Cortellessa, S. Belfio, M. Sortino, G. Totis, and P. Gallina, "Automatic path-planning algorithm for realistic decorative robotic painting," *Automation in Construction*, vol. 56, pp. 67–75, 2015. 55

[57] T. Balkan and M. A. S. Arikan, "Modeling of paint flow rate flux for circular paint sprays by using experimental paint thickness distribution," *Mechanics Research Communications*, vol. 26, pp. 609–617, 1999. 57, 61

[58] K. R. J. Ellwood, J. L. Tardiff, and S. M. Alaie, "A simplified analysis method for correlating rotary atomizer performance on droplet size and coating appearance," *Journal of Coating Technology Research*, vol. 11, no. 3, pp. 303–309, 2014. 57

[59] D. C. Conner, A. Greenfield, P. N. Atkar, A. A. Rizzi, and H. Choset, "Paint deposition modeling for trajectory planning on automotive surfaces," *IEEE Transactions on Automation Science and Engineering*, vol. 2, pp. 381–391, 2005. 57

[60] Y. Chen, K. Chen, H. Yan, L. Wang, and L. Zheng, "Simulation analysis of coating at uniform velocity of robotic spray gun," *Applied Mechanics and Materials*, vol. 246-247, pp. 1175–1180, 2013. 57

[61] M. Fogliati, D. Fontana, M. Garbero, M. Vanni, G. Baldi, and R. Dondeé, "Cfd simulation of paint deposition in an air spray process," *Journal of Coatings Technology Research*, vol. 3, no. 2, pp. 117–125, 2006. 57

[62] P. T. Elliott, M. J. Steffenhagen, and J. E. Glass, "Spray applications: Part iii. assessment of viscosities at high shear rates and dynamic uniaxial extensional viscosities on fan nozzle air sprayability," *Journal of Coatings Technology Research*, vol. 4, no. 4, pp. 341–349, 2007. 57

[63] P. N. Atkar, A. Greenfield, D. C. Conner, H. Choset, and A. A. Rizzi, "Uniform coverage of automotive surface patches," *International Journal of Robotics Research*, vol. 24, pp. 883–898, 2005. 57

[64] H. Chen, F. Thomas, and L. Xiongzi, "Automated industrial robot path planning for spray painting process: A review," in *4th IEEE Conference on Automation Science and Engineering*, (522-527), 2008. 57

[65] P. Haeberli, "Paint by numbers: abstract image representation," in *Proceedings of the 17th annual conference on computer graphics and interactive techniques, vol. 24*, pp. 207–214, 1990. 57

[66] A. Hertzmann, "Painterly rendering with curved brush strokes of multiple sizes," in *Proceedings of the 25th annual conference on computer graphics and interactive techniques*, pp. 453–460, 1998. 58

[67] J. Hays and I. Essa, "Image and video based painterly animation," in *Proceedings of the 3rd international symposium on non-photorealistic animation and rendering*, pp. 113–120, 2004. 58

[68] J. Collomosse and P. Hall, "Painterly rendering using image salience," *20th Eurographics UK conference, Eurographics Association*, pp. 112–118, 2002.

[69] H. Kang, S. Lee, and C. Chui, "Coherent line drawing," in *ACM symposium on non-photorealistic animation and rendering*, pp. 43–50, 2007. 58

[70] M. Held, "Vroni: An engineering approach to the reliable and efficient computation of voronoi diagrams of points and line segments," *Computational Geometry: Theory and Applications, pp.*, pp. 95–123, 2001. 67

[71] M. Held, "On the computational geometry of pocket machining," *Lecture Notes in Computer Science*, vol. 500, 1991.

[72] G. Barequet, T. M. Dickerson, and T. M. Goodrich, "Voronoi diagrams for convex polygon-offset distance functions," *Discrete and Computational Geometry*, vol. 25, no. 2, pp. 271–291, 2001. 67

[73] J. E. Bresenham, "Algorithm for computer control of a digital plotter," *IBM Systems Journal*, 1965. 68

[74] D. C. Munson Jr., "A note on lena," *IEEE Trans. Image Processing*, 1996. 72, 73

[75] S. Seriani and P. Gallina, "A storable tubular extendible member (stem) parallel robot: Modelization and evaluation," *Mechanism and Machine Theory*, vol. 90, pp. 95–107, 2015. 78

[76] J. Lamaury, M. Gouttefarde, M. Michelin, and O. Tempier, "Design and control of a redundant suspended cable-driven parallel robots," in *Latest Advances in Robot Kinematics*, pp. 237–244, Springer, 2012. 78

[77] P. D. Campbell, P. L. Swaim, and C. J. Thompson, "Charlotte's robot technology for space and terrestrial applications," *Training*, vol. 2014, pp. 5–7, 1996. 78

[78] L. C. Lawrence, "Skycam: an aerial robotic camera system," *Byte*, vol. 10, no. 10, pp. 122–132, 1985. 79, 116

[79] R. L. Williams and P. Gallina, "Planar cable-direct-driven robots: Design for wrench exertion," *Journal of Intelligent and Robotic Systems*, vol. 35, pp. 203–219, 2002. 79

[80] R. L. Williams and P. Gallina, "Translational planar cable-direct-driven robots," *Journal of Intelligent and Robotic Systems*, vol. 37, pp. 69–96, 2003. 79

[81] L. Pigani and P. Gallina, "Cable-direct-driven-robot (cddr) with a 3-link passive serial support," *Robotics and Computer-Integrated Manufacturing;*, vol. 30, no. 3, pp. 265–276, 2014. 79

[82] G. Rosati, P. Gallina, and S. Masiero, "Design, implementation and clinical tests of a wire-based robot for neurorehabilitation," *IEEE Trans. Neural Syst. Rehabil. Eng.*, vol. 15, no. 4, pp. 560–569, 2007. 79

BIBLIOGRAPHY

[83] P. Gallina, "Wire driven robots for rehabilitation," *Advances in Rehabilitation Robotics: Human-Friendly Technologies on Movement Assistance and Restoration for People with Disabilities. Lecture notes in Control and Information Sciences*, vol. 306, pp. 365–375, 2004. 79

[84] E. Groskopfs, "Storable tubular extendible member device," tech. rep., 1969. U.S. Patent 3434674 A. 80

[85] J. Christian, S. Jayaram, and M. Swartwout, "Feasibility of a deployable boom aboard picosatellites for instrumentation and control purposes," p. 6187251, 2012. 80

[86] Y. Liu, H. Du, L. Liu, and J. Leng, "Shape memory polymers and their composites in aerospace applications: A review," *Smart Materials and Structures*, vol. 23, no. 2, p. 023001, 2014. 80

[87] C. Cappelletti, G. Martinotti, and F. Graziani, "Unicubesat: A test for a gravity-gradient solar array boom," vol. 5, pp. 4097–4102, 2011. 80

[88] L. Blanchard, G. Aridon, F. Falzon, D. Rémond, and R. Dufour, "A tape-spring hexapod for deployable telescopes: Dynamics," in *Proceedings of the 6th International Conference on Space Optics*, (ESTEC, Noordwijk, The Netherlands), pp. 27–30, June, 2006. 80

[89] G. Aridon, D. Rémond, L. Blanchard, and R. Dufour, "A model to predict the deployment of a space hexapod," in *12th IFToMM World Congress* (Besançon, ed.), pp. 18–21, June 2007. 80

[90] F. Guinot, S. Bourgeois, B. Cochelin, C. Hochard, L. Blanchard, and A. Allez, "Hybrid tape-spring for deployable hexapod," in *50th AIAA/ASME/ASCE/AHS/ASC Structures, Structural Dynamics and Materials Conference*, (Palm Springs, California), pp. 4–7, May 2009. 80

[91] P. Chiacchio, Y. Bouffard-Vercelli, and F. Pierrot, "Force polytope and force ellipsoid for redundant manipulators," *Journal of Robotic Systems;*, vol. 14, no. 8, pp. 613–620, 1997. 80

[92] P. Gallina, G. Rosati, and A. Rossi, "3-d.o.f. wire driven planar haptic interface," *Journal of Intelligent and Robotic Systems: Theory and Applications*, vol. 32, no. 1, pp. 23–36, 2001. 81, 95

[93] S. P. Timoshenko and J. N. Goodier, *Theory of Elasticity*. New York: McGraw-Hill, 1951. 86, 183

[94] S. P. Timoshenko and J. M. Gere, *Theory of Elastic Stability*. New York: McGraw-Hill, 2nd ed., 1961. 86

[95] V. Z. Vlasov, *Thin-Walled Elastic Bars*. Moscow: Fizmatgiz, 2nd ed., 1959. 86, 183

[96] A. Gjelsvik, *Theory of thin-walled bars*. New York: John Wiley, 1981. 86

[97] S. Seriani and P. Gallina, "Variable radius drum mechanisms (vrdms)," *Journal of Mechanisms and Robotics*, vol. 15, no. 1069, p. 1, 2015. 105

[98] L. Yafei and F. Dapeng, "Transmission backlash of precise cable drive system," *Journal of Mechanical Engineering Science*, vol. 227, no. 10, pp. 2256–2267, 2012. 106

[99] S. Ji, S.-J. Kim, and Y.-B. Kim, "Experimental approach for mooring winch control system design," in *Proceedings of the 2013 13th International Conference on Control, Automation and Systems (ICCAS 2013)*, pp. 1025–1028, October 2013. 106

[100] J. M. Lincoln, D. L. Lucas, R. W. McKibbin, C. C. Woodward, and J. E. Bevan, "Reducing commercial fishing deck hazards with engineering solutions for winch design," *Journal of Safety Research*, vol. 39, no. 2, pp. 231 – 235, 2008. 106

[101] Z. Deyao, "Forces in the hoisting wire of a crane barge in waves," *Ocean Engineering*, vol. 12, no. 1, pp. 1 – 16, 1985. 106

[102] A. Kareem, P. Lu, T. Finnigan, and S.-L. V. Liu, "Aerodynamic loads on a typical tension leg platform," *Ocean Engineering*, vol. 14, no. 3, pp. 201 – 231, 1987. 106

[103] E. Kilic, M. Dolen, and A. Bugra Koku, "Experimental evaluation of cable-drum systems as linear motion sensors," in *Proceedings of the 2011 IEEE International Conference on Mechatronics*, pp. 666–671, April 2011. 106

[104] E. Kilic and M. Dolen, "Prediction of slip in cable-drum systems using structured neural networks," *Journal of Mechanical Engineering Science*, vol. 228, no. 3, pp. 441–456, 2014. 106

[105] D. Shin, X. Yeh, and O. Khatib, "Circular pulley versus variable radius pulley: Optimal design methodologies and dynamic characteristics analysis," *IEEE Transactions on Robotics*, vol. 29, no. 3, pp. 766–774, 2013. 106, 107

[106] D. Shin, X. Yeh, and O. Khatib, "Variable radius pulley design methodology for pneumatic artificial muscle-based antagonistic actuation systems," in *Intelligent Robots and Systems (IROS), 2011 IEEE/RSJ International Conference on*, pp. 1830 –1835, sept. 2011. 107

[107] P. Tidwell, N. Bandukwala, S. Dhande, C. Reinholtz, and G. Webb, "Synthesis of wrapping cams," *Journal of Mechanical Design, Transactions Of the ASME*, vol. 116, no. 2, pp. 634–638, 1994. 107

[108] M. Kilic, Y. Yazicioglu, and D. Kurtulus, "Synthesis of a torsional spring mechanism with mechanically adjustable stiffness using wrapping cams," *Mechanism and Machine Theory*, vol. 57, pp. 27–39, 2012. 107

[109] N. Schmit and M. Okada, "Synthesis of a non-circular cable spool to realize a nonlinear rotational spring," in *IEEE International Conference on Intelligent Robots and Systems*, pp. 762–767, September 2011. 107

[110] B. Kim and A. Deshpande, "Design of nonlinear rotational stiffness using a noncircular pulley-spring mechanism," *Journal of Mechanisms and Robotics*, vol. 6, no. 4, pp. 041009–1–041009–9, 2014. 107

[111] T. Okada and T. Kanade, "A three-wheeled self-adjusting vehicle in a pipe, ferret-1," *The International Journal of Robotics Research*, vol. 6, no. 4, pp. 60–75, 1987. 107

[112] G. Endo, H. Yamada, A. Yajima, M. Ogata, and S. Hirose, "A passive weight compensation mechanism with a non-circular pulley and a spring," in *Robotics and Automation (ICRA), 2010 IEEE International Conference on*, pp. 3843–3848, may 2010. 107

[113] N. Ulrich and V. Kumar, *Passive mechanical gravity compensation for robot manipulators*, vol. 2, pp. 1536–1541. IEEE, 1991. 107

[114] E. Kljuno, J. J. Zhu, R. L. Williams, and S. M. Reilly, "A biomimetic elastic cable driven quadruped robot - the robocat," in *Proceedings of the 2011 ASME International Mechanical Engineering Congress and Exposition*, pp. 1 –11, november 2011. 107

[115] S. Hirose, K. Ikuta, and K. Sato, "Development of a shape memory alloy actuator. improvement of output performance by the introduction of a δ-mechanism," *Advanced Robotics*, vol. 3, no. 2, 1988. 107

[116] H. Stachel, "Gears and belt drives for non-uniform transmission," in *Proceedings of EUCOMES 2008 - The 2nd European Conference on Mechanism Science*, pp. 415–422, 2008. 107

[117] P. Gallina, "A new class of rocker-belt mechanisms," *Mechanism and Machine Theory*, vol. 40, pp. 963–976, AUG 2005. 107

[118] M. Hiller, S. Fang, S. Mielczarek, R. Verhoeven, and D. Franitza, "Design, analysis and realization of tendon-based parallel manipulators," *Mechanism and Machine Theory*, vol. 40, no. 4, pp. 429 – 445, 2005. 116

[119] D. R. Woods, "Review of the soviet lunar exploration programme," *Spaceflight*, vol. 18, no. 7-8, pp. 273–290, 1976. 128

[120] A. M. M. Teles, "Mars astrobiology: Recent status and progress," *Planetary Exploration and Science: Recent Results and Advances*, pp. 147–245. 128

[121] H. P. Klein, "The viking biological investigations: Review and status," *Origins of Life*, vol. 9, no. 2, pp. 157–160, 1978. 128

[122] K. C. Clausen, H. Hassan, M. Verdant, P. Couzin, G. Huttin, M. Brisson, C. Sollazzo, and J.-P. Lebreton, "The huygens probe system design," *Space Science Reviews*, vol. 104, no. 1-4, pp. 155–189, 2002. 128

[123] J. Biele, S. Ulamec, B. Feuerbacher, H. Rosenbauer, R. Mugnuolo, D. Moura, and J. P. Bibring, "Current status and scientific capabilities of the rosetta lander payload," *Advances in Space Research*, vol. 29, no. 8, pp. 1199–1208, 2002. 128

[124] A. S. Howe, K. J. Kennedy, and T. Gill, "Nasa habitat demonstration unit (hdu) deep space habitat analog," *AIAA SPACEConference and Exposition*, 2013. 128

[125] A. Muscatello and E. Santiago-Maldonado, "Mars in situ resource utilization technology evaluation," in *50th AIAA Aerospace Sciences Meeting including the New Horizons Forum and Aerospace Exposition*, January 2012. 128

[126] O. Barbera, F. Mailland, S. Hovland, and G. Giacoppo, "Energy and provision management study: A research activity on fuel cell design and breadboarding for lunar surface applications supported by european space agency," *International Journal of Hydrogen Energy*, vol. 39, no. 26, pp. 14079–14096, 2014. 128

[127] L. Levrino, G. Gatto, S. Hall, J. Wellons, E. Gargioli, J. A. Hoffman, P. Maggiore, N. Viola, and M. A. Viscio, "Human life support in permanent lunar base architectures," in *Proceedings of the International Astronautical Congress IAC*, (13), pp. 9690–9700, 2014. 144

[128] Y. Tu, "Multi-spherical-surface geometric configurations and analyses of inflatable combined cable-membrane structure for lunar habitation," *Advances in Space Research*, 2015.

[129] S. S. Schreiner, T. P. Setterfield, D. R. Roberson, B. Putbrese, K. Kotowick, M. D. Vanegas, M. Curry, L. M. Geiger, D. Barmore, J. J. Foley, P. A. Latour, J. A. Hoffman, and J. W. Head, "An overnight habitat for expanding lunar surface exploration," *Acta Astronautica*, vol. 112, pp. 158–165, 2015. 144

[130] I. A. Crawford, "Lunar resources: A review," *Progress in Physical Geography*, vol. 39, no. 2, pp. 137–167, 2015.

[131] L. Borg, D. Des Marais, D. Beaty, O. Aharonson, S. Benner, D. Bogard, J. Bridges, C. Budney, W. Calvin, B. Clark, J. Eigenbrode, M. Grady, J. Head, S. Hemming, N. Hinners, V. Hipkin, G. MacPherson, L. Marinangeli, S. McLennan, H. McSween, J. Moersch, K. Nealson, L. Pratt, K. Righter, S. Ruff, C. Shearer, A. Steele, D. Sumner, S. Symes, J. Vago, and F. Westall, "Science priorities for mars sample return," *Astrobiology*, vol. 8, no. 3, pp. 489–535, 2008. 128, 145

[132] W. Fink, V. R. Baker, D. Schulze-Makuch, C. W. Hamilton, and M. A. Tarbell, "Autonomous exploration of planetary lava tubes using a multi-rover framework," *IEEE Aerospace Conference Proceedings*, vol. 2015, June 2015. 129, 145

[133] F. Cordes, I. Ahrns, S. Bartsch, T. Birnschein, A. Dettmann, S. Estable, S. Haase, J. Hilljegerdes, D. Koebel, S. Planthaber, T. M. Roehr, M. Scheper, and F. Kirchner, "Lunares: Lunar crater exploration with heterogeneous multi robot systems," *Intelligent Service Robotics*, vol. 4, no. 1, pp. 61–89, 2011. 129, 145

[134] F. Cordes and F. Kirchner, "Reconfigurable integrated multirobot exploration system (rimres): Heterogeneous modular reconfigurable robots for space exploration," *Journal of Field Robotics*, vol. 31, pp. 3–34, January 2014. 129

[135] N. Y. Lii, D. Leidner, A. Schiele, P. Birkenkampf, R. Bayer, B. Pleintinger, A. Meissner, and A. Balzer, "Simulating an extraterrestrial environment for robotic space exploration: the meteron supvis-justin telerobotic experiment and the solex proving ground," in *13th Symposium on Advanced Space Technologies in Robotics and Automation (ASTRA)*, (ESA/ESTEC, Noordwijk, the Netherlands), May 2015. 129, 143

[136] G. A. Seriani S, Gallina P, "A modular cable robot for inspection and light manipulation on celestial bodies," *Acta Astronautica*, 2016. 129

[137] J. R. Johnson, W. M. Grundy, and M. T. Lemmon, "Dust depostion at the mars pathfinder landing site: Observations and modeling of visible/near-infrared spectra," *Icarus*, vol. 163, no. 2, pp. 330–346, 2003. 143

[138] K. M. Kinch, J. Sohl-Dickstein, J. F. Bell III, J. R. Johnson, W. Goetz, and G. A. Landis, "Dust deposition on the mars exploration rover panoramic camera (pancam) calibration targets," *Journal of Geophysical Research E: Planets*, vol. 112, p. 6, 2007.

[139] J. L. Campbell, P. L. King, L. Burkemper, J. A. Berger, R. Gellert, N. I. Boyd, G. M. Perrett, I. Pradler, L. Thompson, K. S. Edgett, and R. A. Yingst, "The mars science laboratory apxs calibration target: Comparison of martian measurements with the terrestrial calibration," *Nuclear Instruments and Methods in Physics Research, Section B: Beam Interactions with Materials and Atoms*, vol. 323, pp. 49–58, 2014. 143

[140] M. C. A. L. Nelson, K. W. Folley, *Differential Equations*. D. C. Heath & Co., 1952. 190

Declaration

The thesis work was conducted from 1st January 2013 to 31st December 2015 under the supervision of Prof. Paolo Gallina at the *University of Trieste* (*Università degli Studi di Trieste*).

Trieste,